Improved quantum control of two-dimensional ion crystals in a Penning trap

by

Bryce B. Bullock

B.A., Tulane University, 2018

M.S., University of Colorado Boulder, 2020

A thesis submitted to the

Faculty of the Graduate School of the

University of Colorado in partial fulfillment

of the requirements for the degree of

Doctor of Philosophy

Department of Physics

2025

Committee Members:

Ana Maria Rey, Chair

John Bollinger

Murray Holland

Eric Cornell

Greg Rieker

Bullock, Bryce B. (Ph.D., Physics)

Improved quantum control of two-dimensional ion crystals in a Penning trap

Thesis directed by Prof. Ana Maria Rey and Dr. John Bollinger

Trapped ions are a platform offering exquisite quantum control of small systems, placing them at the frontier of quantum metrology, simulation, and computation. This thesis describes advances in scaling to large ion numbers using two-dimensional ion crystals confined in a Penning trap. Global control of the axial collective center-of-mass (COM) motional mode, coupled to each ion's spin degree of freedom, enabled a quantum simulation of the Dicke model-a fundamental model of quantum optics exhibiting dynamical phase transitions, entanglement generation, and chaotic dynamics. The Penning trap platform allows exploration in a chaotic regime where the collective bosonic degree of freedom participates strongly in the dynamics while remaining highly coherent with minimal dissipation.

Moving beyond global interactions, a novel addressing scheme is demonstrated using a deformable mirror to impart patterned spin rotations onto the ion crystal, which rotates at ∼180 kHz. Using this deformable mirror has also allowed temperature diagnostics of previously poorly characterized in-plane modes in the rotating frame of the crystal. These temperature diagnostics have allowed detailed study of a new cooling technique for the in-plane modes involving a driven coupling between in-plane modes called axialization. Previous studies of axialization in Penning traps have been limited to small systems and coupling between COM modes of motion, with unique previously unexplored dynamics occurring in larger systems. This coupling has allowed roughly an order-of-magnitude reduction in the in-plane temperature, a fundamental issue limiting the stability of the axial modes.

Dedication

For my wife, Adrian, for her never-ending support.

Acknowledgements

Working in the ion storage group on the Penning trap experiment has been an absolute honor. First and foremost I want to thank my advisor John Bollinger. John is the best advisor you could possibly ask for, and I am forever thankful that he let me join the project. Thank you to all former members of the Penning trap experiment, who have produced an absolute marvel of engineering that allows amazing results to keep coming out of the experiment decades on. The success of this thesis is in large part thanks to the experimental contributions of postdocs Matt Affolter, Jenni Lilieholm, and Allison Carter (now staff), who all endured the nightmare of the magnet saga that halted experiments for three years, and new additions postdoc Kurt Thompson and graduate student Diep Nguyen. Special thanks to Adam Shepheard from Scientific Magnetics for traveling to Boulder twice to save my PhD with a heroic weld job to repair the magnet. I am also thankful for theory contributions, in particular from Wes Johnson for theory on cooling the in-plane modes and Sean Muleady for theory contributions on the Dicke model. These results would not be possible without the further theory contributions from Ana Maria Rey, Yicheng Zhang, Robert Lewis-Swan, Arghavan Safavi-Naini, and Athreya Shankar. I also have had an enormous amount of assistance from the ion storage group at large, who are the most incredibly talented and kind group of people you could hope to work with.

On a personal note, I want to thank all the amazing friends I've met who made these seven years an absolute blast. In particular I want to thank Jenni, who has been my German-wheeling, rock-hounding, trapezing partner in crime. Finally, no person helped me more to achieve this thesis than my wife, Adrian, whose love and support have made me the luckiest man on the planet.

Contents

Chapter

Appendix

Tables

Table

Figures

Figure

Chapter 1

Introduction

Working with large-scale quantum systems while maintaining useful quantum coherence is an inherently challenging but exciting regime to be in. The NIST Penning trap experiment has pushed on this frontier, and this thesis builds on that work to further improve the control and tools available to the system.

1.1 NIST Penning trap platform

Trapped ion systems are quantum systems that have demonstrated excellent quantum control, from high-fidelity gates [1, 2] to atomic clocks [3, 4] to precise atomic sensors [5–7]. However, generally these systems work with oscillating electric fields to confine the ions, and are often difficult to scale up to larger sizes while not having detrimental effects from these oscillating fields. Enter the Penning trap, an ion trap that instead utilizes static electric and magnetic fields to confine the ions. Penning traps are often utilized in precision measurement regimes of single particles where the strong magnetic field can allow precision measurements of g-factors and masses of fundamental particles [8–12]. However, in the NIST platform, large ion numbers are readily trapped, cooled until crystallized, and controlled to form 2D crystals [13].

While easily allowing systems of hundreds of ions or even thousands in a 3D geometry to be confined, the Penning trap suffers from a fundamental new challenge where the crystal undergoes rigid body rotation generally at tens to hundreds of kHz. This constraint has made local control of each ion in the rotating frame challenging. Additionally, motion in the plane has been historically difficult to cool and limited the stability and control of the system. The fundamental challenge of 2D arrays in Penning traps is to see how much control can be engineered back into the system, a fundamentally different strategy than many trapped ion quantum information experiments that start with incredible control of a few ions and engineer ways to scale up the system.

Like many ion trap experiments, the system relies on exquisite control of the collective motion of the ions and the spin degree of freedom of each ion. The collective motion comes from each ion acting as a harmonic oscillator in the quadratic confining potential, with each ion strongly coupled to all other ions via the Coulomb repulsion. The spin degree of freedom in our system is roughly the valence electron spin of each $^9\mathrm{Be}^+$ ion. Previous demonstrations in our apparatus include generation of spin-squeezing [14], or equivalently large-scale entanglement between ~ 100 spins, quantum simulations [15–17], near ground state cooling of ~ 100 collective motional modes [18, 19], and precision sensing of weak electric fields below the standard quantum limit [6].

1.2 The NIST Penning trap superconducting magnet

This thesis would not be complete without taking a detour to address the magnet in the room. The NIST superconducting magnet was built around 1990 by Nalorac and ran for approximately 30 years, rarely ever being intentionally warmed up from cryogenic temperatures. After a series of increasingly common quench events, in which the coil runaway heats by having a segment of wire go into a normal resistance state and then dissipates the current, the original coil produced its last magnetic field of more than a Tesla on July 1st 2021. In that final quench the overprotection circuit presumably failed or was broken and dissipated all the heat into the main coil, burning it and producing a small nonzero resistance in the coil. In hindsight, the ultimate reason for this quench was likely due to a small air leak in the helium tower that, particularly in the last few years of use, built up frozen air on the pins used to connect to the magnet coil. To make a connection to the coil, increasingly risky amounts of heat had to be applied to de-ice the pins to allow a clean connection with a demountable lead. Figure 1.1 shows a schematic of the magnet and image of the disassembled magnet during repair.

After making modifications to the trap, baking it out, and re-inserting it into the magnet, the magnet was discovered to be broken in October of 2021. After a few months, the magnet was shipped off to Scientific Magnetics in London for them to retrofit the system with a new coil. Fast forward more than a year of delays, and the magnet arrived from shipping in January 2024. In the retrofitting process a non-ideality was found that requires the liquid helium level to be below around 42% full, or else the heater that allows opening up a connection to the main coil is submerged in liquid helium and cannot open the switch. Additionally, the 4 K can had to be replaced because of an unknown corrosion of the previous aluminum can, making a leak tight weld impossible. The replacement 4 K can is stainless steel which may contribute to the higher helium boil-off rate which increases as the helium levels falls over time.

After hoisting the magnet onto the optics table, it was soon discovered that the weld joints suspending the main 4 K can in the magnet had failed in shipping. After two separate week long visits from an engineer at Scientific Magnetics, the magnet was repaired on site, requiring two blind welds in roughly a 1 inch gap below the chandelier structure and using a mirror to see the weld around the tube attaching to the 4 K can. In this process a liquid helium level meter and a G-10 tube that suspends the coil connection pins broke. A replacement level meter was taken from a retired magnet and a new G-10 tube was manufactured. This weld strategy was not the intended assembly process, with a nesting series of cans and shields needing to be aligned to not have any thermal shorts. This required straps to pull the various cans into alignment to allow enough tolerance on the centering of the assemblies. These straps were in place previously but not under such high tension. When inserting the G-10 tube into the re-welded tube it was found there was a lip that was too large for the tube to fit through. The G-10 tube was therefore cut such that the connection pins are mounted higher up inside the 4 K suspension tubes, potentially leading to a higher boil-off rate, and requiring an additional extension connection to allow the set length demountable lead to seal when inserted.

The magnet finally was ramped up again and stayed at its set field at almost exactly midnight, May 6th, 2024, 37 hours after it had been ramped but failed to form a closed superconducting loop.

Over the 37 hours the magnetic field quickly dropped, likely due to a small non-zero resistance due to the low liquid helium level that prevented the superconducting switch from completely closing. After this a number of connections have successfully been made to modify the currents in the various shim coils in the magnet without much issue. In the intervening emotional rollercoaster of three years while the magnet was down no experiments could be carried out. Extensive work on experimental upgrades and preparation for the magnet's arrival have led to this thesis, with all experimental results covered occurring in the approximate 16 months since the magnet was ramped back to field.

1.3 Outline

This thesis starts with a description of background physics of Penning traps, particularly in the crystallized regime with many ions in chapter 2. Chapter 3 then describes an outline of key experimental subsystems. Chapter 4 finishes out background material by covering the series of calibrations and alignments used to carry out more interesting experiments.

Compared to previous work, this thesis covers one new experimental demonstration and three new experimental tools. Chapter 5 covers a new quantum simulation of the Dicke model, a fundamental model of quantum optics that exhibits many rich physical phenomena. Included in that simulation are previously experimentally unexplored chaotic dynamics in the Dicke model and genuinely quantum dynamics that are not captured at the mean-field level and where dissipation and decoherence play minimal role. Chapter 6 describes a new tool in the experiment called a deformable mirror (DM). This has allowed patterned addressing and, with the addition of a new camera, individual single-shot readout of the ions in contrast to global interactions and measurements in all prior experiments. Chapter 7 describes two new tools: direct temperature measurements of the in-plane motion and a new cooling technique. This improved cooling is currently under investigation, but has allowed roughly an order of magnitude improvement in temperatures of the in-plane modes, with profound future consequences to the fidelity and control possible in future experiments. Chapter 8 concludes with an outlook on a handful of future directions of the experiment.

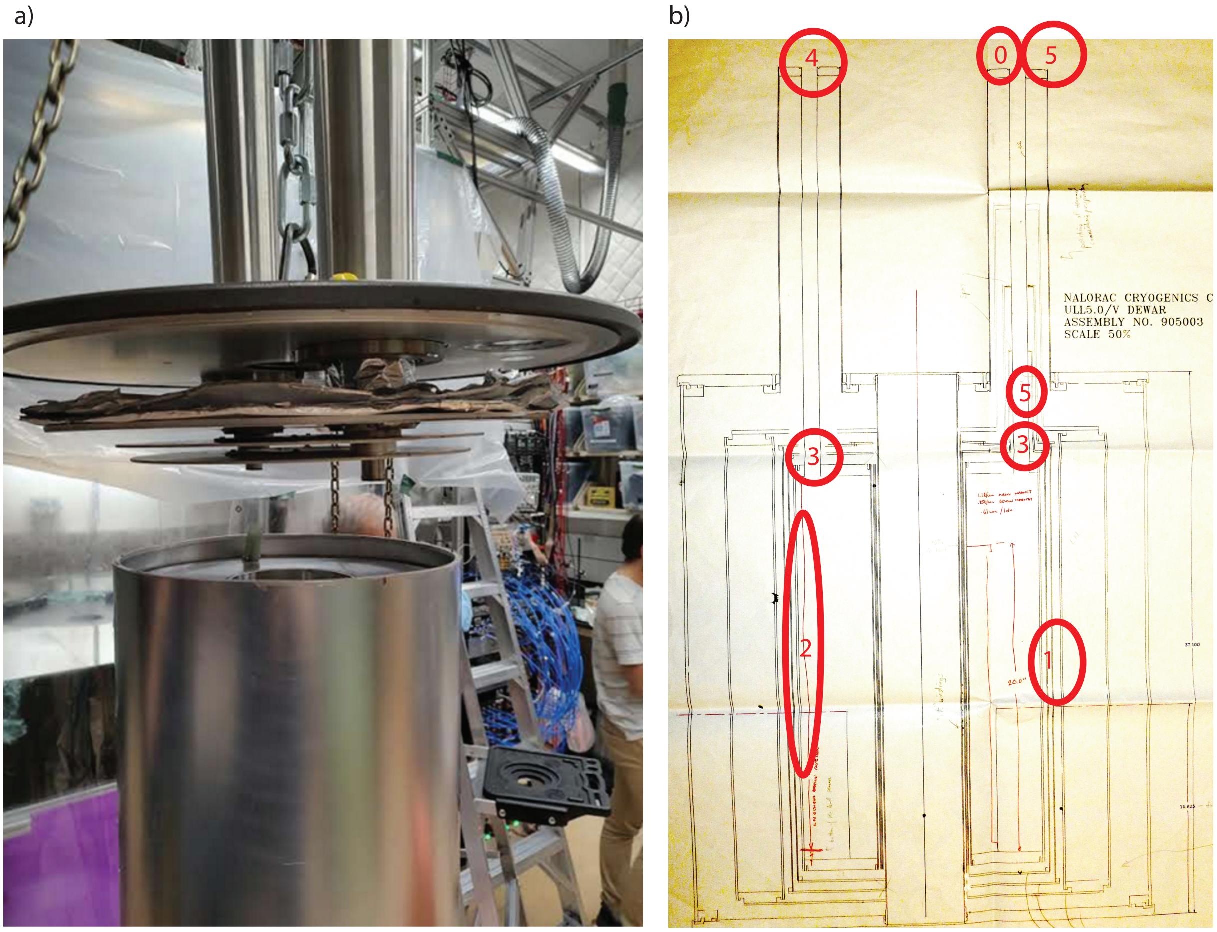

Figure 1.1: Schematic of the magnet and an image of the disassembled magnet. a) The 4 K can with 50 K shield around it is detached from the chandelier structure that suspends all shields and cans. The suspension tubes have broken at the weld joint and jut out from the chandelier structure. The broken green G-10 tube attached to the magnet coil sticks out of the 4 K can. b) Original Nalorac schematic of the magnet with circled numbered areas of major events affecting the magnet repair. 0: The original air leak at the top of the helium tower. 1: The original coil burned out requiring replacement. 2: The aluminum 4 K can was replaced with a stainless steel can due to unknown corrosion of the aluminum can preventing a leak-tight seal. 3: Broken weld joint of the two suspension tubes which were damaged in shipping. 4: Replaced liquid helium fill meter. 5: Replaced G-10 tube which required seating the coil connection pins up the suspension tube rather than inside the 4 K can.

Chapter 2

Penning Trap Physics

This chapter will describe the background physics of large ion crystals in a Penning trap.

2.1 Penning traps

To confine charged particles in three dimensions, one would like a force pointing inward along all three coordinate directions. However, because of Gauss's law, this geometry is not possible using only static electric fields, as there would be a non-zero electric flux. To circumvent this, most ion traps utilize either oscillating electric fields in what is called a Paul, or radio-frequency (RF), trap, or static electric and magnetic fields in what is called a Penning trap [20]. It is worth noting a major drawback of RF traps is micromotion, which is driven motion from the oscillating electric fields when ions are displaced from the null of the electric field gradient. Micromotion is a significant part of why ion traps often utilize 1D chains, as that is the only geometry in which a collection of ions can be confined in the same harmonic well without micromotion. This limitation has restricted most ion trap experiments to 1D geometries of fewer than approximately 50-100 ions. Recent developments in trap fabrication have allowed demonstrations of 2D geometries and larger system sizes in RF traps which constrain all the micromotion to the plane of the crystal [21–23].

In contrast, the Penning trap allows for 2D and 3D geometries with no driven motion, since all confining fields are static. Instead, Penning traps enjoy the challenge of having all ions collectively rotate around the magnetic field to maintain confinement. For this reason, most quantum information trapped ion experiments opt for an RF trap, however, our experiment looks to overcome this challenge with the promise of large system sizes. One way to view this distinction is that the non-thermal degree of freedom corresponds to a rigid body rotation that does not couple into the internal degrees of freedom of the normal modes, unlike the driven micromotion.

Confinement along the magnetic-field axis in a Penning trap is achieved with a static electric quadrupole potential produced by segmented electrodes with DC voltages applied. This produces a radially deconfining electric field perpendicular to the magnetic field, which due to an $\vec{E} \times \vec{B}$ drift force causes the ion to precess around the electric field null. This precession produces the velocity component that gives rise to a radially confining $\vec{v} \times \vec{B}$ Lorentz force. Assuming a perfect electric quadrupole and static axial magnetic field, the equations of motion for a single charged particle are:

$$\Phi = \frac{V}{2R^2}(z^2 - (x^2 + y^2)/2) \tag{2.1}$$

$$\ddot{z} = -\omega_z^2 z \tag{2.2}$$

$$\ddot{x} = \omega_c \dot{y} + \frac{\omega_z^2}{2} x \tag{2.3}$$

$$\ddot{y} = -\omega_c \dot{x} + \frac{\omega_z^2}{2} y, \tag{2.4}$$

where Φ is the applied electric quadrupole potential with characteristic voltage V and electrode radius R, $\omega_z = \sqrt{\frac{qV}{mR^2}}$ is the axial oscillation (trap) frequency, and $\omega_c = \frac{qB}{m}$ is the (bare) cyclotron frequency. The axial motion decouples from the in-plane degrees of freedom and can be well described by a simple harmonic oscillator

$$z(t) = z_0 \sin(\omega_z t - \phi_0). \tag{2.5}$$

In contrast, the in-plane degrees of freedom do not separate into independent simple harmonic oscillator modes along Cartesian directions. We shall see in the multi-ion case that it turns out to be useful to solve the in-plane equations of motion in a rotating frame rotating at frequency ω_r about an axis antiparallel to the magnetic field. This does not modify the axial degrees of freedom, and produces in-plane forces and equations of motion of the form

$$F' = F - 2m\vec{\omega}_r \times \vec{v}_R - m\vec{\omega}_r \times \vec{\omega}_r \times \vec{r}_R - q\vec{\omega}_r \times \vec{r}_R \times \vec{B} \tag{2.6}$$

$$\ddot{x}_R = \omega_c'\dot{y}_R - \omega_\perp^2 x_R \tag{2.7}$$

$$\ddot{y}_R = -\omega_c'\dot{x}_R - \omega_\perp^2 y_R \tag{2.8}$$

$$\omega_c' = \omega_c - 2\omega_r \tag{2.9}$$

$$\omega_\perp^2 = \omega_r\omega_c - \omega_r^2 - \frac{\omega_z^2}{2}. \tag{2.10}$$

Equation 2.6 lists all of the force modifications from the lab frame F to the rotating frame F'. These include the velocity-dependent Coriolis force, radially deconfining centrifugal force, and radially confining Lorentz force from left to right [24]. Combining these effects gives an effective cyclotron frequency ω_c' and effective radial confinement $\omega_\perp$ for coordinates in the rotating frame x_R, y_R. Setting the rotation frequency $\omega_r = 0$ (i.e. returning to the lab frame) returns our original equations of motion 2.3-2.4.

By solving for the eigenvalues of the in-plane equations of motion, we find

$$\begin{pmatrix} \dot{x}_R \\ \dot{y}_R \\ \ddot{x}_R \\ \ddot{y}_R \end{pmatrix} = \begin{pmatrix} 0\ 0\ 1\ 0 \\ 0\ 0\ 0\ 1 \\ -\omega_\perp^2\ 0\ 0\ \omega_c' \\ 0\ \omega_\perp^2\ \ -\omega_c'\ 0 \end{pmatrix} \begin{pmatrix} a \\ b \\ c \\ d \end{pmatrix} = -i\lambda \begin{pmatrix} a \\ b \\ c \\ d \end{pmatrix} \tag{2.11}$$

$$\begin{pmatrix} a \\ b \\ c \\ d \end{pmatrix} \propto \begin{pmatrix} 1 \\ \pm_1 \pm_2 i \\ -i\lambda_{\pm_2} \\ \pm_1 \pm_2 \lambda_{\pm_2} \end{pmatrix} \tag{2.12}$$

$$\pm_1\lambda_{\pm_2} = \pm_1 \frac{\pm_2\omega_c' + \sqrt{\omega_c'^2 + 4\omega_\perp^2}}{2} = \pm_1(\mp_2\omega_r + \frac{\pm_2\omega_c + \sqrt{\omega_c^2 - 2\omega_z^2}}{2}). \tag{2.13}$$

Two eigenvalues $\lambda_{\pm_2}$ are found with a positive and negative copy $\pm_1$ of each. These eigenvalues and eigenvectors show the in-plane motion can be decomposed into two independent circular motions $\begin{pmatrix} x_R \\ y_R \end{pmatrix}(t) \propto \begin{pmatrix} \cos(\lambda_{\pm_2}t) \\ \mp_2\sin(\lambda_{\pm_2}t) \end{pmatrix}$. The first motion is a high-frequency modified cyclotron motion at λ_+, which in the lab frame ($\omega_r = 0$) corresponds to clockwise motion at $\lambda_+(\omega_r = 0) = \omega_+ = \frac{\omega_c + \sqrt{\omega_c^2 - 2\omega_z^2}}{2}$ called the modified cyclotron frequency. The second motion is a low-frequency magnetron motion rotating at λ_-, which is negative in the lab frame. The magnetron motion in the lab frame is therefore associated with clockwise motion at $-\lambda_-(\omega_r = 0) = \omega_- = \frac{\omega_c - \sqrt{\omega_c^2 - 2\omega_z^2}}{2}$ called the magnetron frequency. Shown in figure 2.1 is an example of the two superposed clockwise motions in the lab frame, or by the right-hand rule about a vector pointing in the opposite direction of the magnetic field.

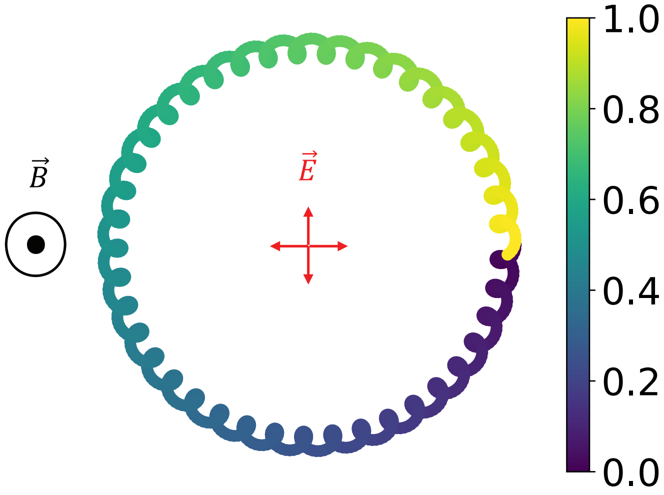

Figure 2.1: Planar motion of a single ion in a Penning trap. The radially deconfining $\vec{E}$ field (red arrows) combines with the out of plane $\vec{B}$ field to cause clockwise $\vec{E} \times \vec{B}$ magnetron motion in the lab frame. This is represented by the larger, slower frequency circular orbit with the color scale representing time increasing going from purple to yellow. Cyclotron motion, corresponding to the faster smaller circular orbits, also rotates clockwise due to the $\vec{v} \times \vec{B}$ Lorentz force. The axial motion would be represented by oscillating in and out of the page at a frequency in between the cyclotron and magnetron frequencies.

Given these large motional frequency differences, it becomes apparent that the high frequency cyclotron motion is kinetic energy dominant and the low frequency magnetron motion is potential energy dominant. This is because the potential energy is given by $\frac{1}{2}\omega_\perp^2 \rho^2$ and is mode frequency-independent, whereas the kinetic energy is motional frequency dependent $\frac{1}{2}\omega_\pm^2 \rho^2$. This is in contrast to simple harmonic oscillator motion that has equal kinetic and potential energy. Looking more closely at this peculiarity: the magnetron motion is not only potential-energy-dominant but also negative energy in the lab frame. This is because the potential energy for the in-plane motion is an unstable potential energy hill from the deconfining electric field. Therefore, the lowest-energy magnetron motion corresponds to ever-larger orbits, until eventually the ion crashes into the electrodes and is no longer trapped. Fortunately, ambient torques in the experiment are small enough that this time scale can be many hours or even days. Cooling of the magnetron motion is therefore defined as adding energy to the magnetron mode to reduce its positional displacement from the center of the trap. Additionally, a stability criterion appears that the axial motional mode frequency be $\omega_z^2 \leq \omega_c^2/2$. At larger axial trap frequencies the radially deconfining electric field is too strong to maintain confinement from the Lorentz force and the trap is unstable. Lastly, note the important fact that $\omega_c = \omega_+ + \omega_-$. This fact along with its generalization to the Brown-Gabrielse invariance theorem [25] ($\omega_-^2 + \omega_+^2 + \omega_z^2 = \omega_c^2$), which holds to first order in trap imperfections, allows for very precise measurements of the mass of charged particles and the g-factors of fundamental particles [8–12].

2.1.1 Non-neutral plasma limit

In the limit of many ions confined by a magnetic field, the collective space charge plays an important role and a non-neutral plasma description becomes appropriate. Largely following the prescription of [26], pages 39-42, along with 110-115, assume a cylindrical non-neutral plasma column of uniform charge density n aligned with a magnetic field. The result of the space charge distribution is a radially deconfining electric field inside the plasma, pointing outward along the cylindrical radial coordinate r,

$$E_r(r) = \frac{m}{2q}\omega_p^2 r, \tag{2.14}$$

where $\omega_p^2 = \frac{nq^2}{\epsilon_0 m}$ is the plasma frequency, determined by the ion density n, charge q, and mass m of each ion. This radially deconfining force will cause an $\vec{E} \times \vec{B}$ drift around the central axis of the plasma column. An equilibrium rotation frequency is then reached that balances the radially deconfining electric and centrifugal force with the radially confining $\vec{v} \times \vec{B}$ force:

$$m\omega_r^2(r)r + m\frac{\omega_p^2}{2}r = qB\omega_r(r)r. \tag{2.15}$$

From this functional form it is clear that, to balance the forces, a rotation frequency independent of radius is required, and therefore non-neutral plasmas confined by a magnetic field undergo rigid-body rotation with a rotation frequency set by

$$n = \frac{2\epsilon_0}{q^2}m\omega_r(\omega_c - \omega_r). \tag{2.16}$$

Therefore, the radial confinement strength is set by the rotation frequency, which determines the ion density. At low rotation frequencies, the ion density is small, giving a small deconfining electric field and hence a low-frequency $\vec{E} \times \vec{B}$ drift. At high frequencies near the cyclotron frequency, the radial confinement is also weak and the ion density is low, with the centripetal acceleration dominating to counter the now much stronger Lorentz force. In between these two rotation frequencies is the Brillouin limit, where the ion density (and therefore radial confinement) is maximized at $\omega_r = \omega_c/2$.

The addition of an external axially confining (and therefore radially deconfining) electric potential largely preserves the above picture. This quadrupole potential supplies no space charge and so does not change the ion density. Instead, the boundary of the plasma deforms such that the space charge distribution cancels the effect of the applied external field, maintaining the above density–rotation frequency relationship while adding an aspect ratio dependence to the plasma (see figure 2.2). Additionally, a minimum deconfining electric field is now present, which changes the range of stable rotation frequencies to lie between the magnetron and modified cyclotron frequencies found previously. By adjusting the rotation frequency near the magnetron or modified cyclotron frequency, eventually the radial confinement becomes so weak that 2D crystals form. Varying the rotation frequency to increase the radial confinement from these points eventually forms two-plane, then multi-plane crystals, leading to the most axially elongated plasmas when rotating at the Brillouin frequency.

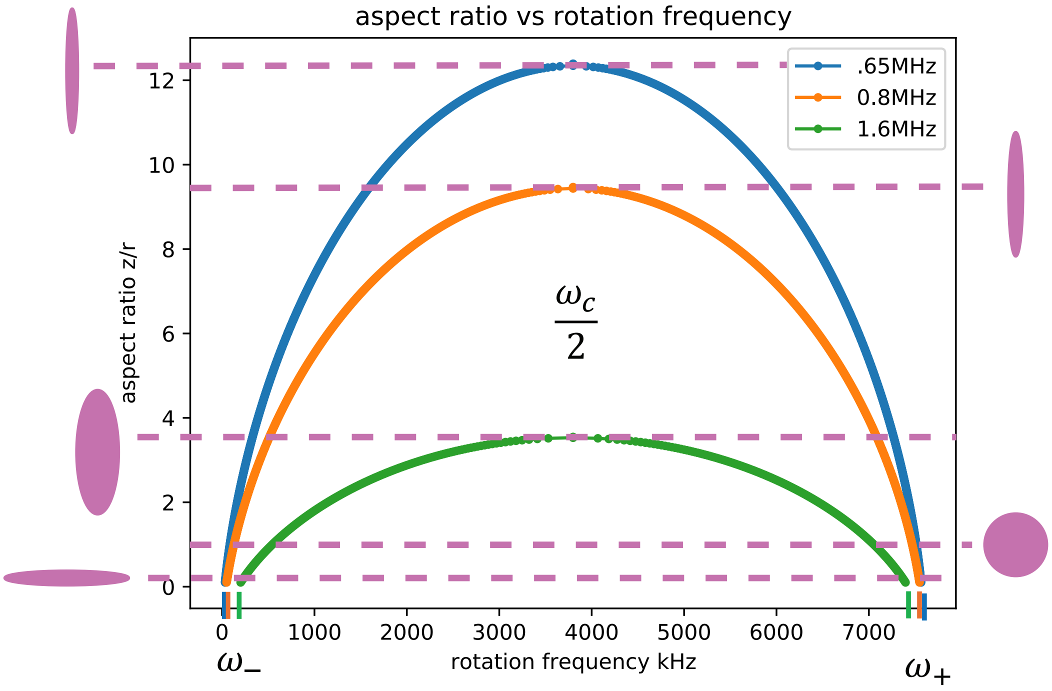

Figure 2.2: Aspect ratio of plasmas as a function of rotation frequency and axial confinement. The blue, orange, and green curves correspond to increasing axial confinement as defined by their axial trap frequencies of 0.65, 0.8, and 1.6 MHz respectively at our cyclotron frequency $\omega_c \approx 7.6$ MHz. For stronger axial confinement the plasma boundary compresses axially to reduce the axial to radial aspect ratio of the cloud while maintaining the same density. As the rotation frequency is varied the radial confinement is changed along with the cloud density. At the Brillouin frequency, $\omega_c/2$, the radial confinement is strongest with the corresponding most elongated axial plasma and highest density. Near the magnetron (ω_-) and modified cyclotron frequencies (ω_+) the ion density is lowest and the radial confinement is weakest, forming the most compressed axial plasmas eventually forming single plane plasmas. The cutoff of stable rotation frequencies is set by $\omega_\pm$, which converge towards $\omega_c/2$ for increasing axial trap frequency. Selected aspect ratio clouds are shown in pink including planar clouds near $\omega_\pm$, spherical clouds at aspect ratio 1, and the most elongated crystals for each axial trap frequency.

2.2 Rotating wall

Experimentally, we apply torques to the crystal that depend on the plasma configuration, and the system naturally reaches a steady-state rotation frequency determined by the balance of torques. Left unperturbed, the crystal slowly loses rotational inertia due to trap imperfections and dissipation of energy into image currents in the electrodes. Over timescales of many hours to days the ions would eventually spin out into the walls of the electrodes. By applying a rotating electric potential with a specific rotation frequency and geometry, we can precisely lock the rotation of the crystal to the potential and control the cloud's rotation frequency. This is accomplished by applying a "rotating wall potential" [27]. The simplest rotating wall potential to understand is a rotating quadrupole. If a rotating potential of the form

$$U = V\rho_{lab}^2 \cos(2(\phi_{lab} + \omega_r t)) = V(x_R^2 - y_R^2), \tag{2.17}$$

is applied, it exerts a torque on clouds that are not rotating at the frequency of the wall. Once the crystal rotation frequency matches that of the wall, the system reaches an equilibrium configuration. Based on the geometry of an mth azimuthal order wall (e.g. m=2 quadrupole wall above), the crystal deforms— stretching along directions where the electric field points outward and compressing where it points inward, as shown in figure 2.3. This results in m azimuthal directions of elongation and m directions of compression. For an m=2 quadrupole wall, this leads to an elliptical crystal, with a stronger rotating wall producing a more elliptical crystal. For an $m = 3$ wall, this produces a triangular crystal, with the three vertices being stretched along where the electric field points outward and the midpoints of the three edges compressed where the electric field points inward. Lastly, an $m = 1$ wall, called a dipole wall, is a uniform rotating electric field in the plane. In principle, this should cause no torque on the ions —only a center-of-mass excitation— and so should not lock the rotation of the crystal. However, ions of different mass will centrifugally separate, with heavier masses experiencing more drag and moving to the outermost edges of the crystal. This mass disparity can enable the dipole potential to lock the crystal rotation, and will displace the center of mass of the two species in the rotating frame [28]. In our system, background gas collisions with hydrogen slowly form BeH^+ over time, which further reacts with other background gases to form $BeOH^+$. Previous demonstrations in our apparatus removed the hydrides by using a 157 nm excimer pulsed laser [29]. However, the laser is no longer installed because evacuating the beam path, necessary to prevent attenuation in air, requires significant overhead. Additionally, during a trap modification to reduce background light scatter, a CaF mirror was removed that previously allowed the beam to be sent from the side of the vacuum system down the vacuum envelope (see section 3.2.1).

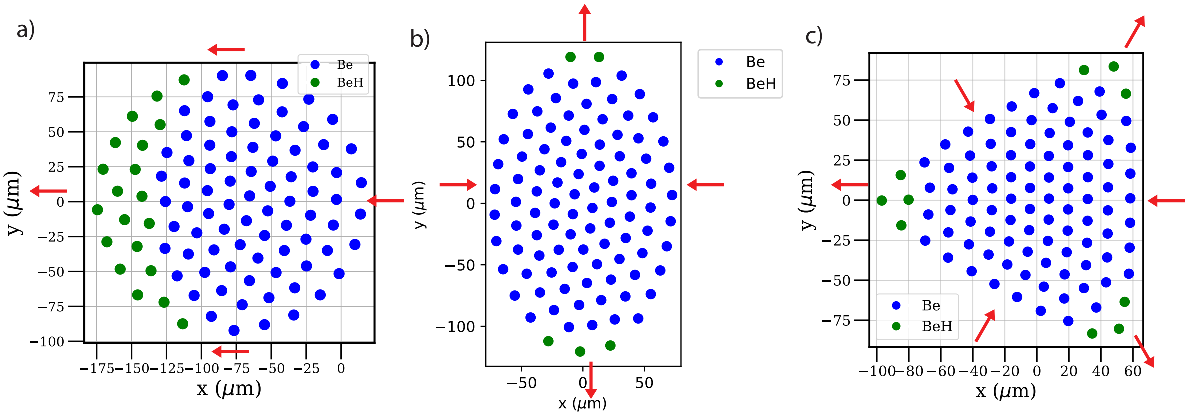

Figure 2.3: Varying order m rotating wall equilibrium crystal configurations in the rotating frame. Simulations done with $\omega_r = 180$ kHz, $\omega_z = 1.5925$ MHz, $B \approx 4.459$ T and 100 ions. a) A dipole $m = 1$ wall is a static uniform electric field in the rotating frame (red arrows), which displaces the crystal to rotate about an off center position. Due to centrifugal separation the heavier BeH$^+$ (green dots) ions go to the further edge of the crystal. b) A quadrupole $m = 2$ wall deforms the crystal into an elliptical shape with the hydrides going to the furthest extended points of the crystal. The static electric potential in the rotating frame deforms the boundary (red arrows). c) A hexapole $m = 3$ wall creates a triangular boundary due to the geometry of the static electric potential in the rotating frame.

2.3 Normal modes

Having discussed the general motion of ions in a Penning trap, a final key feature is the normal mode structure of the crystal when cooled sufficiently. Due to the mutual Coulomb repulsion of the ions, the many-ion crystal will form a collection of 3N collective harmonic oscillator modes. Uniquely in Penning traps, these modes are not simple harmonic oscillators due to the velocity-dependent vector potential modifying the quantization procedure, producing two mode branches for the in-plane motion with characteristics analogous to the magnetron and cyclotron motions of a single particle. For a detailed description of the quantization procedure of harmonic oscillator modes in the presence of a vector potential, the group has historically used [24], which has been adapted to a Python code to simulate 2D crystal configurations and mode structures. More recently, a formal and general derivation from a classical mechanics perspective is given by [30], and has been adapted by Wes Johnson to produce simulations of generalized potentials, including 3D crystals, multiple masses, and dipole walls. Below I follow the derivation of [31] which I find the most approachable and physically intuitive.

To begin, we rewrite the equations of motion for an ion j, this time for a many-ion crystal in a Penning trap.

$$\dot{v}_j^z = -\omega_\parallel^2 z_j + \frac{ke^2}{m}\sum_{i\neq j}\frac{z_j - z_i}{r_{ij}^3} \tag{2.18}$$

$$\dot{v}_j^x = -(\omega_\perp^2 + \omega_W^2)x_j + \omega_c' v_j^y + \frac{ke^2}{m}\sum_{i\neq j}\frac{x_j - x_i}{r_{ij}^3} \tag{2.19}$$

$$\dot{v}_j^y = -(\omega_\perp^2 - \omega_W^2)y_j - \omega_c' v_j^x + \frac{ke^2}{m}\sum_{i\neq j}\frac{y_j - y_i}{r_{ij}^3}. \tag{2.20}$$

These equations have been modified to include the mutual Coulomb repulsion between ions and the presence of a quadrupole rotating wall of strength ω_W. Using these equations of motion, a crystal configuration of ions can be found that minimizes the potential energy, or equivalently where the net force vanishes in the rotating frame (equations 2.18-2.20 equal 0). Taylor expanding for small deviations from these equilibrium configurations ($s_j = s_j^0 + \delta s_j, s \to x, y, z$), the equilibrium position terms s_j^0 cancel. For 2D crystals the first order expansion produces a linear eigenvalue equation of the form:

$$\frac{d}{dt}\left|v_\perp\right\rangle = -\frac{K_\perp}{m}\left|\delta r_\perp\right\rangle + L\left|v_\perp\right\rangle \tag{2.21}$$

$$\frac{d}{dt}\left|v_z\right\rangle = -\frac{K_\parallel}{m}\left|\delta z\right\rangle. \tag{2.22}$$

Here $K_\perp$ and $K_\parallel$ are real, symmetric stiffness matrices describing the couplings between the oscillators that generate the normal modes. However, L is a unique antisymmetric velocity-dependent force that complicates solving for eigenvalues and eigenvectors. Complete descriptions of $K_\perp, K_\parallel$ are given in [24]. For the simpler case of the axial motion, $K_\parallel$ takes the form

$$K_\parallel = \begin{pmatrix} m\omega_\parallel^2 - ke^2 \sum_{1\neq j} \frac{1}{R_{1,j}^3} & \frac{ke^2}{R_{1,2}^3} & \frac{ke^2}{R_{1,3}^3} & \cdots \\ \frac{ke^2}{R_{2,1}^3} & m\omega_\parallel^2 - ke^2 \sum_{2\neq j} \frac{1}{R_{2,j}^3} & \frac{ke^2}{R_{2,3}^3} & \cdots \\ \vdots & \ddots & \ddots & \ddots \end{pmatrix}, \tag{2.23}$$

where $R_{i,j}$ is the distance between ions i, j. Solving for the eigenvectors and eigenvalues gives the axial drumhead modes. The highest frequency mode is the axial center-of-mass (COM) mode with eigenvalue (energy) ω_z, where all ions uniformly move in phase in the axial direction. Going down in frequency the drumhead modes produce shorter spatial wavelength modes. For example, the next pair of modes are two orthogonal tilt modes, then two orthogonal quadrupole modes. The sequence of drumhead modes is given in figure 2.4.

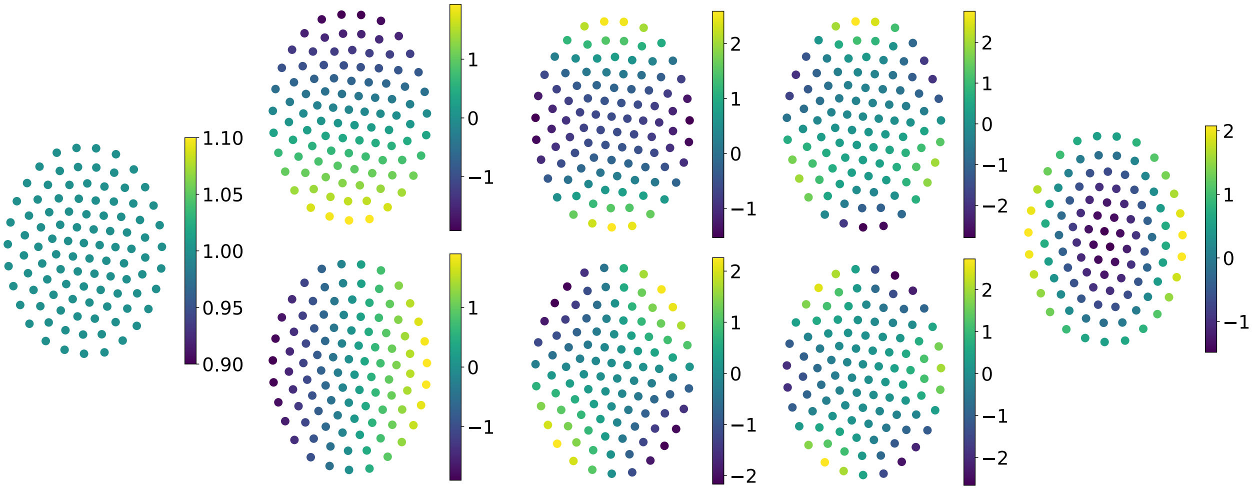

Figure 2.4: Eigenvector mode participations, represented by the color of each ion, of the 8 highest frequency drumhead modes scaled by $\sqrt{N} = 10$. From left to right corresponds to decreasing frequency modes, with the middle 6 modes coming in near-degenerate pairs with the higher energy pair on the top row. The degeneracy of each mode is lifted due to the elliptical aspect of the crystal from the rotating wall, which is slightly taller than wider in these images.

Solving for the normal modes of the in-plane motion largely follows from the single-ion case: composite 4N dimensional position/velocity vectors are required, with the matrix form of the eigenvalue equation matching the single particle form, but now with off diagonal terms analogous to the axial case. Explicitly, the eigenvalue equation takes the form

$$\begin{pmatrix} 0_{2N\times 2N} & I_{2N\times 2N} \\ -K_{\perp}/m & L \end{pmatrix} \begin{pmatrix} \delta r_{\perp} \\ v_{\perp} \end{pmatrix}_n = -i\omega_n \begin{pmatrix} \delta r_{\perp} \\ v_{\perp} \end{pmatrix}_n , \tag{2.24}$$

where 0 is a matrix of zeros and I is the identity. The single ion case reduces to 2.11, where the key characteristics of these in-plane modes were identified. A peculiarity of these modes however is now that the rotating frame frequency ω_r is well defined, the normal mode characteristics are different than the lab frame. In particular, taking positive eigenvalues the single ion eigenvectors position components take the form $\begin{pmatrix} 1 \\ \mp i \end{pmatrix}$ for eigenvalues $\omega_{\pm}$. This corresponds to opposite helicity (handedness) rotation for the cyclotron motion compared to the magnetron motion in the rotating frame. Additionally, the magnetron modes now become positive energy in the rotating frame.

The sequence of normal modes for the in-plane motion is given in figure 2.5, while animations of the modes can be found in reference [24]. The cyclotron branch mirrors the drumhead modes, now with entirely clockwise (CW) motion proportional to the participation of each ion and either in phase or out of phase depending on the sign of participation. The lowest frequency cyclotron mode is the COM mode, and higher frequency modes mirror the drumhead branch such as the tilt and quadrupole modes. In contrast, the lowest frequency magnetron mode is (usually) the rocking mode, which is a combination of nearly equal CW and counterclockwise (CCW) rotation. With no preferred direction to break the azimuthal symmetry, this mode approaches zero frequency in the limit of no rotating wall strength (and no impurities). For larger rotating wall strength, a larger aspect ratio crystal breaks the azimuthal symmetry to produce a larger rocking mode frequency. The magnetron COM motion falls arbitrarily in the magnetron mode number order, often the 7th or 8th lowest frequency mode for common crystals utilized. It consists of almost entirely uniform CCW motion, with a slight CW component from the asymmetry of the crystal due to the rotating wall. Aside from these two modes, no other magnetron modes are uniquely characterized. However, their motion dominantly consists of CCW motion in the rotating frame, and generally becomes more localized on the central ions at higher mode frequencies.

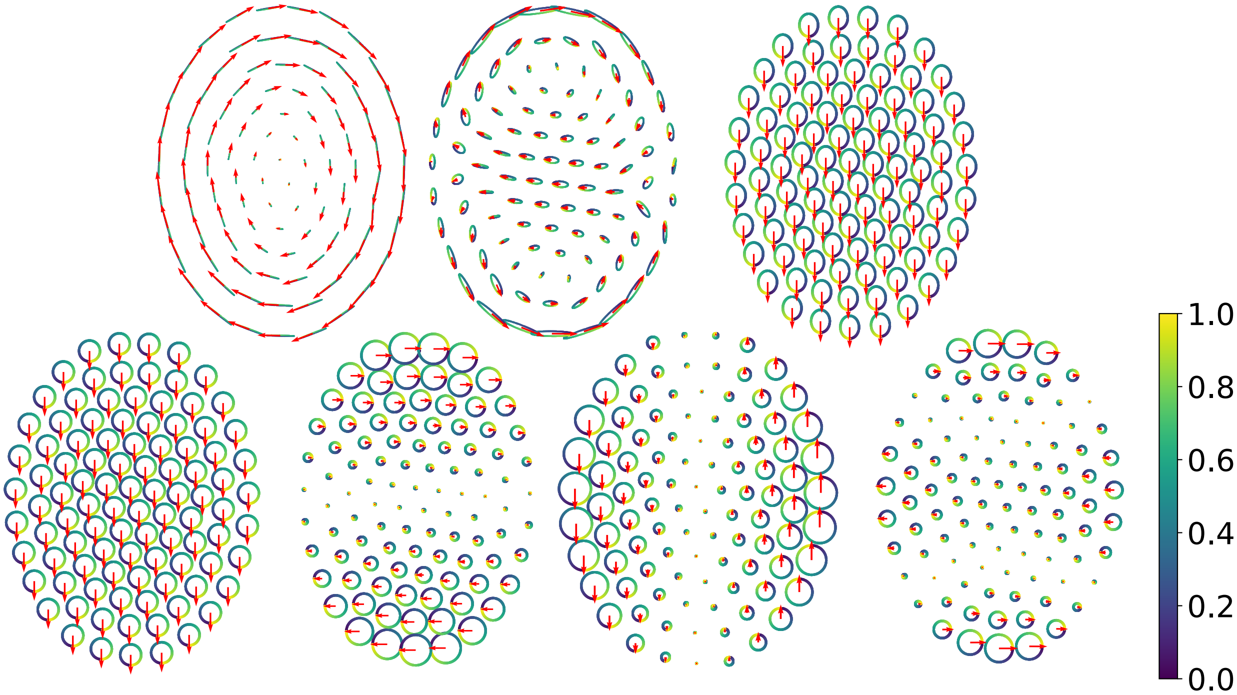

Figure 2.5: Spatial components of the mode participations of selected in-plane modes. The trap conditions are the same as figure 2.4. The red arrows represent a snapshot in time of the ions displaced from their equilibrium position, with the size and direction of the arrow determined by the eigenvectors of the mode. The colored traces represent a complete orbit of the motion with the color representing the motion over time. The top row represents the lowest frequency rocking mode, the next lowest frequency magnetron mode, and the 8th lowest frequency magnetron COM mode from left to right. Note from the color trace of the magnetron COM mode the motion is counterclockwise (CCW). The rocking mode in contrast is roughly equal component clockwise (CW) and CCW motion. Most other magnetron modes look like the middle magnetron mode, with elliptical orbits that are predominantly CCW but without reproducible symmetries like the axial drumhead modes. In contrast the cyclotron modes given in the bottom row mirror the drumhead modes, now with CW circular motion. However, unlike the drumhead modes, the lowest frequency mode is the COM mode, followed by the two tilt modes and the quadrupole mode from left to right.

It is worth emphasizing again that the two in-plane mode branches are not characterized by equal potential and kinetic energy. For standard crystals in the NIST Penning trap, the ratio R_n of potential to kinetic energy for a mode n is upward of 700 for the magnetron modes, and order 1/700 for the cyclotron modes. Figure 2.6 shows the helicity and R_n of the modes for a representative crystal in the NIST Penning trap, along with the corresponding mode frequencies. Helicity of 1 is defined as pure CCW motion and helicity -1 is pure CW motion (see [31] for details). R_n is set by the ratio of the cyclotron to magnetron frequency, so by increasing the axial trap frequency closer to the stability limit the ratio R_n eventually approaches 1. For our current trap configuration the bandwidths of each branch is $\sim$ 80 kHz for $\sim$ 100 modes, roughly 5 times smaller than the axial bandwidth.

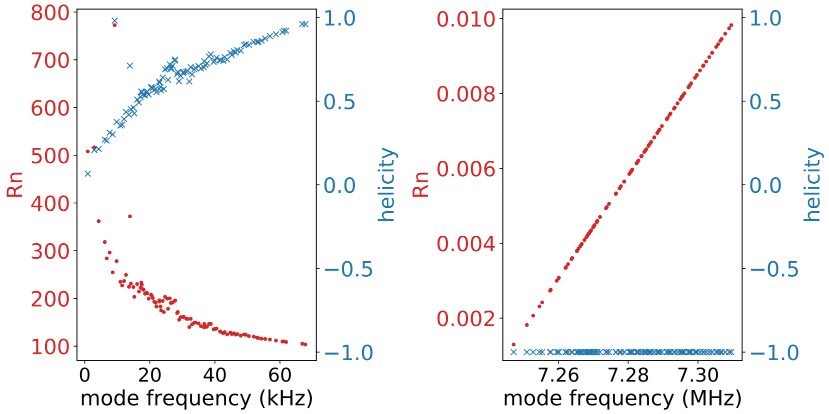

Figure 2.6: In-plane mode ratio of potential to kinetic energy R_n and helicities for the magnetron (left) and cyclotron (right) modes. The trap conditions are the same as figure 2.4. The singular peak near $R_n \sim 800$ corresponds to the magnetron COM mode, which has nearly pure CCW motion (helicity $\sim$1). In contrast the rocking mode is nearly helicity 0 equal CW and CCW motion. The cyclotron modes are nearly pure CW motion (helicity ~ -1) and roughly the inverse of the R_n value of the magnetron modes. For more details on the derivation of the helicity and R_n see [31].

2.4 ^{9}Be$^+$ atomic level structure

So far, this section has focused entirely on the motion of ions in a Penning trap. While direct measurement of the motion is possible by measuring the image currents induced in the electrodes, as done in the first demonstration of laser cooling [32], the only measurement possible in the current NIST Penning trap experiment is laser-induced fluorescence. Our atomic species of choice is ^{9}Be$^+$, which is the naturally abundant isotope of Be with one valence electron after ionization. Be$^+$ is the lightest hydrogen-like ion that can be laser cooled with lasers outside the vacuum-ultraviolet spectrum, with the light mass allowing for high motional frequencies. The large magnetic field in Penning traps substantially modifies the zero-field electronic structure. Considering the $2s^2S_{1/2}$

ground state, the energy levels are described by

$$H = hA\boldsymbol{I}\cdot\boldsymbol{J} - (\boldsymbol{\mu_J} + \boldsymbol{\mu_I})\cdot\boldsymbol{B} \tag{2.25}$$

$$= hA\boldsymbol{I}\cdot\boldsymbol{J} + \mu_B(g_J\boldsymbol{J} + g_I'\boldsymbol{I})\cdot\boldsymbol{B} \tag{2.26}$$

$$= \frac{hA}{2}(m_I m_J + (I_+J_- + I_-J_+)) + \mu_B(g_J m_J + g_I' m_I)B. \tag{2.27}$$

The first term of equation 2.25 is the magnetic hyperfine interaction with $A = -625.008837044(12)$ MHz [33] the hyperfine constant of $^9\mathrm{Be}^+$, and $\boldsymbol{I}, \boldsymbol{J}$ the nuclear spin ($I = 3/2$ for $^9\mathrm{Be}^+$) and electronic angular momentum ($J = L + S = 1/2$ for $2s^2S_{1/2}$ states). The second term describes the electronic and nuclear Zeeman terms, with $\boldsymbol{B}$ the magnetic field and $\boldsymbol{\mu_J}, \boldsymbol{\mu_I}$ the electronic and nuclear magnetic dipole moment operators. These dipole moment operators are expressed in terms of the Bohr magneton μ_B and g factors $g_J = -\mu_J/(J\mu_B)$, $g_I' = -\mu_I/(I\mu_B)$. For $^9\mathrm{Be}^+$ the nuclear dipole moment is negative due to having more neutrons than protons, leading to a negative hyperfine constant. Decomposing into ladder operators and (m_I, m_J) quantum numbers along the $\boldsymbol{B}$ direction gives equation 2.27. At zero field, the eigenstates of equation 2.27 are described by $(F = I + J, m_F = m_I + m_J)$ quantum numbers. The $F = 2$ and $F = 3$ manifolds are split by $2A \approx 1.25$ GHz, with $F = 2$ higher energy due to the negative A value; all m_F levels are degenerate within each F manifold. For non-zero B the F, m_F basis is no longer an eigenstate. Instead the eigenstates are mixed superpositions of (m_I, m_J) states. At low fields, the levels can still be associated with the (F, m_F) labels, whereas at high fields they are better approximated by a single (m_I, m_J). For $J = \frac{1}{2}$ the Breit-Rabi formula [33] gives the exact energies of the system

$$E\left(F = I + \frac{1}{2}, m_F = \pm\left(I + \frac{1}{2}\right)\right) = \frac{hAI}{2} \pm \left(\frac{g_J}{2} + Ig_I'\right)\mu_B B \tag{2.28}$$

$$E\left(F = I \pm \frac{1}{2}, m_F\right) = hA\left(-\frac{1}{4} + \frac{g_I' m_F \mu_B B}{hA} \pm \frac{2I+1}{4}\sqrt{1 + \frac{4m_F}{2I+1}X + X^2}\right) \tag{2.29}$$

$$X = \frac{\mu_B B(g_J - g_I')}{hA(I + \frac{1}{2})}, \tag{2.30}$$

where equation 2.28 is for the case $m_F = \pm(I + \frac{1}{2})$ which are true eigenstates in both the (m_I, m_J) and (F, m_F) basis, also called stretch states. Equation 2.29 is for all other states which will not be true eigenstates at non-zero B. Plotting these levels as a function of B produces the standard Breit-Rabi curve shown in figure 2.7. At our field of ≈ 4.46 T, we are in an intermediate regime where the electronic Zeeman term is dominant (g_J terms), but the nuclear Zeeman terms (g_I' terms) are smaller than the hyperfine interaction terms (hA terms). For this reason, non-eigenstate (m_I, m_J) levels have small but non-negligible admixtures with levels of the same m_F.

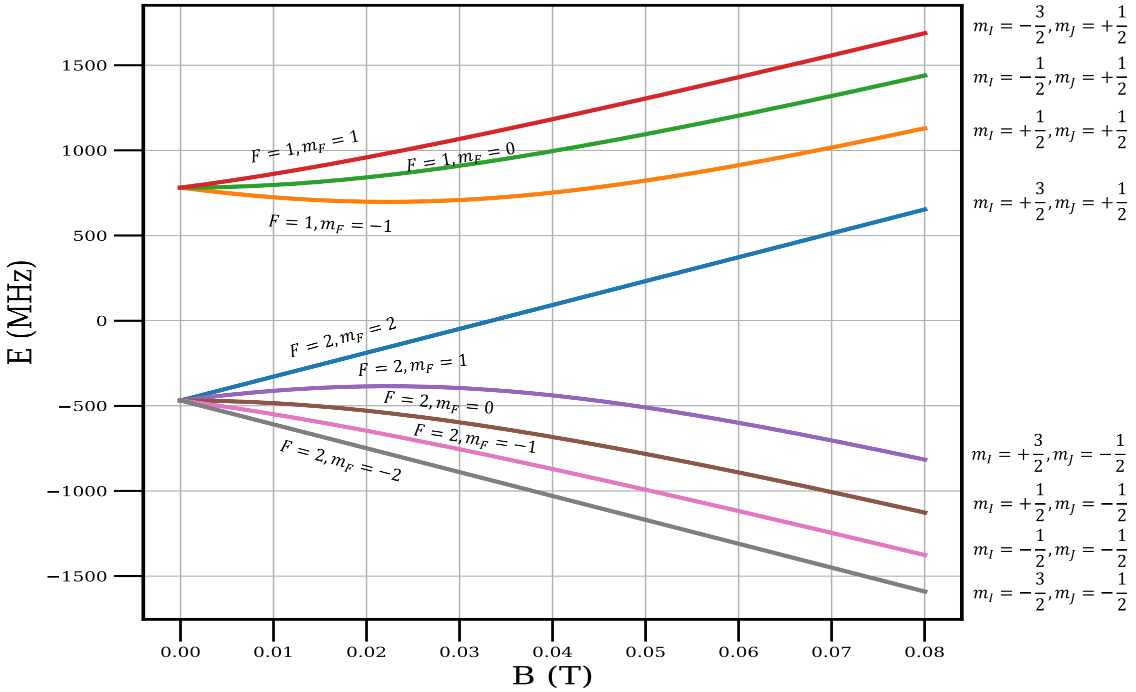

Figure 2.7: The level structure of the $^9\text{Be}^+$ $2s^2S_{1/2}$ ground manifold at intermediate magnetic fields. At zero field true eigenstates given by F, m_F quantum numbers describe the energy levels which are degenerate for varying m_F. At intermediate fields these are no longer eigenstates but can characterized by their dominant contribution at low field. At higher field the (m_I, m_J) basis becomes a better approximation of the true eigenstate, however it still mixes slightly with levels of the same m_F.

In our experiments, we work with an electron spin qubit between the true eigenstate $(m_I = 3/2, m_J = 1/2)$ and the approximate $(m_I = 3/2, m_J = -1/2)$ state, which are split by ≈ 124.02 GHz. Experiments are only sensitive to laser fluorescence that distinguishes being in the $(m_I =$

$3/2, m_J = 1/2)$ level or not, by exciting to the $2p^2P_{3/2}(F = m_F = 3)$ state, which, by selection rules, can only decay back to the $2s^2S_{1/2}(m_F = 2)$ stretch state. The complete level diagram of $^9\text{Be}^+$, including the ground state and excited $2p^2P_{1/2}$ and $2p^2P_{3/2}$ levels, is shown in figure 2.8 excluding nuclear structure in the excited states. Nuclear structure, particularly in the $2p^2P_{3/2}$ level, is more complicated [34] and exhibits much smaller hyperfine splittings. Instead these levels can largely be ignored due to optical pumping [35]. Transitions from $2s^2S_{1/2}(m_J = 1/2)$ to $2p^2P_{3/2}(m_J = 3/2)$ either remain in the stretch state and decay back down to the same $m_I = 3/2$ state, or, because the states are not pure (m_I, m_J) eigenstates, can mix to cause a spin flip and net increase in the nuclear spin, repeating until the population is trapped in $m_I = 3/2$.

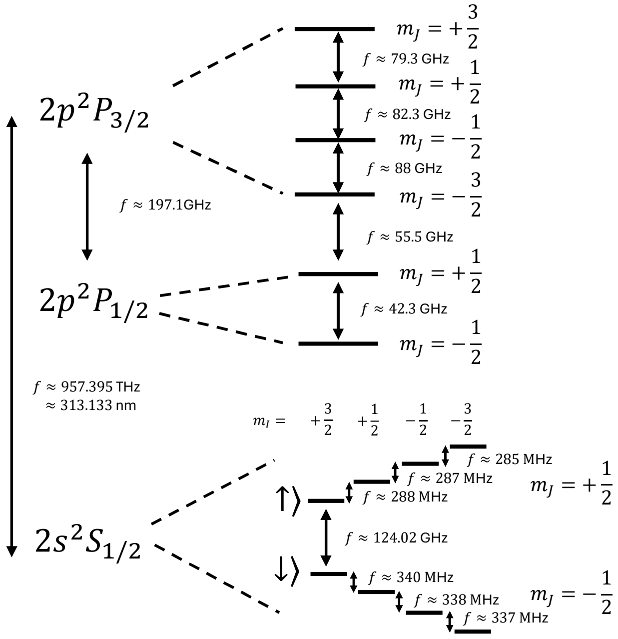

Figure 2.8: $^9\text{Be}^+$ level structure at 4.459 T ignoring nuclear structure in the excited $2p^2P_{1/2}, 2p^2P_{3/2}$ levels. The nuclear spin states in the ground $2s^2S_{1/2}$ manifold are split by 280-340 MHz, with the ordering set by whether the hyperfine interaction Am_Im_J increases with increasing m_I $(m_J = -1/2)$ or decreases with increasing m_I $(m_J = 1/2)$. At $\sim$ 80 T the nuclear Zeeman interaction would overtake the hyperfine interaction and the order would flip for $m_J = -1/2$. The electron spin qubit is labeled with $|\uparrow\rangle, |\downarrow\rangle$, corresponding to the $m_I = 3/2, m_J = \pm 1/2$ states. The excited $2p^2P_{3/2}, 2p^2P_{1/2}$ levels are split by $\approx$ 197.1 GHz, while the zero magnetic field $2s^2S_{1/2} \rightarrow 2p^2P_{3/2}$ transition is at $\approx$ 313.133 nm. At our magnetic field the $2p^2P_{3/2}, 2p^2P_{1/2}$ levels approximately split into m_J levels each separated $\sim$ 40-90 GHz.

Chapter 3

Experimental Subsystems

This section gives an overview of the main subsystems of the experiment excluding newly added tools in chapters 6 and 7.

3.1 ARTIQ control system

During the three-year down period when the magnet was being replaced, my largest contribution to the experiment was a replacement of the control system from a home-built system called HFGUI to ARTIQ. ARTIQ stands for Advanced Real-Time Infrastructure for Quantum Physics. ARTIQ is a Python-based framework for sending commands in real-time to an FPGA (field-programmable gate array), which can control an array of devices including TTLs (transistor–transistor logic switches), DDSs (direct digital synthesizers), and DACs (digital-to-analog converters) with fast (1.25 ns for our system) and precise timing. Unlike many FPGA control systems, which often pre-load a sequence of precise timing instructions from a computer slowly and then execute that sequence in real time repeatedly, ARTIQ maintains a stack of instructions on the core (FPGA) that is continuously updated by the host computer, allowing real-time decision-making. Additional USB controlled devices separate from the FPGA can then also be seamlessly integrated with this framework, since they are the same remote procedure calls (RPCs) as the instructions being sent to the FPGA. With this flexibility comes the new challenge of slack, defined as the time interval between when the last instruction on the stack will be executed and the current wall-clock time. Writing instructions onto the stack from the computer is in general slow. If many fast instructions are written on the stack they will be executed faster than they can be written onto the stack and precise timing will be lost once there is no slack.

Our ARTIQ hardware consists of a home-built crate identical to the first hardware developed in the ion storage group when creating ARTIQ. It includes a KC705 FPGA, 48 TTLs with 8 configured as 2 SPI (serial peripheral interface) communication channels, and 24 AD9914 DDSs. The system is clocked from our 100 MHz low phase noise reference (see section 3.4), which is multiplied up by 24 to set the DDS clock rate at 2.4 GHz. Each DDS has an internal sync clock that is derived by dividing down by 24 the 2.4 GHz clock source. This sync clock is the rate at which updates can be executed on the DDS, such as changing the frequency, phase or amplitude. Because each DDS separately generates their sync clock by dividing down the 2.4 GHz reference, each DDS can be in 24 different timings relative to the other DDS's when an update will execute. Without correction, when the FPGA sends an update to a DDS, it will wait a different—but repeatable—delay until the rising edge of the sync clock occurs for each DDS. However, if the DDS is reset or power cycled it will now be in a different repeatable random phase state. If multiple DDSs are set to the same frequency and phase, they may be out of phase from each other by up to 10 ns. To fix this, a phase synchronization procedure is executed where a further divided down sync output of one DDS is sent to all DDSs with the same cable length to maintain the same phase. Each DDS is then programmed to update its clock sync to match the rising edge of the sync output. Finally, one of the DDSs sync clocks is outputted to produce the clocking signal for the FPGA at 100 MHz. The FPGA then multiplies this up by 8 to produce output timing of 800 MHz or once every 1.25 ns. Since the DDS only updates on the coarser 10 ns timing, setting the DDS phase must account for the delay between setting the DDS and the sync clock rising edge.

One final bug that I painstakingly identified is a serious downside of clocking the FPGA via a DDS sync clock: the signals programming the DDS stem from the FPGA, and therefore depend on the DDS clocking. For this reason, a longstanding not understood issue was initializing the DDS using this phase synchronization procedure jumps the reference DDS sync clock and ruins the clocking of the FPGA. Sequences after this clock jump would fail to execute. Many labs in the ion storage group did not understand this issue and avoided phase-synchronizing their DDSs as a result, eventually switching to commercial hardware that avoids this bug. Our crate accounts for this clocking issue and carefully resets the core after the clocking error to correctly phase synchronize all our 24 DDSs.

Our experiments generally consist of a simple pulse sequence that ends with counting the arrival of photons on a PMT. We usually run this sequence repeatedly and scan some variable that changes one aspect of the pulse sequence. Photon counts are then averaged over the number of repeats, plotted in real time as a function of the scan variable, and fitted. This process is automated in a framework called the ARTIQ scan framework, which was originally developed by Philip Kent in the ion storage group. I worked to adapt new features including 2D scans, continuous scans which just repeatedly measure something, the ability to return multiple measurements from a single experiment, and some overhaul of the applet plotting functionality. Using this framework, most experiments can be written in less than 40 lines of code, with a separate model file that handles dataset management, plotting elements, and fitting—all of which is largely repeatable once a fit is written.

3.2 Trap details

3.2.1 Trap schematics and mechanical assemblies

The physical Penning trap is composed of a series of segmented electrodes housed in a room-temperature ultra-high-vacuum (UHV) system. A series of five electrodes, referred to as the load electrodes (L1-L5), are centered on four oven sources located in holes in the L3 electrode. Three ovens now contain neutral ^{9}Be, while the 4th oven is ^{24}Mg. Below the load electrodes is another series of 5 electrodes labeled T1-T4, with a rotating wall electrode in between, capped with a wire mesh at the end of the stack, as shown in figure 3.1. Estimates of the pressure from a vacuum gauge are in the low 10^{-11} Torr range—likely somewhat higher at the ion location. To allow optical access, the extended electrode structure is enclosed in a precision glass blown glass vacuum envelope, shown in figure 3.1. The trap is held fixed roughly centered in the bore of the magnet using a centering sleeve with three spring-loaded contacts, as shown in the inventor schematic of figure 3.2. This allows tilt alignment of the trap using a translation stage at the suspension point of the whole trap mounted on a plate resting on three legs, each a few feet in length, mounted on top of the magnet (see section 4.2.5 for details).

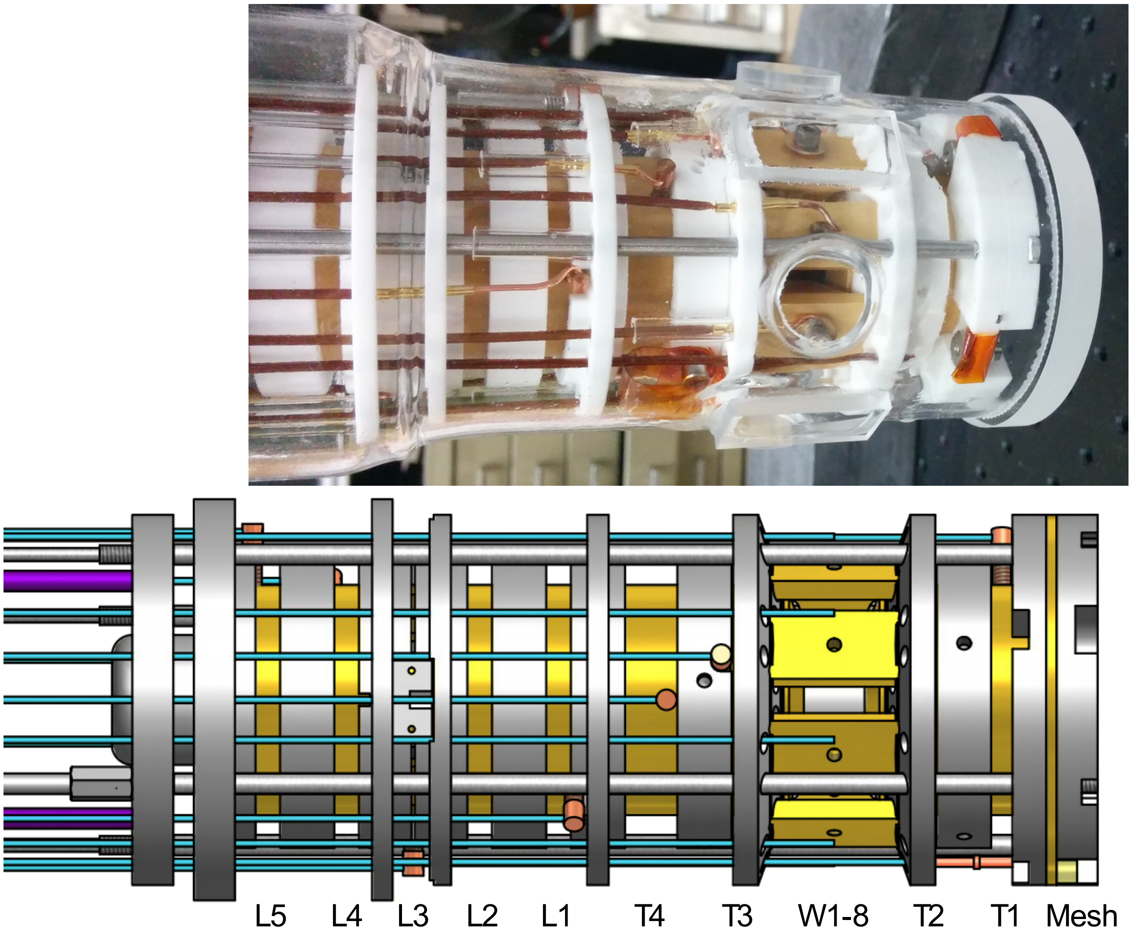

Figure 3.1: Trap electrodes and vacuum envelope. Top image shows the precision glass blown envelope with circular and rectangular view ports at the azimuthal gaps in the rotating wall electrodes. White insulating Macor spacers are placed in the gaps between the tan colored electrodes. Shown below the image is a schematic lined up to correspond roughly to the electrode and Macor spacers. From right to left are the wire mesh, electrodes T1, T2, rotating wall, T3, and T4 corresponding to the experimental zone. From right to left continuing on are the electrodes L1-L5 used in the load zone centered on electrode L3 that sources the neutral Be^9.

The magnet supporting the trap is mounted on an optical breadboard supported by four

~1-foot-tall legs which are roughly centered[1] on an aluminum optical table with a hole cutout to allow access from below the table. The optical table supports a complex optics setup for many laser beams, which are sent up the bore of the magnet using stationary mirrors positioned using what we refer to as the "mirror tower" shown in figure 3.2. The tower consists of a "base crown" with seven 45° mirrors aligned azimuthally with the entry ports between the rotating wall electrodes and rigidly mounted to the underside of the magnet breadboard. The eighth entry path without a mirror corresponds to a side-view f/5 imaging objective path (see section 3.3), with the opposite side the entry path for a 124 GHz microwave source to drive global spin flips of all the ions (see section 3.4). Clockwise from the imaging/microwave pair are the optical dipole force (ODF; see section 3.7) beam pair and counter-propagating electromagnetically induced transparency (EIT; see section 3.8) beam pairs. Neighboring clockwise from there are the parallel and perpendicular cooling paths (see section 3.5). Notably, the parallel beam passes through a cantilever system that brings it to the tower's center and directs the beam centered up the bore of the magnet. The top crown has fixed mirrors of either 45 degrees to send beams horizontally through the trap like the perpendicular cooling beam, or at ± 10 degrees for the ODF/EIT path. The last unused beam path has optional larger ±17.5 degree mirrors. The system is designed such that the top crown can slide up the bore of the magnet using four rods that slide through holes in the bottom crown before being set at an adjustable height with a set screw. A bottom-view f/2 objective can be brought up the center of the mirror crown to image the ions from below (see section 3.3). Modifications to the base crown now allow the cantilever system to sit on separate adjustable-length support rods to adjust its height, and separately allow the f/5 to be lifted directly up the bore through a cutout in the base crown.

3.2.2 Trap potentials

A series of segmented electrodes are used to trap, transport, and control the rotation of the ions. Ideally, static electric potentials applied to cylindrical electrodes would create a confining harmonic potential axially, and by the divergence-free condition of electrostatics, a radially deconfining

---

[1] Note the magnet is not actually centered on the optics table! It's one row of screw holes (1 inch) off center.

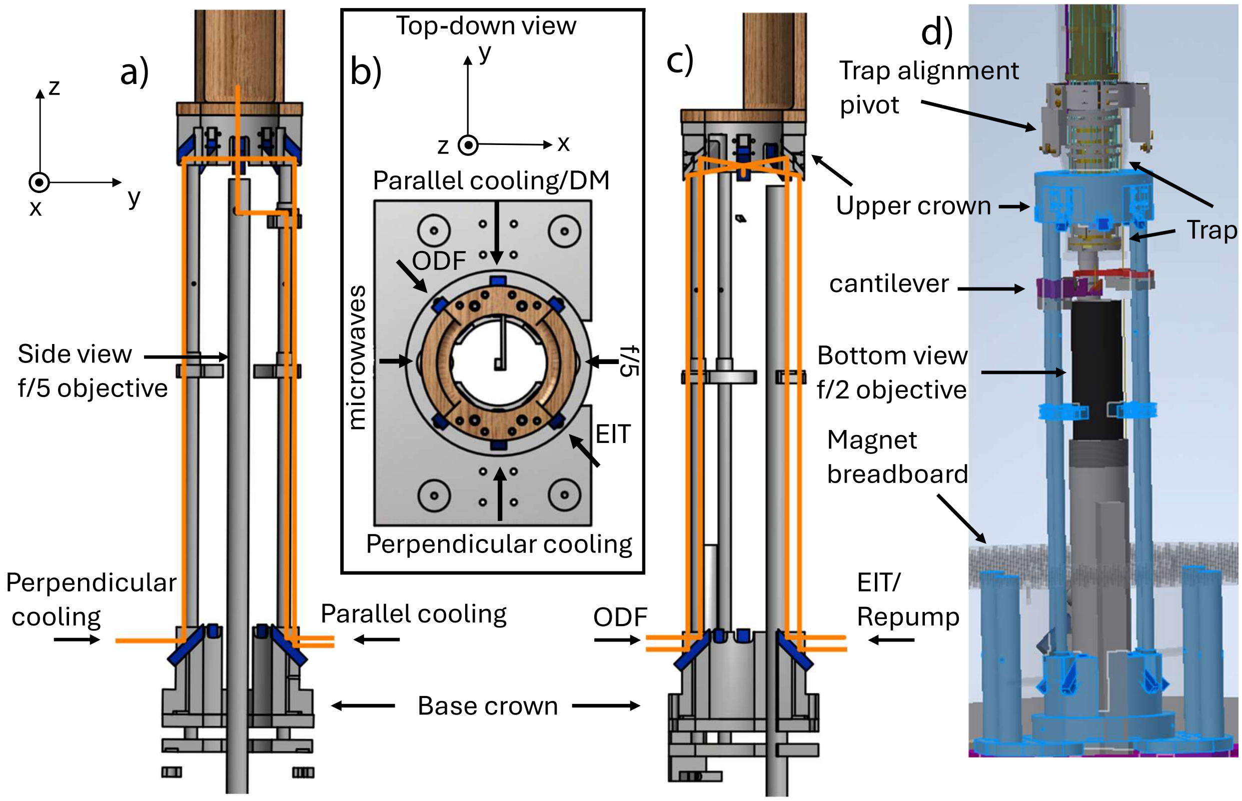

Figure 3.2: Mechanical assembly schematics. a) The mirror crown system viewed orthogonal to the cooling beam paths. From this view the f/5 system goes up an entry port in between the two cooling paths. The parallel cooling/deformable mirror (DM see chapter 6) path has a cantilever system near the upper crown that brings the beam path up the center of the trap aligned with the magnetic field. b) A top down view shows each corresponding entry port. c) A cross section view orthogonal to the ODF/EIT beam paths. The upper crown mirrors are split and angled to produce ± 10 degree crossing angle beams. d) An Inventor schematic with the mirror crown highlighted in blue. In addition to the mentioned elements the mounting structure to the underside of the magnet breadboard is shown. Left out of the other mirror tower schematics is the bottom-view f/2 objective that is raised through the center of the crown shown by a black cylinder. A trap alignment pivot holds the vacuum envelope centered in the upper crown, allowing tilt adjustments via translation of the trap mounting point more than a meter above the pivot (not shown).

harmonic potential.

$$\Phi = \frac{1}{2} m\omega_z^2 \left(z^2 - \frac{r^2}{2} \right) \tag{3.1}$$

To model this, the potential from each electrode is decomposed into a polynomial expansion about the trap center. This can be accomplished by simulating the potential when 1 V is applied to a single electrode while all others are grounded and calculating the multipole expansion of the potential about the center of the trap.

$$U = \sum_{l=0}^{\infty} \sum_{m=0}^{l} \left(\frac{r}{d}\right)^l P_l^m(\cos(\theta))(A_{l,m}\cos(m\phi) + B_{l,m}\sin(m\phi)), \tag{3.2}$$

where r, θ, and ϕ are the spherical radius, polar angle, and azimuthal angle, and P_l^m is the associated Legendre polynomial of degree l and order m. The argument of the Legendre polynomial $\cos(\theta)$ can equivalently be written as $\frac{z}{r}$, where z is the axial coordinate along the magnetic field. A length scale d, taken as the 1 cm electrode radius, normalizes the coefficients, preventing them from becoming excessively large. Assuming approximate cylindrical symmetry, the azimuthal $m\phi$ dependence can be removed leaving the simplified expansion:

$$U = \sum_{n=0}^{\infty} C_n \left(\frac{r}{d}\right)^n P_n\left(\frac{z}{r}\right), \tag{3.3}$$

where P_n is the Legendre polynomial of degree n. Electrostatic simulations were carried out in COMSOL using a 3D computer model of the electrodes, shown in figure 3.2.2. The resulting potentials were fitted to equation 3.3 to extract the coefficients C_n listed in table 3.1.

Table 3.1: Coefficients C_n in V/cm^n when 1 V is applied to the given electrode(s). T1* includes the trap mesh, Vm includes the middle T2/T3 electrodes, and Ve includes all electrodes excluding T2,T3, and Rw the rotating wall electrodes.

Coef	L2	L1	T4	T3	Rw	T2	T1*	Vm	Ve
C_0	5e-5	7e-4	.037	.255	.413	.255	.038	.511	.076
C_1	-7e-5	-1e-3	-.086	-.43	0	.43	.087	0	0
C_2	5e-5	1e-3	.095	.187	-.567	.187	.097	.374	.193
C_3	-9e-5	-1e-3	-.069	.197	0	-.197	.07	0	0
C_4	8e-6	7e-4	.034	-.262	.456	-.262	.034	-.524	.068
C_5	4e-5	2e-4	-.01	.073	0	-.073	.009	0	0
C_6	-2e-5	-2e-4	-.003	.149	-.291	.149	-.003	.298	-.006

To calculate the trap frequency from these coefficients, the C_2 coefficient are scaled by the applied voltages. The most common potential applied in our system uses voltages of –1.959 kV to the rotating wall, –1.7 kV on T2, –1.695 kV on T3, and –30 V on T4 with all other electrodes

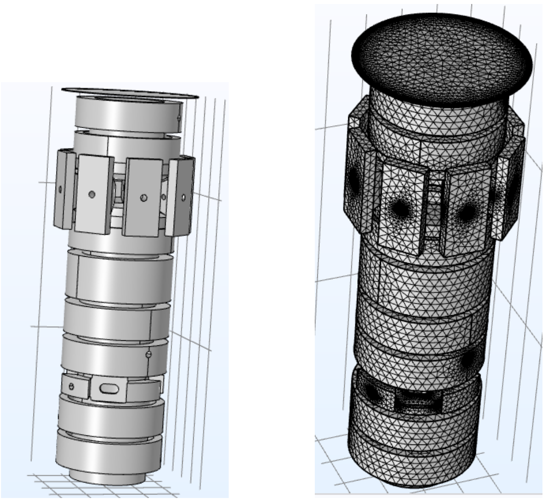

(a) Solid model (b) Solid model mesh

Figure 3.3: Electrode models used in COMSOL simulations. From top to bottom: the top mesh, electrodes T1–T2, the eight segmented rotating wall electrodes, electrodes T3-T4, and load electrodes L1–L5. (a) 3D model (b) finite-element surface mesh.

grounded. This gives 473.2 V/cm^2, and using $\omega_z = \sqrt{2qC_2/m}$ gives a trap frequency estimate of 1.602 MHz. This disagrees with the true measured trap frequency of 1.5927 MHz by approximately 1%, which may partly be due to experimental uncertainties in the applied voltages. Measurements of the C_1 coefficients from displacements caused by applying voltages to L1 and T4 put their error around 5-10%.

Azimuthal dependence of equation 3.2 remains important for the rotating wall electrodes. To simulate these electrodes further with varying potentials applied, a single electrode was bisected by the x-axis and 1 V was applied while grounding all other electrodes. The resulting data was fit to a modified expansion of equation 3.2, setting $z = 0$ and removing the $\sin m\phi$ terms by assuming an even potential:

$$U = \sum_{l=0}^{\infty} \sum_{m=0}^{l} \tilde{A}_{l,m} (\rho/d)^l \cos(m\phi) \tag{3.4}$$

Here only the cylindrical radius ρ is necessary since $z = 0$. The coefficients $\tilde{A}_{l,m}$ absorb the $P_l^m(0)$ factor from equation 3.2 into $A_{l,m}$, but notably for $l - m$ terms that are odd this factor vanishes, so these terms were not included in the fit. Fits listed in table 3.2 were extracted for a single electrode at 1 V and the rest grounded, in addition to all electrodes combined in an $m = 2$ and $m = 3$ wall configuration. See the next section 3.2.3 for details. Previous modeling found $m = 2$ and $m = 3$ rotating wall potential coefficients of 0.537 V/cm^2 and 0.45 V/cm^3 respectively. Table 3.2 states values of 0.504 V/cm^2 and 0.462 V/cm^3 for the m=2 and m=3 rotating wall potentials applied. However, previous fits had removed a factor of 3 and 15, corresponding to $P_2^2(0)$ and $P_3^3(0)$ respectively. Rough measurements of the $A_{1,1}$ coefficient carried out by imaging displacements of the crystal agreed within 10%. Simulations of the aspect ratio of the crystal from a quadrupole wall compared to ion images suggest potentially a 20% reduction in the true $A_{2,2}$ coefficient. Section 3.2.3 describes in detail why $m = 2$ and $m = 3$ rotating wall configurations only have $m = 2, 6$ and $m = 3, 5$ terms, respectively.

Table 3.2: Coefficients $\tilde{A}_{l,m}$ in V/cm^l when 1 V is applied to either a single bisected wall electrode, or all rotating wall electrodes in an $m = 2$ or $m = 3$ rotating wall configuration.

Coef	0,0	1,1	2,0	2,2	3,1	3,3	4,0	4,2	4,4
single	0.052	0.124	0.036	0.126	0.062	0.115	0.022	0.052	0.097
$m = 2$	0	0	0	0.504	0	0	0	0.207	0
$m = 3$	0	0	0	0	0	0.462	0	0	0
Coef	**5,1**	**5,3**	**5,5**	**6,0**	**6,2**	**6,4**	**6,6**	**7,1**	**7,3**
single	0.035	0.047	0.075	0.013	0.024	0.036	0.049	0.002	0.002
$m = 2$	0	0	0	0	0.087	0	0.197	0	0
$m = 3$	0	0.180	0.300	0	0	0	0	0	0.026
Coef	**7,5**	**7,7**	**8,0**	**8,2**	**8,4**	**8,6**	**8,8**		
single	0.019	0.031	-0.007	0.007	-0.004	0.020	0.012		
$m = 2$	0	0	0	0.048	0	0.085	0		
$m = 3$	0.087	0	0	0	0	0	0		

3.2.3 Rotating wall electrodes

To create a rotating wall potential, an azimuthally dependent potential is required, which requires dividing a trap electrode azimuthally. Consider n electrodes equally spaced $360/n$ degrees; in our case n=8. The potential created when applying a voltage to a single electrode which is bisected along the x axis can be expanded in terms of Associated Legendre polynomials as described in equation 3.2. Terms with odd $l - m$ vanish ($A_{l,m} = 0$) due to symmetry about z, and $B_{l,m}$=0 by bisecting the electrode along the x axis. Each rotating wall electrode ideally has the same Legendre expansion, but shifted in ϕ by an angle $2\pi/n$. By applying an oscillating drive on each electrode with the correct phase advance to match the desired symmetry, the counter rotating terms can ideally be canceled. To see this, figure 3.4 shows applying an oscillating potential at frequency $m'\omega_r$ with phase shifts of $-\frac{m'2\pi k}{n}$ to each electrode k.

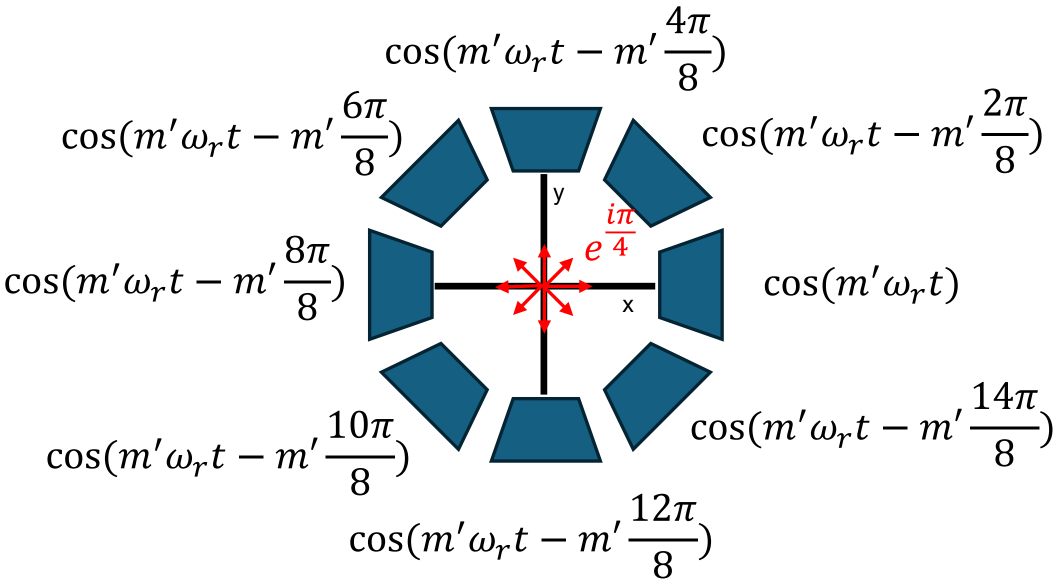

Figure 3.4: Schematic of the applied drives and phases in our eight-electrode rotating wall setup for an m'-order rotating wall. The applied potential each electrode k is summed over in equation 3.5. Each phase in equation 3.7 can be represented in complex coordinates (red arrows, where $m - m' = 1 \mod n$) to represent a sum over the roots of unity that will add to zero except when $m = \pm m' \mod n$.

Summing equation 3.2 over all electrodes in this configuration gives:

$$U = \sum_{k=0}^{n-1} \sum_{l=0}^{\infty} \sum_{m=0}^{l} A_{l,m} \left(\frac{r}{d}\right)^l P_l^m(\cos(\theta)) \cos(m\phi + m\frac{2\pi k}{n}) \cos(m'\omega_r t - \frac{m'2\pi k}{n}) \tag{3.5}$$

Focusing on just the azimuthal dependence of this formula gives:

$$\sum_{m=0}^{l}\sum_{k=0}^{n-1}\frac{1}{2}\left[\cos\left(m\phi+m'\omega_r t+(m-m')\frac{2\pi k}{n}\right)+\cos\left(m\phi-m'\omega_r t+(m+m')\frac{2\pi k}{n}\right)\right] \tag{3.6}$$

$$=\sum_{m=0}^{l}\sum_{k=0}^{n-1}\frac{1}{4}\left[e^{i\left(m\phi+m'\omega_r t+(m-m')\frac{2\pi k}{n}\right)}+c.c.+e^{i\left(m\phi-m'\omega_r t+(m+m')\frac{2\pi k}{n}\right)}+c.c.\right], \tag{3.7}$$

where *c.c.* means complex conjugate of the prior term. This equation gives the sum of oscillating potentials with phase factors which look like sums over the roots of unity which will add to zero. The formula for a geometric series gives:

$$\sum_{k=0}^{n-1}\beta^k=\begin{cases} n, & \beta=1 \\ \dfrac{1-\beta^n}{1-\beta} & \text{otherwise}\end{cases}. \tag{3.8}$$

For $\beta=e^{i(m\pm m')2\pi/n}$, the sum equals 0 for $m\neq\mp m' \mod n$. Defining $\delta_{m,m'\mathrm{mod}n}=1$ when $m=m'$ mod n and 0 otherwise:

$$U=\sum_{l=0}^{\infty}\sum_{m=0}^{l}\frac{n}{2}A_{l,m}\left(\frac{r}{d}\right)^l P_l^m(\cos(\theta))[\delta_{m,m'\mathrm{mod}n}\cos(m\phi+m'\omega_r t)+\delta_{m,-m'\mathrm{mod}n}\cos(m\phi-m'\omega_r t)] \tag{3.9}$$

$$\approx\frac{n}{2}A_{m',m'}\left(\frac{r}{d}\right)^{m'} P_{m'}^{m'}(\cos(\theta))\cos(m'(\phi+\omega_r t)). \tag{3.10}$$

Equation 3.9 shows that rotating walls are produced of azimuthal order $\pm m' \mod n$ and all higher order degrees l. For example, with $n=8$ and $m'=2$, rotating walls of azimuthal order 2 and 6 will form, with the sixth order wall counter-rotating at $\omega_r/3$. For our system ions are typically confined on length scales much smaller than the electrode radius, leading to higher order potentials being very weak at the ions' locations. This leads to the strongest wall corresponding to the $A_{2,2}$ wall. The strength of the wall is $\frac{n}{2}$ times the single electrode strength. Because potential strengths decrease for higher order m, higher voltage is necessary to drive higher-order walls. In practice, errors in amplitude and phase matching, variations in $A_{l,m}$ coefficients from machining and mechanical assembly, patch potentials, and capacitive pickup on neighboring electrodes make it difficult to apply an $m = 3$ wall. Instead, errors give rise to $m = 1$ walls rotating at $3\omega_r$ dominating over the $m = 3$ wall strength.

3.3 Imaging

Images of the ions are acquired using three cameras and two imaging objectives. Two Andor iXon cameras image the ions from the side—using an f/5 objective and a relay lens system with 10x magnification—and from below the trap along the magnetic field axis using an f/2 objective and relay lens system with 20x magnification. The side-view objective was modified for easier insertion through a cutout of the bottom mirror crown and juts out to be rigidly held by an updated 3 axis stage now mounted completely under the magnet breadboard. The stage mounting adjustment now allows the underside of the magnet to be enclosed without obstruction. A relay lens attachment allows for apertures and variable magnification, followed by a bellows connection to a motorized, TTL-controlled flipper mirror to switch between the side-view Andor and a photomultiplier tube (PMT). The bottom-view objective is raised through the center of the mirror crown system and rigidly held by a 3 axis stage for fine adjustment. It similarly consists of a relay lens, bellows, and rotating mirror system to allow for 4 different imaging paths. In addition to the Andor, a bottom-view PMT and another camera make up the three currently used imaging paths.

Due to the rotation of the crystal, imaging of the crystal from along the magnetic field axis (bottom view) produces ring patterns as the ions fluoresce at variable times in their orbit as shown in figure 3.5. To produce images of the ions in the rotating frame, one can stroboscopically gate the camera at the rotation frequency. However, this leads to lower count rates and inherent blurring of the ions, particularly at larger radii and higher rotation frequencies. Instead, we utilize a single photon X,Y,T counting camera from Roentdek to tag the arrival time of every photon. The coordinates X, Y can then be de-rotated based on the phase of the rotating wall at the photon arrival time. The Roentdek camera shown in figure 3.6 consists of a sealed vacuum tube containing a photocathode, microchannel plate (MCP), and resistive anode to produce a pulse of charge when a photon is detected. Three crossed wires in a hexagonal mesh pattern capacitively pick up the pulse. By precisely measuring the time difference between the pulse arrival at the two ends of each wire, a distance from the center of the mesh can be extracted.

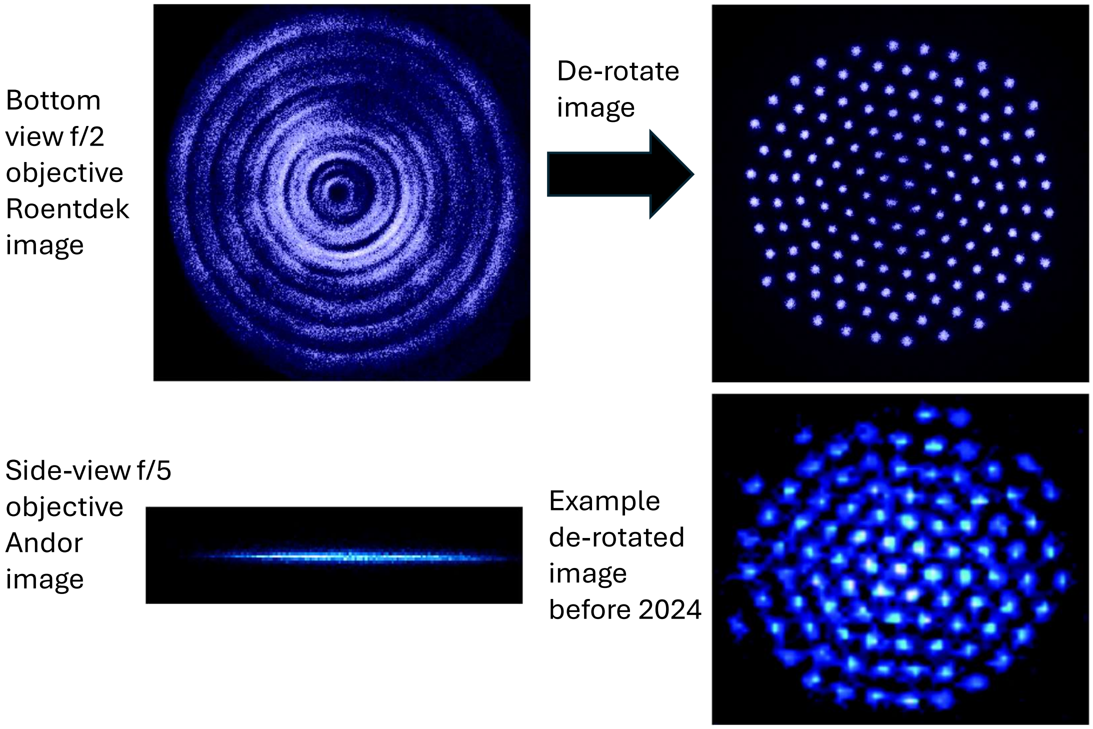

Figure 3.5: Experimental images of ions from the bottom view (top row and bottom right images) and side view (bottom left). The top two images correspond to the same photons collected from the Roentdek, with the left corresponding to the lab frame image of rings as ions fluoresce randomly in their orbit and the right de-rotating the time of arrival of each photon. The localization and separation of each ion is dramatically improved compared to old images shown in the bottom right, which is representative of images taken prior to 2024. Images from the side view show a thin line of a single plane crystal like in the bottom left image.

Reading out the timing of the pulse is done using an amplifier, a constant fraction discriminator, and a time-to-digital converter (TDC). Each pulse generally has a variable width around 5 ns. By adding an inverted, delayed copy of the pulse with a fractional amplitude, a sharp error signal—or equivalently, a zero crossing—is produced, enabling much finer timing resolution. Delay of the copied pulse is tuned by physically varying a length of cable to introduce few nanoseconds of delay. A TDC then records the rising edge of the pulse to a few-ps resolution. Data are binned at 25 ps resolution for image reconstruction, corresponding to 100 μm resolution on the camera. With a 40 mm-diameter photocathode, this gives a 400 by 400 pixel image.[2] Of these, only approximately 360 $\times$ 360 of the pixels corresponds to the active area. To image onto such a large area, an additional magnification stage is added to give an effective magnification of around 125,[3] corresponding to ~0.8 μm per pixel at the ions.

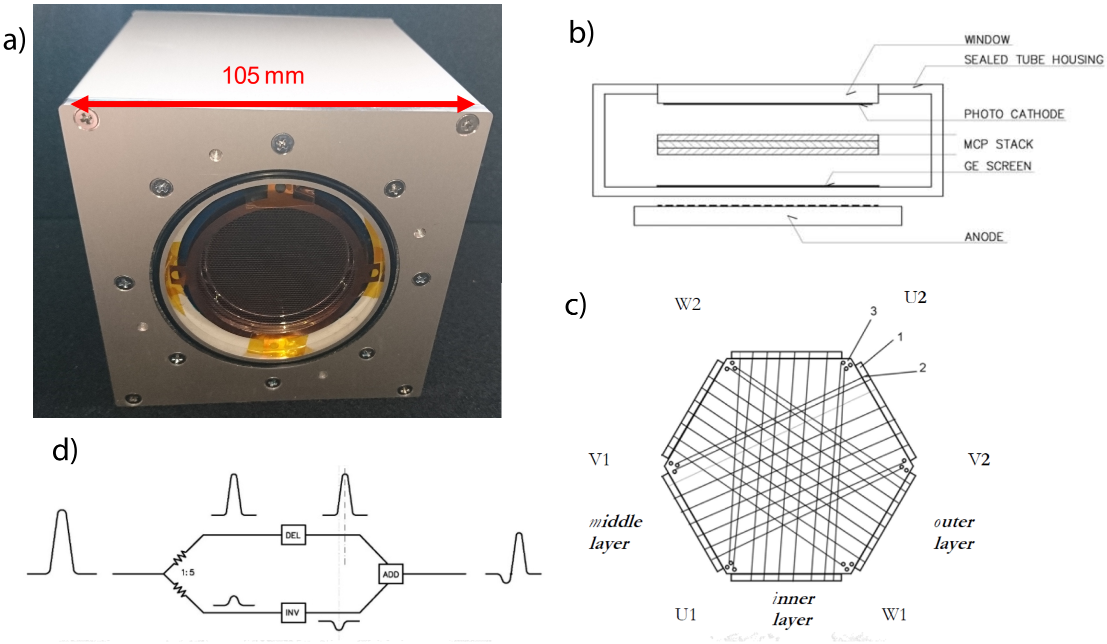

Figure 3.6: Roentdek camera components. a) The physical housing of the Roentdek camera is contained in a cube of side length 105 mm, with the innermost circle the area of the photocathode. b) Photons pass through the window and sealed tube housing to hit the photocathode, which generates photoelectrons that are amplified by the MCP before generating pulses of charge on a resistive anode. c) The resulting pulses are capacitively picked up on three crossing wires, with the timing difference between the (U1-U2), (V1-V2), and (W1-W2) wire ends giving the coordinates along the wire where the pulse arrived. d) The pulse is amplified and then split into an inverted and delayed copy with a set fraction split between the two paths. The sum of the two signals generate a steep ~ps sensitive zero crossing from the much wider ~5 ns pulse. A final time-to-digital converter bins the arrival time of each pulse to set a timing and position resolution of ~25 ps and 100 μm.

Imaging with the Roentdek camera—combined with reduced background light scatter from replacing the vacuum envelope and removing unnecessary optics inside the vacuum system—has produced a revolutionary capability for the experiment. Previous images used a Quantar camera

---

[2] Actual image files are outputted in 441 $\times$ 441 arrays.

[3] Best estimates now suggest magnification of 143.

limited to approximately a 100 kHz count rate, whereas the Roentdek is specified to handle up to 1 MHz. However, the quantum efficiency of the Roentdek has dropped precipitously over the approximate 1 year of use in the experiment, with rough estimates suggesting quantum efficiencies as low as a few percent compared to the specified $\approx 10 - 15\%$. Detecting with higher scattering rates to compensate heats the crystal faster than the in-plane modes can be cooled, thus limiting the Roentdek to as low as 500 counts per ion per second. Despite these disappointing count rates, remarkably improved images are shown in figure 3.5. Improvements in the in-plane cooling providing a large contribution in the image quality detailed in chapter 7. Furthermore, the first experiments have been carried out utilizing single-shot detection of individual ions, as detailed in chapter 6. Replacing the Roentdek camera with a higher-quantum-efficiency device less susceptible to degradation could enable routine single shot detection on similar time scales comparable to PMT detection. Additionally, reduced detection power could be used to limit in-plane heating for more stable crystals.

3.4 Microwaves

Precise control of the spin states of the $^9\mathrm{Be}^+$ ions requires a low phase-noise oscillator at ∼124 GHz. Without such a reference, when the ions' spin states are rotated to the equator of the Bloch sphere, they will rapidly precess at 124 GHz and the oscillator will be quickly lose track of the orientation. To produce a low phase noise reference, we first use a Spectra Dynamics LNFR-100 low-noise crystal oscillator with 5 MHz and 100 MHz quartz references. The phase noise properties are set by the 5 MHz oscillator for offset frequencies between .25 Hz and 100 Hz, and set by the 100 MHz quarts oscillator for higher offset frequencies. For frequencies below .25 Hz the 5 MHz oscillator is phase locked to a 5 MHz maser reference produced at NIST and referenced to UTC.

A 15.2 GHz Lucix Inc. dielectric resonator oscillator (DRO) is then disciplined by the 100 MHz reference giving it good phase noise performance. An ARTIQ DDS signal at ∼300 MHz, which is referenced to the same 100 MHz source, is mixed with the 15.2 GHz to produce a ∼15.5 GHz source. The resulting signal goes through an amplification and 8x multiplication chain, shown in fig 3.7, with an output power of around 200 mW. Besides tracking the spin state orientations using this reference oscillator, global spin flips can be driven using the magnetic dipole moment of the electron and an oscillating $\vec{B}$ field orthogonal to the trap magnetic field.

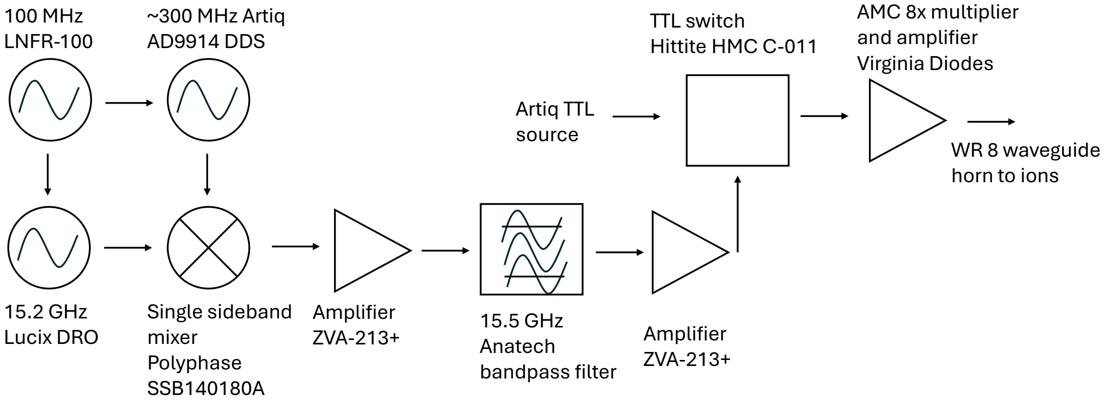

Figure 3.7: Diagram showing all components used to generate ~200 mW of ~124.02 GHz radiation at the ions. A low phase noise 100 MHz source is used to discipline a 15.2 GHz DRO. It additionally clocks the ARTIQ crate which generates a tunable frequency ~300 MHz tone. After mixing these two tones together, they are amplified and passed through a 15.5 GHz bandpass filter. After another amplification stage the signal passes through a TTL-controlled RF switch, allowing quick switching using an ARTIQ TTL source. This feature is no longer used heavily, however, as described in section 4.1.3. Finally, the signal is multiplied up by 8 and amplified before being routed to the ions via a WR 8 waveguide and microwave horn.

3.5 Cooling and detection lasers

Doppler laser cooling works on the principle of preferential scattering from a laser opposing the direction of motion. When resonant absorbers travel towards a laser source the radiation will be Doppler shifted higher in frequency. By red-detuning a laser source slightly below the resonance frequency, light will preferentially absorb and scatter when traveling towards the laser source. After many cycles of absorption and emission, this can net slow the resonant absorber. The cooling limit is usually set by the linewidth of the transition being driven, with optimal cooling achieved setting the red detuning to half the natural linewidth. The Doppler limit $T = \hbar\Gamma/2k_B$, corresponds to ~0.4 mK for the transition used in the experiment. The first demonstration of laser cooling was performed on a distant predecessor to this experiment: a Penning trap with Mg^+ ions at NIST [32]. Cooling of the ion crystal is achieved using two beams: one parallel and one perpendicular to the magnetic field, both red-detuned from the $2s^2S_{1/2}(m_J = +1/2) \rightarrow 2p^2P_{3/2}(m_J = +3/2)$ transition. This transition corresponds to ~313 nm light, the wavelength used for all Be^+ lasers in the experiment. For detection, the parallel cooling beam is shifted to be ~1 MHz red of resonance to increase the scatter rate while being conservatively on the red side of the transition to avoid heating.

The cooling light is produced by a Coherent dye laser using a circulating jet of Kiton Red dye, pumped in a bow-tie cavity by a 4-6 Watt Verdi 532 nm diode pumped solid state laser, yielding ≈ 400 mW of 626 nm light. A small portion of the 626 nm light is used in a saturation-absorption spectroscopy setup of an iodine gas cell to stabilize the frequency to ~1 MHz or better. After fiber coupling, the light is frequency-doubled to 313 nm using another bow-tie cavity with a beta barium borate (BBO) crystal. Pulse amplitude, timing, and fine frequency control are implemented using an acousto-optic modulator (AOM) in a double pass configuration. The AOM is a crystal driven with an acoustic wave that deflects the beam and shifts its frequency ~200 MHz. Fine control of the amplitude and frequency is achieved by modulating the RF tone generating the acoustic wave. Amplitude control relies on a proportional-integral feedback loop using feedback from a photodiode to measure the power and a custom ARTIQ-integrated, fast, low noise DAC to set the reference voltage level. Updates to the DAC voltage level adjust the servo setpoint to increase the parallel beam intensity to scatter more photons during detection.

As described in chapter 2, the magnetron motion is negative energy in the lab frame and therefore requires a modification of standard Doppler cooling. Figure 3.8 shows the perpendicular laser beam is focused to a small waist and offset from the center of the crystal radially such that the beam travels in the direction of the crystal rotation to apply a torque that adds energy to the magnetron motion and thus “cools” it. The magnetron cooling rate is set by the gradient in the scattering rate of the laser beam, preferentially scattering more to apply a larger torque when displaced off center. Cyclotron cooling is achieved by the red detuning of the laser following standard Doppler laser cooling principles. Detailed studies of this cooling, including the effect of the rotating wall, are described in [36]. The Torrisi study suggested temperatures near the Doppler limit could be achieved for both the magnetron and cyclotron motion. However, recent studies have pointed out the critical importance of the nature of the in-plane modes. The original study had quantified the cooling of the kinetic energy. However, since the magnetron motion is potential energy dominant this substantially underestimated the achievable magnetron temperatures. Further studies suggest the achievable temperatures are limited to ∼10 mK [37]. The same study also shows a way to couple the magnetron motion with the axial motion by tuning the crystal rotation frequency near the 1-2 plane transition, where the lowest frequency axial mode can be near resonant with the magnetron modes [37]. Extensions to this show adiabatic ramps can reduce the temperature further and reduce the constraint of working near the 1-2 transition [38]. Alternatively, a technique to couple the magnetron and cyclotron motions has recently been implemented to substantially improve the cooling as will be described in chapter 7.

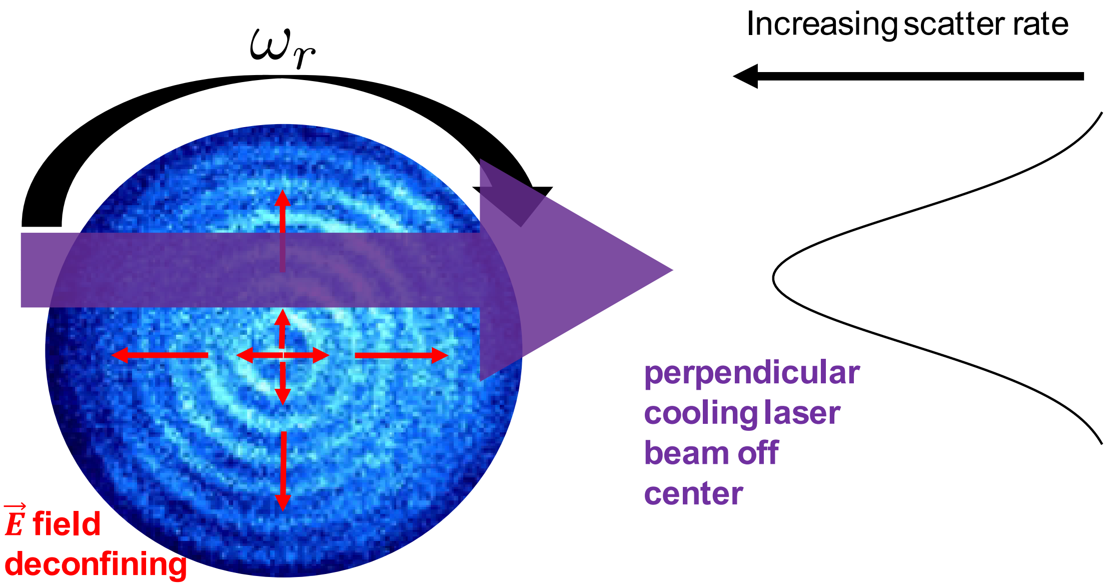

Figure 3.8: Diagram showing the Doppler cooling of the in-plane motion. Radially deconfining electric field lines emphasize the unstable potential energy dominant magnetron motion that is negative energy in the lab frame. The perpendicular beam is focused to a ∼20-30 μm beam waist and offset a similar distance to apply a torque in the direction of the crystal rotation. The scattering rate profile has a sharp gradient at the central ion, applying a restoring force to reduce the negative energy magnetron motion. Magnetron cooling rates are therefore set by the beam waist and intensity, with sharper gradients and smaller beam waists able to achieve larger magnetron cooling rates. Cyclotron cooling occurs due to the red-detuning of the beam analogous to standard Doppler cooling.

3.6 Loading

One of the largest time impediments in the past has been the startup procedure to obtain ions. For details about the prior load procedure, see Kevin Gilmore's thesis [39]. Prior to the magnet repair, the standard procedure to start each day was to first start up the dye laser. This involved a roughly one-hour startup time, which has now almost entirely been eliminated by remote startup of the pump 5 W, 532 nm laser and dye reservoir chiller.

Next, a neutral beryllium "oven", which consists of a tungsten wire coated with beryllium, is heated by running roughly 1 A of current through it. This produces a neutral flux of Be atoms which is generated in the load zone centered on electrode L3 (see figure 3.2.2). To produce ^{9}Be$^+$, the neutral atoms are either hit with high energy >12 eV electrons in impact ionization, or photoionized. Photoionization is implemented using a two-step resonant photon excitation via a few mW 235 nm ~1 mm diameter laser beam that is generated in a UV bow-tie cavity with a BBO frequency doubling crystal mounted atop the trap and sent counter propagating to the parallel cooling beam. To trap these ions, ~-3 V is applied to the L3 electrode while neutral Be is ionized for ~5 seconds, or 60 seconds with electron impact ionization. The magnetic field at the load zone is ~5 cm away from the experimental zone where the magnetic field is uniform and maximum, likely reducing the field by a few % in the load zone.

Ideally, the photoionization beam is perfectly centered on the trap electrode, which we attempt to achieve by aligning the parallel cooling beam with the magnetic field (see section 6.4 for example details), and by aligning the trap electrodes to the magnetic field (see section 4.2.5). In impact ionization, the electron beam is ideally well centered because the electrons will follow the magnetic field lines as it travels down the bore of the magnet. Because of the fringing magnetic field,[4] this will have a lensing effect that focuses them to the center of the trap. When a single ion is produced, the magnetron energy is largely set by how off center the ion is ionized, and the cyclotron energy is dominantly set by the kinetic energy of the neutral Be in the plane. However, the axial direction

---

[4] The electron source is a wire filament called an electron gun or egun. There are four filaments one of which is burned out. All are located far up the vacuum envelope to make this fringing field non-negligible.

is where this picture goes awry, particularly with multiple ions. Because these ionization beams (electron or photoionization) are not tightly focused, there is no preferential ionization along the axial direction. Ionizing on center axially of the L3 electrode would impart no excess energy from the trap potential itself. However, loading 1 mm off-center axially will impart a very high energy into the ^{9}Be$^+$, on the order of hundreds of meV (thousands of degrees C). If this energy couples at all to the radial motion via Coulomb repulsion between ions, the ions could be expelled to large-radius orbits.

One idea is to relax the axial well confinement and lower the trap depth to impart less energy from the trap. However, as the axial confinement is reduced, stray electric fields displace the center of the electric potential well, loading ions further off center. Even worse, to transport the ions to the experimental zone the electric potential is raised, ideally adiabatically, which creates deeper wells and higher trap frequencies. Although this process is adiabatic, energy is added to the motion and much of the gain is lost from loading in a weaker potential as the ions are heated up further.

All of these issues lead to ions being potentially quite hot and possibly kicked out to far radii orbits. Because we can only image and cool ions within ∼0.5 mm of the center of the trap we have no way of characterizing these potential large orbit hot ions. The problem is not evident in the ions until a precise characterization of the axial temperature is done, or ion resolved bottom-view images can identify elevated in-plane temperatures. Even though the ions are far away and weakly coupled, they can be very hot and have extremely long time constant cooling while still perturbing the axial center-of-mass motion.

The old solution to this problem was simply waiting. The ions would be loaded and left to sit in the dark for 30 minutes, presumably cooling the highest energy ions via background gas collisions at room temperature, possibly spinning out of the trap as well, followed by another 30 minutes with the lasers a few GHz detuned to mitigate hydride formation while applying cooling to the hottest ions. Ions were then brought to the center of the trap using a "spin up" procedure. The perpendicular cooling beam was offset far from the trap center and the detuning swept from several GHz red to several GHz blue of the cooling resonance to apply a torque on the ions. This was repeated in offset increments of 200 μm, starting from 1 mm, until brought to the center. In total more than two hours a day was spent before ions could be worked with. If hot ions at far radii still managed to get past this wait period or if a new load was desired a further hour wait and spin up was required.

The new load procedure, along with automated remote startup of the dye laser, has reduced this startup time to approximately 15 minutes. This is mostly to tune up the dye laser, with an optional 30 minutes at the start of the day to let the dye laser settle more after the jet starts circulating, which is not started remotely. The idea behind the procedure is to pulse the potential in the experimental zone to very low well depths, either allowing easier sympathetic cooling from the lower frequency magnetron motion, or kicking out ions hotter than the lowered well depth. We first lower the axial confinement to approximately -80 V applied to only the rotating wall electrodes, which corresponds to ∼500 kHz axial trap frequency. Using a TTL controllable low noise high voltage switch we jump the voltage down as low as -0.35 V. We constantly apply the cooling beams locked to the cooling frequency and with many mW of power, remaining in the lowered well for short bursts of less than a second for trap voltages below -0.5 V. At these low potentials stray electric fields displace the crystal center eventually off the side-view imaging field of view, and move the perpendicular cooling beam to the blue side of the crystal. We compensate for this by offsetting the perpendicular beam ∼280 μm to allow stable trapping down to as low as -0.35 V. With the spin up requirement removed this procedure can almost entirely be automated with TTL control of the high voltage switch and external DACs to set the well depth. If hot ions at far radii still occur this procedure can be repeated to remove or cool them without reloading. However, this procedure has shown good reliability in producing cold clouds without evidence of hot ions at large radii.

3.7 Optical dipole force (ODF)

3.7.1 ODF theory and polarization details

To utilize the collective normal modes of motion, it is necessary to couple the spin and motion together. The workhorse of almost all experiments in the NIST Penning trap has been the Optical

Dipole Force (ODF), which utilizes a spatial gradient of an AC Stark shift (ACSS) in the axial direction to produce spin-motion coupling. While the magnet was being repaired, a detailed study of the ODF and an alternative coupling, the Mølmer-Sørensen (MS) gate, were investigated [40]. For this thesis, the ODF was almost exclusively operated at a specific condition of nulling the ACSS of each beam individually, as described in detail below.

Assume two laser beams of nearly equal frequency and linear polarization incident at shallow angles from each other in the axial direction as shown in figure 3.9. Taking a small angle approximation, the polarization of each beam can be decomposed into a component aligned with the magnetic field ($\hat{\pi}$-polarized), and a component orthogonal to the magnetic field ($\hat{\sigma}$-polarized). Due to selection rules of the dipole moment operator, the $\hat{\pi}$ component only interacts with transitions $\Delta m_j = 0$, and the $\hat{\sigma}$ component is a nearly equal superposition of circular polarizations that interact with $\Delta m_j = \pm 1$ transitions (see equations 3.25, 3.26 for estimates of the imbalance in $\hat{\sigma}_+/\hat{\sigma}_-$). Using the detuning of the laser frequency from each possible transition in the $P_{1/2}, P_{3/2}$ manifolds, an ACSS can be calculated for each spin state in the $S_{1/2}$ manifold for $\hat{\sigma}, \hat{\pi}$ polarization (see [40]). The difference in the ACSS for the $|\uparrow\rangle$ and $|\downarrow\rangle$ states is called the differential ACSS, and is a shift in the precession frequency of the spins. If the differential ACSS has opposite signs for the $\hat{\sigma}, \hat{\pi}$ polarizations, then there will be a polarization angle ϕ_0 that cancels the differential ACSS from a single beam. If both beams had this polarization, a standing wave intensity gradient would be produced that has no differential ACSS, but can produce a spin-independent force. In contrast, if these beams are cross-polarized by setting the polarization angles to $\pm\phi_0$, then a polarization gradient will be produced that can produce a non-zero ACSS from the interference of the two beams polarizations.

To demonstrate this, assume two beams of equal intensity and polarization angles ϕ of equal

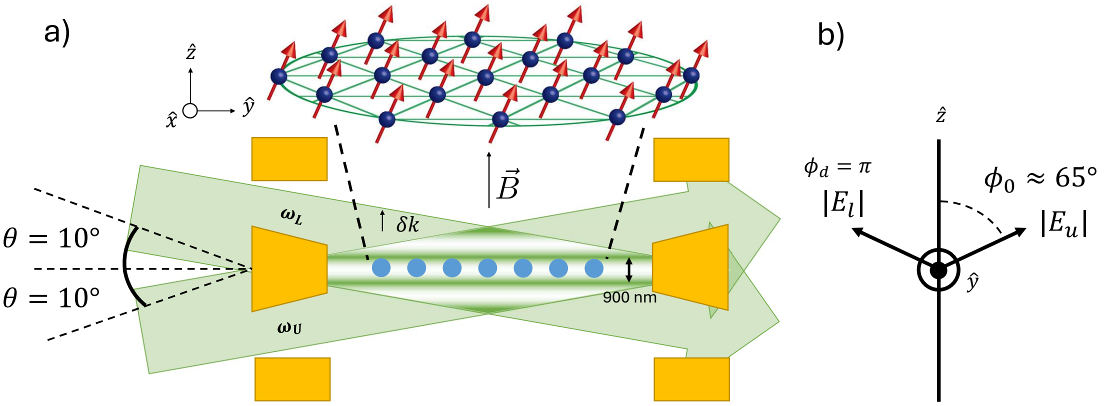

Figure 3.9: Cartoon depiction of the ODF setup. a) The lower (E_l, ω_L) and upper (E_U, ω_U) beams hit the ions at a shallow ± 10 degree angle. The lower beam is represented above the upper beam in this diagram because of the orientation of the magnetic field and z axis that defines the crystal rotation. Previously this was pointing against gravity, but the new magnet has the magnetic field pointing towards the earth. The interference forms a gradient along the z direction, with $2k\sin(\theta) \approx 2\pi/900$ nm. b) The polarizations of the upper and lower beams looking along the propagation y direction. When the ACSS is nulled and the polarizations cross-polarized $(\phi_d = \pi)$, the polarizations are at $\approx \pm 65$ degrees.

ratio $\hat{\sigma}, \hat{\pi}$ polarization as follows:

$$E_x = E_0 \sin(\phi)(\cos(\vec{k}_u \cdot \vec{r} - \omega_u t) + \cos(\vec{k}_l \cdot \vec{r} - \omega_l t - \psi)) \tag{3.11}$$

$$= 2E_0 \sin(\phi)\cos(k\cos(\theta)y - \frac{\omega_u + \omega_l}{2}t - \frac{\psi}{2})\cos((2k\sin(\theta)z - (\omega_u - \omega_l)t + \psi)/2) \tag{3.12}$$

$$= 2E_0 \sin(\phi)\cos(k\cos(\theta)y - \frac{\omega_u + \omega_l}{2}t - \frac{\psi}{2})\cos(\beta/2) \tag{3.13}$$

$$E_z = E_0 \cos(\phi)(\cos(\vec{k}_u \cdot \vec{r} - \omega_u t) + \cos(\vec{k}_l \cdot \vec{r} - \omega_l t - \psi - \phi_d)) \tag{3.14}$$

$$= 2E_0 \cos(\phi)\cos(k\cos(\theta)y - \frac{\omega_u + \omega_l}{2}t - \frac{\psi}{2})\cos((\beta + \phi_d)/2) \tag{3.15}$$

$$ACSS_{\uparrow/\downarrow} = 4A_{\uparrow/\downarrow}\cos(\phi)^2\cos((\beta + \phi_d)/2)^2 + 4B_{\uparrow/\downarrow}\sin(\phi)^2\cos(\beta/2)^2 \tag{3.16}$$

$$= 2A_{\uparrow/\downarrow}\cos(\phi)^2(1 + \cos(\beta)\cos(\phi_d) - \sin(\beta)\sin(\phi_d)) + 2B_{\uparrow/\downarrow}\sin(\phi)^2(1 + \cos(\beta)) \tag{3.17}$$

Equations 3.11, 3.14 give the sum of the electric fields in the x and z directions respectively from the upper and lower beams. The upper beam is assumed to have linear polarization with k vector $\vec{k}_u$ and frequency ω_u. The lower beam similarly is characterized by a k vector $\vec{k}_l$ and frequency

ω_l. Additionally, the lower beam has the same ratio of polarizations given by ϕ, the polarization angle, but can have arbitrary elliptical polarization given by ϕ_d, and includes an overall phase shift ψ from the upper beam. In equations 3.13, 3.15, the electric field decomposes into a spatial term β that is oscillating slowly at the difference frequency of the beams, multiplied by a fast oscillating term at the average frequency of the two beams. Because the dipole moment operator will sum over transitions independently for the two polarizations, the total ACSS is characterized by the sum of the square of the electric fields along the x, z axes. We can therefore square each electric field component and associate the fast oscillating term with the single beam ACSS $A_{\uparrow/\downarrow}$($\hat{\pi}$ polarization), $B_{\uparrow/\downarrow}$($\hat{\sigma}$ polarization) for each spin state and for $\hat{\pi}, \hat{\sigma}$ polarizations respectively. The last important detail is ϕ_d, which represents the relative phase of the polarization of the upper beam compared to the lower beam. For example, when $\phi_d = 0$, the beams' polarizations match, and when $\phi_d = \pi$ they are cross-polarized. To see the effect of ϕ_d we write the effective Hamiltonian given by equation 3.17:

$$\hat{H} = \hat{I}(ACSS_\uparrow + ACSS_\downarrow)/2 + \hat{\sigma}_z(ACSS_\uparrow - ACSS_\downarrow)/2 \tag{3.18}$$

$$\begin{aligned}(ACSS_\uparrow + ACSS_\downarrow)/2 &= (A_\uparrow + A_\downarrow)\cos(\phi)^2 + (B_\uparrow + B_\downarrow)\sin(\phi)^2 \\ &+ \cos(\beta)[(A_\uparrow + A_\downarrow)\cos^2(\phi)\cos(\phi_d) + (B_\uparrow + B_\downarrow)\sin^2(\phi)] \\ &- \sin(\beta)[(A_\uparrow + A_\downarrow)\cos^2(\phi)\sin(\phi_d)]\end{aligned} \tag{3.19}$$

$$\begin{aligned}(ACSS_\uparrow - ACSS_\downarrow)/2 &= (A_\uparrow - A_\downarrow)\cos(\phi)^2 + (B_\uparrow - B_\downarrow)\sin(\phi)^2 \\ &+ \cos(\beta)[(A_\uparrow - A_\downarrow)\cos^2(\phi)\cos(\phi_d) + (B_\uparrow - B_\downarrow)\sin^2(\phi)] \\ &- \sin(\beta)[(A_\uparrow - A_\downarrow)\cos^2(\phi)\sin(\phi_d)]\end{aligned} \tag{3.20}$$

$$(A_\uparrow - A_\downarrow)\cos(\phi)^2 = U_1 = -(B_\uparrow - B_\downarrow)\sin(\phi)^2 \tag{3.21}$$

$$\phi_d = \pi + \epsilon \tag{3.22}$$

$$(A_\uparrow + A_\downarrow)\cos(\phi)^2 = U_2 = (B_\uparrow + B_\downarrow)\sin(\phi)^2 \tag{3.23}$$

$$\hat{H} \approx \epsilon U_2 \hat{I}\sin(\beta) - U_1\hat{\sigma}_z(2\cos(\beta) - \epsilon\sin(\beta)) \tag{3.24}$$

Equation 3.18 describes an identity term with no spin-dependence given by the sum of the ACSS on the two spin states, and a $\hat{\sigma}_z$ spin-dependent term given by the differential ACSS. Equation 3.19 gives the spin-independent terms, with the first line describing a global energy shift to both spin states that will produce no measurable change to the spin precession and can be ignored. Line two and three of equation 3.19, however, have a spatial dependence of the energy shift and will give rise to a spin-independent force, with line two and three being out of phase of each other by 90 degrees. Following the same structure, the first line of equation 3.20 gives a uniform energy shift on the spins, this time a differential shift between the two spin states. This will give rise to a shifted spin precession rate, and as alluded to previously can be canceled by setting the polarization angle ϕ to cancel the differential ACSS of each beam as described by equation 3.21. Lines two and three of equation 3.20 describe two spatially dependent ACSSs which will produce two spin-dependent forces 90 degrees out of phase of each other. The net result will be a single spin-dependent force with the phase of the force determined by ϕ_d. Additionally, if $\phi_d = 0$, meaning the polarizations of the two beams are aligned, the ACSS nulling condition will similarly be satisfied for the spin-dependent force and only a spin-independent force will be produced. In contrast, with the beams cross-polarized, $\phi_d = \pi$, the spin-independent force can be canceled if equation 3.23 is satisfied.

The experiment now operates at a detuning from resonance such that equation 3.21 and 3.23 are simultaneously satisfied, which occurs at a singular laser frequency $\approx$ 12 GHz blue of the $2s^2S_{1/2}(m_J = +1/2) \rightarrow 2p^2P_{3/2}(m_J = +1/2)$ transition, which is $\approx$ 30 GHz red of the $2s^2S_{1/2}(m_J = -1/2) \rightarrow 2p^2P_{3/2}(m_J = -1/2)$ transition, and with polarization angle $\phi_0 \approx 65$ degrees. Under such conditions, a small phase shift ϵ from $\phi_d = \pi$ can be described in equation 3.24, in which the spin-dependent force slightly rotates its phase and a small spin-independent force is produced primarily out of phase of the spin-dependent force. This condition was also found when the experiment was moved to its current lab around 2014. However, from ∼2018-2022 the ODF was operated at a different frequency 9 GHz blue of the expected optimal point. At this other detuning, a separate ϕ_0 angle was found that satisfied equation 3.21, however equation 3.23 should not have been satisfied. This should have produced a spin-independent force in phase with the spin-dependent force ($\cos(\beta)$ term) for $\phi_d = \pi$. Suspiciously $A_\uparrow + A_\downarrow \sim 0$ at this detuning that is equally detuned from the nearest π transition for each spin state but with opposite signs. This means by setting $\phi_d \neq \pi$, the spin-independent force could be any relative phase to the spin-dependent force, but it should not have been possible to cancel both forces simultaneously unless $B_\uparrow + B_\downarrow \sim 0$.

Looking only at the closest transitions which dominate the ACSS for $B_{\uparrow/\downarrow}$, $B_\uparrow$ is detuned ~59.3 GHz red of the $\hat{\sigma}_+$ transition to the $P_{3/2}(m_J = 3/2)$ state, while $B_\downarrow$ is detuned ~68 GHz blue of the $\hat{\sigma}_-$ transition to the $P_{3/2}(m_J = -3/2)$ state. If the beams were perfectly orthogonal to the magnetic field, there could be no imbalance in these two polarization components and so a small non-zero spin-independent force should exist. However, because the beams enter at a shallow angle it is, in principle, possible to have some small imbalance between $E_{\hat{\sigma}_+}/E_{\hat{\sigma}_-}$. Since the transitions are detuned with opposite signs and similar magnitudes only a small ~2 degree imbalance is necessary to set $B_\uparrow + B_\downarrow = 0$. This is just slightly out of reach with the shallow angle of the beams using these rough numbers, but it is very close. Writing the true general polarization state of one beam gives:

$$\vec{E} = E_0[\cos(\phi)\hat{z} + e^{i\delta}\sin(\phi)(\cos(\theta)\hat{x} + \sin(\theta)\hat{y})]. \tag{3.25}$$

As before ϕ sets the ratio of $\hat{\pi}$ to $\hat{\sigma}$ electric field components, and $\theta = \pm 10^\circ$ is the angle of the beams (see figure 3.9). Now an ellipticity δ of a single beam is defined and the component of the electric field in the $\hat{y}$ direction is no longer ignored. The ratio of $|E_{\hat{\sigma}_+}|^2/|E_{\hat{\sigma}_-}|^2 = |\vec{E}\cdot(\hat{x}+i\hat{y})|^2/|\vec{E}\cdot(\hat{x}-i\hat{y})|^2$ is then given by

$$\left|\frac{E_{\hat{\sigma}_+}}{E_{\hat{\sigma}_-}}\right|^2 = \frac{1 - s\sin\delta}{1 + s\sin\delta} \tag{3.26}$$

$$s = 2\cos\phi\sin\phi\sin\theta, \tag{3.27}$$

giving a maximum ratio of squared electric fields of 1.128 for a polarization null angle of 65.8° and beam angles of ±10°. This is slightly smaller than the ratio of ~ 1.147 needed using the naive estimate of the detunings above to set $B_\uparrow + B_\downarrow = 0$. If this indeed was the mechanism by which the nulls were achieved previously, a detailed comparison would need to be done to see if the ratio of spontaneous emission to spin-dependent force strength and sensitivities to polarization and frequency drifts are improved.

3.7.2 ODF experimental details

The ODF was previously generated using the dye laser that is now used as the cooling laser. While the magnet was repaired, it was replaced with a 313 nm fourth harmonic generation (FHG) Toptica system capable of outputting up to 800 mW of UV, mounted underneath the optics table to avoid any fiber coupling loss and make space for the large laser. In general the ODF has been remarkably stable—even more so than the previous ODF—likely due to a custom cut enclosure around the whole magnet table. However it is clear that mounting underneath the table has been non-ideal, with any weight being put on the table slightly adjusting the beam pointing of the system. Motorized mirrors allow precise alignment of the ODF without having to work near the optics table once roughly set up, allowing up to a few months of runtime before more major realignment is necessary. Similar to the cooling beams, the pulse timing and intensity is servoed using amplitude modulation of the RF tone applied to AOMs. In addition, the beams can be picked off and interfered to measure a beatnote between the two beams to stabilize the relative phase. After mixing down the beatnote with a reference DDS it can be fed back onto a frequency source using a proportional integral feedback loop to a voltage controllable frequency modulation source. The frequency of the laser is stabilized to $\sim$100 MHz using a wavemeter reference with feedback to a piezo inside the laser. Polarization control of the beams is done using three motorized waveplates. A motorized half waveplate in each beam path sets ϕ_0 of each beam. Another half waveplate in the upper beam path is rotated about an axis normal to the optics table with its fast axis aligned with vertically on the table to adjust ϕ_d. The idea is that by entering at non-normal incidence the beam travels a larger distance in the half waveplate, imparting a tunable relative phase shift in the horizontal relative to vertical polarization components.

3.8 Electromagnetically induced transparency (EIT)

To achieve temperatures below the Doppler cooling limit an interaction must be generated with a narrower resonance than that set by the lifetime of the cycling transition $2s^2S_{1/2}(m_J = 1/2) \rightarrow 2p^2P_{3/2}(m_J = 3/2)$. Common techniques to achieve this are sideband cooling [41] and electromagnetically induced transparency (EIT) cooling [42]. Sideband cooling involves resolving a transition that removes a single quanta of motion, called a red sideband, and is generally not well suited to our experiment which will have potentially hundreds of modes to cool. In contrast, EIT cooling involves generating a narrow Fano-like resonance tuned to resonantly enhance red sideband transitions over completely suppressed carrier transitions which make no change to the quanta of motion but can cause heating from recoil (see [42]), and strongly suppressed blue sideband transitions which add one quanta of motion. The bandwidth of EIT cooling is generally similar to the mode frequencies being cooled. EIT cooling has the advantages of being fast, broad-bandwidth, and largely insensitive to experimental parameters such as mode frequencies, detunings, and pulse timings. The main downside to EIT cooling is that it cannot get as cold as resolved sideband cooling, with our experimentally measured limit around 0.3 quanta of our 1.6 MHz axial COM mode.

To generate the narrow Fano-like resonance, a three-level system is used which includes the two $S_{1/2}$ levels, coherently coupled via an auxiliary third $P_{3/2}(m_J = 1/2)$ state as shown in figure 3.10. These lasers are generated with two Toptica second harmonic generation (SHG) systems that output 600–800 mW of 626 nm light. The $\hat{\sigma}_+$-polarized higher frequency beam, called the sigma beam, is locked to an iodine line similarly to the Doppler cooling beam. The $\hat{\pi}$-polarized beam, called the pi beam, is offset locked to the sigma using an in-fiber fast 31 GHz photodiode which measures the beatnote between the two lasers at 1252 nm. This beatnote is mixed down with a 31 GHz source made by mixing a 15.2 GHz DRO with a ~300 MHz Novatech DDS, with the resulting ~15.5 GHz frequency doubled. The DC voltage representing the phase of the two laser's beatnote is then actively fed back using a Fast Analog Linewidth Control (FALC) Toptica servo to the pi laser diode current for frequency feedback with bandwidths of a few hundred kHz.

After fiber coupling the red light over to the magnet table the beams are frequency doubled using a home-built UV doubling cavity and an Agile Optic doubling cavity similar to the cooling beams, followed by double pass AOMs and telescopes. The EIT beams are counter-propagated along the ODF beam path for good starting alignment. Final powers at the ions with our beam waists required ∼20 mW in the sigma beam and ∼5 mW in the pi. The power constraints on the sigma are our most demanding in the experiment due to drifts of alignments reducing the doubler and AOM efficiencies on weeks timescales. The sigma beam also is used as a repumping beam to pump any population from $|\downarrow\rangle$ to $|\uparrow\rangle$ by exciting to the $P_{3/2}(m_J = 1/2)$ level.

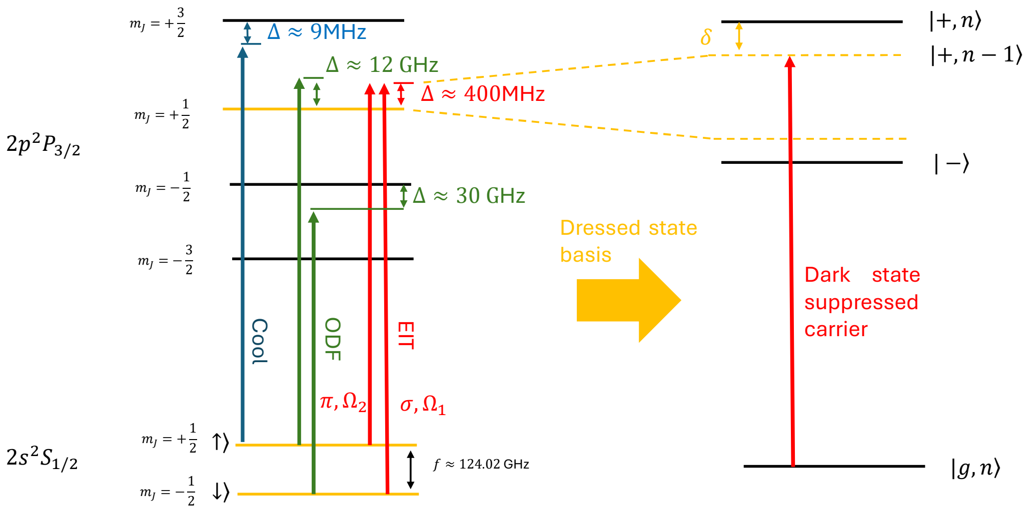

Figure 3.10: EIT level scheme. a) Level diagram of EIT cooling along with the previously described cooling and ODF transition frequencies. A $\hat{\sigma}_+$ ($\Delta m = +1$) and $\hat{\pi}$ ($\Delta m = 0$) polarized beam with frequency splitting of the 124.02 GHz qubit frequency form a coherently coupled three level system. b) In the dressed basis, the pair of lasers ideally would evolve the system into a dark state superposition of $\uparrow, \downarrow$ given by g and motional quanta n. Due to destructive interference between the $g \rightarrow +, g \rightarrow -$ transitions no fluorescence can occur. However, a narrow Fano resonance centered δ (the ACSS) away at the $+$ state can drive transitions through a strongly enhanced red sideband $n \rightarrow n - 1$.

Chapter 4

Calibrations and Alignments

This chapter details the day to day operational details of running the penning trap experiment to calibrate and align the various subsystems discussed in chapter 3.

4.1 Microwave calibrations

4.1.1 Microwave Rabi calibrations

Most experiments involve a microwave operation at some point in their pulse sequence, usually to control the initialization, readout, and echoing of the dynamics via global spin rotations. For this reason the overwhelming majority of experiments first involve a calibration of the microwave resonant frequency, and drive strength of the 124 GHz radiation at the ions. An oscillating magnetic field orthogonal to the magnetic field resonant with the energy splitting can interact with the ions' spins via the magnetic dipole interaction to induce oscillation between the spin up and down states at a rate Ω, also called Rabi oscillations[43]. Assuming the ions are initialized in the $|\uparrow\rangle$ state via repumping, if the radiation is detuned $\Delta = \omega - \omega_0$ from resonance, the spin state at time t is described by:

$$P_\uparrow = 1 - \frac{\Omega^2}{\Delta^2 + \Omega^2} \sin^2\left(\frac{\Omega t}{2}\sqrt{1 + \left(\frac{\Delta}{\Omega}\right)^2}\right) \tag{4.1}$$

$$= \cos^2(\Omega t/2), \Delta = 0 \tag{4.2}$$

At $\Omega t_\pi = \pi$ and on resonance, a "π pulse" is achieved that flips the spin state from bright to dark and is called the "π time". By setting the pulse duration to close to this π time and scanning the frequency a resonance dip can be found and fitted to estimate the microwave frequency and π time. A more precise estimate of the π time is then achieved by driving on resonance and varying the drive time and fitting the corresponding oscillation.

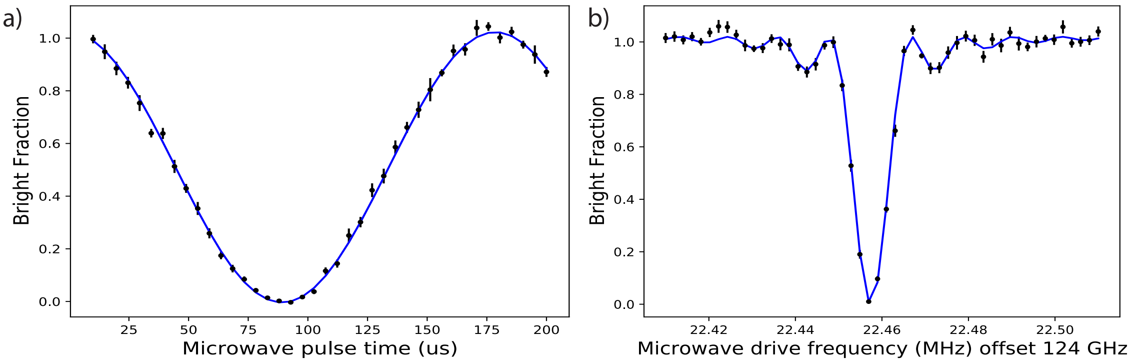

Figure 4.1: Rabi microwave calibrations. a) Scanning the microwave pulse time on resonance generates a $\cos^2$ curve as described in equation 4.2. A fit extracts a π time estimate of 89.7 ± 0.5 μs. b) Setting the microwave pulse time roughly to a π pulse and scanning the microwave frequency gives a resonance feature that can be fit to measure the resonance frequency, as described in equation 4.1. The fit gives a resonance frequency of 124,022,457,401 ± 43 Hz.

4.1.2 Microwave Ramsey calibrations

Rabi flopping can be visualized by an effective vector pointing along the direction of the oscillating magnetic field. This requires rotating the reference frame of the spins to co-rotate at the Larmor precession rate. In this co-rotating reference frame, the spins will rotate about this effective magnetic field vector. Therefore, if the phase of the microwave drive is changed, the axis about which the spins rotate can be varied. Additionally, if the microwave drive is detuned it can be represented as an effective magnetic field vector tipped away from the equator of the Bloch sphere. Finally, if the spin states are initialized along some axes on the equator of the Bloch sphere with the drive turned off, if the frequency of the reference microwave oscillator is different from the true Larmor precession frequency, this will appear as a rotation of the phase of the effective magnetic field at the detuning between the reference oscillator and the true Larmor frequency.

This picture can be used to explain Ramsey interferometry [44], where the π pulse is split into two $\pi/2$ pulses with a long precession period T between. By scanning the frequency of the reference oscillator in the wait time the phase accumulation between the reference oscillator and the true Larmor frequency is scanned and produces Ramsey fringes described by

$$P_{\uparrow} \approx \sin^2\left(\frac{(\omega-\omega_0)T}{2}\right) \tag{4.3}$$

Importantly, this produces Ramsey fringes with frequency widths set by the free precession time T. Unlike the frequency dependence of a Rabi scan, the Ramsey scan has multiple fringes that can incorrectly fit the resonant frequency if the central frequency is not known well enough to identify which fringe is correct.

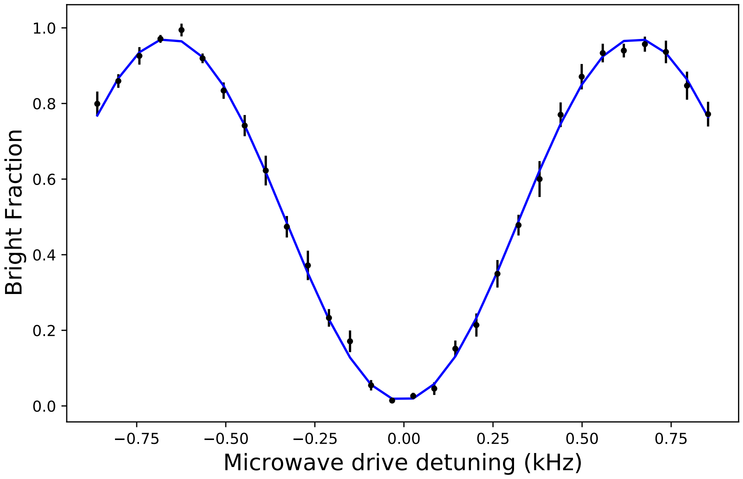

Figure 4.2: Ramsey microwave calibration. By scanning the detuning between the true Larmor frequency and the reference oscillator, the final microwave pulse phase will rotate around at the detuning causing Ramsey fringes as described in equation 4.3. Setting a free precession time of $T = 700$ us gives a fringe width of ~ 1.3 kHz, slightly narrower than $1/T$ due to the non-zero $\pi/2$ pulse time which are not driven on resonance. The fit gives a resonance frequency of 124,022,457,681 ± 2.5 Hz.

4.1.3 Microwave frequency chirp

A peculiar issue was identified with the microwave system where the resonance frequency found from a Ramsey scan was systematically different than that found from a Rabi scan. Upon further investigation, it was found that the delay time since the microwaves were last pulsed effectively shifted the frequency and π time of the microwaves. This could be demonstrated by plotting the fitted microwave frequency as a function of Rabi pulse time, which showed a frequency deviation that increased dramatically for shorter delays. Additionally, by doing repeated $\pi/2$ pulses with varying delays, it was found that the microwaves would gradually over-rotate or under-rotate depending on the delay between the pulses. This effect is believed to be a thermal effect with the microwaves, and so to alleviate the issue the microwaves are now left constantly on at full power on the ions, with the frequency jumped order 20-100 MHz off resonant by default. This requires careful phase tracking of the microwave phase, since the frequency is now jumped between microwave pulses (see section 3.1 on the ARTIQ control system and DDS's).

4.2 Magnetic field calibrations and alignments

4.2.1 Axial magnetic field gradients

With the ability to measure the Larmor precession frequency precisely, it is straightforward to measure the magnetic field uniformity. By applying a voltage to a distant electrode such as T1 or T4, the crystal to first order displaces axially a distance set by the axial confinement strength. By calibrating this displacement and measuring the Larmor frequency at each axial displacement, an axial magnetic field gradient can be measured. Importantly, if the shift is small enough, the overall drift of the magnetic field during the time it takes to displace the crystal matters, and if the displacement is far enough, the perpendicular cooling beam height must be adjusted to move with the crystal.

When the magnet was first ramped up to field the field uniformity was carefully measured and shimmed using a nuclear magnetic resonance (NMR) probe. In the previous magnet it was found that this shimming did not hold once the mirror crown was inserted into the bore of the magnet, along with the trap. In 2019, an attempt to compensate this gradient accidentally increased the gradient to ~ 400 Hz/um, or equivalently ~ 150 mG/mm. This large axial magnetic field gradient made the coherence of the spins extremely sensitive to axial motion, and made microwave control of multi-plane crystals impossible. Using the ions to adjust the current in the axial shim coil, the gradient in the new magnet was reduced to ~ 6 Hz/um or 2.5 mG/mm, which was partially limited at the time by bad microwave coherence times of a few hundred microseconds due to the low phase noise 100 MHz source being repaired.

4.2.2 Planar magnetic field gradients

In addition to an axial magnetic field gradient, the experiment has uncompensated magnetic field gradients in the planar directions. These gradients are less impactful because the first-order planar gradients are rotationally averaged over. This means that the primary effect of planar magnetic field gradients is to reduce the effective microwave power hitting ions at larger radii, as the effective phase modulation puts more power into the first rotational sideband. This produces a small shift in the π time, resulting in slower Rabi rates further from the center of the crystal. To quantify this, the microwaves can be driven at a rotation sideband of the resonant Larmor frequency. However, another equivalent effect occurs from Doppler shifts on the microwave radiation from any component of the microwave k vector in the plane, with the two effects distinguishable from their rotation frequency dependence. For our rotation frequencies and crystal sizes, in general these effects are of the same size making them hard to distinguish, but in general are very small effects. The effective Rabi rate of the rotation sidebands is $\sim$20x smaller than the resonant Rabi rate.

Alternatively, the planar magnetic field gradients can be measured by applying a voltage to two orthogonal rotating wall electrodes and measuring the shift in Larmor frequency, analogously to the axial case. Experimentally, this is not as straightforward as the axial case as we do not have independent DC voltage control on each rotating wall electrode. Measurements have placed this gradient around 8 mG/mm, pointing largely orthogonal to the ODF beam path.

4.2.3 Magnetic field stability

In addition to magnetic field uniformity, the magnetic field stability is an important magnet specification. From June 2024 to August 2025 the microwave frequency drifted down approximately 1 MHz, or equivalently a fractional drift of around 10^{-9}/hr, meaning the half life of the magnet if kept cold is order of magnitude 100,000 years, much longer than the last magnet lasted. Experimentally, much faster fluctuations in the magnetic field, likely from various metal moving around in neighboring labs, dominate magnetic field changes on the few seconds time scale. As an example, moving our oscilloscopes mounted over the optics table can shift the microwave frequency 10s of kHz, enough to shift the microwave frequency more than a few weeks of magnetic field drift (or equivalently the drift can be compensated for a few weeks by moving the scopes a few inches a day).

4.2.4 Fast magnetic field noise and coherence times

On much faster timescales than a second the most critical magnetic field fluctuations set the fundamental coherence time of the experiment. Fluctuations of the magnetic field while the spins are on the equator of the Bloch sphere lead to random precessions that grow in time and lead to the reference oscillator losing track of the orientation of the spins. By flipping the spins about the axis of the equator they originally pointed, any low frequency noise can be canceled in what is called a spin-echo sequence. Magnetic field noise or oscillator phase noise at much higher frequencies is ideally averaged over, but for frequencies on the same time scale of the two arms of the spin echo the noise will not be canceled. The timescales of this noise can be characterized by a Ramsey sequence, where the spins are allowed to freely precess between two microwave $\pi/2$ pulses for a variable time that is scanned. After careful calibration of the microwave frequency this will lead to the ions being dark if the orientation of the spins is retained, and eventually complete dephasing of the spins giving random 50% bright population. This could be more precisely characterized by scanning the final microwave phase to determine the contrast of the oscillation as the phase is varied, to discriminate between coherent rotations and spin dephasing. The timescale of this dephasing is often referred to as the T2* coherence time in NMR, with the * usually dominated by dephasing due to inhomogeneity, unlike in our case. More often we are interested in the decoherence time with a spin echo to cancel low frequency magnetic field fluctuations, which involves sandwiching a π pulse about an axis rotated $\pi/2$ between the Ramsey microwave $\pi/2$ pulses. This is often referred to as the T2 time, which cancels inhomogeneous dephasing and low-frequency dephasing.

Ignoring any coherent rotations and associating all decreases in bright fraction to decrease in contrast or spin dephasing gives

$$P_{\uparrow} = \frac{1}{2}(1 + e^{-\frac{(2\Gamma\tau)^2}{2}}), \tag{4.4}$$

where 2τ is the total Ramsey precession time, and Γ is the rms frequency fluctuations of the resonant microwave frequency, either between arms if measured in a spin echo, or over the total precession time. Γ corresponds to 1/T2, or 1/T2*, depending on if the sequence included a spin echo or not.

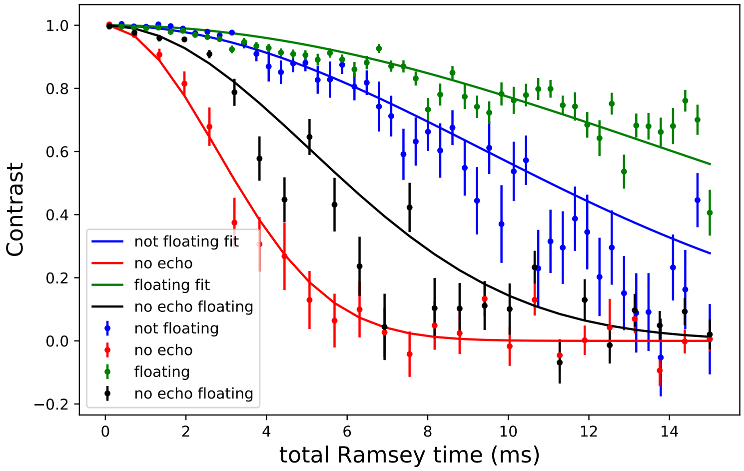

Figure 4.3: Calibrations of decoherence due to magnetic field fluctuations. Fits give rms fluctuations without an echo of 360 ± 15 Hz, 197 ±10 without (red curves) and with floating the table (black curves) respectively. With an echo these rms fluctuations reduce to 107 ± 4 Hz, 72 ± 2 Hz without (blue curves) and with (green curves) floating the table respectively.

The phase noise of the 100 MHz reference oscillator has been carefully tested and suggests a T2 limit of around 100 ms. Experimentally, we find much shorter T2 timescales of 10 to 25 ms, depending on whether the optics table which the magnet sits on is floated or not. We therefore attribute most of the low-frequency magnetic field noise to vibrations (possibly coupling through induced emfs or changes in the coil)[45].

4.2.5 Magnetic field alignment

Another desirable specification of the magnetic field is how well the electric quadrupole can be aligned with the magnetic field. If this is poorly aligned, the component of the electric quadrupole mis-aligned with the magnetic field axis will appear in the rotating frame as an oscillating electric field drive. If a motional mode of the crystal is resonant in the rotating frame with the drive a heating resonance occurs. These “zero frequency modes”, so called because they are excited by zero frequency static field errors in the lab frame, also called Trivelpiece-Gould Modes (TPGM)[46], can be identified by sweeping the rotation frequency until the l, m modes of a three dimensional crystal become zero frequency in the lab frame. Example heating resonances and l, m structures are shown in figure 4.4. These heating resonances were first demonstrated by varying the torque applied with a perpendicular cooling beam [47]. Subsequently they were shown in the original experimental realization of a rotating wall potential, and show hysteresis, or dependence on the direction of the rotation frequency sweep [27].

When first inserted, the trap is misaligned enough that higher order l, m modes are strong enough to drive heating resonances at lower rotation frequencies. To align the trap to the magnetic field, the cooling beams are far detuned such that heating of the crystal when sweeping the rotation frequency increases the fluorescence rate as it is heated into resonance via Doppler shifts. With the new ARTIQ control of the rotating wall frequency, updates can be done in a few microseconds, allowing fast fine frequency steps of the rotation frequency as shown in figure 4.4. The whole vacuum system is then mounted on a two-axis translation stage, with a pivot point created by a sleeve attached around the vacuum envelope approximately 10 cm above the ion crystal far down the bore with spring loaded arms centering the envelope in the bore. Moving the translation stage then displaces the top of the vacuum system approximately 1 m away from the pivot point that remains stationary, and therefore undesirably shifts the center position at the ions $\sim 1/10$th the distance.

By tilting the trap, the heating resonances strengths are empirically found to change, indicating the direction to tilt. Care must be taken to move the perpendicular cooling beam commensurate with the trap translation so that fluorescence changes are not attributed to Doppler shifts of the perpendicular cooling beam, and the in-plane cooling remains on the correct side of the crystal. Because the heating resonances are static in the lab frame, spatial dependence of the heating resonances can be seen on the side and bottom view images as shown in figure 4.4. This procedure is repeated first in a lower axial confinement of around 890 kHz to get a first alignment, and subsequently in the standard 1.6 MHz axial frequency configuration with stronger heating resonances. Once well aligned, the signal can be inverted by operating in standard conditions and looking for heating of the crystal producing a drop in fluorescence. This requires very good alignment as the signal is much more sensitive to heating the crystal off the rotating wall compared to far detuned cooling beams. Sitting on the dip or peak of the resonance, small adjustments of the translation stage are made to increase or decrease the count rate corresponding to decreasing the heating.

Experimentally, at least two additional confounding heating resonances can make identifying the zero frequency modes that are sensitive to alignment difficult. The first confounding source of heating is from the rotating wall drive itself. For this reason, a dipole wall is generally used rather than a higher order wall that require larger drive strengths and produce more heating resonances. Additionally, varying the wall drive strength is useful to check if the heating is driven by static field errors as opposed to from the wall itself. Lastly, heating resonances from impurities, particularly $BeOH^+$ and BeH^+ cyclotron resonances, and axial center of mass mode heating resonances take careful rotating wall conditions to not heat the cloud too strongly when swept over. For example, when sweeping over a $BeOH^+$ cyclotron resonance or axial COM heating resonance the wall may be reduced in strength or jumped in frequency rather than smoothly ramping over the resonance. The ultimate sensitivity of this technique is found to be much better than .001 inches adjustments on the micrometer stage over a ~ 1 meter lever arm, corresponding to an angle of $<.01$ degrees.

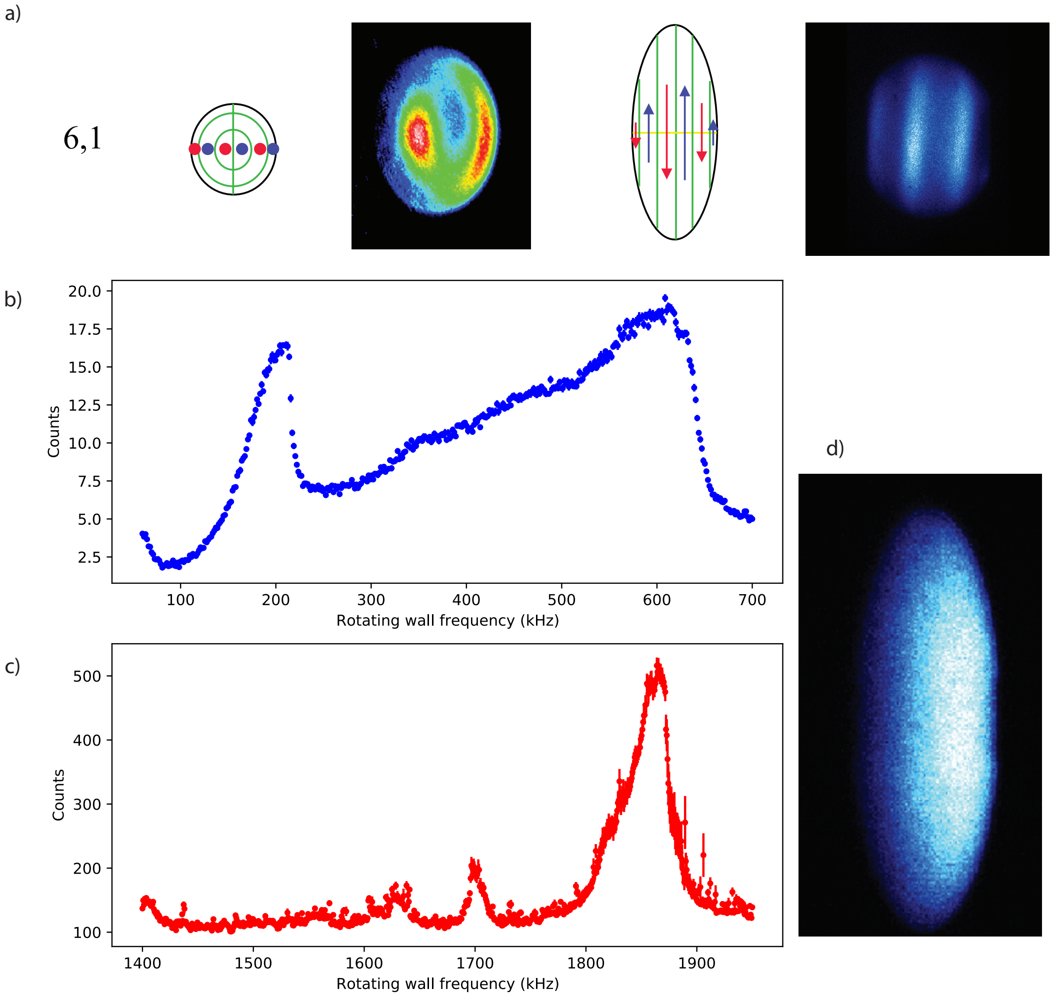

Figure 4.4: Excited $m = 1$ zero frequency mode (TPGM) heating resonances due to static field errors used to align the trap to the magnetic field. a) The top row from left to right shows an example 6,1 excited mode with the bottom view and side view electric fields which have 6th order radial dependence. When the ion motion is towards the parallel beam (red arrows), the parallel cooling laser Doppler shifts into resonance increasing fluorescence. Experimental images of the (6,1) mode are from a previous trap. b) Initial alignment when the trap was placed in the new magnet gave heating resonances in the 880 kHz axial frequency trap around rotation frequencies 200-700 kHz, likely (6,1) modes. Increasing counts corresponds to Doppler shifting the far detuned beams into resonance from heating. c) Final (2,1) mode heating resonance just below 1.9 MHz rotation frequency in the deeper 1.6 MHz axial frequency trap, along with erroneous resonances that are not from trap misalignment. d) image of the heated (2,1) mode at around 1.9 MHz associated with c).

4.3 ODF calibrations and alignments

4.3.1 ODF alignment

With the ion's spin states well characterized and controlled with our microwave source, the next main tool of the experiment is the ODF (see 3.7 for an overview). The goal of the ODF is to couple the collective motion of the ions to the spin states. Specifically, the axial motion is the desired motion to couple to, and so the first requirement of the ODF is to align the k vector difference of the upper and lower beam with the magnetic field axis (see Chapter 7 for an exception to this). We can approximate the Hamiltonian of the system with a tilted k vector as

$$H_{ODF} = \sum_i U\cos(k_\parallel z + \mu t + \Psi + k_\perp \rho_i \sin(\phi_i - \omega_r t - \phi_0))\hat{\sigma}_z^i \tag{4.5}$$

$$\approx \sum_{i=1}^{N}\sum_{n=0}^{\infty} \frac{\tilde{U}_i}{2^{\delta_{0,n}}} J_n(k_\perp\rho_i)[\cos(\mu t + \Psi + n(\phi_i - \omega_r t - \phi_0)) + (-1)^n\cos(\mu t + \Psi - n(\phi_i - \omega_r t - \phi_0))]\hat{\sigma}_z^i \tag{4.6}$$

$$= \sum_{\pm}\sum_{i=1}^{N}\sum_{n=0}^{\infty} \frac{\tilde{U}_i}{2^{\delta_{0,n}}} J_n(k_\perp\rho_i)(\pm 1)^n\cos(\mu t + \Psi \pm n(\phi_i - \omega_r t - \phi_0))\hat{\sigma}_z^i. \tag{4.7}$$

In equation 4.5, $k_\parallel$ is the k vector component aligned with the magnetic field and is approximately $2\pi/900$ nm, $k_\perp$ is the component of the k vector in the plane, and U is the ACSS amplitude.[1] The equilibrium position of an ion i is given by the radius ρ_i and azimuthal coordinate ϕ_i. The relative phase of the two ODF beams is given by Ψ, while the orientation of the wavefront tilt in the lab frame is given by ϕ_0, which rotates at the crystal rotation frequency ω_r in the rotating frame. Taking $z = 0$ reduces U to $\tilde{U}_i = U\exp(-(k_\parallel z_{rms,i})^2/2)$, which is a Debye-Waller factor[2] reduction in the maximum gradient of the interaction due to thermal averaging over fluctuations in the axial positions of the ions. From here on the DWF is assumed approximately uniform across the crystal. The notation $\delta_{0,n} = 1$ if $n = 0$ and is 0 otherwise. The expansion was carried out using the Jacobi-Anger

---

[1] Note this U definition which will be used throughout this thesis is really half the differential ACSS, as the shift applied to the state $|\uparrow\rangle$ ($|\downarrow\rangle$) is $+U$ $(-U)$.

[2] See [14] supplementary material for estimates of this factor and its variation across the crystal.

identity $e^{iz\sin(\omega t)} = \sum_{-\infty}^{\infty} J_n(z)e^{in\omega t}$, which describes expanding phase modulation of modulation index z in terms of sidebands at frequency multiples of the modulation frequency ω. The strengths of the sidebands are then characterized by cylindrical Bessel functions of the first kind J_n. If this Hamiltonian is applied resonant with a rotation sideband $\mu = m\omega_r$, removing the fast-rotating terms leaves

$$H_{ODF}(\mu = m\omega_r) \approx \tilde{U} \sum_i J_m(k_\perp \rho_i) \cos(m(\phi_i - \phi_0) + \Psi)\hat{\sigma}_z^i. \tag{4.8}$$

By applying this Hamiltonian with the spins initialized on the equator of the Bloch sphere, a pattern will be imprinted that is static in the rotating frame of the crystal. The patterns will have azimuthal order m and radial dependence $J_m(k_\perp \rho_i)$, with the azimuthal orientation of the pattern rotated $\Psi + \frac{\pi}{2}$ from the orientation of the lab frame pattern for $m = 1$.

By stabilizing the ODF phase Ψ, imprinting this pattern, and detecting the spin states of the ions in the rotating frame, in principle it is possible to exactly calculate the tilt of the ODF beams and the orientation of the tilt correction necessary. This is described in more detail in 7 for characterizing larger tilts. With global fluorescence, all spin rotations will average to 0 unless the cloud is displaced off-center with a dipole wall. For this reason, it is also in principle possible to identify the orientation and size of the tilt by applying a large dipole wall strength and measuring the average rotation of the spins as a function of the relative phase of beatnote to the rotating wall frequency.

In practice, instead multiple rotation sidebands are measured with global fluorescence, with the ODF phase left unstabilized and rotations converted into deviations from dark with a microwave $\pi/2$ pulse in phase with the initializing $\pi/2$ pulse to measure spin dephasing. In general, due to the shallow angle vertically of the beams the tilt is largely dominated by horizontal misalignment. Using a spin echo pulse sequence of arm time τ and beatnote $m\omega_r$, with a phase advance in the second arm to add coherently with the first, the bright fraction averaged over a uniform disk of radius R can be written as

$$P_\uparrow = \frac{1}{2} - \frac{1}{R^2}\int_0^R \rho J_0\left(\frac{4\tilde{U}\tau}{\hbar}J_n(k_\perp\rho)\right)d\rho. \tag{4.9}$$

Taking small angle approximations of the argument of the J_0 term gives

$$P_\uparrow = \left(\frac{\tilde{U}\tau}{\hbar}\right)^2 \left\langle J_n(k_\perp\rho)^2\right\rangle, \tag{4.10}$$

where $\langle J_n(k_\perp\rho)^2\rangle = \frac{1}{R^2}\int_0^R \rho J_n(k_\perp\rho)^2 d\rho$. Taking small arguments of $J_n(x) \approx \frac{1}{n!}(\frac{x}{2})^n$ gives the ratio of rotation sideband n to $n-1$:

$$\frac{P_{\uparrow,n}}{P_{\uparrow,n-1}} \approx \frac{k_\perp^2 R^2}{4n(n+1)}. \tag{4.11}$$

This formula can be used to estimate the k vector misalignment for small tilts. Experimentally, a continuous measurement is taken that measures multiple rotation sidebands to give an idea of the misalignment. Simultaneously, motorized mirrors attempt to walk with a calibrated ratio of tilts between the last two motorized mirrors on the optics table before being sent up the magnet bore. Because of hysteresis in the mirrors this calibration is not reliable enough for the smallest tilts, and so periodically the beams must be re-centered on the ions.

Ideally, the sidebands are reduced when walking in the correct direction, with the higher order sidebands decreasing first, in contrast to all sidebands reducing from tilting off the ions. However, in addition to spin precession from tilts of the ODF, axially driven motion from the rotating wall can also be sensed when the beatnote is at the rotating wall drive frequency. The source of the drive is likely from asymmetric capacitive pickup on the neighboring T2/T3 electrodes. For this reason, alignments are done with a dipole wall, rather than a quadrupole wall that excites the second rotation sideband. Phase sensitive measurements of driven motion using the quadrupole wall confirmed this drive could be canceled with an external axial electric field drive, with the strength corresponding to ∼6 nm amplitude motion. Notably the further out the crystal radius is, corresponding to larger dipole wall strengths and larger crystals, the more sensitive the measurement becomes. Additionally, once the sidebands are reduced largely to the first and second sideband, the arm times are increased to increase the sensitivity. Ultimately, non-idealities in the beams such as wavefront mismatch and intensity non-uniformity likely limit the ability to eliminate the sidebands.

When poorly aligned, many rotation sidebands are visible and limit the ability to couple the axial motion to the spins as shown in figure 4.5. As alignment is improved the axial drumhead modes become measurable, with the ratio of the spin-dependent force to decoherence sensitive to the small errors in the alignment. Rough estimates of the best alignment achievable suggest tilts of order .01 degrees, with the horizontal direction being $\sim$ 3 times more sensitive than the vertical.

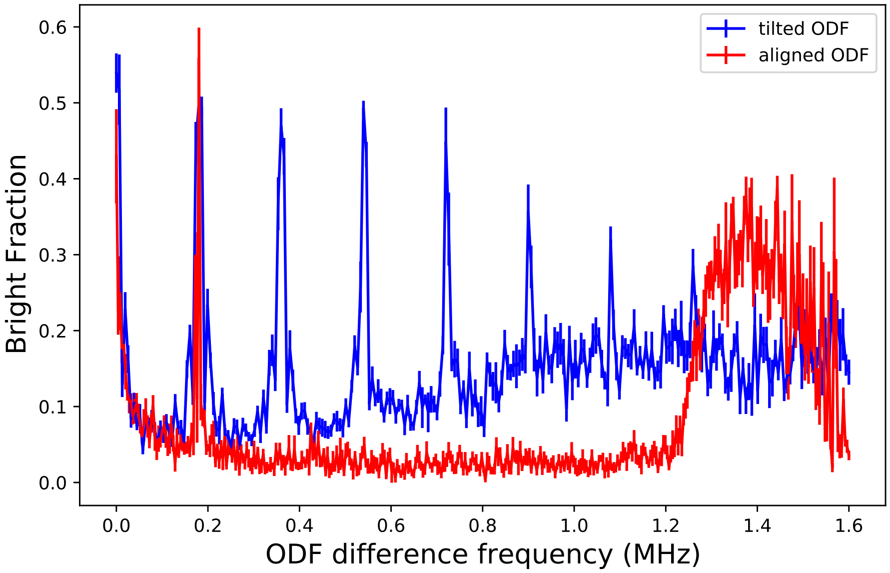

Figure 4.5: ODF alignment measurement as gauged by the strength of rotation sidebands given by the spikes in spin dephasing at multiples of 180 kHz. An intentional tilt of roughly 3 mrad or .15 degrees is achieved by a motorized actuator tilting a 1 inch mirror 70 microns across its surface, which is walked back onto the ions using a second motorized mirror. Roughly 7 rotation sidebands (blue curve) are then visible, with the axial drumhead modes no longer distinctly identifiable. In contrast when well aligned (red curve) only a single rotation sideband is visible and the drumhead modes are far separated from the nearest rotation sideband. Note the red curve is actually at 178 kHz rotation frequency on a different crystal than the blue curve.

4.3.2 Spontaneous emission

Often the primary decoherence mechanism in the experiment is spontaneous emission due to off resonant light scatter from the ODF beams. For a given ODF laser frequency and polarization the ratio of the spin-dependent force to spontaneous emission rate is fixed. Increasing the laser power of the ODF increases both the spontaneous emission rate and the spin-dependent force strength linearly. To achieve a better ratio, the beams can be detuned further from resonance at expense of requiring more laser power and no longer being able to satisfy both nulling of the ACSS and spin-independent forces. Without careful intensity stabilization the ratio will quickly be dominated by intensity fluctuations in the beams varying the ACSS, making operating at an ACSS null vital to achieving good coherence.

Experimentally we carry out the same T2 coherence time measurement described in section 4.2.4, now with either one or both beams on during the Ramsey free precession times. The decay of contrast can then be fitted to

$$P_{\uparrow} = \frac{1}{2}(1 + e^{-\frac{(2\Gamma_{mag}\tau)^2}{2} - 2\tau\Gamma}), \tag{4.12}$$

where Γ_{mag} is the decoherence from the magnetic field fluctuations and $\Gamma = \frac{1}{2}(\Gamma_{ram} + \Gamma_{el})$ is the total spontaneous emission rate from Raman and elastic scattering, with $\Gamma_{el} \approx 4\Gamma_{ram}$ for our operating condition.

Figure 4.6 shows representative decoherence rates from the ODF in our system. Calculated decoherence rates are in reasonable agreement based on the measured ACSS when $\hat{\pi}$ polarized. By including a spin echo any residual ACSS is ideally canceled. However, if the ACSS is not nulled the decoherence rate becomes dominated by intensity fluctuations in the beams rather than from spontaneous emission. Additionally, when measuring the decoherence rate with both beams on the beatnote is set 50 kHz detuned above the highest frequency axial COM mode. Experimentally it is found that the decoherence rate from the two beams separately does not sum to the decoherence rate of both beams, which we attribute to higher order Lamb-Dicke effects. To support this we find

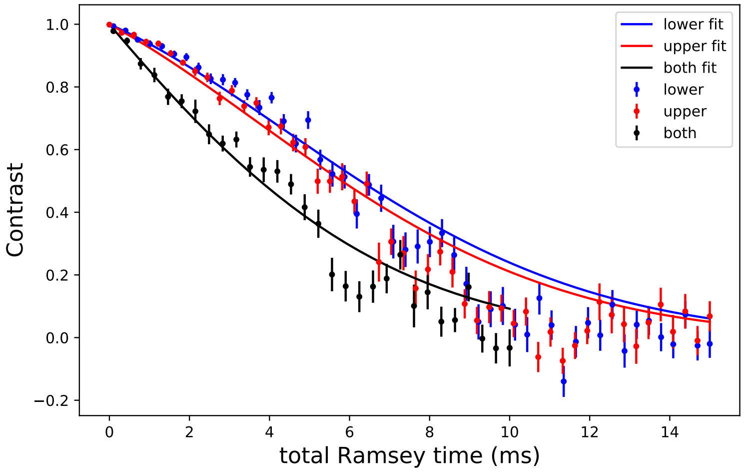

Figure 4.6: Calibration of decoherence due to spontaneous emission. A spin echo sequence while turning on either one or both beams during the free precession leads to spin dephasing which we measure as loss of coherence of the Bloch vector. A contrast of 1 represents full coherence and 0 no coherence. The single beam decoherence is tuned to be roughly equal by setting equal intensities on the ions. Decoherence rates of the lower (blue curve) and upper (red curve) beams extracted from the fits are estimated at 56 ± 4 Hz and 69 ± 4 Hz for the lower and upper beams respectively. With both beams applied simultaneously detuned 50 kHz above the axial COM mode (black curve), a decoherence rate of 152 ± 7 Hz is measured. This 20 % inflation compared to the decoherence of each beam added together is thought to be caused by higher order Lamb-Dicke effects. This discrepancy has been found to be sensitive to the ODF alignment and whether EIT or Doppler cooling is used. All of these curves are with Doppler cooling only.

that EIT cooling the axial modes near the ground state substantially reduces the discrepancy to $\sim 10\%$, compared to up to 50% for Doppler cooled crystals. Additionally, errors in the alignment inflates this discrepancy further, possibly coupling to in-plane motion.

4.3.3 ACSS nulling

To null the ACSS, first each beam is set to nominally $\hat{\pi}$ polarization by setting a motorized half wave plate in each beam path to vertical within a few degrees. A Rabi experiment as described in section 4.1.1 is carried out scanning the microwave frequency, this time with one of the ODF beams on during the microwave drive. The fitted frequency is subtracted from the calibrated resonance frequency to give the differential ACSS. By repeating this scan and tilting the horizontal and vertical knob of each final ODF mirror the optimal tilt can be found to maximize the ACSS on the ions.

From here, the intensity of the beams can be adjusted by a DAC voltage setting the intensity servo level to choose a desired ACSS. The servo level must be set less than the maximum power level at full AOM drive power, generally set with at least 20% overhead.

With the ODF beams aligned to the ions and at the desired ACSS strength, the motorized waveplate in each beam path is set to the last found nulling angle that minimizes the ACSS of each beam. From here, a Ramsey experiment as described in section 4.1.2 is carried out, this time with the microwaves always set to the calibrated resonant frequency while the half waveplate angle is scanned. At the optimal nulling angle, the Ramsey sequence will result in the ions dark, and off this optimal angle a shifted Larmor frequency rotates the phase of the final $\pi/2$ pulse to give Ramsey fringes. As the calibration is a Ramsey sequence, the minimum may not be on the correct fringe, so the ACSS can be measured with a Rabi experiment as described for the vertical polarization to check. For even more precision, the microwave frequency can be tracked with an interleaved scan as described in chapter 5, with Hz level resolution possible. Polarization and frequency drifts on the hour time scale will shift this nulling 10s of Hz for our ACSS strengths of order 40 kHz. Experimentally we have seen thermal effects from the strength of the RF drive applied to the AOM varying the polarization state. This was seen by measuring the polarization nulling angle vary with power stabilization level, proportional to the RF power applied to the AOM. Increasing the laser power and thereby decreasing the required AOM power further distinguished the effect as due to the RF power. Adding polarization optics after the AOM effectively converts these polarization rotations into amplitude fluctuations that can be servoed away.

4.3.4 COM frequency and mean-field calibration

With the ODFs aligned, the ACSS nulled, and the decoherence rate calibrated, the next calibration of the ODFs is the spin-dependent force strength. This can already be estimated by knowing the k vector, ACSS of the beams when vertically polarized, the polarization nulling angle, and some estimate of the Debye-Waller factor (DWF). However, it is difficult to generally estimate the DWF and so an experimental measurement is useful. One previously unexplored option would

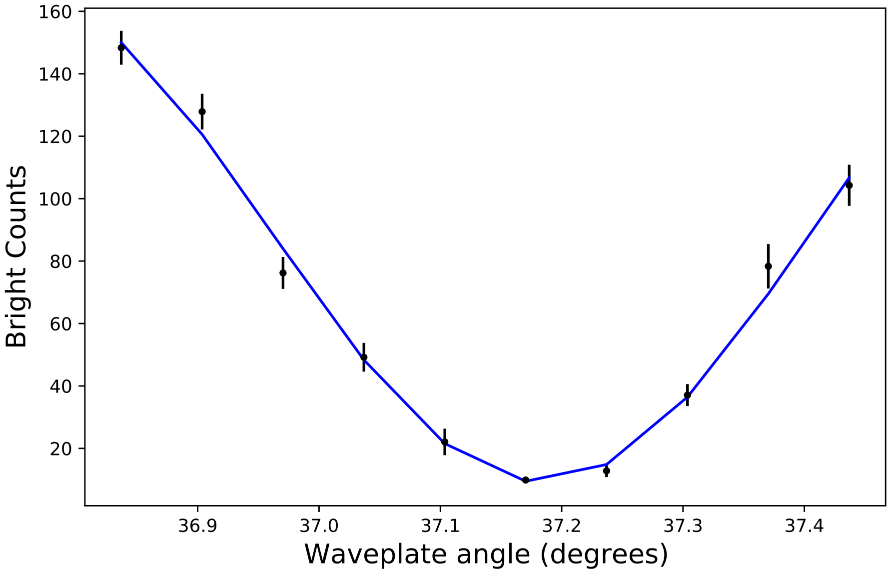

Figure 4.7: Calibration nulling the ACSS of a single ODF beam. A Ramsey sequence is applied with the phase of the final microwave pulse shifting due to a non-zero ACSS from an ODF beam as the waveplate is adjusted from the optimal null. A free precession time of 600 μs and ACSS of order 40 kHz for a single beam when $\hat{\pi}$ polarized gives a resonance width around 0.5 degrees. The fitted waveplate angle is 37.183 ± 0.004 degrees. Interleaved with the scan the resonant microwave frequency was tracked to order 5 Hz.

be to set the two ODF beams to the same frequency to produce a static ACSS dependent on the relative phase of the beams. The ACSS amplitude in the nulled configuration can then be directly measured with Ramsey and Rabi experiments for different ODF relative phases, and the k vector can be directly measured by displacing the ions a calibrated distance to measure the phase shift for a given displacement. These ACSS measurements will already include the DWF in them, and simple algebra can then convert from the ACSS amplitude and k vector wavelength to a force. However, this technique relies on phase stability of the ODF, which with passive stability of enclosing the optics table with better boxing is possible but not ideal.

Alternatively, the spin-dependent force strength has been calibrated using a mean-field spin precession experiment. This first requires knowledge of the axial center-of-mass (COM) mode frequency, which is found by scanning the frequency of an applied axial electric field near resonant with the COM mode (see figure 4.8(a)). On resonance this rapidly heats the ions and leads to a decrease in the ion fluorescence. By applying the ODF detuned from the COM mode some detuning δ, the spin-dependent force drives the spin up and down states in different loops in phase space (see figure 4.9 for example). By setting the arm time of a loop to be $\tau = \frac{2\pi}{\delta}$, the motion undergoes closed loops in phase space leaving the spin and motion disentangled. However, the driven loops enclose some area in phase space that give rise to an acquired phase depending on the area enclosed. For a single ion and $F_\uparrow = -F_\downarrow$, this gives rise to the same acquired phase for spin up and down. For the case of two ions driving the COM mode, the net force is canceled in the anti-ferromagnetic phase (anti-aligned spins), and encloses the same non-zero area for the ferromagnetic cases (aligned spins). A positive (negative) detuning will cause clockwise (counter-clockwise) motion in phase space, which enclose a positive (negative) area, leading to an anti-ferromagnetic (ferromagnetic) interaction since aligned spins are higher (lower) energy than anti-aligned spins (see [48] for an alternative analysis of this based on the energy of the Coulomb interaction and the phase of the displacement). For many spins the Hamiltonian can be described as the Ising Hamiltonian,

$$H_{ising} = \frac{1}{N}\sum_{i<j} J_{i,j}\hat{\sigma}_i^z\hat{\sigma}_j^z, \tag{4.13}$$

where $J_{i,j}$ describes the coupling between spins i, j and depends on the mode participation of the ions in the mode being driven, along with the enclosed area determined by the spin-dependent force and detuning. For the COM mode, $J_{i,j}$ is equal for all ion pairs and given by:

$$J_{i,j} \approx \bar{J} = \frac{F_0^2}{4\hbar m_{Be}\omega_z\delta} = \frac{F_0^2 z_0^2}{2\delta\hbar^2}, \tag{4.14}$$

where F_0 is the strength of the spin-dependent force giving rise to the Hamiltonian $H_{ODF} = F_0\cos(\mu t)\sum_i \hat{z}_i\hat{\sigma}_i^z$, and $z_0 = \sqrt{\frac{\hbar}{2m\omega_z}}$ is the rms ground state wavefunction size of the axial COM mode.[3] Taking a mean-field approximation, each ion i sees an effective magnetic field $B_i = \frac{2}{N}\sum_{j\neq i} J_{i,j}\langle\hat{\sigma}_j^z\rangle$, giving a mean-field Hamiltonian $H_{MF} = \sum_i \frac{B_i}{2}\hat{\sigma}_i^z$.

---

[3] Note the rms displacement of a single ion from the COM motion is $z_0/\sqrt{N}$, which comes from the COM mode participation of each ion being equal. Additionally the sign of $\bar{J}$ is set by the sign of δ as defined in equation 4.14

To measure B_{MF}, which is equal for all ions for the COM mode, the ion's spins are initialized with some $\langle \hat{\sigma}_i^z \rangle$ set by a tipping angle θ from all spins in spin $|\uparrow\rangle$. Application of H_{MF} leads to rotation about the z axis, which is added constructively between two arms via a spin echo which reverses the sign of $\langle \hat{\sigma}_i^z \rangle$ and the rotation accumulated in the first arm, as shown in figure 4.8(c). This echo cancels any uniform rotation of the spins that might occur from magnetic field drifts. However, the cancellation relies on high fidelity π and $\pi/2$ pulses, which if the π time is not calibrated well or issues described in section 4.1.3 are not accounted for will lead to erroneous rotations. The rotations from B are then read out with a microwave $\pi/2$ pulse about the same axis as the echo such that deviations from pointing in the $y - z$ plane are converted into deviations in populations from 50%. Assuming no erroneous rotations, the spins should end at the equator when the tipping angle initializes the spins along the equator (90, 270 degrees) as the average B is zero, and when initialized along the poles (0, 180, 360 degrees), as the spins are in eigenstates that are unaffected by the rotation B. The sign of the population deviation from 50% is then set by whether J and $\langle \hat{\sigma}_i^z \rangle$ of the initial tipping angle state are positive or negative and the axis of rotation the spin is read out.[4] The resulting curve can be fit to

$$P_{\uparrow}(\theta) = \frac{1}{2}\left(1 + e^{-\frac{(2\Gamma_{mag}\tau)^2}{2} - 2\tau\Gamma} \sin(\theta)\sin(2\bar{J}\cos(\theta)2\tau)\right) \tag{4.15}$$

to extract $\bar{J}$, which has the same sign as the detuning δ. Here Γ_{mag}, Γ are the fitted decoherence rates found from magnetic field fluctuations (see section 4.2.4), and from spontaneous emission with both beams applied (see section 4.3.2). Since $\bar{J}$ is detuning dependent, it is often useful to report $J_{1kHz} = \frac{\bar{J}\delta}{1\text{kHz}}$, which is proportional to F_0^2 times constants.

---

[4] Previously (pre-2022) the experiment's convention was to apply initial pulses along y and echo pulses about x, which requires phase lagging the microwave pulse by $\pi/2$. Since the new magnet (2024 onward) all experiments have (unintentionally) phase advanced by $\pi/2$ so the convention has been changed to about x initially and about y for echos. This inverts the sign of the deviations from 50% for the mean-field experiment. Equivalently the detuning sign pre-2022 was always positive and since has largely been negative to give the same curve.

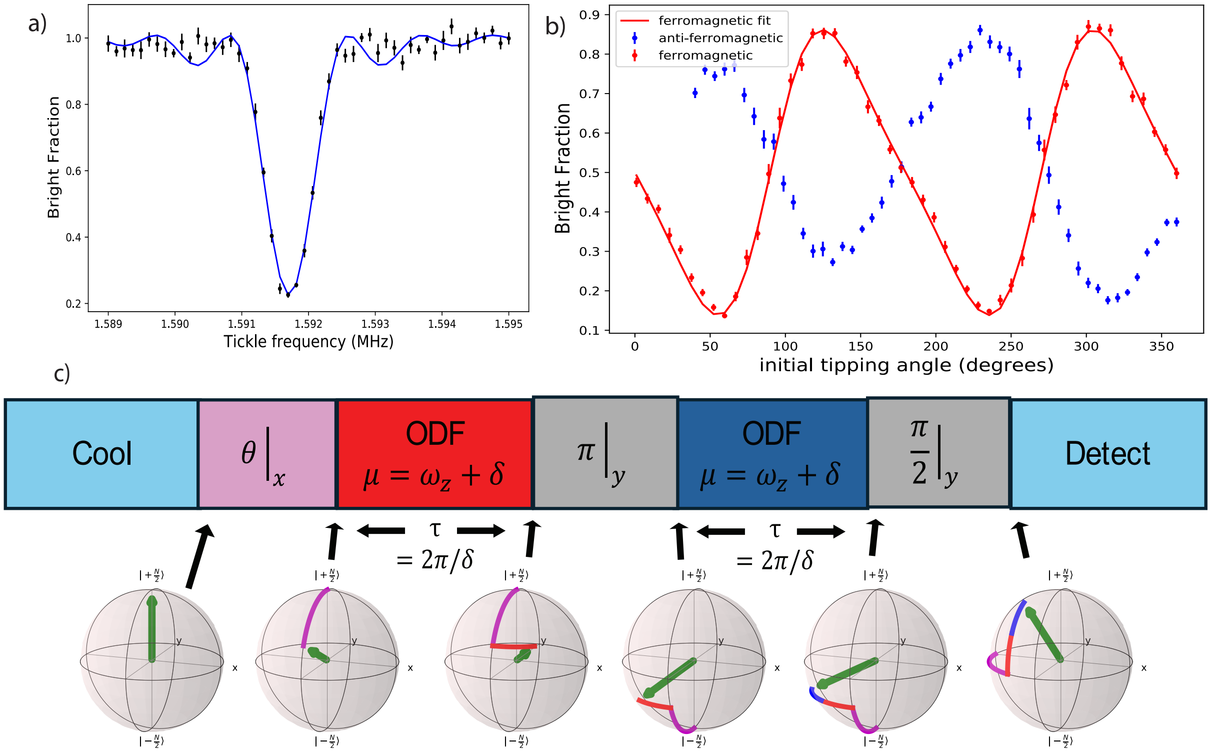

Figure 4.8: Axial COM and ODF mean-field strength calibrations. a) The axial COM frequency is calibrated by an axial electric field heating the crystal, with the axial electric field's frequency scanned and detecting the fluorescence rate. A fit gives a COM frequency estimate of 1,591,710±8 Hz using a 1 ms drive time. b) Mean-field spin precession curves as a function of initial tipping angle along with a fit to calibrate the ODF strength. The red curve is ferromagnetic with a negative detuning, and the blue curve is anti-ferromagnetic with a positive detuning. A fit of the blue curve is left out due to uncompensated microwave issues described in section 4.1.3 giving unequal deviations from 50%. In contrast the red curve has corrected for the issue and gives a fit of $J = 2610 \pm 47$ rad/sec, equivalent to $J_{1\text{kHz}} = 13050 \pm 230$ rad/sec. c) Pulse sequence and Bloch sphere representation of the mean-field calibration experiment. A purple curve represents the initial tipping angle θ about x. Next the effective B rotates the spins along the red curve about z depending on the tipping angle and sign of δ. A microwave echo rotates the traces 180 degrees about y. Due to the change in sign of $\langle\hat{\sigma}_z\rangle$, the precession of the second arm (blue trace) rotates opposite the first arm (red), which adds together coherently because of the inversion of the first (red) rotation due to the echo. Finally a 90 degree rotation about y maps all rotations out of the $y-z$ plane (red and blue traces) into deviation in population from 50 %.

4.3.5 COM mode temperature measurement

After calibrating the strength of the spin-dependent force, the ODF can be used to measure the axial COM temperature. Scanning the beatnote frequency of the ODF near the COM mode creates spin-motion entangled states, along with spin-spin entanglement. These two effects can be calculated separately to predict the measured bright fraction. Starting with the ODF Hamiltonian detuned δ from the axial COM mode,

$$\hat{H} = \frac{\hbar f}{2\sqrt{N}}(\hat{a}e^{i\phi} + \hat{a}^\dagger e^{-i\phi})\sum_i \hat{\sigma}_i^z - \hbar\delta\hat{a}^\dagger\hat{a} \tag{4.16}$$

$$\hat{D}_{sd}(\alpha) = e^{(\alpha\hat{a}^\dagger - \alpha^*\hat{a})\sum_i \hat{\sigma}_i^z} \tag{4.17}$$

$$\alpha = -i\frac{fe^{-i\phi}(1 - e^{i\delta\tau})}{2\sqrt{N}\delta} \tag{4.18}$$

Where $\hat{D}_{sd}(\alpha)$ is a spin-dependent displacement, f is the strength of the spin-dependent force, and ϕ is the phase of the spin-dependent force.[5] For the simplest case of a coherent motional state α_0, applying a microwave $\pi/2$ pulse followed by $\hat{D}_{sd}(\alpha)$ with $\delta = 0$ produces the single ion state

$$|\psi\rangle = \frac{1}{\sqrt{2}}(|\uparrow\rangle \hat{D}(\alpha)\hat{D}(\alpha_0) + |\downarrow\rangle \hat{D}(-\alpha)\hat{D}(\alpha_0))|0\rangle \tag{4.19}$$

$$= \frac{1}{\sqrt{2}}(e^{i\theta_0}|\uparrow\rangle|\alpha_0 + \alpha\rangle + e^{-i\theta_0}|\downarrow\rangle|\alpha_0 - \alpha\rangle) \tag{4.20}$$

$$|\alpha\rangle = e^{-\frac{|\alpha|^2}{2}}\sum_{n=0}^{\infty}\frac{\alpha^n}{\sqrt{n!}}|n\rangle, \tag{4.21}$$

where $|\alpha\rangle, |n\rangle$ are coherent and Fock states respectively of the axial COM mode, and $\theta_0 = \mathrm{Im}(\alpha^*\alpha_0)$. Naively, equation 4.20 looks like a coherent rotation of $2\theta_0$ about the z axis if the the spin-dependent displacement $\alpha = 0$. Evaluating the overlap of the states $\langle\alpha_0 + \alpha|\alpha_0 - \alpha\rangle$ to calculate $\langle\hat{\sigma^x}\rangle, \langle\hat{\sigma^y}\rangle$ reveals that in fact a coherent rotation of $4\theta_0$ occurs, in addition to a shortening of the Bloch vector by $e^{-2|\alpha|^2}$ due to spin-motion entanglement [49]. Classically the factor of 4 stems from the differential ACSS being twice the amplitude $U\hat{\sigma}_z$ and from converting the coherent state α_0 to the amplitude of motion $z_{amp} = 2|\alpha_0|z_0$.[6] The rotation $4\theta_0$ is proportional to the size of the coherent state displacement α_0 orthogonal to the spin-dependent displacement α, allowing precise

---

[5] [49] derives this ignoring spin-motion entanglement, but note has a sign error in ϕ going from the Hamiltonian to the displacement α.

[6] note z_0 is an rms size and $z_{rms} = \sqrt{2}|\alpha_0|z_0$.

phase-sensitive sensing of small coherent displacements of the axial COM mode, which degrades in sensitivity if the spin-motion entanglement is not removed.

Now to evaluate the many ion case, it is useful to decompose the dynamics into a spin-spin and spin-motion propagator given by[7]:

$$\hat{U}_{ss}(t_0, t_1) = \exp\left(i\Phi(t_0, t_1)\sum_{i,j}\hat{\sigma}_i^z\hat{\sigma}_j^z\right) \tag{4.22}$$

$$\hat{U}_{sm}(t_0, t_1) = \hat{D}_{sd}[\alpha(t_0, t_1)], \tag{4.23}$$

where $\alpha(t_0, t_1), \Phi(t_0, t_1)$ are the net spin-dependent displacement and enclosed geometric phase respectively between times t_0, t_1. If a Ramsey sequence is performed with both propagators applied in between the microwave pulses, the resulting $\langle\hat{\sigma}^z\rangle$ (which is uniform for all ions for the COM mode) for an initial coherent state α_0 is given by:

$$\langle\hat{\sigma}^z\rangle_{\alpha_0} = e^{-2|\alpha_T|^2}\cos(4\text{Im}(\alpha_T\alpha_0^*))\cos(4\Phi_T)^{N-1} \tag{4.24}$$

$$P_\uparrow = \frac{1}{2}(1 + \langle\hat{\sigma}^z\rangle_{th}) \tag{4.25}$$

$$= \frac{1}{2}(1 - e^{-\frac{(2\Gamma_{mag}\tau)^2}{2} - 2\tau\Gamma}e^{-2|\alpha_T|^2(2\bar{n}+1)}\cos(4\Phi_T)^{N-1}). \tag{4.26}$$

Here α_0 represents a coherent initial state, $\langle\hat{\sigma}^z\rangle_{th}$ represents a thermal average over coherent states with mean phonon occupation $\bar{n}$, and Φ_T, α_T represent the total enclosed geometric phase and spin-dependent displacement respectively.

The form of equation 4.26 can be interpreted as shortening of the Bloch vector from spin dephasing from four sources (see figure 4.9(d) for a visual of this effect). The first source is general decoherence from magnetic field fluctuations and spontaneous emission as previously described. Dephasing is dominantly caused by thermal averaging over coherent rotations from the spin-motion coupling ($4|\alpha_T|^2\bar{n}$ term). Once the temperature is low enough, the spin-motion entanglement term,

---

[7] The derivation here follows [50], which includes generalization to coherent thermal states and motional squeezing. Generalizations with multiple modes can be found in the supplement of [18], which has a sign convention difference in $\hat{U}_{ss}$.

$2|\alpha_T|^2$, becomes comparable in size to that caused by thermal motion. Equivalently, this term can be associated with stemming from the zero-point fluctuations of the COM mode. Lastly, dephasing from spin-spin interactions can be associated with shearing of the Bloch vector uncertainty due to spin-squeezing, eventually shearing enough to wrap around the Bloch sphere. As with the spin-motion entanglement, the spin-spin interaction term is generally negligible until the temperature approaches the ground state, unless the net spin-dependent displacement is canceled. For a spin echo sequence with a phase shift of the ODF ϕ_{adv} in the second pulse, α_T, Φ_T are given by:

$$\alpha_T = -i\frac{fe^{-i\phi}}{2\delta\sqrt{N}}(1 - e^{-i\theta_1})(1 - e^{-i\theta_2}) \tag{4.27}$$

$$\Phi_T = \frac{f^2}{2\delta^2 N}(\sin(\theta_1) - \theta_1 + [1 - \cos(\theta_1)]\sin(\theta_2)), \tag{4.28}$$

where $\theta_1 = \delta\tau$, $\theta_2 = \delta(\tau + t_\pi) + \phi_{adv}$. As described above, the spin dephasing will primarily be set by the form of α_T. α_T describes driving loops in phase space as shown in figure 4.9, with the orientation of the second loop set by the delay from the π time t_π of the microwave, the phase advance of the ODF ϕ_{adv}, and reversing sign from the spin echo. When $\delta\tau = 2\pi$, loops close in phase space in each arm leading to no dephasing due to motion, only from spin-spin interactions. On resonance the displacement is canceled for no phase advance, and maximized for a phase advance $\phi_{adv} = \pi$, with the form of α_T asymptotically approaching $-\frac{i\tau f e^{i\phi}}{2\sqrt{N}}(1 - e^{-i\phi_{adv}})$. Scanning over the detuning a fit can extract the center of mass mode temperature $\bar{n}$.

4.3.6 Phase flopping spin-independent forces

As was described in section 3.7, in addition to spin-dependent forces generated by the ODF, non-ideal polarizations and laser frequencies can lead to spin-independent forces. To first order, errors in $F_\uparrow \neq F_\downarrow$, which are forces in phase with the spin-dependent force, are due to not having the correct laser frequency, and spin-independent forces 90 degrees out of phase are due to imperfections in the polarizations being cross polarized. These spin-independent forces, when applied simultaneously with the spin-dependent force, will give rise to differential accumulated geometric phase between

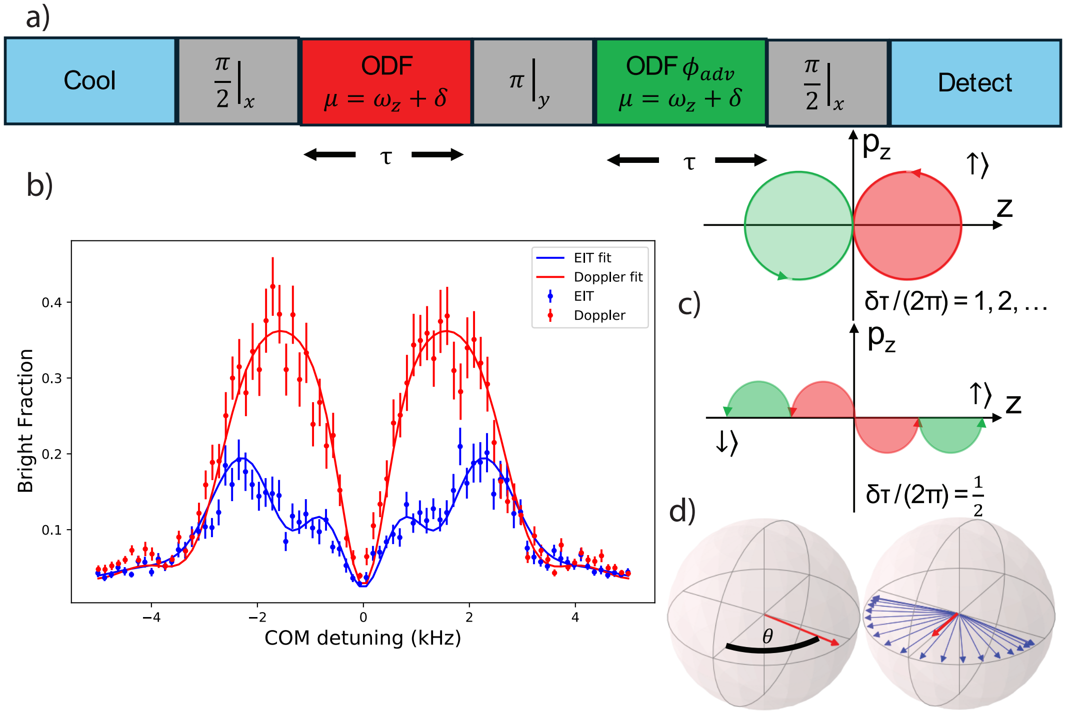

Figure 4.9: Axial COM mode temperature calibration. a) The pulse sequence used to calibrate the COM temperature. Two ODFs of arm time τ are applied in a Ramsey spin echo sequence, with the beam's detuning δ from the COM mode scanned, and an optional phase advance ϕ_{adv} in the second arm. Deviations from measuring dark are due to various spin dephasing sources described in the text. b) Experimental traces of the COM mode with fits to extract temperatures, with arm times of 300 μs and $\phi_{adv} = 0$. The red curve corresponds to Doppler cooled with a fitted $\bar{n}$ of 6 ± 0.4 quanta. The blue curve is EIT cooled with a fitted $\bar{n}$ of 0.21 ± 0.05 quanta. c) A phase space diagram of the COM mode from the spin-dependent force in the two arms. When $\delta\tau = 2\pi$ a complete loop is enclosed, and no spin dephasing occurs due to the motion. In contrast, at $\delta\tau = \pi$ the two arms add together creating a large separation in the $|\uparrow\rangle$ and $|\downarrow\rangle$ motional states. d) representation of shortening of the Bloch vector due to spin dephasing. In contrast to a coherent rotation θ given by any one instance of a measurement, the motion is in a thermal state that randomizes the rotation. Averaging over all the rotations looks like an effective vector that has undergone no coherent rotations but is shortened in coherence (red arrow).

the $|\uparrow\rangle$ and $|\downarrow\rangle$ states that cause coherent rotations. To distinguish between shortening of the Bloch vector due to dephasing from coherent rotations, the final microwave phase can be varied in what we call a "phase flop". The amplitude of the oscillation then corresponds to the dephasing from full contrast, and the phase of the fit determines what coherent rotations, if any, were applied. By doing a two dimensional scan of the ODF detuning over the COM mode, along with a phase flop at each detuning, we can then see the structure of the coherent rotations, or equivalently, the enclosed differential geometric phase. Shown in figure 4.10 is an example two dimensional scan with large spin-independent forces. When on resonance, any enclosed geometric phase must be due to out of phase spin-independent forces. Coherent rotations from in phase spin-independent forces are anti-symmetric about 0 detuning. When first set up, taking these phase flopping scans while adjusting the polarization and frequency can steer the experiment towards the correct operating point. Once close to the correct operating point, two more sensitive experiments are used to independently tune the two spin-independent forces.

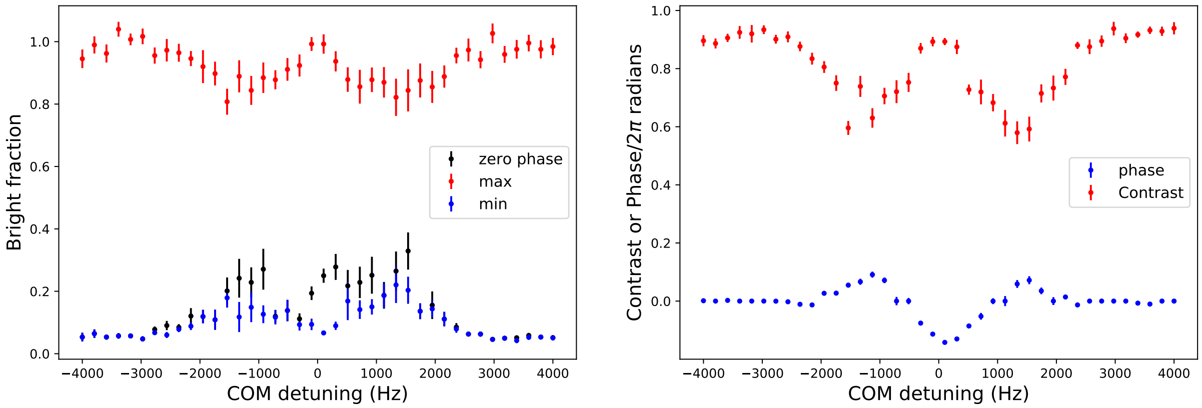

Figure 4.10: Phase flopping spin-independent forces. At each detuning from the axial COM mode the pulse sequence of figure 4.9(a) was carried out repeatedly while varying the final microwave phase to be about axes other than x. The "zero phase" measurement corresponds to no phase shift to remain about x. With spin-independent forces the black dots of the zero phase measurement shown in the left plot give a lineshape which differs from figure 4.9(b). Also plotted on the left plot in red (blue) are the maximum (minimum) bright fraction from the microwave phase subscan (not shown), showing the true reduction in contrast reproduces the lineshape of figure 4.9(b). The right plot shows the fitted amplitude and phase of the phase flop subscan. Plotted in red is the fitted amplitude or contrast corresponds to the reduction in the length of the Bloch vector. Shown in blue is the fitted phase in radians/2π. A fitted phase of 0 corresponds to no coherent rotation, with the large coherent rotation at zero detuning suggesting an error in the out of phase spin-independent force nulling.

4.3.7 Spin-independent force out of phase nulling

To sensitively null the spin-independent out of phase force, a half waveplate is mounted on a rotation stage to rotate about an axis normal to the optics table. At normal incidence this imparts a π phase shift of horizontally polarized compared to vertically polarized light. At non-normal incidence, the path length traveled in the birefringent material is lengthened, to first approximation applying a larger than π phase shift.[8] This means rotating either direction from normal incidence should impart the same sign phase shift. If lucky, a small phase lag is needed and so a small tilt is needed, but if the relative phase needs to shift in the opposite direction, a large tilt is needed to impart nearly a 2π additional phase shift. We experimentally find the later, and so to reduce the necessary angle nominally align the polarizations at normal waveplate incidence (as opposed to cross polarized at normal incidence) and then impart an additional $\sim \pi$ phase shift. The sequence to sensitively null this force is then to sit on resonance with the axial COM mode, and cancel the spin-dependent displacement with a second arm of a spin echo with no ODF phase advance. This will produce no motion-dependent dephasing except due to COM frequency fluctuations for large arm times. However, any spin-independent force out of phase will net enclose a differential area that leads to a spin precession. Carrying out a Ramsey spin echo experiment while the waveplate angle is scanned leads to a minimum dip in coherent rotations which is fitted to as shown in figure 4.11. We find this adjustment is not perfectly independent of the polarization angle to null the differential ACSS, and so iteration between these two alignments is necessary.

4.3.8 Spin-independent force in phase nulling

The final ODF calibration and alignment is to null the in-phase spin-independent force. This is done by adjusting the ODF frequency while ideally sensing coherent rotations due to an in-phase spin-independent force. This is done by doing the same sequence for the out of phase spin-independent force, but now with the detuning of the ODF set such that $\delta\tau = 2\pi$ in each arm, and the detuning sign is switched between the two arms. If $F_{\uparrow} \neq F_{\downarrow}$, this will drive unequal loops in phase space between the spin up and spin down states leading to a coherent rotation. It will also lead to spin squeezing, which can be canceled via the detuning sign change in the second arm, which adds in phase the coherent rotation of each arm. By varying the last microwave pulse duration applied along

---

[8] Note a naive estimate of the phase imparted from just geometrical arguments of increased path length is not accurate, but the general effect still holds.

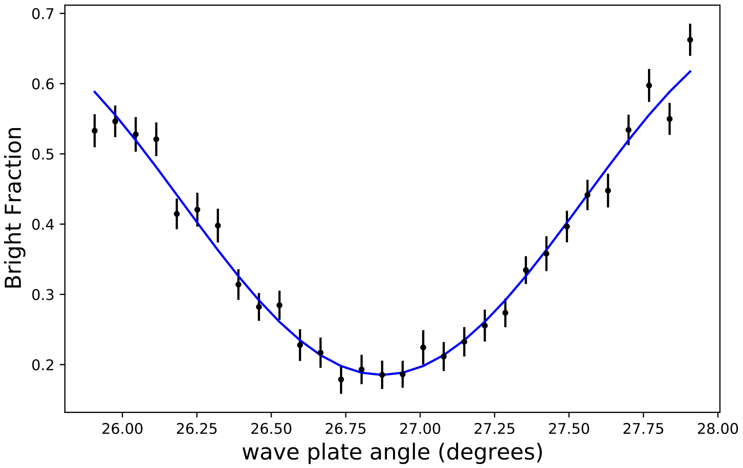

Figure 4.11: Nulling the out of phase spin-independent force. The center point of figure 4.9(b) with $\delta = 0$ and arm time 400 μs is measured where dephasing from spin motion entanglement should be canceled between the two arms. By varying the waveplate angle, spin-independent forces out of phase with the spin-dependent force are adjusted to enclose varying geometric phases giving rise to an effective ACSS that is zero when nulled. A fit to a Ramsey feature equivalently to the waveplate ACSS nulling scheme of figure 4.7 gives a nulling angle of 26.87 ± .01 degrees. Similar to figure 4.7, an interleaved update of the microwave resonance frequency tracks to $\sim$ 5 Hz.

the echo axis y, any coherent rotation produces an oscillation in population about 50% as shown in figure 4.12. Repeating this microwave pulse duration scan, the ODF laser frequency is tuned until a flat line at 50% bright fraction is produced. Experimentally we find this is sensitive to $\sim$ 100 MHz shifts in the $\sim$ 12 GHz detuning, and additionally changes the optimal ACSS nulling angle, requiring some iteration. This sequence is not strictly only sensitive to in-phase spin-independent forces, as out of phase spin-independent forces can also give rise to this signal. Therefore, iteration between ACSS nulling and spin-independent in phase and out of phase nulling are all required. Lastly a wavemeter frequency stabilization lock is applied to adjust the laser piezo voltage to keep the frequency stable to $\sim$ 100 MHz which drifts due to wavemeter calibrations drift likely caused by temperature changes in the lab.

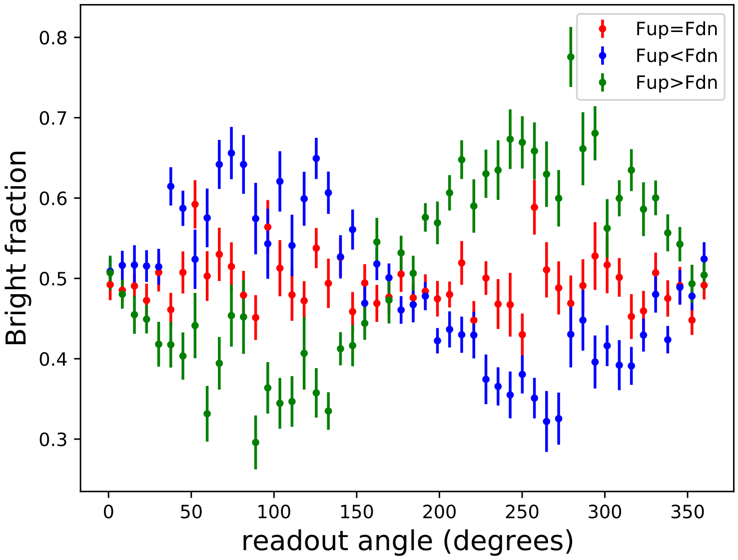

Figure 4.12: Calibration to null the in phase spin-independent force, also sometimes called the squeeze unsqueeze experiment. The red points correspond to $F_\uparrow = -F_\downarrow$, with the final microwave rotation about y showing no signs of coherent rotations. The blue curve corresponds to the laser frequency being tuned below the optimal nulling frequency order 1 GHz, which leads to $|F_\uparrow| < |F_\downarrow|$ and a coherent rotation that leads to deviations in 50 % bright fraction as the final microwave pulse duration about y is varied. In contrast the green curve has the laser frequency detuned order 2 GHz above the optimal frequency, and inverts the sign of the coherent rotation.

4.4 EIT calibrations and alignments

Precise calibration and analysis of the EIT beams is much worse characterized than the ODF beams. This is largely due to the lack of coherent observables from the EIT beams with their much closer detuning of $\sim$ 400 MHz. At this detuning spontaneous emission quickly decoheres many observables, so most characterization is done $\sim$ 3-6 GHz detuned from resonance.

4.4.1 EIT alignment

To align the EIT beams, first a good ODF alignment is achieved as described in subsection 4.3.1. Overlapping the EIT beams by back-propagating them along the ODF beams gives a good starting alignment. Note because of the $\sim$ 124 GHz frequency difference between the beams a small k vector component in the plane will be present even if the ODF beams are perfectly aligned with the EIT beams perfectly overlapping. As done in the ODF alignments, an ACSS with the beams detuned ~ 3 GHz from resonance is measured repeatedly while the final mirrors are tilted to optimize the alignment on the ions. This is done without automated mirrors in contrast to the ODF beams, as sadly the piezo controlled adjustment of the EIT mirrors is far too small of range to measurably change the alignment. With the beams well centered on the ions, applying both beams with the offset frequency locked to the microwave frequency causes coherent Rabi flopping. Scanning the detuning of the beams by varying one of the beam's AOM frequencies in a Rabi experiment produces a lineshape analogous to the microwave Rabi calibrations. Fitting the center frequency measures the effective ACSS of both beams being applied, and scanning the drive time while on this resonant dip gives the effective π time. In addition to a dip at the ACSS shifted frequency (called the carrier), dips on either rotation sideband at $\pm\omega_r$ are present with the strength of their π times set analogously to the dephasing rate of the ODF rotation sidebands.

Using these measurements of the carrier frequency and π times, a scan is repeated that measures the carrier π pulse and the rotation sidebands with some larger effective π time interleaved while the beams are walked. Walking involves tilting a beam off and then re-optimizing it by minimizing the bright fraction of the carrier π pulse sequence. This will then change the sideband Rabi rates to increase or decrease the bright counts consistent with worse or improved alignment. In practice, we have found sideband ratios of order 20:1 at best alignment, and surprisingly have found some imbalance in the two sidebands.

With the EIT beams aligned, the ACSS is then set by adjusting the powers of the beams. By estimating the detuning at the operating condition versus at ~ 3 GHz the ACSS is set to ideally produce ~ 1.6 MHz shift in the resonance frequency with both beams. This corresponds to $\sim \pm$ 100 kHz ACSS at ~ 3 GHz detuning.

4.4.2 In-plane heating

A systematic study of the sensitivity of EIT performance versus alignment, intensity, detuning, crystal size, etc. has not been carried out and would be very helpful in experimental implementation of EIT, particularly as EIT is hopefully scaled to 3D crystals. However, a key issue in evaluating the performance of EIT is the effect on the in-plane motion. Experimentally we have found a variety of unexplained phenomenon suggestive of non-ideal effects harming the in-plane motion. The first phenomenon we have found is under certain conditions the crystal will be torqued off the rotating wall into a high rotating state above the Brillouin zone. This is accompanied by crystal fluorescence going away until the experiment is stopped, and the crystal is spun down via adjustments to the perpendicular cooling.

In addition, and theorized to be related, we see effects on the COM lineshape resembling phase flop curves suggestive of spin-independent forces coherent with the ODF. The main way such a spin-independent force should appear is from a polarization or frequency change in the ODF. A potential explanation therefore is some in-plane motion is getting excited to cause a large Doppler shift of the ODF, enough to shift the frequency order ~ 100 MHz to create a non-negligible spin-independent force. Experimentally we have found increasing the EIT cooling time exacerbates these issues, often with a certain maximum EIT cooling time that can be applied before losing the crystal. This is complicated by the length of Doppler cooling time, as likely this situation becomes a competing rate equation between the cooling rate and time of the Doppler cooling and the heating rate and time of EIT. Currently, the solution to these effects has been to set the EIT cooling time to the minimum required to achieve a desired temperature, and careful tune up of the perpendicular cooling beam is required to give a fast enough in-plane cooling rate to compensate. Beyond this, it is unclear how torque from the parallel beam, or in-plane heating from parallel scatter affects this. Another future possibility is to limit the beam waist to reduce the maximum Doppler shift present from the crystal rotation. This could allow working with bigger crystals that have larger Doppler shifts for ions further out. Larger beam waists were chosen to try and satisfy the EIT cooling condition for the axial COM mode on average across the crystal. Finite beam waists will therefore have EIT conditions at lower axial motion frequencies on average than the axial COM motion as the intensity decreases.

Chapter 5

Dicke Model Simulation

This section describes recent experimental simulations of the Dicke model, a fundamental model of quantum optics that exhibits rich phenomenon such as dynamical phase transitions, chaotic dynamics, and entanglement generation while remaining computationally tractable. These simulations probe the Dicke model in rich experimentally unexplored regimes where decoherence and damping play minimal role, and in a regime where chaotic dynamics appear.

5.1 The Dicke Model

The Dicke model [51] is an iconic model of quantum optics that describes collective light matter interactions given by the Hamiltonian

$$H_D/\hbar = -\delta \hat{a}^\dagger \hat{a} + \Omega \hat{S}_x + \frac{2g}{\sqrt{N}} \hat{S}_z (\hat{a} + \hat{a}^\dagger), \tag{5.1}$$

where $\hat{a}^\dagger, \hat{a}$ create and annihilate excitations of a bosonic mode with angular frequency δ, Ω is a transverse field strength, N the number of spins, and $\hat{S}_k = \sum_{i=1}^{N} \hat{\sigma}_i^k$ collective spin operators. The spin and boson degrees of freedom are coupled with strength characterized by g. While a relatively simple model, the Dicke model exhibits several rich phenomena such as dynamical phase transitions, superradiance, and chaotic dynamics. The dynamics of the system can be determined by two parameters, Ω/δ and $\tilde{g} = 2g/\sqrt{\Omega\delta}$. Broadly speaking, Ω/δ sets the relative participation of the spins and boson in the dynamics, while $\tilde{g}$ sets the strength of the coupling between the spins and boson. For $\Omega, g \ll \delta$, bosonic excitations are energetically unfavorable and the spin degree of freedom dominates the dynamics, allowing the bosons to be adiabatically eliminated. This integrable regime is called the spin-dominated regime with the bosons locked to the spin dynamics. In contrast, for $\Omega \gg \delta, g$ spin excitations along the x direction are much less energetically favorable than bosonic excitations. This integrable regime is called the boson-dominated regime with the spins rapidly oscillating about an orbit locked to the boson's dynamics. Around $\Omega/\delta \sim 1$, the boson and spins equally contribute to the dynamics and this nonintegrable regime is called the resonant regime [52].

In the boson-dominated and spin-dominated regimes the dynamics can be described classically an effective particle moving in a 1D potential [52] as shown in figure 5.1. The potential is given only in terms of the dominant variable $\langle \hat{S}_z \rangle$ ($\langle \hat{\mathcal{X}} \rangle$), where the brackets mean quantum mechanical expectation value, for the spin (boson) dominated regime, where $\hat{\mathcal{X}} \propto (\hat{a}^\dagger + \hat{a})/\sqrt{2}$ is the phase space position operator of the boson. For the spin-dominated regime, the effective potential can be thought of as a competition between the transverse field which favors spins aligned or opposing the transverse field along x on the equator of the Bloch sphere, and an effective Ising interaction from the spin motion coupling term with $\langle \hat{a} + \hat{a}^\dagger \rangle \propto \langle S_z \rangle$ on average, which favors spins aligned along the poles of the Bloch sphere. For $\tilde{g} = 0$, the potential energy then looks like a harmonic well with the lowest energy state along the equator. A classical particle initialized along the north or south pole explores the whole potential, oscillating back and forth between the north and south pole. With nonzero $\tilde{g}$, a hump in the middle of the well occurs that moves the minimum energy states off the equator of the Bloch sphere. A particle will then be trapped in one of the two wells given it is initialized with an energy smaller than the barrier described by strength $\tilde{g}$.

Experimentally a dynamical phase transition–distinct dynamical behaviors separated by a critical point–has recently been demonstrated in the spin-dominated regime in an atom-cavity system [53], along with a similar demonstration in a 1D chain in trapped ions [54]. In this limit the

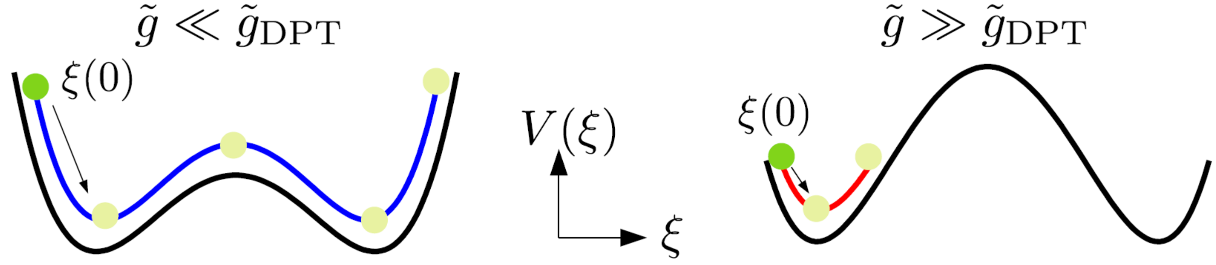

Figure 5.1: Classical double well potential representation of the Dicke model in the integrable spin and boson dominated regimes, borrowed from reference [52]. With the non-dominant variable adiabatically eliminated, the dynamics can be captured by a double well potential expressed in terms of the dominant variable $\xi = \langle \hat{S}_z \rangle$ (spin dominated) or $\langle \hat{\mathcal{X}} \rangle$ (boson dominated). In the spin-dominated regime, a classical particle initialized at the south pole (green dot) will explore the full potential as long as the barrier $\tilde{g}$ is less than the initial energy (left potential), equivalent to Rabi flopping. When the barrier is larger than the initial energy, e.g. $\tilde{g} > \tilde{g}_{DPT} = \sqrt{2}$ for an initial state along the poles of the Bloch sphere, the particle remains trapped in one of the wells (right potential). Spins initialized pointing along or opposing the transverse field are at an unstable fixed point corresponding to the center of the barrier. An equivalent double well potential characterizes the boson-dominated regime with the spin degree of freedom quickly oscillating about an average population locked to the slower boson dynamics (see supplement of [52] for more details). Outside these integrable limits, the adiabatically eliminated degree of freedom cannot be ignored and a complex 2D surface characterizes the dynamics. With spins initialized along the poles of the Bloch sphere, this manifests as erratic jumping between the two trapped wells even when the barrier is larger than the initial energy, made possible by the participating boson dynamics.

Hamiltonian reduces to the LMG Hamiltonian [55] given by:

$$H_{LMG} = \frac{\chi}{N}\hat{S}_z^2 + \Omega \hat{S}_x, \chi \equiv \frac{4g^2}{\delta}. \tag{5.2}$$

With the boson adiabatically eliminated, the bosons now mediate a spin-spin interaction, also called one-axis twisting, with strength χ. This shearing of the spins competes with the transverse field of strength Ω such that there is a dynamical phase transition between an untrapped Rabi flopping state ($\Omega > \chi/2$) and a trapped state ($\chi/2 > \Omega$) shown in figure 5.2(d). This transition can be characterized by the time averaged magnetization $\overline{\langle \hat{S}_z \rangle} \equiv \lim_{T\to\infty}(1/T)\int_0^T \langle \hat{S}_z(t)\rangle dt$, with untrapped (trapped) dynamics corresponding to $\overline{\langle \hat{S}_z \rangle} = 0\,(\neq 0)$ (see figure 5.2(b)). Equivalently, $\tilde{g} = \sqrt{\chi/\Omega}$, showing that in the spin-dominated regime $\tilde{g}$ can be associated with the relative strength of the spin-spin interaction to the transverse field. For spins initialized along the poles of the Bloch sphere and in the spin-dominated regime, the dynamical phase transition happens at $\Omega/\chi{=}1/2$, and $\tilde{g} = \sqrt{2}$. In the trapped regime the spin-spin interaction rephases the transverse field faster than the transverse field can drive population past the equator. The two dynamical phases are also sometimes called the normal (untrapped) and superradiant (trapped) phase, as the trapped phase exhibits a coherent occupation of the mediating boson shown in figure 5.2(e). In systems with dissipation of the cavity this gives rise to superradiant emission from the cavity [51, 53, 56].

To implement the Dicke model in our system, a transverse field is created using a resonant microwave drive between the spin $|\uparrow\rangle, |\downarrow\rangle$ states with a strength Ω set by the intensity of microwave radiation at the ions. The mediating boson is the axial COM mode driven with a detuning $\delta = \mu - \omega_Z$ of the ODF beatnote from the COM mode, represented in figure 5.2(a). In contrast to cavity systems, the COM mode has minimal dissipation, dephasing, or heating on time scales relevant to decoherence from spontaneous emission and magnetic field noise. This means the superradiant emission from the cavity will be absent in our system. Instead, in the superradiant phase the bosonic x quadrature is on average directly proportional to $\langle \hat{S}_z \rangle$, giving on average a non-zero bosonic occupation which does not damp the spin dynamics from bosonic decay. However, this lack of dissipation is a feature in the resonant regime $\delta/\Omega \sim 1$, where the bosonic dynamics are no longer adiabatically eliminated. In this regime cavity systems may struggle to avoid cavity dissipation dominating the coherent dynamics. Instead of integrable dynamics described by the effective potential of figure 5.1, the resonant regime dynamics has another dimension to the potential surface. In the strong coupling $\tilde{g} \sim \delta \sim \Omega$ regime and with the spins initialized on the poles of the Bloch sphere, this gives rise to chaotic dynamics that looks like being trapped in one minimum but erratically slipping to another trapped state, made possible by the equally participating bosonic dynamics [52].

Chaotic dynamics can be described classically by replacing the Hamiltonian with its classical (infinite N) counterpart and calculating the Lyapunov exponent shown in figure 5.2(c) [57]. The Lyapunov exponent is generally non-zero for chaotic dynamics and a measure of exponentially diverging trajectories for small changes in initial conditions. However, if the spins are initialized along the equator aligned or opposing the transverse field they are at an unstable fixed point. This unstable fixed point is present even in the integrable limit as shown in figure 5.1 in the spin (boson) dominated regimes, but also in an integrable limit of the resonant regime $\delta \sim \Omega$ for small $\tilde{g}$. However, since the dynamics is integrable this is not chaotic despite the Lyapunov exponent being non-zero for trajectories encompassing this infinitesimal unstable fixed point. Taking an average Lyapunov exponent from neighborhoods excluding this point distinguishes this effect as shown in figure 5.3. To probe this effect, experimentally we operated in the resonant regime $\delta = \Omega$ and varied $\tilde{g}$ with the spins initialized at the unstable fixed point pointing along $-x$, i.e. aligned opposing the transverse field direction. In this case a crossover –a smooth change in behavior rather than a non-analytical sharp transition in behavior– from integrable to chaotic dynamics is measurable from the time averaged transverse magnetization as shown in figure 5.3 that corresponds to the crossover in the average Lyapunov exponent.

5.2 Tracking and experimental calibrations

To implement the Dicke model, the transverse field strength Ω, coupling strength g, and the detuning δ needed to be characterized. In addition, erroneous $\hat{\sigma}_z$ interactions will modify the dynamics, most evidently in the small Ω regime in the spin-dominated regime which will modify the dynamical phase transition location. Initial data taken to measure the dynamical phase transition in the spin-dominated regime found that a combination of drifts in the magnetic field and changing ACSSs from the ODF beams, which are ideally nulled, were as large as ∼100 Hz and were non-negligible for dynamics with $\Omega \sim 300$ Hz. To counter this, much finer nulling of the ODF ACSS was done using a larger arm time as discussed in section 4.3.3. However, this alone would be limited by drifts of the resonant microwave frequency during the scan. To compensate these drifts during the nulling, along with drifts during simulations of the Dicke model, a new feature was added to the experiment called tracking.

Tracking is carried out in a largely modular, scalable, automated fashion in the Artiq scan framework. To track something, a tracker code is written that consists of a measurement scheme of 3 points, a track parameter, and a track feedback scale and user adjustable gain setting. The

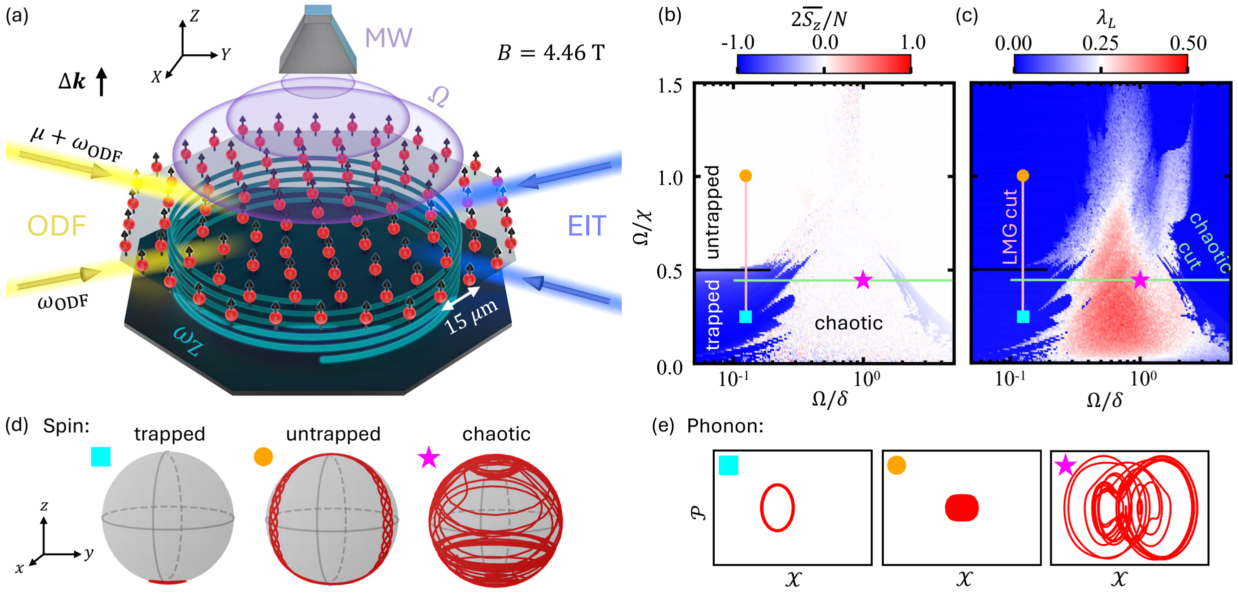

Figure 5.2: Experimental setup and phase diagram of the Dicke model. a) The Dicke model Hamiltonian is implemented in our system via the ODF beams (yellow) coupling the axial COM mode (teal spring) to the spin degree of freedom of the ions (black arrows) while simultaneously applying a resonant transverse microwave drive (purple). We vary the initial thermal state of the COM mode by optionally applying additional EIT cooling (blue) to reduce the temperature below the Doppler limit. b) Classically calculated time averaged magnetization $\overline{\langle \hat{S}_z \rangle}$ plotted over the phase space of the Dicke model characterized by Ω/χ and Ω/δ. Dynamics are calculated assuming ground state bosonic occupation and initial spins along the south pole. Two experimental cuts are overlaid on the phase space plot corresponding to a cut in the LMG regime transitioning from a trapped (blue) to untrapped (white), and a chaotic cut transitioning from trapped to chaotic. c) The corresponding Lyapunov exponent on the same phase space coordinates showing the chaotic nature at $\Omega \sim \delta$ and small Ω/χ. d) Example trajectories of the spin dynamics in the trapped, untrapped, and chaotic regimes. e) Corresponding phonon dynamics in canonical phase space $(\mathcal{X}, \mathcal{P})$ showing a macroscopic boson occupation in the trapped regime and chaotic bosonic occupation in the chaotic regime.

measurement scheme is defined to set the tracked parameter in a pulse sequence to a center value that is tracked, along with two shifted side points, also called the left right and center points. To track something the pulse sequence generates a resonance on center that has two points of steepest slope of opposite signs at the left and right points. By measuring the bright fraction at the left and right point, an imbalance in population is then scaled to an adjustment of the center tracked parameter to re-center the resonance on the optimal center value. The center point measurements are then taken as a reference to ensure the tracker is on a resonance. With this general scheme, the user can choose how often in a scan (after how many scan points) the tracker should measure the

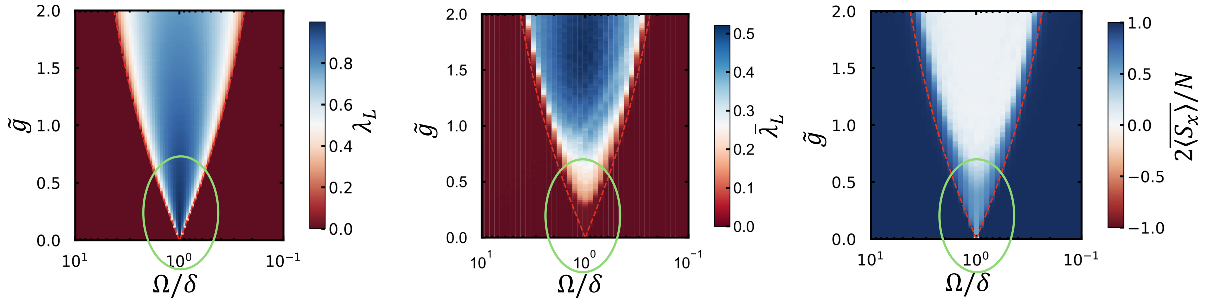

Figure 5.3: Unstable fixed point dynamics in the resonant regime $\delta \sim \Omega$. For spins initialized pointing along or opposed the transverse field, when $\tilde{g}$ is large and $\delta \sim \Omega$ the dynamics are chaotic with a non-zero Lyapunov exponent. However, at small $\tilde{g}$ the dynamics are integrable but still give a nonzero Lyapunov exponent as shown in the leftmost plot. If an average Lyapunov exponent $\overline{\lambda}_L$ is taken for neighboring initial states that exclude the unstable fixed point, an exponent of zero is recovered correctly identifying the dynamics as integrable (middle plot) in the green circled region. By measuring the time averaged transverse magnetization (right plot), a crossover occurs in agreement with the predicted change in the average Lyapunov exponent, correctly identifying the crossover from integrable to chaotic in contrast to the Lyapunov exponent in the circled green region. The non-zero average transverse magnetization occurs due to coherent collapses and revivals of the spin's coherence at long times due to a two mode squeezing Hamiltonian. In contrast at large $\tilde{g}$ the chaotic dynamics damps the coherent revivals manifesting in a crossover to ~ 0 time averaged transverse magnetization.

three points, with an adjustable setting for how many repetitions of the left/right point and the center point separately are carried out. This is done to allow better duty cycles by limiting how much the center point, which is not used in feedback, is measured.

As an example, a tracker for the microwave frequency is carried out using a Ramsey sequence described in section 4.1.2. The center point is initialized using the most recently found/tracked resonance frequency, and the side points are offset by $\pm s\frac{1}{2(T+t_\pi)}$ where T is the Ramsey time, t_π is the pi pulse time, and s is a user adjustable scaling that defaults to 0.5 (half the linewidth). This ideally makes the left and right point populations 50% and at the steepest slope of the lineshape. From equation 4.3, if the center point is in error by some small frequency ϵ, the population at the left and right points will be

$$P_{R/L} \approx \frac{1}{2}(1 \pm \sin(2\pi\epsilon T)) \tag{5.3}$$

$$P_R - P_L \approx \sin(2\pi\epsilon T) \approx 2\pi\epsilon T, \tag{5.4}$$

where $\pm$ corresponds to $R(+)/L(-)$. Therefore, the center parameter is adjusted by $-\epsilon \approx g(P_L - P_R)/2\pi(T + t_\pi/2)$, where $P_{L(R)}$ correspond to the measured population of the left (right) point, g is a user adjustable gain to reduce or increase the feedback gain if the contrast isn't 100%, and the effective Ramsey time T is adjusted by half the pi time t_π. From the estimated scaling and standard deviation of the measured $P_{L/R}$, an uncertainty can be estimated of how well known the center tracked parameter is.

In addition to a tracker for the microwave frequency, a tracker for the axial COM mode frequency and the bright and dark counts are interleaved in a background scan between experiments, and the microwave and COM tracker are implemented periodically in the simulations of the Dicke model. The COM tracker is implemented using an axial electric field drive to decrease the fluorescence from the parallel beam as described in section 4.3.4. The bright/dark counts are tracked using only two points rather than three with the dark counts measured using a microwave pi pulse and the ion number adjusted from the measured counts and a calibration of the count rate versus ion number. Figure 5.4 shows an example Dicke model simulation with interleaved microwave and axial COM frequency tracking.

With the COM and microwave trackers the σ_z terms and δ errors are converted from drifting estimates of up to $\sim$ 100 Hz to random fluctuations of $\sim$ 5 Hz. The σ_z terms from the ODF ACSS null were also periodically checked to stay within $\sim$ 10 Hz, which drifted out of this range over 10's of minutes timescales. This drift can be much worse without polarizing beam splitters added after the AOMs to convert polarization noise to intensity noise. Experimentally we have seen thermal effects from the strength of the RF drive applied to the AOM varying the polarization state. This was seen by measuring the polarization nulling angle vary with power stabilization level, proportional to

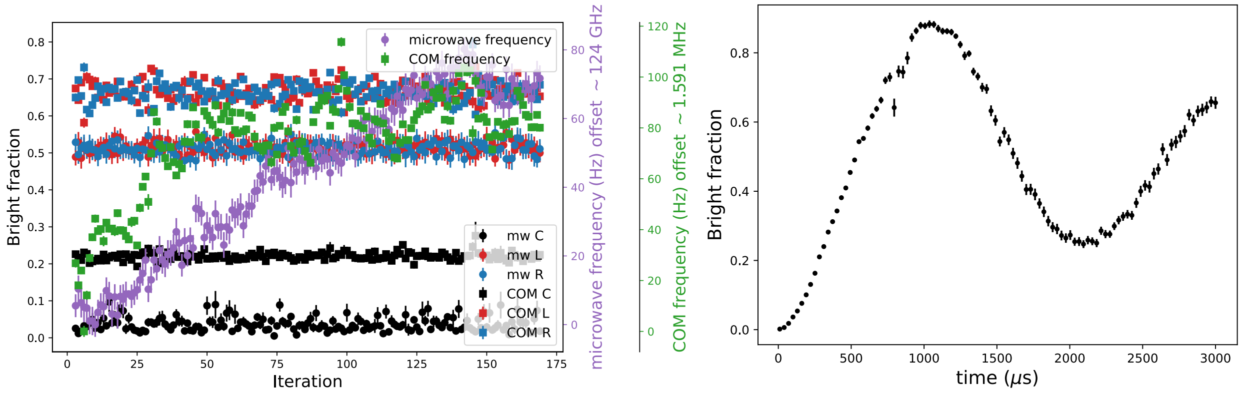

Figure 5.4: Example Dicke model simulation with interleaved tracking. The right plot shows the simulated Dicke model dynamics with $\Omega/\delta = 1/8$ and $\tilde{g}$=1.2. The simulation was run with 100 time steps and 5 passes for a total of 500 scan points, with each scan point consisting of 30 repetitions of the measurement for a total of 15,000 measurements of the dynamics. Every third scan point a COM and microwave frequency tracker measurement was carried out with 30 repetitions of the left and right points each and 10 repetitions of the center point, as shown on the left plot. On the left y axis is the bright fraction corresponding to the left (red) right (blue) and center (black) measurements for the microwave (circles) and COM (squares) trackers. On the right y axes are the tracked center microwave (purple circles) and COM (green squares) frequencies, offset by their minimum values of 124.022438602 GHz and 1.59127 MHz respectively. The trackers used a tickle time and Ramsey time of 1 ms. Estimated uncertainties suggest order ±1,4 Hz for the COM and microwave frequencies respectively. Drifts of the center frequencies over the course of the scan suggest without active feedback errors as large as 80 and 120 Hz would have occurred for the microwave ($\hat{\sigma}_z$ errors) and COM (δ errors) frequencies respectively.

the RF power applied to the AOM. Increasing the laser power and thereby decreasing the required AOM power further distinguished the effect as due to the RF power. Adding polarization optics after the AOM effectively converts these polarization rotations into amplitude fluctuations that can be servoed away.

To calibrate g, a mean-field spin precession calibration was carried out as described in section 4.3.4, with $g = \sqrt{J\delta/2}$ where δ is the COM detuning used in the mean field calibration. The last remaining parameter Ω is set by the strength of the microwave drive, which is adjusted with a voltage controllable attenuator of the 124 GHz radiation and is stable over long enough time scales to not necessitate active tracking. An initial 2D scan of the Rabi time scan described in section 4.1.1 fits the effective $\Omega = \pi/t_\pi$ while varying the attenuator voltage set by an Agilent E3646A DC voltage supply adjusted remotely over serial communication. To run an experiment the user then selects the detuning and estimated attenuator voltage from the 2D scan, with δ, Ω adjusted depending on the calibrated value of g and the parameter regime desired.

To ensure Ω is well calibrated for each experiment, and to allow a check of basic functionality of the scan, a first calibration scan is run before the full simulation which interleaves the Dicke model simulation with two other calibration curves shown in figure 5.5. The first calibration curve is simple Rabi flopping with the attenuator voltage set to match the Dicke simulation allowing a fit to the true Ω after the scan is run, along with potentially any decoherence from the microwaves and magnetic field. The second calibration curve is the same Rabi flopping but with the ODF beams on and detuned from the COM mode by 50 kHz to make $g \sim 0$. This can be used to gauge that the ACSS are well nulled and what the decoherence rate of the ODFs is. In practice these decoherence rates did not need to be extracted from the reference curves, and instead independent calibrations of the decoherence rates described in sections 4.3.2, 4.2.4, as well as COM temperatures (including with EIT cooling) described in section 4.3.5 were taken before a set of scans. Unwanted $\hat{\sigma}_z$ terms were also eliminated from spin-independent forces using calibrations described in sections 4.3.8, 4.3.7.

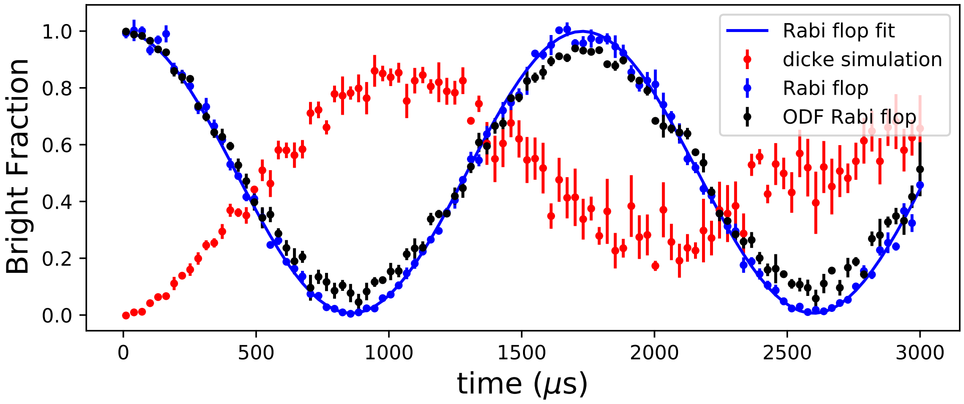

Figure 5.5: Example reference curves taken before the full Dicke model simulation shown in figure 5.4. The fitted Rabi flopping curve (blue) gives an estimate of $\Omega = 575 \pm 1$ Hz. The decoherence from the ODF is visible in the damping of the black curve, which does not exhibit an obvious additional ACSS which would shift the average bright fraction from 50% (the intersection point with the Rabi flopping curve stays near 50%), allowing a quick spot check of the ODF $\hat{\sigma}_z$ errors and decoherence rate. Uncertainties of the Dicke simulation are much greater than the full simulation, with these calibration curves only taking 5 repeats, 1 pass, and 100 time steps speeding up the scan to take roughly 1/30th the time.

5.3 LMG cut

As a first demonstration of previously explored regimes of the Dicke model, a cut through phase space in the integrable spin-dominated regime characterized by the LMG model was simulated to characterize the dynamical phase transition from the normal to superradiant phase. To set the dynamics in the spin-dominated regime, a constant Ω/δ of 1/8 was set, with the product of $\Omega\delta$ varied with g held fixed to vary Ω/χ across the dynamical phase transition. At each value of Ω/χ, the spins were initialized in $|\downarrow\rangle$ and the COM mode either Doppler or EIT cooled as shown in figure 5.6(a). The dynamics were then turned on for times varying from 0 to 3 ms in 100 time step increments, with 30 repetitions at each time step, 5 passes of the time steps, and interleaved feedback of the microwave and COM frequencies approximately every 3rd scan point as described in figure 5.4. At the end of each shot of the experiment the spin state was read out using ~ 0.5 ms of fluorescence readout on a photomultiplier tube (PMT) using the side-view f/5 imaging system. Ideally longer readout would be used to reduce detection shot noise and be projection noise limited, but shorter readout times were used to reduce in-plane heating to maintain somewhat stable bottom view images during the experiment to allow individual ion resolvable images for checking the ion number.

Shown in figure 5.6(b-e) are time traces of the dynamics with EIT cooling across varying parameter ranges of Ω/χ transitioning from trapped to untrapped. The dynamics are well characterized by a theoretical semiclassical model (solid blue lines for EIT, orange for Doppler cooled) that accounts for decoherence sources and the initial thermal state using a method called the Discrete Truncated Wigner Approximation (DTWA) [58]. Additionally, the dynamics are well described by a classical mean-field model (lavender line), showing that the dynamical phase transition is well characterized at the mean-field level. The measured transition is compared in figure 5.6(f) to a classical calculation without any decoherence and a longer time averaging of the dynamics showing that decoherence and finite simulation time limits the sharpness of the transition. While unmeasured, the time averaged phonon occupation is plotted in figure 5.6(g) as a function of Ω/χ. Although the boson is largely adiabatically eliminated in the spin-dominated regime, the transition to the superradiant phase is characterized by a non-zero occupation of the boson as the boson's dynamics are locked adiabatically to follow the spins.

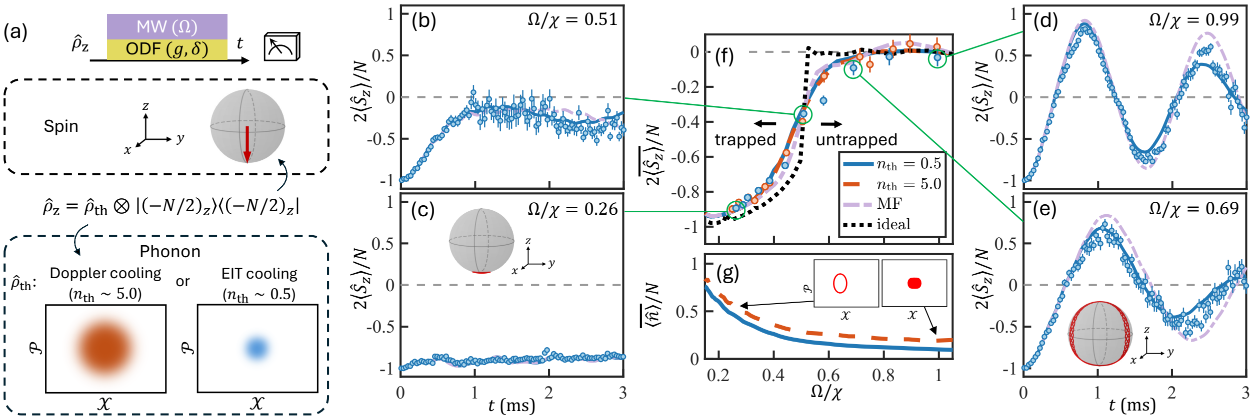

Figure 5.6: LMG dynamical phase transition. a) The spins are initialized in the $-z$ state with the COM mode either Doppler or EIT cooled. The Dicke Hamiltonian dynamics are then quenched on for a variable time and the average magnetization ($\langle S_z \rangle$) is measured using fluorescence readout. b-e) time traces of the quenched dynamics for varying Ω/χ across the dynamical phase transition. Inset on c,e are Bloch sphere representations of the spins trajectories showing the characteristic trapped and untrapped behavior. The data (blue dots) are in good agreement with DTWA (blue solid lines) and mean-field (lavender dashed lines) calculations. f) The time averaged magnetization is plotted as a function of Ω/χ, including the Doppler cooled data (orange dots) and EIT data (blue dots) along with a mean-field (lavender dashed) and DTWA calculation shown in blue and orange for EIT and Doppler cooled respectively. The transition is less sharp than a classical calculation without decoherence and for longer time averaging (dashed black line). g) The time averaged bosonic occupation (unmeasured) is theoretically calculated and plotted as a function of Ω/χ showing the macroscopic occupation in the trapped regime $\Omega/\chi < 1/2$.

5.4 Chaotic cut

To explore dynamics beyond mean-field and in the chaotic regime of the Dicke model, a cut through phase space at fixed $g, \tilde{g} = \sqrt{\chi/\Omega}$, equivalent to fixing g and $\delta\Omega$, was taken while varying Ω/δ to explore outside the spin-dominated regime and in the chaotic regime of $\delta/\Omega \sim g \sim 1$. Figure 5.7(a-d) show example time traces as Ω/δ is varied from the spin-dominated to the resonant regime, and finally to the boson-dominated regime. In the spin-dominated regime (figure 5.7(a)) the state is near the dynamical phase transition but is in a trapped regime for the fixed value of $\tilde{g} \sim 1.5$. In contrast the boson-dominated regime at small Ω/δ is not trapped due to the initial phonon occupation not being large enough to initialize the system in a trapped state, equivalent to initializing near the unstable fixed point of the bosonic degree of freedom in the boson-dominated regime. In between in figure 5.7(b) at Ω/δ=0.65 the dynamics shows erratic jumping between the two trapped states which are damped due to a combination of thermal effects, decoherence, and quantum fluctuations. The Doppler cooled data shows the effect of damping from thermal occupation, which is highly suppressed in the EIT cooled case. In the mean-field case the damping is not adequately captured suggesting quantum fluctuations in the chaotic dynamics are driving the damping.

To further support the identification of chaos, plots 5.7(e-h) show the corresponding trajectories in the $y - z$ plane as extracted from the smoothed time derivative of the $\langle \hat{S}_z \rangle$ experimental data. In contrast to the regular dynamics in the trapped (figure 5.7(e)) and untrapped (figure 5.7(h)) cases, the dynamics show damping near the onset of the chaotic regime in figure 5.7(g) and evidence of the erratic jumping between the two trapped states in figure 5.7(f). Figure 5.7(i) shows the time averaged magnetization as Ω/δ is transitioned into the chaotic regime, with a reasonable agreement between the mean-field prediction and DTWA calculation. Additionally, the integrable untrapped regime at large Ω/δ is not distinguishable from the chaotic region of $\Omega/\delta \sim 1$ in just the time averaged value of the magnetization. Instead, disagreement with the mean-field dynamics and evidence of chaos is only evident in the time dynamics of the simulation. In figure 5.7(j) the unmeasured time averaged bosonic occupation is calculated for the Doppler (orange) and EIT (blue) cooled cases, showing in the chaotic resonant regime $\Omega/\delta \sim 1$ the boson experiences substantial dynamics due to the equally participating dynamics of the boson and spin degrees of freedom.

5.5 Resonant regime dynamics at an unstable fixed point

To exhibit the strongest signatures of quantum dynamics and more clearly delineate the onset of chaotic dynamics, a third experimental cut was probed with a new initial condition at an unstable fixed point. Here the the spins were initialized opposing the transverse field and with $\delta = \Omega$ as shown in figure 5.8(a). At this unstable fixed point no dynamics can be produced classically except due to thermal fluctuations, while quantum mechanically the dynamics can be driven completely by

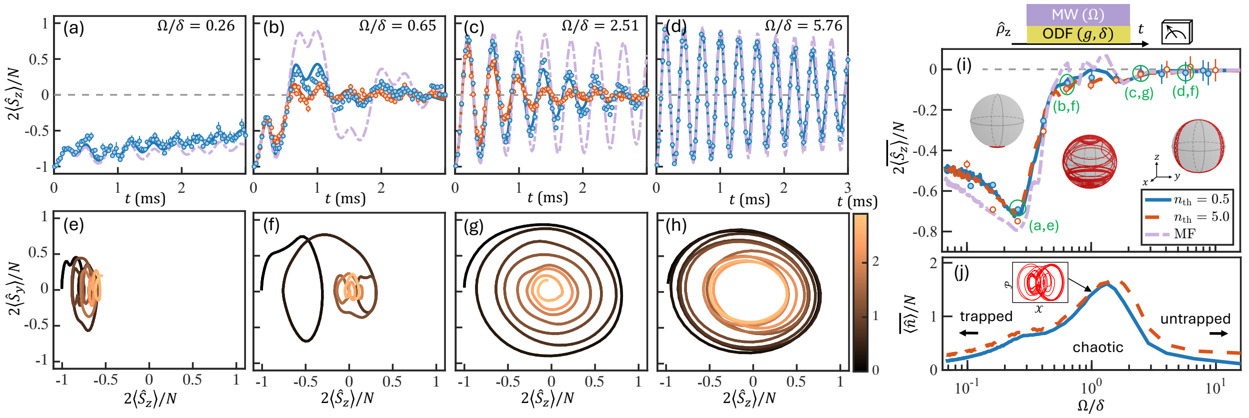

Figure 5.7: Chaotic dynamics outside the spin-dominated regime. a-d) Experimental time traces of the dynamics in the trapped ($\Omega/\delta = .26$) chaotic ($\Omega/\delta = 0.65$) and untrapped ($\Omega/\delta = 5.76$) regimes and in between the chaotic and untrapped integrable regime $\Omega/\delta = 2.51$ compared with mean-field (lavender dashed lines) and DTWA (blue and orange solid lines) calculations. Doppler cooled (orange) and EIT cooled (blue) initial conditions are compared in and around the chaotic regimes showing the contribution of thermal fluctuations to the damping of the oscillations. e-h) Spin trajectories over time in the $y - z$ plane as extracted from the experimental traces using the time derivative of $\hat{S}_z$ to estimate $\hat{S}_y$. i) Time averaged magnetization measured experimentally with Doppler (orange dots) and EIT cooled (blue dots) initial conditions compared with DTWA calculations (orange and blue curves) and a mean-field calculation (lavender dashed) showing agreement in the transition from integrable to chaotic at the mean-field level, with discrepancy only identifiable in the time dependent dynamics of (b,c). Inset are example calculated spin trajectories in the trapped, chaotic, and untrapped regimes. j) Calculated time averaged bosonic occupations as Ω/δ is varied showing the large bosonic dynamics in the chaotic regime.

quantum fluctuations. In the rotating frame of the transverse field and the boson the Hamiltonian can be written as $\hat{H}^{rot} = \hat{H}^{rot}_{\text{pair}} + \hat{H}^{rot}_{\text{t}}$ with[1]

$$\hat{H}^{rot}_{\text{pair}} \equiv \hbar\frac{-ig}{\sqrt{N}}\left(\hat{a}^\dagger \hat{S}_+^{(x)} e^{i(\Omega-\delta)t} - \hat{a}\hat{S}_-^{(x)} e^{-i(\Omega-\delta)t}\right) \qquad \hat{H}^{rot}_{\text{osc}} \equiv \hbar\frac{-ig}{\sqrt{N}}\left(\hat{a}\hat{S}_+^{(x)} e^{i(\Omega+\delta)t} - \hat{a}^\dagger \hat{S}_-^{(x)} e^{-i(\Omega+\delta)t}\right), \tag{5.5}$$

where we have defined raising and lowering operators in the x basis: $\hat{S}_y \equiv (\hat{S}_+^{(x)} + \hat{S}_-^{(x)})/2$ and $\hat{S}_z \equiv (\hat{S}_+^{(x)} - \hat{S}_-^{(x)})/(2i)$.

By setting $\delta = \pm\Omega$, either approximate beam splitter terms ($\hat{a}\hat{\mathcal{S}}^+$) or two mode squeezing terms ($\hat{a}\hat{\mathcal{S}}^-$) can be resonant, with the other term being off-resonant by a detuning 2δ. When g is

---

[1] This comes from the annihilation operator rotating like $ae^{-i\omega_Z t}$, so that the a terms are associated with $e^{+i\delta t}$ and the unitary transformation going rotating in the frame of the transverse field associating $S^+_{(x)}$ with $e^{i\Omega t}$.

small compared to this detuning, equivalent to $\tilde{g} < 1$, the fast rotating term can be ignored and the dynamics are well described by correlated spin-boson excitations. Taking the large N limit and with the spins initialized along $-\hat{x}$, the spins can be mapped using the so called Holstein-Primakoff (HP) transformation to a bosonic operator $\hat{\mathcal{S}}_{+}^{(x)} \approx \sqrt{N}\hat{b}^{\dagger}$ and $\hat{S}_x = -N/2 + \hat{b}^{\dagger}\hat{b}$. In this large N limit the mapping gives rise to a true two mode squeezing Hamiltonian $\hat{H} \approx i\hbar g(\hat{a}\hat{b} - \hat{a}^{\dagger}\hat{b}^{\dagger})$ between the bosonic and spin degree of freedom.

For our initial states near the ground motional state and spins aligned along $-x$, the two mode squeezing operator cannot annihilate what appears approximately as vacuum for both $\hat{a}$ and $\hat{b}$. Instead, only correlated pairs are produced that flip a spin in the x basis while simultaneously creating one quanta of motion as shown in figure 5.8(j). These correlated pairs produce two-mode squeezed quadrature $\hat{\mathcal{V}}_{+} \equiv (\hat{\mathcal{P}} + \hat{S}_z/\sqrt{N/2})/\sqrt{2}$ and $\hat{\mathcal{W}}_{+} \equiv (\hat{\mathcal{X}} + \hat{S}_y/\sqrt{N/2})/\sqrt{2}$ and antisqueezing along conjugate quadratures $\hat{\mathcal{V}}_{-} \equiv (\hat{\mathcal{P}} - \hat{S}_z/\sqrt{N/2})/\sqrt{2}$ and $\hat{\mathcal{W}}_{-} \equiv (\hat{\mathcal{X}} - \hat{S}_y/\sqrt{N/2})/\sqrt{2}$ shown in figures 5.8(f-i). These rapidly produced entangled states can have high metrological utility in both sensitivity to motion and spin precessions [59, 60]. However, given the finite number of spins at longer times the dynamics do not continue to produce correlated pairs and instead exhibits collapses and revivals in coherence which are not fully periodic but damped due to the complex spectra of the Dicke model. In spinor BECs pair production between different spin levels due to spin-dependent collision scattering lengths has been shown experimentally [61–66]. However, these dynamics have been restricted to short time scales such that collapses and revivals in coherence from long time driven dynamics have not previously been experimentally demonstrated.

In contrast to these collapses and revivals of coherence at long times in the regular integrable regime, when $\tilde{g} \sim \Omega = \delta$ the rotating terms are no longer fast oscillating compared to the strength of the dynamics and the system is non-integrable. In this chaotic regime the coherent revivals are completely damped by the chaotic dynamics from the non-integrability of the system. This smooth crossover from integrable to non-integrable dynamics manifests itself in a change in the time averaged transverse magnetization between an integrable $\overline{\langle \hat{S}_x \rangle} \neq 0$ and a chaotic non-integrable $\overline{\langle \hat{S}_x \rangle} = 0$ regime, distinct from the dynamical phase transitions explored in the previous two cuts which exhibited a sharp non-analytic change in time averaged magnetization. As mentioned previously, at this unstable fixed point the dynamics erroneously has a non-zero Lyapunov exponent despite being regular dynamics for $\tilde{g} < \delta = \Omega$. However, taking a modified Lyapunov exponent that averages over neighboring initial spin states reveals a change in behavior in the average Lyapunov exponent from zero to nonzero that qualitatively agrees with the change in the time averaged transverse field magnetization and the onset of chaotic dynamics, as shown in figure 5.3. The relationship between the time averaged transverse magnetization and average Lyapunov exponent remains an area of fundamental investigation, with only a qualitative agreement in their change in behavior.

Comparisons between the experimentally measured time traces at the various conditions transitioning between the integrable and non-integrable regime are shown in figure 5.8(b-f). A DTWA calculation accounting for decoherence sources predominantly from spontaneous emission and fast noise in the magnetic field fully captures the measured dynamics. Shown in black dashed lines are the exponential growth of correlations between the spin and motion, which does not capture the collapses and revivals due to the finite N at longer times. A clear change is measured in the chaotic regime $\tilde{g} = \sqrt{\chi/\Omega} > 1, \Omega/\chi < 1$ where the coherent revivals are completely damped by the onset of chaotic non-integrable dynamics, and shown in the change in time averaged transverse magnetization in figure 5.8(f). The crossover is not ideally to 0 in the chaotic regime due to the finite time scale that is averaged over. Additionally the separation between the two equilibrium time averages is reduced due to decoherence in the integrable regime of large Ω/χ from magnetic field fluctuations, spontaneous emission, and thermal fluctuations.

In addition to DTWA comparisons, estimates from a mean field calculation and from a classical model with inflated thermal fluctuations show that the dynamics are not well captured at the mean-field level. Ideally at zero temperature the dynamics are at an unstable fixed point suggesting no dynamics should occur at the mean field level. For our finite temperatures some dynamics are present, but the temperature must be inflated by a factor of 5 compared to the measured temperature to capture the experimentally observed dynamics. Using the full DTWA model an estimate of the minimum achievable variance in the two mode squeezed state is calculated with and without experimental sources of decoherence in figure 5.8(f-i). The minimum variance state is achieved in the integrable regime at large Ω/χ, with a minimum value of $\sim$ 7 dB reduction in variance below the standard quantum limit (SQL), reduced to $\sim$ 4 dB below the SQL accounting for modeled experimental decoherence sources.

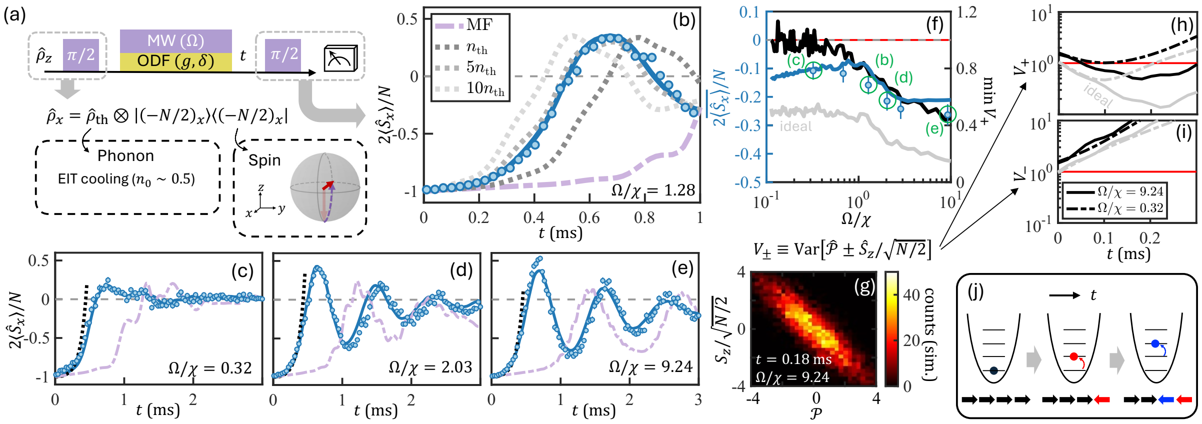

Figure 5.8: Unstable fixed point dynamics in the resonant regime. a) To prepare in the unstable fixed point we instead initialize the spins pointing along $-x$ instead of along $-z$, and measure the transverse magnetization using a final $\pi/2$ pulse about $-y$. All unstable fixed point dynamics were simulated with EIT cooling. b) Experimental data (blue dots) is well captured by the DTWA calculations (solid blue line), while in contrast the mean-field (lavender) cannot capture the dynamics. Inflating the measured temperature up to 5 fold is required to get better agreement with experiment suggesting thermal fluctuations in a classical model cannot explain the measured dynamics. c-e) Example time traces measured transitioning from non-integrable chaotic (c) to integrable (e) as Ω/χ is increased. f) A transition in the time averaged transverse magnetization agrees with theory characterizing the same chaotic transition shown in c-e. On the right axis are predicted minimum variances of the two mode squeeze states produced at short times with and without experimental decoherence. g) An example simulated two mode squeezed state in the integrable regime taken 0.14 ms into the dynamics at the minimum variance time. h-i) Theoretically calculated two mode state variances with (black) and without (gray) experimental decoherence as a function of time for the integrable (solid $\Omega/\chi = 9.24$) and chaotic (dashed $\Omega/\chi = .32$) cases. Shown in red is the standard quantum limit, or variance equal to the ground state wavefunction size. j) Representation of the pair production process showing correlated spin flips and COM excitations over time.

5.6 Conclusion and future outlook

In conclusion we have experimentally simulated the Dicke model across an array of parameter regimes and a number of key initial conditions. We first demonstrated a dynamical phase transition between a trapped and untrapped regime initialized spins along the south pole of the Bloch sphere in the spin-dominated regime characterized by the LMG model. This spin-dominated regime is insensitive to the motional state, which we initialized at both the Doppler temperature $\bar{n} \sim 5$ and near the ground state $\bar{n} \sim 0.5$ using EIT cooling. Theory calculations using the DTWA are in good agreement with experimental measurements, with the dynamics well characterized at the mean-field level. In contrast, we have also simulated the Dicke model in the resonant regime and seen a transition from the trapped state to an untrapped chaotic phase which is not well captured at the mean-field level in the time dynamics. Damping from thermal fluctuations is mitigated using EIT cooling to demonstrate the damping of the dynamics is largely driven by quantum fluctuations and chaotic dynamics. To further distinguish this chaotic transition we lastly initialized in an unstable fixed point of the spins pointing opposing the transverse field. In this regime a two-mode squeezing operation between the spin and motion degree of freedom gives rise to an exponential pair production at short times. At longer times and in the integrable $\tilde{g} < 1$ regime we see collapses and revivals of coherence due to the finite number of spins which has not been experimentally demonstrated previously in the Dicke model. Leaving the small $\tilde{g}$ integrable regime the system evolves from integrable to chaotic dynamics as inferred from the time averaged transverse magnetization due to the chaotic dynamics destroying the revivals in coherence. These dynamics are not captured at the mean-field level without substantially inflating the true thermal state of the system. Theory calculations suggest the minimum variance entangled state produced at short times can be ~ 7 dB below the SQL, with experimental decoherence reducing this to ~ 4 dB.

While a number of key features of the Dicke model have now been demonstrated with this work, all measurements have been restricted to time averaged magnetization that do not fully characterize the quantum and chaotic features of the model. Future work could potentially measure the bosonic occupation and work with varying initial coherent states with phase stabilization of the ODF phase allowing precise measurements of the dynamics of the bosonic degree of freedom. This requires a repumping of the spins that will project any spin-motion entanglement into a mixed state of the motion. Additionally recoil from the repumping will slightly perturb the motional occupation but would be negligible above $\bar{n}$ of more than ~ 1 quanta. A beam splitter operation using $\delta = \Omega$ and time reversal of the dynamics can enable the complex two mode squeezed state and degree of entanglement to be directly characterized [6, 59]. These entangled and chaotic states can in principle be used as sensitive metrological states to enhance measurement sensitivity beyond the SQL [59, 60]. Further work to reduce the decoherence sources in the experiment, either by detuning further off resonant with the ODF beams or using parametric amplification could also improve the metrological utility of these states. Finally, the chaotic dynamics can be more explicitly characterized using time reversal schemes to study information scrambling in analogs to black holes [67].

Chapter 6

Patterned Addressing

In all previous quantum simulation and sensing experiments in the NIST Penning trap, global readout and interactions were utilized. An array of interesting simulations can be engineered that use non-uniform initial states and interactions, and individual ion readout. Towards that goal, this chapter discusses patterned addressing of the spins largely using a deformable mirror (DM) to imprint patterns in the rotating frame of the ions.

6.1 Imprinting and detecting patterns with the ODF

Before discussing how to use the DM to imprint non-uniform spin patterns, it is worth discussing the few non-uniform spin patterns that have been produced and imaged using the ODF beams. The easiest pattern to impart from the ODF beams is a linear gradient in the rotating frame, produced as described in section 4.3.1. By setting the beatnote of the ODF to the mth multiple of the rotation frequency, patterned spin precession is produced of the form of equation 4.8, repeated here:

$$H_{ODF}(\mu = m\omega_r) \approx \tilde{U} \sum_i J_m(k_\perp \rho_i) \cos(m(\phi_i - \phi_0) + \Psi)\hat{\sigma}_i^z. \tag{6.1}$$

Notably for large enough k vector component in the plane, higher order azimuthal patterns are possible with reduced strength of $J_m(x) \approx \frac{1}{m!}(x/2)^m$. To identify the direction of the k vector tilt requires stability of Ψ, the relative phase of the ODF to the rotation frequency. It is clear that even coarse control of the radial dependence of the imprinted pattern is difficult, as on the fly adjustment of the ODF tilt is not feasible in the current setup. Fine control of the radial dependence is not possible, as the form of the radial dependence will always be $J_m(k_\perp \rho_i)$, unless some additional control of the ODF beam radial intensity or wavefronts could be adjusted.

One other method of generating non-uniform patterns from the ODF beams is using the axial drumhead modes. As described in subsection 4.3.5, applying the ODF in a Ramsey sequence near an axial drumhead mode leads to combinations of coherent spin precession and spin dephasing for coherent and thermal motions respectively. Displacements for each ion are given by the mode participation in the mode as shown in figure 2.4. As was shown in subsection 4.3.5, a coherent motional state gives rise to coherent spin rotations determined by the component of the coherent motion orthogonal to the spin-dependent force. Therefore, the coherent rotations applied to each ion will be proportional to the mode participation of each ion.

In principle, arbitrary spin patterns can be produced by generating the correct motional coherent state for each mode, and then applying the ODF out of phase on resonance with every single mode to impart arbitrary patterns by virtue of the normal modes being a complete orthogonal basis. In practice, this pursuit is foiled by frequency fluctuations of the drumhead modes, making each mode and its corresponding mode participations impossible to identify for all but the highest frequency most stable modes. Additionally, many modes are closely spaced or degenerate in frequency, making the resolution of each mode inherently time intensive.

Nevertheless, as a first demonstration of this we have for the first time experimentally imprinted the pattern of the axial drumhead modes onto individual ion resolved images as shown in figure 6.1. For these demonstrations we relied on spin dephasing of a thermal state rather than coherent state spin-precessions. The experimental sequence was a Ramsey spin echo sequence with a phase advance of the ODF in the second arm to coherently add spin precession between the two arms when on resonance. The resulting spin dephased state was rotated dark such that spin dephasing from motion resulted in increased population and brighter ions. At the time, single shot detection was not set up, so images are built up over hundreds of experimental repetitions over one second of integration. For this reason, the sign of the mode participation is not measured, which would require single shot detection or coherent motional states, and the resulting brightness of each ion is proportional to the absolute value of the mode participation of that ion.

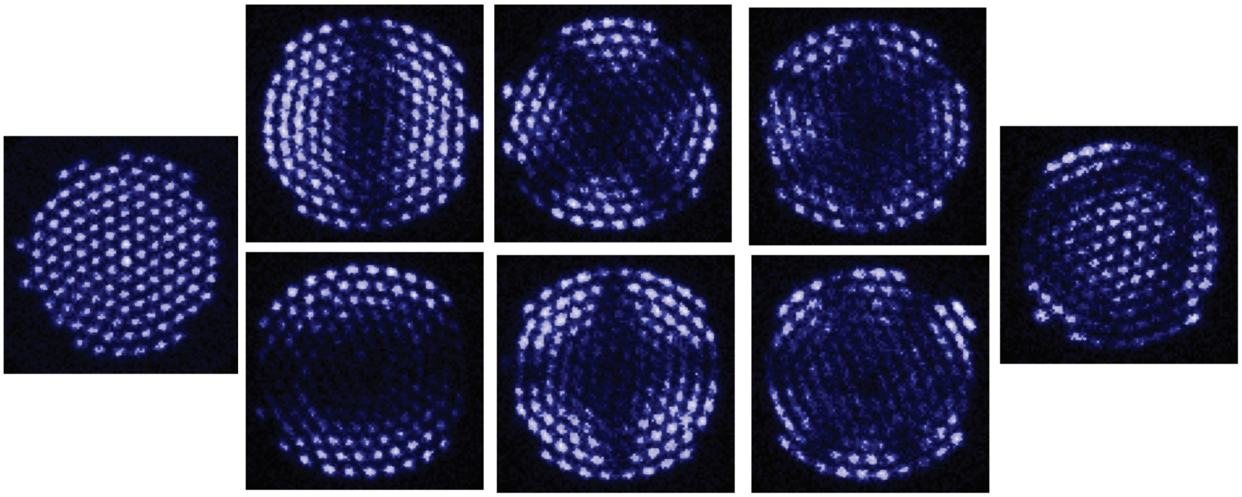

Figure 6.1: Imprinted drumhead mode patterns generated from spin dephasing caused by the ODF driven near resonant to various drumhead modes. The brightness of each ion corresponds to the absolute value of the participation of that ion in the given drumhead mode. See figure 2.4 for descriptions of the modes. The left most "COM mode" was not generated from spin dephasing but is instead a representative crystal with all ions bright. To assist in separating the modes in frequency the crystal was set at a rotation frequency of 190 kHz near the 1-2 plane transition.

6.2 DM patterned addressing overview

Analogously to the ODF using tilted wavefronts, a deformable mirror (DM) can be used to apply an ACSS pattern in the plane of the ions that is static in the rotating frame [68]. The DM we use is a Boston Micromachines (BMC) Multi-C-1.5 DM, which uses a continuous aluminum membrane surface with a series of 137 piston actuators that can deform the mirror surface shown in figure 6.2(a,b). Each piston is 300 × 300 μm giving an active diameter of 3.9 mm, with a maximum piston displacement of 1.5 μm. In comparison to other spatial light modulator (SLM) techniques which often fail to work in the ultraviolet regime or are extremely laser power inefficient, the aluminum membrane surface allows high power efficiencies at ultraviolet wavelengths with reflectivities $\sim 90\%$. Additionally, many SLMs have slow settling times and update rates whereas surface settling times can be as fast as 10's of μs for the BMC DM. However, DMs are limited by the difficulty in making many small piston actuators, relegating them to much fewer actuators in comparison to SLMs that often have millions of pixels, or much greater cost to produce more actuators. Additionally, even with many actuators it is difficult to reduce their size leading to potentially large mirrors for many actuators, requiring more magnification to match a fixed crystal size.

To utilize the DM, a laser beam off resonant from a Be^+ transition is reflected off the mirror with the piston displacements imprinting a phase pattern onto the (nominally flat) wavefronts of the beam profile as shown in figure 6.2(c). This phase pattern is imaged onto the ions using a simple $\sim$ 10:1 magnification telescope shown in figure 6.2(d).[1] At the ions the intensity of the beam leads to an AC Stark Shift (ACSS), equivalent to a modified precession rate of the spins. The imparted phase pattern therefore ideally does nothing with just a single beam as only the intensity of the beams determines the ACSS. By interfering this beam with a secondary beam at nearly the same frequency that has not undergone wavefront distortion, constructive and destructive interference set by the wavefronts' relative phases gives rise to an intensity pattern, or equivalently an ACSS pattern in the plane of the ions. For a 313/2=156.5 nm displacement of a single actuator, a 2π phase shift is imparted onto the wavefront at that actuator position. In principle phase deformations of almost 20 π are therefore possible.

Using a DM can provide a much more flexible addressing scheme as described in [68] compared to only linear gradients from tilting the ODF beams. By expanding upon the derivation of equation 4.8 (repeated above in equation 6.1), replacing the tilted wavefront deformation to be an arbitrary deformation that can decompose into a radial $\delta^m(\rho_i)$ and azimuthal $\cos(m\phi_{lab} + \phi_0)$ dependence

---

[1] The phase imparted along the longitudinal direction by an actuator is not magnified, rather the transverse direction is de-magnified to map the 3.9 mm diameter surface to 390 μm.

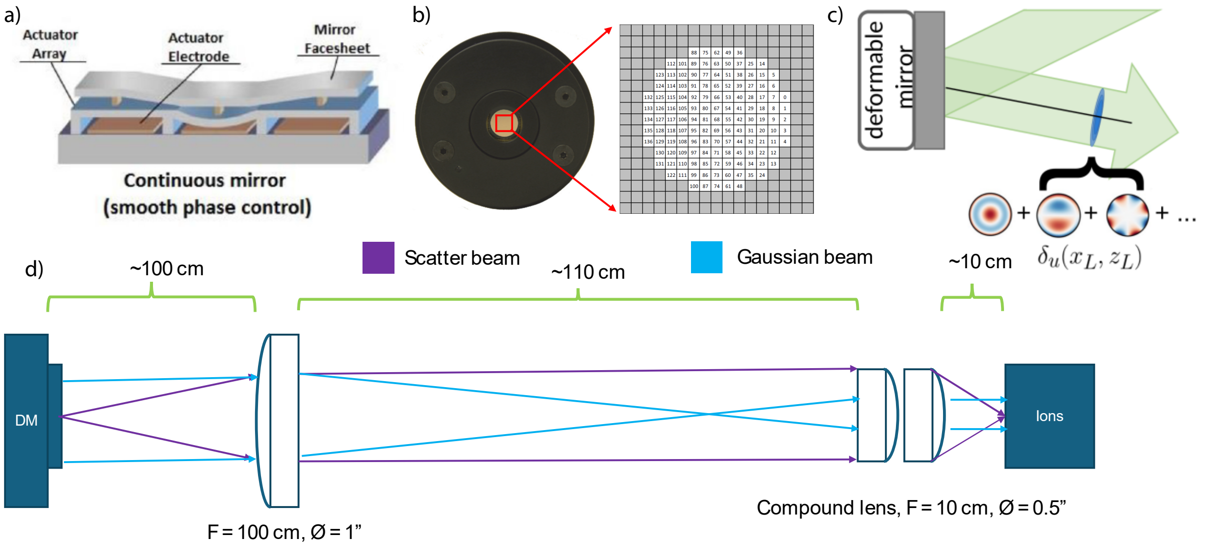

Figure 6.2: DM principle of operation. a) Our DM is a continuous surface aluminum membrane with a piston actuator grid underneath. b) An image of the DM, with the gold colored surface the mirror and the boxed red area the activate area of the mirror surface. Expanded from that is the actuator grid of which 137 actuators are present in the white boxes. c) A depiction of the patterned wavefront deformations imparted onto a laser beam reflected off the mirror. These deformations can be decomposed into various azimuthal orders useful for imprinting static patterns in the rotating frame of the crystal. d) A simple imaging system to image the surface of the DM onto the ions using a 10:1 magnification Keplerian telescope. Scattered light from the surface is re-imaged onto the ions, while a gaussian beam is de-magnified by 10 and remains a collimated beam. The imaging resolution of the system is then set by the numerical aperture (NA) of the imaging system.

gives:

$$H_{DM}(\mu = 0) \approx U \sum_i \cos(\delta^0(\rho_i) - \Psi)\hat{\sigma}_z^i \tag{6.2}$$

$$H_{DM}(\mu = m\omega_r) \approx U \sum_i J_1(\delta^m(\rho_i)) \cos(m(\phi_i + \phi_0) + \Psi)\hat{\sigma}_i^z. \tag{6.3}$$

In contrast to the ODF case which only could apply an $m = 1$ tilt of the wavefronts and imparted radial dependencies of $J_m(k\rho_i)$ for higher azimuthal orders m, now the radial dependence can be tuned arbitrarily to $J_1(\delta^m(\rho_i))$, with the J_1 dependence selected because a $\cos(m\phi)$ pattern is applied. As was the case with the ODF, lower order $0 < m' < m$ patterns can also be static when setting the beatnote to $m\omega_r$ if m/m' is an integer, but will have a $J_{m/m'}(\delta^{m'}(\rho_i))$ dependence, so ideally will be small. Additional terms oscillating at multiples of the rotation frequency can be exactly canceled by setting $\mu\tau = 2\pi l$ for an integer l [68]. Note the $m = 0$ case can still be described in terms of a Bessel function expansion, but all terms become resonant in the sum and so skipping the expansion is more illuminating. However, any $\delta^{m\neq 0}(\rho_i)$ term will also multiply equation 6.2 by a $J_0(\delta^{m\neq 0}(\rho_i))$ term for the $\mu = 0$ case, which will ideally be close to 1 since $J_0(x) \approx 1 - (x/2)^2$. By applying various $m, \delta^m(\rho_i)$ patterns with beatnote $m\omega_r$, any arbitrary pattern can be created. This can be more clearly seen by describing $\delta^m(\rho_i)$ in terms of Zernike polynomials, which form a complete basis, but experimentally it is useful to simply decompose into azimuthally separable functions.

6.3 DM setup and previous ideas

Originally the DM proposal was to implement wavefront deformations directly onto the ODF beams. This proved infeasible, as an anamorphic magnification was required due to the shallow angle the ODF beams interfere at. A test setup using multiple meters of path length and many cylindrical lenses led to the conclusion that, even if correctly setup, the imaging resolution is set by the effective numerical aperture (NA) of the system, which was very poor for the anamorphic setup even with multiple lenses in the bore of the magnet.

Ideally, to get the best imaging resolution the beams would be sent along the f/2 bottom-view imaging system, which is our best NA lens in the experiment. However, the gaussian beam component of the DM beams would stay on center and be blocked by the cantilever that sits above the f/2 lens and sends the parallel cooling and detection beam aligned with the magnetic field. Future alternatives would require parallel beams that come off axis and torque the crystal, or much less likely the parallel beam can be combined with a PBS, either in the f/2 or replacing the cantilever mirror with a PBS to allow DM light to transmit on center. This would very likely overwhelm the imaging due to background fluorescence. Possibly two off axis beams could be introduced that net applied no torque, but this remains fairly unexplored. Another idea is to use a far off resonant laser beam of a different frequency to allow the background light from the DM to be filtered, but would not solve the parallel beam issues.

As an alternative to applying the DM on the ODF beams, or going along the f/2 imaging objective, the deformable mirror beams have instead been introduced co-propagating with the parallel beam path (see section 3.2.1 for an overview). A beam path schematic is shown in figure 6.3. To get good imaging resolution, a lens must be put up the bore of the magnet as close as possible to the ions. To accomplish this, the cantilever was modified to be able to slot in a 1/2 inch diameter lens, specifically two 19.5 cm lenses to form a compound 9.75 cm lens with less aberrations (from here out referred to as a 10 cm lens). An ≈ 10:1 telescope is then formed by sending a collimated beam through a 1 m lens mounted on a translation stage ideally 1.0975 meters away. The surface of the DM is then imaged onto the ions by being placed ≈ 1 meter before the 1 meter lens. A telescope before the DM expands the beam to be ≈ 2-3x larger than the DM active area to ideally create flat wavefronts and a uniform intensity beam. Another beam path going through a copy of this telescope (from here on called DM1) is used to provide an interference with the beam distorted by the DM (from here on called DM2). A polarizing beam splitter combines the parallel cooling and DM1 beam, which have orthogonal linear polarizations when combined. The DM1 and parallel combined beams go through a remotely controllable motorized half waveplate, while the three beam system goes through a motorized half waveplate and manually adjustable quarter waveplate to allow arbitrary polarizations of the two DM beams. Independent control of the DM2 beam was attempted, but the polarization was found to scramble if adjusted before the DM, and not enough space was left to cleanly put a waveplate before the beams were combined. As a side effect this means adjusting the polarizations of all beams will adjust the parallel beam fluorescence as the ratio of σ_+/σ_- is adjusted.

For all imaging work the beams were set with vertical polarization before the quarter waveplate and σ_- polarization at the ions while the parallel beam had maximum fluorescence from being σ_+ polarized. Additionally, the two DM beams were red detuned 3 GHz from the $S_{1/2}(m_J = -1/2) \rightarrow P_{3/2}(m_J = -3/2)$ transition. This allowed the required intensity of the DM to be reduced substantially at the expense of increased spontaneous emission. However, due to amplitude noise on the beams the improvement from further detuning the beam was largely limited beyond this ~ 3 GHz detuning. Reduced total scattering from the DM was desired to minimize the degradation of the Roentdek camera quantum efficiency. Only later (see chapter 7) were motorized half waveplates added to allow for nulling of the ACSS of each beam. By cross polarizing the beams analogously to the ODF setup interference of the two beams can give rise to a non-zero ACSS while each beam is individually nulled.

6.3.1 DM experimental alignments

The first major change necessary to implement the DM was to add a lens in the bore of the magnet seated in the cantilever. This required removing the f/2 bottom-view objective any time the cantilever lens was added or removed to allow the cantilever to slide down the bore using the adjustable support rods added to the mirror tower (see section 3.2.1 for details). A careful alignment procedure when gluing the mirrors tried to ensure the cantilever mirrors were 45 degrees. This involved a red laser beam oriented vertically down on a countertop, which was checked by placing a mirror underneath the beam that back reflected up the beam path and carefully overlapping the back-reflection. While the glue was settling the cantilever mirror was adjusted to keep the reflected alignment beam level on the counter top, checked over a few meter path length. This procedure was successful at keeping the vertical tilt of the mirrors close to 45 degrees, however nothing was done to ensure horizontal alignment of the mirror. Simply placing the lens centered in the cantilever therefore led to substantial disturbance of the beam due to the horizontal tilt of the cantilever mirrors, along with whatever tilt and translation was necessary to align to the magnetic field and ions.

To successfully find parallel fluorescence with the cantilever lens inserted, first the parallel beam was well aligned with the magnetic field and centered on the ions without the lens in place. After that alignment, the counter-propagating photo-ionization beam was carefully overlapped with the parallel beam. Next the cantilever lens was added and the parallel beam was re-aligned to overlap the back-propagating photo-ionization beam. This involved substantial beam changes, including remounting the last mirror before sending up the magnet order a centimeter away. Additionally, the

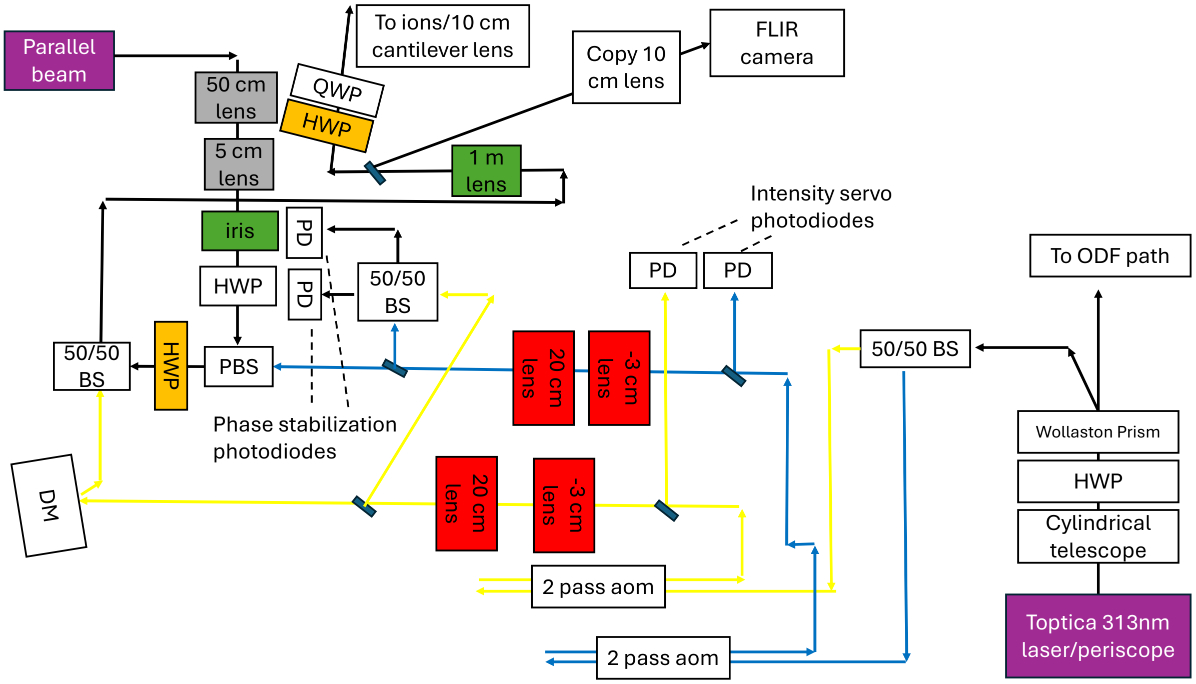

Figure 6.3: DM and parallel beam paths. Purple boxes represent the 313 nm laser sources for the parallel cooling and ODF/DM beams. The Toptica 313 nm laser is brought from underneath the table via a periscope, where it passes through a cylindrical lens telescope to compensate an elliptical beam profile. A half waveplate (HWP) adjusts the polarization going into a Wollaston prism to chose the ratio of light going into the ODF path and the DM path. The DM path then splits into two paths with a 50/50 beam splitter (BS), with the yellow path corresponding to DM2 and the blue DM1. After twice passing through acousto-optic modulators (AOMs) to minimize beam pointing changes with frequency adjustment, the beams are sampled (blue rectangles) for photodiode (PD) readings of the power for intensity stabilization (generally not used in experiment). Red blocks correspond to expansion telescopes of each DM beam, which is picked off and interfered on a 50/50 BS for optional active stabilization of the phase (unimplemented in experiment). The DM1 path is combined with the parallel beam on a polarizing BS (PBS), before a motorized (orange) HWP adjusts the linear polarization of the combined DM1 and parallel beam. DM2 reflects off the deformable mirror (DM) and is combined with the DM1 and parallel beam on another 50/50 beam splitter. The three beam system goes through a 1 m lens and is sampled to go through a copy 10 cm lens to image onto a CMOS FLIR camera. The main beam path goes through another motorized HWP and final quarter waveplate (QWP) to set the circular polarizations of the beams. The combined beams are sent up the bore of the magnet to pass through a 10 cm lens in the cantilever and imaged onto the ions. Before being combined, the parallel beam path is expanded with the gray lens pair telescope, next passing through an adjustable iris (green) to allow a reference centering on the ions and FLIR camera.

parallel beam was expanded with a 10:1 telescope, and then de-magnified through the 10:1 telescope formed with the cantilever lens.

With the parallel beam successfully hitting the ions with the cantilever lens in place, the cantilever height was adjusted. To find the focus position of the cantilever lens, first the parallel beam collimation was set by adjusting the 10:1 expanding telescope to keep the beam size relatively constant over a long propagation distance sent across the room. Next, the 1 meter lens was removed, causing the collimated beam going through the 10 cm cantilever lens to focus very sharply (see figure 6.4(a)). The cantilever (see figure 6.4(b)) was designed to slide along 1/2 inch diameter rods that set the mirror crown height, with the height of the cantilever set by a second pair of thin rods held at an adjustable height underneath the base crown. This involved machining the base crown to add through holes for the adjustment rods. By adjusting the rod heights while monitoring the fluorescence from the side-view of a very low density large cloud, the gaussian beam propagation could be mapped out to find the minimum spot size. Slight translation adjustments of the 1 meter lens were necessary over large cantilever translations to compensate the horizontal tilt of the cantilever mirrors.

With the cantilever height set, the f/2 objective could be re-inserted to the system to allow bottom-view images. On first insertion it was found that an original 10 cm lens design required lowering the cantilever into the f/2. After removing the f/2, swapping to shorter focal length backup lenses (effective focal length 9.75 cm), and re-inserting the f/2 we have not since had to remove the f/2. With bottom-view imaging, the parallel beam could be aligned to the ions and magnetic field. To do this, an iris is roughly centered on the expanded parallel beam and at smallest aperture reduces the parallel fluorescence size on the bottom-view to give a centering of the parallel beam on the ions (see figure 6.4(c)). Next, the 1 m lens is removed and the beam is tilted using a mirror to center the focused beam on the ion crystal center. With this alignment procedure and iteration the parallel can be centered on the 1 m lens and the ions. Next the beam was walked with the 1 m lens removed ending with the focused beam centered on the crystal, and then re-centered on the ions with the 1 m lens by translating the 1 m lens added back in and apertured with the iris. Subsequently, the magnetic field alignment was checked either by spinning up the crystal to a high rotating state and looking for Doppler shifts in the parallel beam, or by simply torquing the crystal with only the parallel beam (turning off the rotating wall and perpendicular beam) to evaluate the alignment. Iterating this procedure led to reasonable alignment of the parallel beam on the ions with and without the 1 m lens, and minimal torque from the parallel beam.

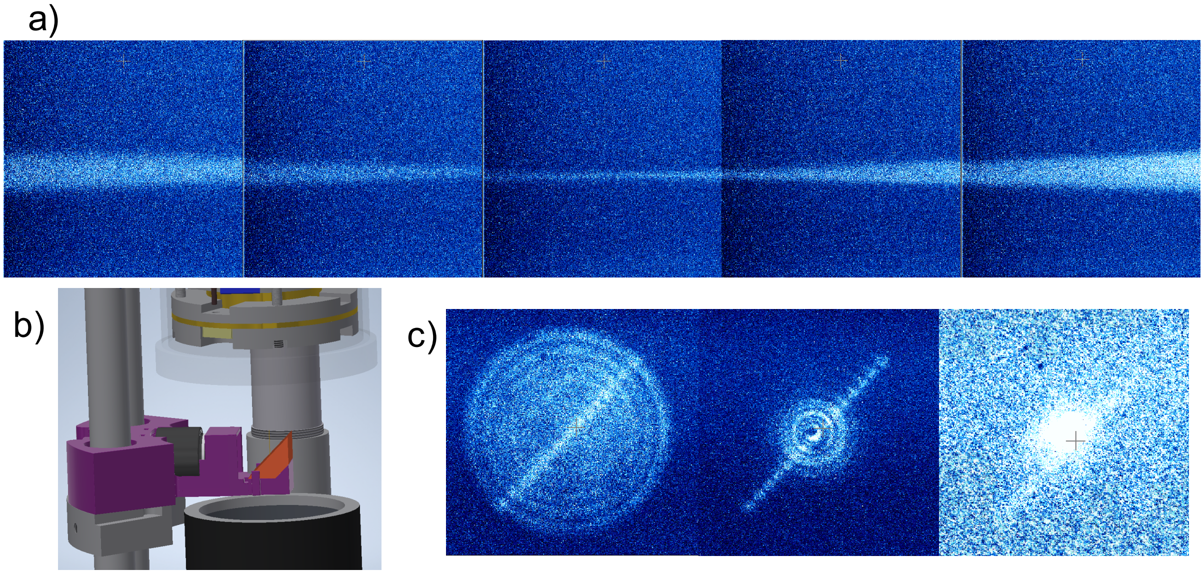

Figure 6.4: DM alignments. a) Five side-view images stitched together showing the focus of the collimated parallel beam with the 1 m lens removed and focused by the 10 cm cantilever lens. Each image shows a roughly 800 × 800 μm image of a diffuse ion plasma with the tightly focused parallel beam passing through it. Each image was taken after moving the cantilever up roughly 800 μm which corresponds to 2 turns of an 80 thread per inch adjustment screw. Setting the focus of the cantilever height is then set much better than 100 μm, likely limited by how well collimated the parallel beam can be set. b) A 3D model of the cantilever (purple) set above the f/2 imaging objective (large black cylinder) and below the trap envelope and electrodes (transparent cylinder above the cantilever) showing the modification to allow a 1/2 inch diameter lens tube shown in black holding a $\sim$ 10 cm focal length lens in between the two mirrors (one mirror shown in orange). The cantilever slides along the 1/2 inch rods in gray and is supported by adjustable height support rods (not shown) to set the height from the ions. c) Bottom-view images of the crystal. From left to right: fluorescence from the parallel beam without aperturing the beam, with the beam apertured, and focused and centered with the 1 m lens removed producing much larger background scatter.

With the parallel beam and cantilever height well set the DM beams could be adjusted. To start, each beam is roughly collimated with their respective expanding telescopes and then roughly overlapped with the large parallel beam. A pick-off in the beam path after the 1 m lens is imaged with an exact copy 10 cm[2] lens onto a CMOS FLIR camera. To mimic the image formed at the ions, the lens to camera distance is set by removing the 1 m lens and translating the copy 10 cm lens to find the smallest parallel beam spot size. The distance from the 1 m lens to 10 cm lens in the two paths luckily isn't critical, as ray tracing from the image (the ions) backwards through the 10 cm lens gives a collimated source that doesn't matter where the 1 m lens appears. However, the distance from the DM to 1 m lens would matter for imaging resolution. No optimization was ever done to improve this, and rough placement on the table was sufficient to get good interference images on the FLIR camera. Discrepancy between the FLIR path and the ion path for the 1 m to 10 cm lens distance will largely give rise to a magnification difference. This was also never carefully optimized, with the 10 cm lens roughly placed to get a somewhat collimated beam out with the 1 m lens in place.

Fine adjustment of the DM beams involved matching their alignments with the parallel beam, their wavefront matching (collimation and tilt agreement), and their centering on the ion crystal center, as set by the iris on the table. The two DM beams were set to the same frequency to see interference fringes on the FLIR camera. Radial interference fringes suggested collimation mismatch between the beams, and linear strip patterns suggested tilts between the two beams. Further, the collimation for each beam could be roughly set by removing the 1 m lens and adjusting the expanding telescopes to find the minimum spot size on the FLIR camera. Finally, centering can be adjusted by setting an “X” pattern on the DM, or any other pattern that identifies the central actuator clearly. Monitoring this interference pattern formed with both DM beams, and with the parallel beam on and apertured down tightly, the DM1 beam is walked to center the X pattern on the apertured parallel beam.

6.3.2 Wavefront compensation

Adjustments of the collimation and tilt of the DM beams allows for fairly uniform, flat wavefront interference patterns, but residual wavefront disagreement remains that can't be compensated with

---

[2] Actually two 19.5 cm focal length lenses for an effective 9.75 cm focal length

global beam adjustment. Instead, fine wavefront compensation can be carried out by measuring the interference pattern of the two beams on the FLIR camera and adjusting the actuators of the DM to compensate distortions. To accomplish this, first the wavefronts are set as flat as possible and centered on the ions and parallel beam aperture using the procedures described above. Next, an X pattern is set and a 13x13 grid of equal size squares is overlaid on the image, set by a square size and center of the grid in pixels as shown in figure 6.5(a). The center pixel and square size are manually adjusted to roughly match the grid onto the X pattern created. Experimentally it is found this isn't perfect as some distortion appears to modify the size of the pixels to not be uniform size when interfered on the FLIR. Additionally, the edge pixels are particularly susceptible to rapid phase wrapping before the edge of their boundaries.

With the grid overlapped to mimic the locations of the DM actuators, a measurement of the phase of the wavefront interference is carried out for each binned grid square to determine the necessary compensation. A sequence of 11 images is taken in roughly 1 second, with the DM beams set to the same frequency and a phase adjustment of only DM1 by 36 degrees per image. Using the identified grid, all counts from each pixel within an effective DM actuator are binned to give a 13x13 count array for each phase image. Plotting the counts of each DM pixel as a function of the DM phase gives a sine curve, assuming the counts from each pixel are below the saturation of the camera and phase distortions within a DM pixel are not too large. The phase of the sine wave gives a measurement of the relative phase of the wavefronts between the two beams. The offset gives the average intensity of the interference. The amplitude gives a measure of the contrast of the interference, or equivalently the amplitude and polarization agreement of the beams. Ideally, the amplitude would equal the offset, and any reduction from this corresponds to uneven amplitudes, non-overlapping polarizations, or phase non-uniformity across a DM pixel. Fitting each effective DM pixel's counts as a function of DM phase then gives a wavefront phase estimate of each DM pixel, which can be used to calculate the deformation necessary to match, or "flatten", the wavefronts of the two beams, as shown in figure 6.5(b). Specifically, the center phase is offset to be zero so no compensation is applied to the center pixel, and all other pixel phases are offset by the same phase offset. For flat (matching) wavefronts all DM phases are zero.

Taking the measured phase in radians and adjusting the DM actuator by $313/4 \approx 78$ nm for a π phase shift ideally cancels any wavefront deformations. With this simplistic method, wavefront errors of amplitude > 78 nm are incorrectly compensated because the fitting scheme only has an output range of $\pm\pi$. This is avoided by setting the starting alignment as optimally as possible, and checking the fitted phase for any neighboring DM pixel phase wraps of > 78 nm before applying compensations. After a single round of compensation, usually a few nm of error remains largely on the outermost pixels, which can be reduced to $<$1 nm for the central actuators after $\sim$ 3 iterations of compensation.

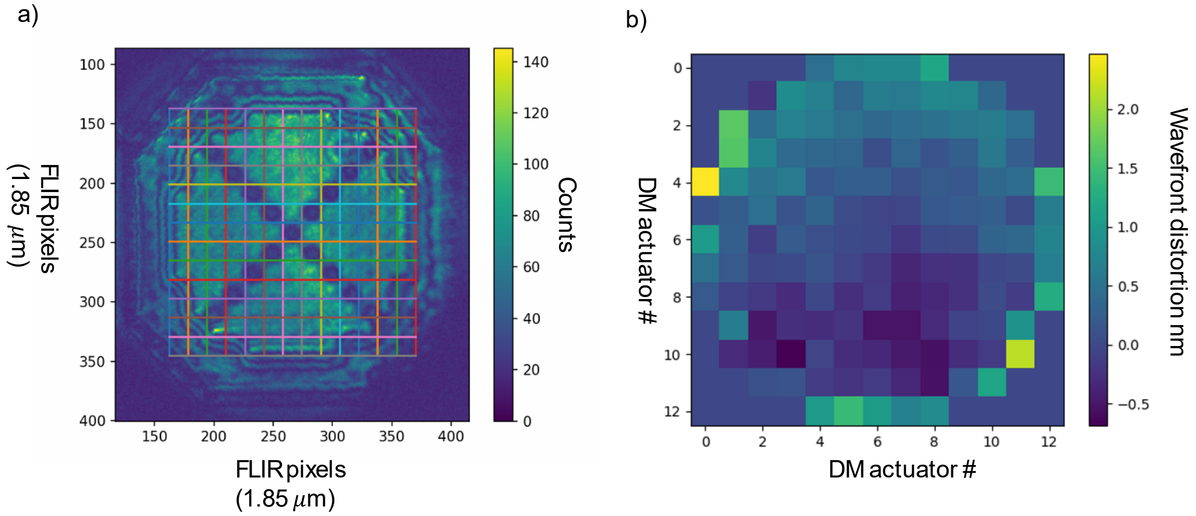

Figure 6.5: DM wavefront compensation. a) A FLIR image taken with an "X" pattern set on the DM surface. An overlaid grid set by a center pixel and square size in pixels is manually adjusted to roughly overlap the actuator locations. A series of 11 images are taken with a phase shift of 36 degrees between them, with counts from each pixel within an overlaid grid square binned together. Fitting the counts as a function of DM phase for each grid square results in an estimate of the wavefront from each DM actuator like figure b). b) An estimated wavefront flatness in nm from a sequence of 11 phase images. This image was produced after a few rounds of compensation after setting the wavefronts nominally flat from the image on the left. Note only the circular 137 subset of actuator correspond to DM actuators, with the 8 grid squares in each corner left unfit. Errors on the boundary actuators of $\sim$ 2 nm are common, with the central actuators usually displaying wavefront errors of $<$ 1 nm.

Experimentally, the wavefront flatness can be partially validated analogously to rotation sideband dephasing of the ODF as described in section 4.3.1. In practice, the 1st sideband can potentially be suppressed further at the expense of non-flat wavefronts to compensate potential amplitude and short wavelength phase non-uniformity of the beams. Section 6.5.1 describes further analysis of how well a global uniform $\hat{\sigma}_z$ rotation can be applied.

6.4 DM calibrations and analysis

6.4.1 DM phase flopping

Figure 6.6 shows a standard DM pulse sequence used to imprint a pattern. Assuming flat wavefronts and $\mu = 0$, for a single pulse Ramsey experiment the applied ACSS[3] is given by:

$$ACSS = 2U_0(1 + \sin(\phi_{DM})) \tag{6.4}$$

where ϕ_{DM} is the relative phase of the two beams at the ion, and U_0 is the single beam ACSS, assuming aligned polarizations and equal intensities. If the polarizations or intensities do not match the contrast of the interference will be reduced from U_0 when at the standard ≈ 3 GHz detuned point (note cross polarization schemes modify this see section 7.7.1). By implementing a spin echo with no phase advance, the spin precessions in the first arm will ideally be canceled in the second limited by amplitude and phase jitter. With a phase advance of π, ideally the sign of the interference term is reversed to add coherently with the first arm, while the offset average ACSS stays constant and is canceled. For this sequence the effective applied ACSS is then given by:

$$ACSS \approx 2U_0 \sin(\phi_{DM}) \tag{6.5}$$

Varying the relative phase of the beams ϕ_{DM}, called "phase flopping", while setting $\mu = 0$ with flat wavefronts will therefore vary the effective ACSS sinusoidally about 0. The amplitude of the maximum ACSS is set by the sum of the two DM beam's ACSS (assuming aligned polarizations and

---

[3] ACSS refers to the differential AC Stark Shift.

equal intensities). By applying the DM beams for a short precession period in a spin-echo sequence with a DM phase advance, applying the final microwave pulse about y (the echo axis) converts spin precessions into deviations in population about 50%. These populations can then be converted into a precession angle, and therefore an estimate of the ACSS using the arm time like so:

$$\theta \approx 2\sin^{-1}(\sqrt{P_\uparrow}) - \pi/2 \tag{6.6}$$

$$ACSS \approx \frac{\theta}{4\pi\tau}, \tag{6.7}$$

where ACSS is in units of Hz, and $P_\uparrow$ is the bright fraction of the ions. This estimate of the ACSS is a bit poor, particularly at large ACSS, due to turn on effects slightly reducing the effective arm time τ, and fails if the maximum accumulated phase goes beyond $\pm\pi/2$. Regardless, the sine wave oscillation is fitted to extract the relative phase of the beams at the ions. To apply a given ACSS, the relative phase of the beams is then set to $\phi_{DM} + \phi_{sin}$, where ϕ_{sin} is the fitted phase of the oscillation, giving an effective Hamiltonian $\hat{H} = \sum_i U \sin(\phi_{DM})\hat{\sigma}_z^i$ where $U = U_0$.[4]

6.4.2 DM phase tracking and $\pi/4$ time calibration

No active stabilization is applied to the beams besides interleaved updates of ϕ_{sin} from the ions using a DM phase tracker. Passive stability when the optics table is enclosed leads to drifts over seconds with fast noise at ≈60 Hz multiples. To implement the tracker, a three point probe experiment is done that ideally sits at the 50% population points (called left and right points) and the minimum population point (called center point) of the phase flop curve in figure 6.6. Measurements of the center point are simply a diagnostic reference to check the contrast of the tracker, with less repetitions allotted to its measurement to improve the duty cycle of the experiment. Given a population measurement of the left and right point, the functional form of the sine curve of the phase flop could be inverted to exactly calculate the optimal compensation. In practice, a simpler linear extrapolation assuming small deviations from 50% is implemented. Assuming a small deviation from

---

[4] There is a factor of 1/2 going from differential ACSS $2U_0$ to a $\hat{\sigma}_z^i$ amplitude $U_0\hat{\sigma}_z^i$. U will refer to half the differential ACSS in general.

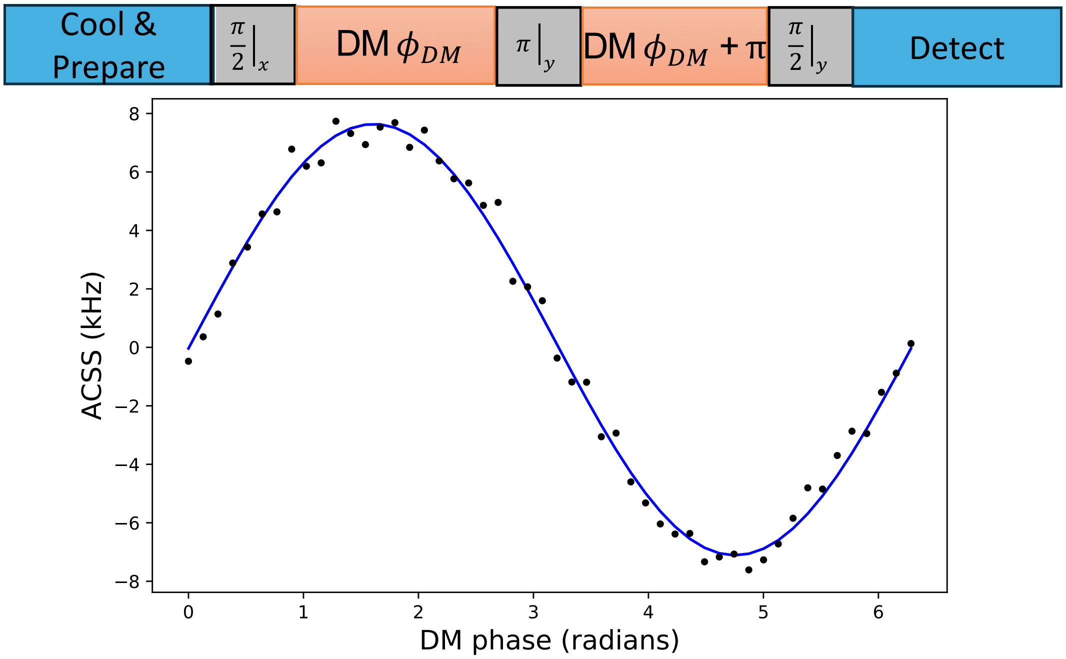

Figure 6.6: DM phase flopping calibration of the DM beam's relative phase with flat wavefronts. A Ramsey spin echo sequence with a phase advance of π in the second DM arm imparts a coherent rotation measured by applying a final $\pi/2$ pulse about y. Varying the DM beam's relative phase with flat wavefronts then produces a sinusoidally oscillating ACSS, which can be fit to estimate the phase necessary to get a desired ACSS. The ACSS is calculated from the measured bright fraction as described in equation 6.6. The fit gives an estimated ϕ_{sin}= 0.06 ± .01 radians.

the optimal center phase ϵ, the bright fraction of the left and right points P_L, P_R is given by

$$P_{\uparrow} = \frac{1}{2}(1 + \sin(4\tau U \sin(\phi_{DM})) \tag{6.8}$$

$$P_{R/L} \approx \frac{1}{2}(1 \pm 4\tau U\epsilon) \tag{6.9}$$

$$\epsilon \approx \frac{(P_R - P_L)}{4\tau U} \approx \frac{2(P_R - P_L)}{\pi}. \tag{6.10}$$

Equation 6.10 describes the optimal center phase adjustment for a population imbalance between the left and right point. The last step of equation 6.10 assumes the two arms of the echo cause a maximum total $\pm\pi/2$ rotation to map the maximum positive and negative ACSS to fully bright and dark giving full contrast. An error in the code had previously overestimated this compensation a factor of $\pi/2$. However, the arm time used for the phase tracker was often less than the optimal

$\pi/4$ arm time (giving a $\pi/2$ total rotation), and any non-uniform phase pattern would decrease the amplitude of the oscillation such that this overcompensation was still stable. After feedback on the center DM phase, ϕ_{sin} was updated by adding $\pi/2$ to the center phase.

From the statistical uncertainties in the measured $P_{L/R}$, a rough estimate of the phase uncertainty suggest uncertainties as low as $\sim \pm 2$ degrees with 10 repeats per point, which can be as fast as $\sim$ 20 ms when the Doppler cooling time is reduced to 1 ms. This phase measurement feedback was often carried out every 5 repetitions of imprinting a pattern to have the slow drift rate of the phase be similar scale to the measurement uncertainty.

With active DM phase tracking a global $\pm\pi/2$ rotation can be calibrated by tracking ϕ_{sin} and setting $\phi_{DM} = \pm\pi/2$ (see figure 6.7). This phase setting gives the maximum positive (negative) ACSS, such that a Ramsey spin echo sequence with a final microwave $\pi/2$ pulse about y results in all ions bright (dark) for $\phi_{DM} = +\pi/2$ $(-\pi/2)$ using an arm time $\tau = \frac{\pi}{8U}$, equivalent to a $\pi/4$ arm time. Using this standard arm time and ϕ_{DM}, modifying flat wavefronts by adding $m = 0$ patterns maps 313/4 nm actuator displacements into spin flips relative to the tracked flat wavefronts. Setting $\phi_{DM} = \pm\pi/2$ gives first order insensitivity in phase fluctuations and therefore the highest fidelity operations. Setting $\phi_{DM} = 0, \pi$ gives ideally no effective ACSS, but is first order sensitive to fluctuations in the relative phase ϕ_{DM}.

6.4.3 Roentdek imaging setup and analysis

To precisely determine the imparted pattern onto the ion crystal, single shot detection is highly desirable. However, this is complicated by the non-uniform fluorescence rate across the crystal due to parallel beam non-uniformity, perpendicular fluorescence, and quantum efficiency degradation on the center of the Roentdek that has been exposed to the most fluorescence. Often ion experiments threshold based on known histograms of bright and dark counts to separate whether a single ion image is bright or dark. However, this would require generating a histogram of bright and dark counts for every ion for that specific crystal and image, something that is prohibitively time consuming for our long detection times imposed by our low quantum efficiency.

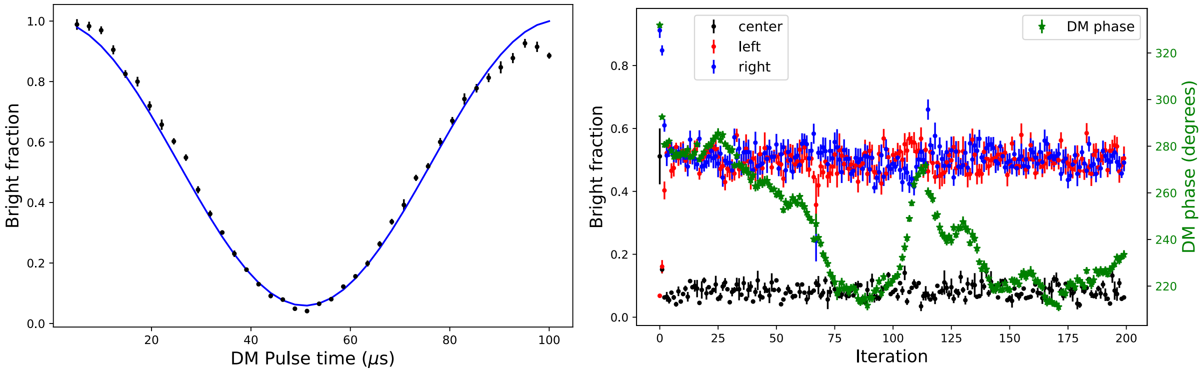

Figure 6.7: DM phase tracking and $\pi/4$ time calibration. The left plot gives the measured bright fraction as the applied total DM pulse time is scanned. The final microwave pulse is about $-x$ to start with all ions bright for no rotation, causing either positive or negative ACSSs to rotate the population dark over time. A fit to a Rabi time scan gives an estimated π time of 58.9 ± 0.3 μs. By setting a single arm time of ~ 15 μs for a $\pi/4$ arm time, ions will be rotated bright or dark depending on if $\phi_{DM} = \pm\pi/2$ using the pulse sequence in figure 6.6 with flat wavefronts. Interleaved at every 5 repeats and every pass of the time scan experiment a phase tracking 3 point measurement is taken shown on the right plot. The tracked center phase is plotted in green on the right axis, with error bar estimates too small to see of $\sim \pm 2$ degrees. The left (red) and right (blue) points correspond to an average of 10 repetitions of the phase tracker, and the center point (black) only 2 repetitions. As shown in the first three points the starting phase was poorly estimated initially and quickly comes into lock by the around the 3rd iteration. Each feedback measurement of 22 total L/R/C measurements takes ~ 35 ms and the total scan took ~ 10 seconds.

Instead, a detection scheme is used that first detects for 25 ms to project into spin up or down, and a second image is taken with a microwave π pulse in between. During these detections both parallel and perpendicular cooling beams are on with a coupling drive described in section 7.6 to maintain a cold in-plane temperature. From these image pairs, the location of every ion can be confirmed since every ion is bright in the combined image, and approximate bright and dark histograms can be built up for each ion individually for that crystal configuration (see figure 6.8). For simplicity, we label an ion bright if the first detection is brighter than the second, and dark if brighter in the second. More advanced analysis can be carried out as described in detail in reference [69]. For our laser intensities and quantum efficiency, we achieve ~ 15 counts for a bright ion, and ~ 1 count for a dark ion. On the rare occasion an ion is identically bright between the two detections that ion's state in the image is left undetermined and ignored. This scheme is susceptible mostly to off-resonant pumping from $|\downarrow\rangle \rightarrow |\uparrow\rangle$ during detection, which we roughly measure to be $\sim 1-3\%$ using global fluorescence PMT counts after applying a scanned detection pulse up to 50 ms when initialized dark. This low off-resonant pumping rate is due to the large magnetic field separating the levels far from resonance in the $P_{3/2}$ manifold, along with a low saturation intensity. The low saturation intensity is experimentally set to get more stable crystals such that the in-plane cooling rate is not overwhelmed by the in-plane heating from parallel scatter.

For analysis on the software end, the Roentdek images are tagged via a TTL pulse input to the Roentdek time to digital converter that acts as an image counter. Every grouping of three images is extracted to form a Doppler cooling image and two subsequent detections. Images are then combined in groups of 5 repetitions of the experiment to build up a more discernible ion image, and displayed less than a minute after the scan for spot checking of data. An off-line analysis script compares each total Doppler image built up over 5 repetitions to measure changes in the images that roughly correlate with reconfigurations. The longest chain of images with a single configuration is used to identify the ion locations for that configuration, as shown in figure 6.8. This is accomplished with a script that utilizes the Python Scikit-image library to find features in the image as an initial guess. Subsequently, a custom written recursive script tries to optimize the found features to overlap with ion positions. Each position found is attributed a pixelated circle region with radius determined by its nearest neighbor distance, with the pixel circles precomputed in memory to reduce calculation times. The total counts contained in each pixel circle is calculated and compared with a single pixel movement of the pixel circle in any neighboring direction to steer the optimal center onto the ion center. This recursive procedure is repeated until no coordinate adjustments lead to more optimal centers. In addition, coordinate positions can be steered to overlap with other found features, at which point one of the copies is removed and the nearest neighbor distance recalculated. This procedure takes much less than a second and fairly reliably finds all ions, but is hindered when total accumulated counts are low, and when ions are poorly localized.

Using the identified longest segment of data and ion positions and radii, the total counts within the corresponding pixelated circles represents the total fluorescence of each ion for each image. Each detection image pair is then evaluated for each ion to determine whether the ion is bright, dark, or undetermined. The bright fraction is then calculated over all detections in the segment for each ion. Most experiments used 50 ms Doppler cooling time, 50 ms total detection time, and 250 repetitions, taking a cumulative ∼ 30 seconds due to time spent tracking the DM phase every 5th repetition. The longest segments achieved have approached the full 30 seconds without a reconfiguration, but often segments of 5-15 seconds corresponding to 50-150 images are achieved.

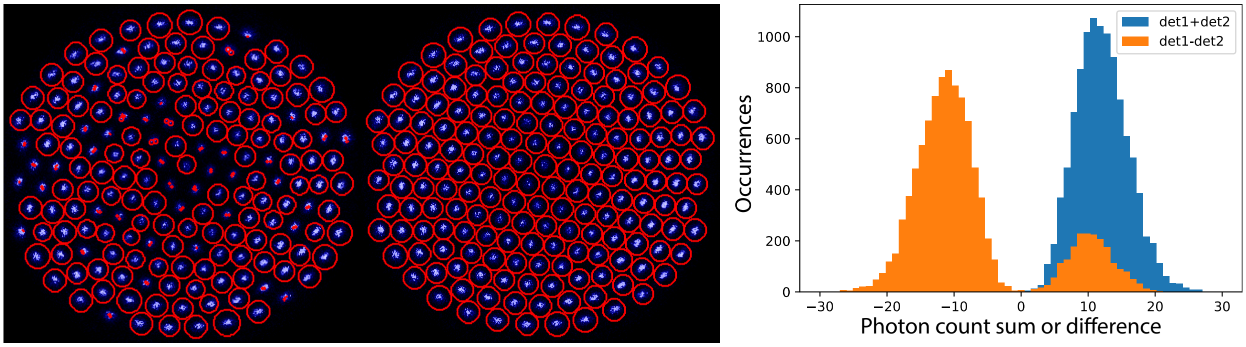

Figure 6.8: Roentdek image analysis. A reference image combined from sixty 50 ms long Doppler cooling images is shown with features circled in red circles. The leftmost image shows the initial features found using a Python image analysis library that finds peak local maxima, with the radius of each circled set by the nearest neighbor distance. Too many features are found with small separations, which are combined following the recursive optimization algorithm described in the text producing the image to the right. Each ion count is then found by the total counts enclosed in the red circular region for each ion for each detection image. The histogram shows the difference and sum of the first and second detection for every ion for this experiment. The imprinted pattern was to make all ions dark except a ring of radius 2 DM pixels bright, giving the asymmetry of the difference histograms showing the average bright fraction across the crystal is mostly dark. Of the 180 ions across 60 images giving 10,800 detections, 6 were the same brightness and 4 were only separated by 1 count, giving ∼ 0.1% error. This excludes any additional error from off resonant pumping not captured in these cases.

6.4.4 FLIR image analysis and predicted pattern

Utilizing the FLIR images, arm time, tracked ϕ_{DM}, final microwave phase ϕ_{mw}, azimuthal order m, and the ACSS strength should ideally give enough information to predict the imparted pattern. The FLIR images can in principle give additional information about amplitude non-uniformity of the interference and shorter wavelength phase errors. Identically to the wavefront flattening procedure, 11 phase images are taken, however this time every individual image pixel is fitted rather than binned over a DM pixel to extract a finer resolution amplitude and phase array, also called phase and amplitude maps. Also fitted is an offset that is ideally canceled due to the DM phase advance and is ignored. From here, the imprinted pattern is directly calculated as

$$\theta(\rho,\phi) = \int_0^\tau 2U(\rho,\phi-\omega_r t)\sin(\Phi(\rho,\phi-\omega_r t) - m\omega_r t + \phi_{DM}) \tag{6.11}$$

$$P_\uparrow \approx \frac{1}{2}(1-\cos(2\theta+\phi_{mw})). \tag{6.12}$$

Here ϕ_{mw} is the phase of the last microwave pulse, ρ, ϕ are the polar coordinates of the FLIR camera image in pixels, U, Φ are rescaled fitted amplitude and phase maps, m is the beatnote rotation sideband applied, and ϕ_{DM} the global relative DM phase. As an example, for $m = 0$ often the desired scheme is $\phi_{DM} = -\pi/2, \phi_{mw} = \pi/2$, U is ideally uniform, $4U\tau = \pi/2$, and Φ has only radial dependence giving:

$$P_\uparrow \approx \frac{1}{2}\left(1-\sin\left(\frac{\pi}{2}\cos(\Phi(\rho))\right)\right). \tag{6.13}$$

For flat wavefronts $\Phi = 0$, making all ions dark. Displacing a ring of actuators 313/4 nm therefore would ideally flip a ring of ions bright. Changing sign of ϕ_{DM} or ϕ_{mw} would invert this to have all ions bright except the ring of displaced actuators.

A few technical challenges are involved in carrying out the integration of equation 6.11 and predicting the imparted pattern on the ions. First, the calculated bright fraction as a function of ρ, ϕ FLIR coordinates needs to be re-scaled spatially to match the size of the crystal. One independent analysis we've carried out used an imaged crystal with no BeH$^+$ that was compared to simulations using our best estimated trap parameters. It suggested based on the crystal aspect ratio an adjustment of our rotating wall C_2 parameter reducing it $\sim 20\%$ (see table 3.2 for details). It also suggested a magnification of the bottom view imaging system of 143, with the expected magnification 125. The FLIR image pixels can simply be scaled by 1.8 μm per pixel. From here there can be a discrepancy between the magnification of the copy telescope onto the FLIR camera compared to the beam path going to the ions, or day to day variance in the imaging magnification. Therefore, in some analysis this was left as a free parameter, but in general was constrained to be $\sim$ 10% away from our estimate. Next there is the conversion from the amplitude map given in photon counts hitting the FLIR camera to an ACSS amplitude. The amplitude in photon counts is first scaled to have the average central pixel's amplitude correspond to the measured U. In some analyses this baseline scaling was then allowed to freely vary to best match the measured pattern, often being inflated ~ 15 %. Other analysis set a uniform assumed U such that $U\tau = \pi/4$.

The phase map does not need any rescaling and is trusted to be a representative estimate of the phase. However, the global phase offset of the phase map is equivalent to an adjustment of ϕ_{DM}. Ideally, the phase tracker sets a flat phase map to 0, and then any phase pattern imparted relative to the flat phase map should match the measured FLIR phase map. For example, if the center actuator isn't displaced a global offset can be chosen to set the center FLIR phase map to 0. However, at the time of our experiments our DM PCIe (Peripheral Component Interconnect Express) card was broken and did not allow fast updating of the surface. This meant that our phase tracker tracked a DM phase such that the average bright fraction was 50% given the applied pattern. For an $m > 0$ pattern this doesn't affect the tracked phase, but for an $m = 0$ pattern this will shift the tracked center phase. For this reason, in most analyses ϕ_{DM} was freely varied to optimize the agreement with the measured pattern to find what the tracked phase was. Additionally, for $m > 0$ patterns ϕ_{DM} sets the rotation of the pattern, which is well controlled by synchronizing the DM beatnote to the rotating wall. However, the arbitrary, but repeatable, rotation of the pattern for $m > 0$ patterns was not carefully set and instead was fit to via a combination of varying ϕ_{DM} and rotating the predicted bright fraction map.

To implement the integration the phase and amplitude maps at each time step were calculated by rotating the image by the given angle $-\omega_r t$. The Scipy Ndimage Python library implements this rotation by interpolating the image to calculate an arbitrary rotation of the image. This interpolation fails if the phase map has phase wraps due to phases near or larger than $\pm\pi/2$. Therefore a further unwrapping of the phase is necessary using the skimage.restoration library unwrap_phase function. Critical to these rotations is what the center of the rotation is. Ideally this center is chosen by using a reference phase map taken during the day with a feature that clearly identifies the center such as a displacement of the center actuator. The center is then assumed to well match the ion crystal using the centering procedure described in section 6.3.1. However, in post processing of the analysis it appears some features are quite sensitive to the exact centering and there is some evidence of ∼5 μm errors in the centering. For some analysis the center pixel is therefore varied to better match the measured pattern. To do this the phase and amplitude map arrays can be shifted over, leaving empty data at edges of the array that only affect the rotational averaging at radii larger than the crystal radius of all experiments.

6.5 DM demonstration

6.5.1 Imprinting flat wavefronts

To analyze the potential fidelity of the patterns imprinted from the DM, a uniform global rotation of all spins was imprinted for varying arm times as shown in figure 6.9(a). To do this $\phi_{DM} = -\pi/2, \phi_{mw} = \pi/2$ was set such that all spins started at 50% bright and at an arm time of 12.05 μs all spins were rotated dark, corresponding to a global $-\pi/2$ rotation. Bright fraction estimates from side-view PMT counts suggest an infidelity of $\sim 0.2\%$ for a global $-\pi/2$ rotation. Image analysis from 135 shots of a 136 ion crystal at the $\pi/2$ time produced the histogram of figure 6.9(d). Of the 18360 ion detection events, 42 had either 1 or less count different between the two detection events ($\sim .2\%$), and 152 were brighter in the second detection corresponding to a $\sim 0.8\%$ bright fraction. At longer times non-uniformity of the applied rotations becomes more sensitive, corresponding to a decrease in the contrast of the oscillation in figure 6.9(a). For example, the bright fraction of a $-5\pi/2$ pulse corresponding to the blue star in figure 6.9(a) is 6.7%, as measured with separate experiments involving only side-view PMT counts and using analyzed bottom view images.

Plotted in figure 6.9(b) are the bright fractions of each ion as a function of radius to show the radial non-uniformity of the applied ACSS at longer times, with the three curves corresponding to the three points highlighted in figure 6.9(a). From the bright fraction the total rotation of each ion can be extrapolated, except that the sinusoidal bright fraction is not completely invertible. Checking the accumulated phase at the green triangle point, along with smaller arm times not shown, allows the total rotation to be unambiguously inverted, with the radial dependence of the global rotation overlapping for all arm times when rescaled by the arm time. Figure 6.9(c) shows the corresponding radial dependence of the imparted rotation shown by the black curve, produced by calculating the total rotation for each ion in the green curve of figure 6.9(b) divided by the maximum rotation.

From FLIR images the calculated ACSS pattern was averaged over azimuthally and rescaled by the maximum effective ACSS shown in the blue curve. The strength of the ACSS should fall off radially from the gaussian beams having a finite waist, and from power being removed from rotation sidebands due to non-ideal azimuthal patterns in the phase and amplitude maps. The overall decrease in strength radially is overestimated by the FLIR images by roughly a factor of 2. Ignoring any amplitude non-uniformity the calculated effective ACSS azimuthally averaged is given by the red curve of figure 6.9(c). Phase non-uniformity alone underestimates the radial decrease of the ACSS pattern. In addition to the overall decrease in intensity radially, there are oscillations at shorter wavelength that are periodic on similar length scales to the DM pixelation, possibly originating from short wavelength rms fluctuations of the DM surface that cannot be compensated because of the finite actuator number. These oscillations can partially be captured by FLIR images, but small adjustments in the centering of the image can dramatically change the locations of the oscillations.

The inability of the FLIR images to completely capture these dynamics suggests there is a mismatch between the pattern at the ions and the pattern measured on the FLIR camera. Possible explanations are path length differences, aberrations differences from the 10 cm lens, centering differences, and the presence of an ND filter before the FLIR camera. Regardless, the FLIR images can still capture much of the dynamics at short times or at lower fidelities for longer arm times.

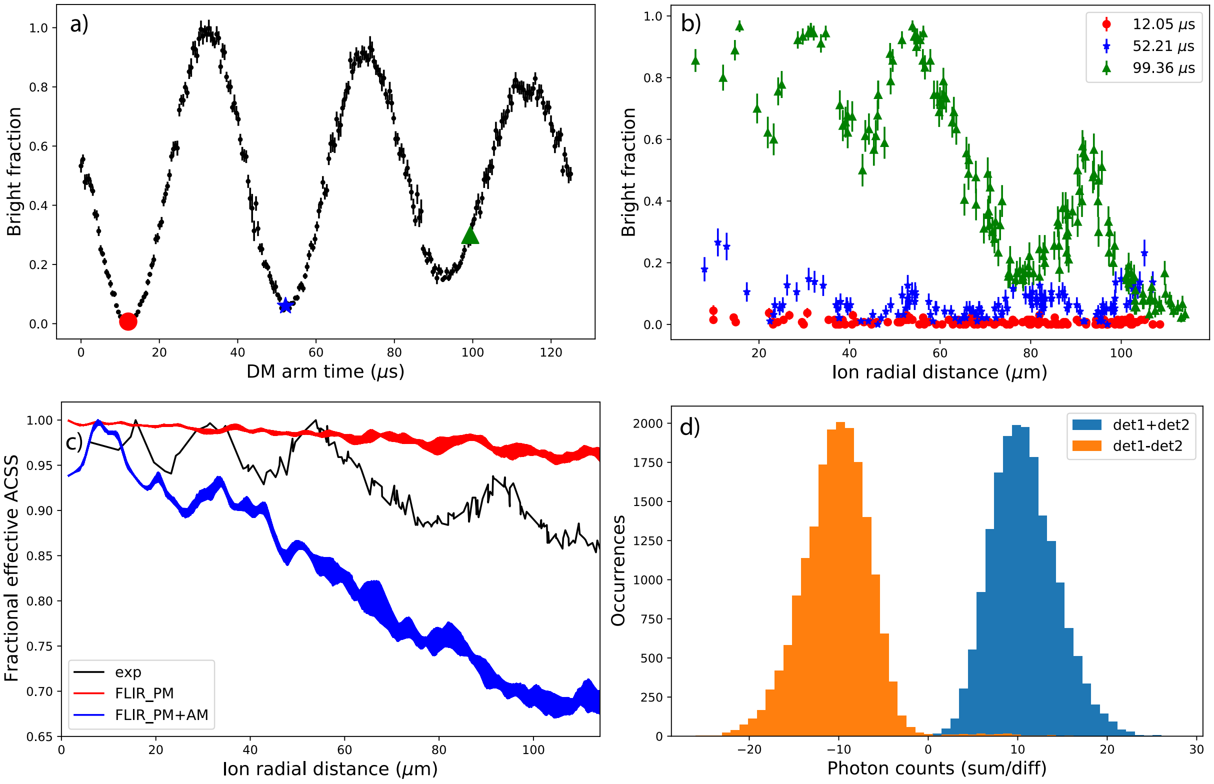

Figure 6.9: Imprinting flat wavefronts analysis. a) Oscillations in the bright fraction as a global rotation is imparted for longer arm times. Measurements are taken with side-view PMT counts with short ~ 0.5 ms detection times with only the parallel beam. Rotations of $-\pi/2, -5\pi/2$ are highlighted by the red circle and blue star with corresponding bright fractions of 0.2% and 6.7% respectively. b) Experiments repeated at the red, blue, and green highlighted points in (a) with bottom view detections. Plotted is the bright fraction of each ion as a function of radius. Error bars are given by the standard error of the mean $\sqrt{p(1-p)/N}$, where p is the measured bright fraction and N is the number of images.[6] Red circles show the high fidelity $-\pi/2$ rotation, while the radial dependence of the pattern becomes clearer in the infidelity in the blue stars. The green triangles further separate the ion's bright fraction by sitting near a first order sensitive point of the bright fraction and at a long arm time of 99.36 μs. c) Calculated effective ACSS radial dependence from the green triangle points of (b) given by the black curve. In blue (red) FLIR images are used with (without) the extracted amplitude map to calculate a predicted ACSS radial dependence. d) Histograms produced from bottom view images taken at the red circle point of (b) showing 0.8% bright fraction with very few bright events.

---

[6] Technically a better estimate should account for trials that are 100% bright or dark, but better estimates will be similar or smaller than the size of the point on the plot so are negligible.

6.5.2 Imprinting rings

As described in subsection 6.4.4, a ring of ions can ideally be flipped by displacing a ring of actuators 313/4 nm, while setting $\phi_{DM} = -\pi/2, \phi_{mw} = \pi/2$, $4U\tau = \pi/2$. Because of limited actuator numbers, a pixelated circle was used with an actuator being included in a given radius ring if its radius from the center DM actor in pixels rounded to the set radius. This pixelation reduces the effective displacement when averaged azimuthally, with the effect worsening for larger radii giving a smaller effective phase shift at larger rings. An example measured phase pattern from FLIR images is shown in 6.10(c). Additionally, since an $m = 0$ deformation is applied the DM phase tracker no longer tracked the ideal center DM phase for flat wavefronts. Instead, the tracked phase is shifted off by a larger amount when tracking larger radii rings that flip more spins. This can be simply fixed by running the DM phase tracker with flat wavefront, but at the time the DM data was taken the PCI card that takes TTL inputs to trigger an update to the surface was broken. Figure 6.10(a) shows experimental images of imprinted ring patterns for radius 0 through 3, with 0 corresponding to displacing the central actuator $\sim$ 78 nm. Plotted in figure 6.10(b) is the radial dependence of the bright fraction for the 4 ring patterns. Plotted in dashed lines are estimates of the bright fraction calculated using FLIR phase and amplitude maps while allowing the ACSS amplitude, DM phase, and imaging magnification to vary to match the measured pattern. Solid lines are calculated patterns only varying ϕ_{DM} and adjusting the center pixel $\sim 5\ \mu$m with a constant uniform ACSS amplitude and magnification. Disagreements between the measured pattern and the calculated pattern are order 1-4% averaged over all ions. Fits to ϕ_{DM} from the fixed amplitude simulations suggest phase errors of ϕ_{DM} of 14, 21, and 35 degrees for the rings 1-3, with the ring 0 consistent with the set ϕ_{DM}. The decrease in bright fraction for larger radii ring patterns can largely be attributed to a roughly equal contribution of the phase tracker not being at the ideal phase and the reduced azimuthally averaged phase at larger radii due to pixelation of the ring pattern.

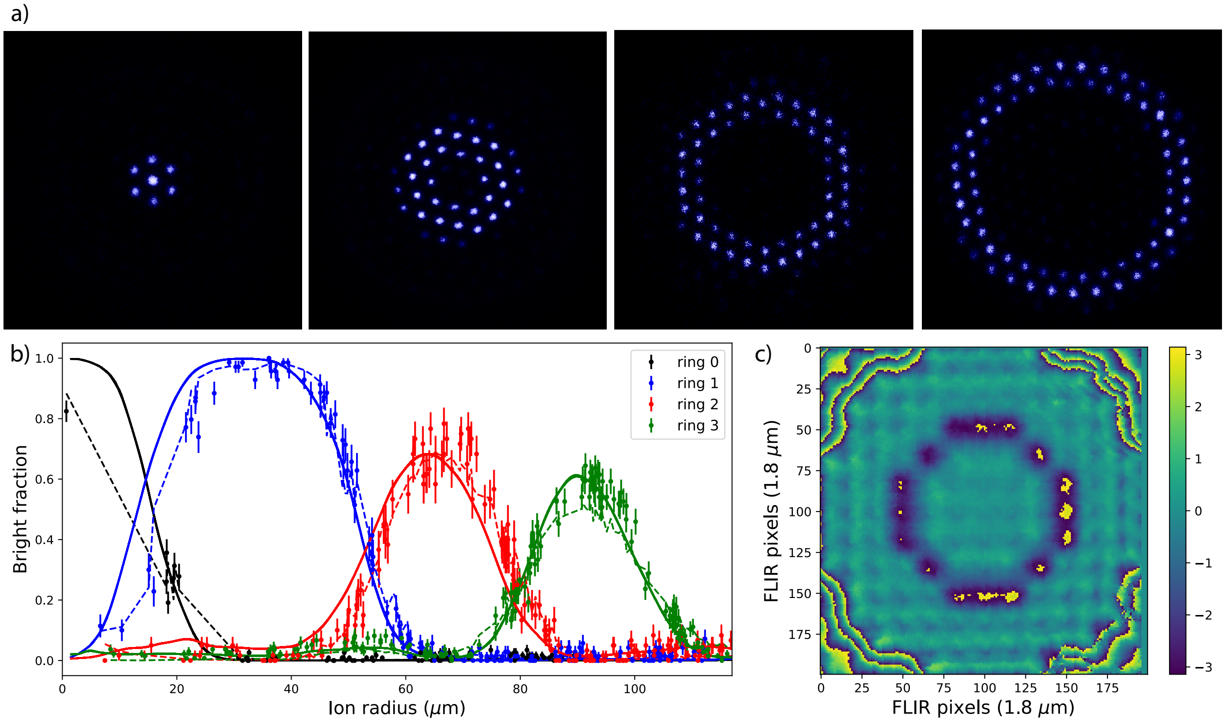

Figure 6.10: Imprinted ring patterns. a) Images of imprinted patterns onto the crystal from left to right corresponding to actuators with radius rounded to 0,1,2, and 3 pixels displaced $\sim$ 78 nm. b) Plotted measured bright fraction of each ion as a function of ion radius for each ring pattern. Black, blue, red, and green traces correspond to rings of radius 0,1,2,3 respectively. Plotted dashed lines in the corresponding ring pattern color show simulated bright fractions using the FLIR images and allowing free adjustment of the DM phase, amplitude scale, and imaging magnification. Solid lines are optimized patterns only using the FLIR phase map and adjusting ϕ_{DM} and the image center $\sim$5 μm off center. Average disagreement between the pattern and fitted pattern is order 1-4%. c) Example measured ring 3 phase pattern with the color scale in radians the fitted phase of the wavefronts. The ring of actuators is displaced 78 nm corresponding to $-\pi$ for the fitted phase. Pixelation of the DM surface reduces the effective phase when azimuthally averaged over.

6.5.3 Imprinting radial gradients

Radial gradients linear in ρ have utility as a temperature diagnostic of the in-plane motional modes in the rotating frame, see chapter 7 for details. This is due to steep gradients that are static in both the lab and rotating frame by nature of being an $m = 0$ pattern. To characterize the sensitivity of the DM to in-plane temperatures the shortest wavelength linear gradient is desired with a calibration of the wavelength of the radial gradient critical. Figure 6.11 shows an example calibration of a short wavelength radial gradient set by displacing each DM actuator 156 nm times the radius of the actuator in pixels (not rounded). To keep the pattern from applying a larger displacement than the range of an actuator, the surface was shifted by the average displacement such that the displacement was opposite sign for the center actuator compared to the furthest out radius pixels. This gives a 2π phase wrap every 30 μm, equivalent to a Hamiltonian $\hat{H}/\hbar = U\cos(k_r\rho + \phi_{DM})$, where $k_r = \frac{2\pi}{30\mu\text{m}}$.

Shown in black in figure 6.11 is the measured bright fraction of each ion versus the radial position, with the imprinted pattern using the same pulse sequence settings as the ring and flat wavefront patterns. Shown in blue is a best fit of the predicted pattern using the measured phase map from the FLIR images and only varying ϕ_{DM}. Plotted in orange is the optimal predicted pattern varying only the center pixel location with the optimized ϕ_{DM}, with the optimal center ~7.5 μm off center. All calculated patterns used a fixed magnification and uniform ACSS $4U\tau = \pi/2$. The resulting predicted and measured pattern deviate by an average of 8%. For longer wavelength radial gradients the sensitivity of the imprinted pattern to centering errors reduces substantially (see section 7.7.2). The reduced amplitude of the oscillation from being off center is expected as power is removed from the $m = 0$ tone to sidebands at multiples of the rotation frequency (see section 7.7.2). Reduction in the amplitude of the oscillation corresponds to reduced effective ACSS strength and therefore reduced temperature sensitivity. Using this measurement conversely can be used to help improve the centering of the pattern by setting as steep a radial gradient as achievable and maximizing the contrast of the oscillations.

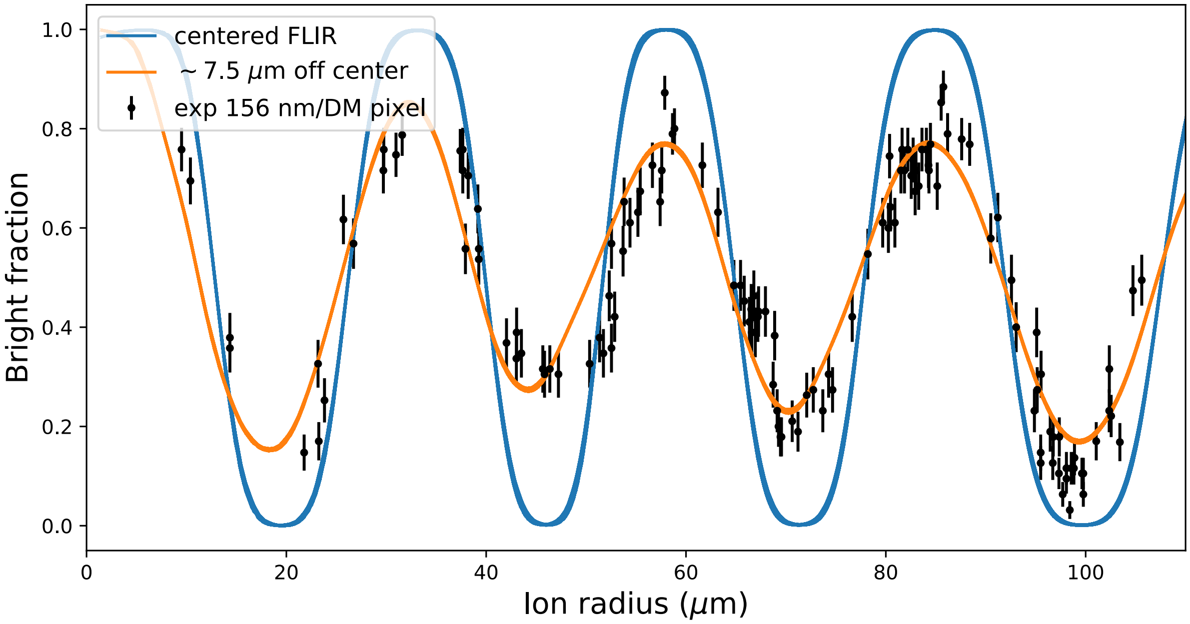

Figure 6.11: Imprinted radial gradient pattern. Plotted in black is the measured bright fraction of each ion as a function of radius using the imparted 156 nm/DM pixel radial gradient. Plotted in blue is the predicted ideal pattern fitted to match the effective ϕ_{DM} tracked by the phase tracker. The agreement improves substantially in the orange curve allowing the centering to be adjusted $\sim$ 7.5 μm off center, giving an $\sim$ 8% average bright fraction discrepancy.

6.5.4 Imprinting Zernike polynomials

A number of $m \neq 0$ patterns were implemented and analyzed using the same imprinting scheme as before, now with the DM beatnote frequency set to $m\omega_r$. Most patterns investigated were Zernike polynomials Z_n^m of azimuthal order m and radial degree n. The corresponding pattern set on the DM is then given by:

$$Z_n^m = R_n^m(\rho)\cos(m\phi) \tag{6.14}$$

$$Z_n^{-m} = R_n^m(\rho)\sin(m\phi) \tag{6.15}$$

$$R_n^m = \sum_{k=0}^{\frac{n-m}{2}} (-1)^k \binom{n-k}{k} \binom{n-2k}{\frac{n-m}{2}-k} \rho^{n-2k}, \tag{6.16}$$

where ρ, ϕ are polar coordinates of the DM actuators, with ρ scaled such that the furthest radial actuator has a radius $\rho = 1$, and n, m are non-negative. $\binom{n}{k}$ represents the Binomial coefficient n choose k, the number of ways to choose an unordered subset of k elements from a set of n elements. The set displacement of each piston actuator is then scaled by an amplitude A in nm multiplied by the Zernike polynomial Z_n^m evaluated at the ρ, ϕ coordinate of the actuator.

To more clearly see spin precession closer to the center of the DM, larger amplitudes A, higher radial order n, and longer arm times were used. Shown in figure 6.12(a,b) are two ion images from imprinted Z_4^2, Z_5^3 Zernike patterns set to 156 nm amplitudes and imprinted for 50, 25 μs respectively. For these patterns equation 6.3 can be used to estimate the imparted $\hat{\sigma}_z^i$ rotation angle θ_i for each ion located at position ρ_i, ϕ_i:

$$\theta_i \approx 4U\tau J_1(2\pi R_n^m(\rho_i/\rho_{max}))\cos(m\phi_i), \tag{6.17}$$

where 2π corresponds to the 156 nm amplitude scaling and $\rho_{max} \sim 192$ μm is the scaled maximum radius of a DM actuator in ion radial coordinates. For small arguments $J_1(x) \approx x/2$, with $J_1(0.586\pi) \sim 0.58$ the maximum of J_1. Therefore if an azimuthal ring $A\cos(m\phi)$ has amplitude displacements A larger than ~ 46 nm the effective precession rate decreases and the polynomial no longer monotonically increases. Additionally, the maximum precession rate is decreased by the maximum $J_1(0.586\pi) = 0.58$, so the corresponding arm time to impart the same rotation must be increased 1.72 times. For the Z_4^2 pattern the maximum Bessel function argument is crossed at an ion radius of ~ 65 μm, which with a 50 μs arm time gives a rotation of $\sim 1.4\pi$. Tracing the bright fraction from the center outward radially results in ions oscillating from fully bright to mostly dark again, and fully dark to mostly bright again at the dimple points in the pattern. Ions at larger radii than this decrease the accumulated rotation due to the argument of the J_1 Bessel function being larger than 0.586π. For the Z_5^3 pattern the maximum Bessel function argument is crossed at a radius of ~ 90 μm, which accumulates a total phase of $\sim 0.67\pi$ resulting in slight over-rotation from fully bright/dark.

Figures 6.12(c,d) show the measured bright fraction of each ion. At the time the double detection scheme was not implemented. Instead only one detection image was taken for 50 ms each shot of the experiment, with ions sorted as bright or dark based on thresholding from the total cumulative histogram of all ions from all images. Comparisons are made to theory by finding a minimum error using FLIR phase and amplitude maps and allowing ϕ_{DM}, the ACSS scaling, and the magnification to freely vary. Figures 6.12(e,f) show the predicted pattern showing good agreement with the measured pattern. Average disagreement between the measured and predicted pattern is $\sim 4\%$ and $\sim 8\%$ for the Z_5^3, Z_4^2 patterns respectively.

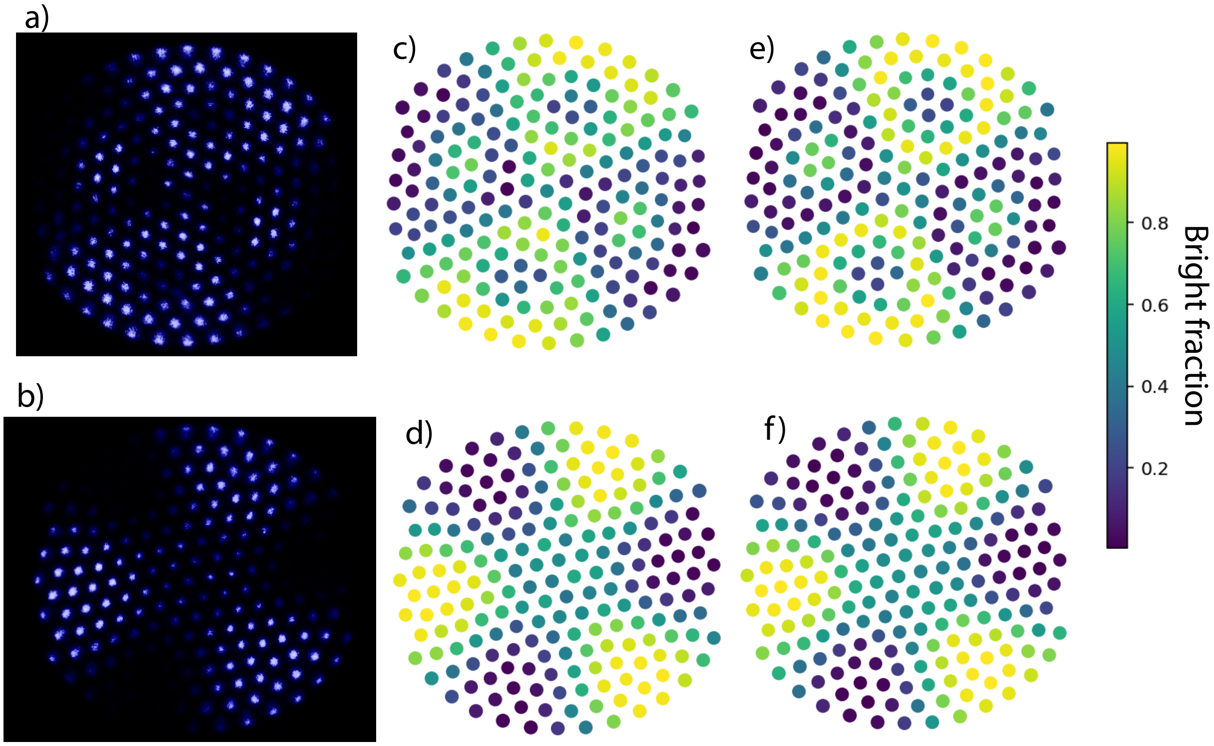

Figure 6.12: Imprinted Zernike patterns. a-b) Experimental images of imprinted Z_4^2 (a) and Z_5^3 (b) patterns with the actuator displacements scaled as described in the text by 156 nm and for arm times of 50, 25 μs respectively. c-d) Measured bright fraction of each ion as calculated by thresholding the cumulative histogram of all ions in all 130 (c) and 180 (d) images. e-f) Optimally calculated pattern to match the corresponding measured pattern in (c-d). Average disagreement between the predicted and measured patterns are $\sim 8\%$ (e), 4% (f).

6.5.5 Spelling NIST and CU

As a final fun exercise and demonstration of implementing multiple azimuthal orders, we attempted to spell the letters for NIST and CU shown in figure 6.13. For the "n", "C", and "S" in particular, this requires at least two azimuthal order patterns. At the time, our deformable mirror control PCI card was broken and not able to accept TTL inputs for rapid updates of the surface. For this reason we were further constrained to attempt to set the multiple order patterns on a single surface. To start, to make an "I" you ideally would have a string of ions vertically, which corresponds to an extremely high azimuthal order and so would be difficult to decompose into a few low order azimuthal orders. If the "I" is allowed to have some azimuthal spread, much lower orders are possible. However, in general getting the center ion bright requires an m=0 pattern as it is not possible to apply a non-zero $m > 0$ deformation on just the central actuator, leading to the central ion always having no spin precession for $m > 0$. As a trick, this ion is instead mapped to bright with no spin precession with $\phi_{mw} = \pi$, thus ideally making a bright line of ions along the null of any applied $m > 0$ pattern. Therefore, the chosen displacement was $A\cos(\phi)$, with no radial dependence and amplitude $A \sim 46$ nm such that the maximum of the J_1 Bessel function was selected. The arm time was set to 3.44 times the ideal $\pi/4$ arm time to impart a π rotation for ions at ϕ_i 90 degrees from the null lines. Using the same idea, the null lines of an $m = 2$ pattern were mapped to the bright lines of an "X" and "t" (more accurately "+"), setting a displacement $A\cos(2\phi)$ with the same A and arm time, and rotating the image, or equivalently adjusting ϕ_{DM}.

To make the letters "s" and "c/u/n" (from here out referred to as "c"), two azimuthal orders were required. The "s" was decomposed into 2 azimuthal orders $m = 0, 2$. The $m = 0$ component of the pattern displaced the center actuator 78 nm to map the central ions to bright with most ions dark using a $\pi/4$ arm time and $\phi_{DM} = -\pi/2$. The $m = 2$ pattern applied was an $m = 2$ ring of radius 2, and an $m = 2$ ring of radius 1 phase shifted 45 degrees. An azimuthal ring is given by $A\delta_{r,r_0}\cos(m\phi)$, where an actuator is displaced only if the pixel radius rounds to the set ring radius r_0. The sign of the 45 degree shift determined whether a "z/2" or an "s" were made. The amplitude of the $m = 2$ rings was set to ~ 46 nm such that with the arm time inflated by 1.72 times the $\pi/4$ arm time, ideally the maximum and minimum of the rings were mapped to bright and dark. This relied on the imparted $m = 0$ pattern keeping the ions in the ring nearly 50% bright from the J_0 component of the $m = 2$ rings while all other ions were mapped dark except the central ring 0 ions which were mapped bright.

The "c" was decomposed into 3 orders, with the idea being applying a fixed ring with a sum of $m = 0, 1, 2$ azimuthal order. An $m = 1$ pattern also impacts the imprinted $m = 0, 2$ order patterns, so a single $m = 1$ azimuthal ring was set of amplitude ~ 78 nm, and pixel radius 2. First an $m = 0$ pattern was imparted for the $\pi/4$ arm time to make all ions dark except the ring of ions at DM radius 2. The ring of ions is then about 50% bright based on J_0 of the set azimuthal ring. Subsequently, the $m = 1$ pattern was applied for twice the $\pi/4$ arm time to mostly made a "c". This arm time was set to accommodate the reduced J_1 Bessel function strength from setting a displacement larger than the maximum argument of J_1. Ideally, the imparted gradient along the ring would rotate ions nearly fully bright and fully dark at the two ends of the "c". The top and bottom edges of the "c" would not be fully bright, which is why an extra $m = 2$ pattern was applied. This was applied for half the $\pi/4$ time, with the idea to compensate further canceling the pattern at the dark spot of the "c" and adding at the orthogonal slightly darker portion of the "c".

6.6 Conclusion and future outlook

We have demonstrated a novel patterned addressing technique in the rotating frame of a 2D ion crystal using a deformable mirror. In characterizing the performance of the system we've also demonstrated single shot individual ion readout in our system for the first time, competitive or potentially even higher fidelity than other Penning trap individual ion state detection fidelities [70, 71] despite substantially degraded quantum efficiency. Fidelities of the imprinted patterns can be better than 95%, limited by the number of actuators giving a finite resolution of pattern adjustment, competitive with the only other individual ion addressing demonstrated in a Penning trap [71], but demonstrated globally on large crystals of more than 100 ions. Additionally, amplitude

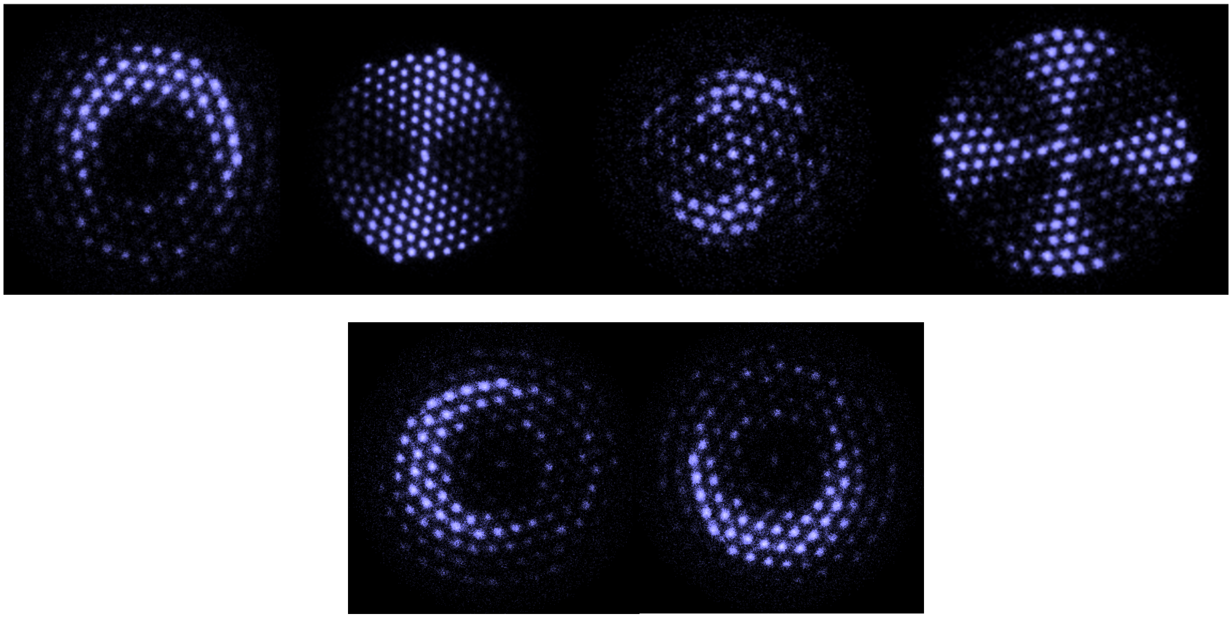

Figure 6.13: Imprinted patterns spelling NIST and CU. Note the "n","c" and "u" are rotated copies of the same image.

non-uniformity and phase non-uniformity of the beams reduce the fidelity but can in principle be compensated using a DM with more actuators. Improvements in the centering of the beams and retaking data with the fixed TTL trigger can allow analysis with less or even no free parameters. Immediate patterns that can be produced that may be of interest are radial domain walls, linear gradients, and radial gradients useful for in-plane temperature measurements of modes in the rotating frame of the crystal. Immediate extensions could produce chiral spin textures (see 8.3 for details), while more complicated patterns may require a finer resolution deformable mirror to achieve individual addressing. Recent demonstrations with piston actuated micro mirrors without a continuous membrane have demonstrated actuator arrays of 256 by 256 geared towards UV applications in neutral atom arrays with kHz update rates [72].

Chapter 7

In-Plane Motion Thermometry and Cooling

This chapter discusses theoretical modeling, simulations, and experimental efforts geared towards direct temperature diagnostics of the in-plane motion of 2D ion crystals in Penning traps. Additionally, a newly implemented cooling technique to couple the cyclotron and magnetron modes together to allow efficient magnetron cooling is theoretically modeled and experimentally diagnosed. Using these techniques, substantially reduced magnetron temperatures have been achieved and directly measured.

7.1 Motivation and introduction

Penning trap motion in the plane normal to the magnetic field (in-plane motion) is inherently difficult to cool. Due to the velocity-dependent force from the magnetic field, in-plane modes no longer act as simple harmonic oscillators, and instead branch into high frequency cyclotron motion, and low frequency magnetron motion. Magnetron modes are dominated by potential energy and are negative energy modes in the lab frame, requiring energy to be added to the mode to "cool" them, making standard Doppler cooling ineffective. In the NIST Penning trap experiments with 2D crystals of hundreds of ions, we previously had indirect experimental evidence and theoretical modeling predicting our cooling setup to be inefficient for these magnetron modes. Theoretical modeling from molecular dynamics simulations [37] suggested temperatures on the order of 10 mK, as compared to the Doppler cooling limit of 0.43 mK. Indirect experimental evidence comes from broadening of the axial drumhead mode frequencies, which theoretical modeling [31] suggests can be accounted for due to inflated in-plane temperatures of ~ 10 mK, making all but the highest frequency drumhead modes unresolvable. This section discusses schemes to directly measure the in-plane mode temperatures, along with simulations modeling experimental measurements for various temperatures and configurations. Experimental results of implementing these measurement schemes are then shown, along with a new in-plane cooling technique that has allowed for much colder magnetron temperatures.

The idea behind these experimental protocols is to create AC stark shifts (ACSS) dependent on the in-plane coordinates of the ions (x, y or ρ, ϕ). Ion motion will then cause the ACSS of the ion to modulate over time, causing spin precession (dephasing generally without stabilized phase and coherent motion) proportional to the size of in-plane motion. The strength of this signal is roughly characterized by the strength of ACSS gradient the ion sees in comparison to its in-plane motion. However, because the ions are located at various in-plane equilibrium positions, ACSS gradients generally cause much larger spin precession due to the equilibrium position's ACSS than the motion relative to these equilibrium positions. The solutions are to either spin echo the signal to cancel equilibrium position ACSS precession, or else to modulate the signal in some other way to cancel this background.

7.2 Radial gradient analytic expressions

One of the simplest mathematical description of a potential setup is to create an in-plane radial ACSS gradient, which will then be static in the lab and rotating frame due to the absence of azimuthal dependence. This pattern can be generated by interfering a beam that has undergone wavefront deformations from a deformable mirror (DM) with a beam that has flat wavefronts. To simplify the interactions it is often useful to operate in the regime where the wavelength of the spatial interference is large compared to an ion's motion about its equilibrium, often called the Lamb-Dicke regime, analogously to the ODF for sensing axial motion. This criteria is given by $\epsilon_i = k_r \tilde{\rho}_i(t) << 1$, where k_r characterize the effective wavelength or strength of the radial gradient $k_r = 2\pi/\lambda_r$, and $\tilde{\rho}_i(t)$ is the radial displacement over time of an ion from its equilibrium position.

We can then approximate our Hamiltonian as follows:

$$
\begin{aligned}
H_{DM}/\hbar &= \sum_i U \sin(k_r \rho_i(t) + \mu t)\hat{\sigma}_z^i && (7.1)\\
&= \sum_i U \sin(k_r(r_i + \tilde{\rho}_i(t)) + \mu t)\hat{\sigma}_z^i && (7.2)\\
&= \sum_i U \sin(k_r r_i + \epsilon_i(t) + \mu t)\hat{\sigma}_z^i && (7.3)\\
&= \sum_i U\hat{\sigma}_z^i[\sin(k_r r_i + \mu t) + \epsilon_i \frac{\partial}{\partial \epsilon_i}\bigg|_{\epsilon_i=0} \sin(k_r r_i + \epsilon_i(t) + \mu t) + O(\epsilon_i^2)] && (7.4)\\
&\approx \sum_i U\hat{\sigma}_z^i[\sin(k_r r_i + \mu t) + \epsilon_i(t)\cos(k_r r_i + \mu t)], && (7.5)
\end{aligned}
$$

where μ is the difference frequency of the DM beams, r_i is the equilibrium radius of an ion i, and $\epsilon_i(t)$ is the time dependent radial displacement of an ion from its equilibrium position times k_r. Additionally, U represents an ACSS in units of radians/second, with $\hat{\sigma}_z^i$ the Pauli z operator, meaning U is half the maximum differential ACSS. Looking at a single in-plane mode m (see fig 2.5), we can approximate $\epsilon_{i,m}$ for ions off center as:

$$
\begin{aligned}
\epsilon_{i,m}(t) &= k_r \tilde{\rho}_{i,m}(t) && (7.6)\\
&\approx k_r \kappa_{i,m} \frac{\sqrt{2}\tilde{\rho}_m}{\sqrt{N}} \cos(\omega_m t + \phi_{i,m}) && (7.7)\\
\tilde{\rho}_m &= \tilde{\rho}_{0,m}\sqrt{2\bar{n}+1} = \sqrt{\frac{\hbar(2\bar{n}+1)}{(1+R_m)m\omega_m}} && (7.8)\\
\kappa_{i,m} &\approx \frac{\sqrt{N}|\vec{\rho}_{0,i} \cdot \vec{u}_{i,m}|}{|\vec{\rho}_{0,i}||\vec{u}_m|}. && (7.9)
\end{aligned}
$$

See appendix A for a detailed derivation of these formulas. Equation 7.7 takes the total rms motion $\tilde{\rho}_m$ of all ions in mode m and gives the single ion component of the motion along the radial direction using the factor $\kappa_{i,m}$. Note the factor of $\sqrt{2}$ is a conversion from rms motion ($\tilde{\rho}_m$) to the amplitude of the displacement ($\tilde{\rho}_{i,m}(t)$). All motion from here out can be assumed as referring to rms motion $\tilde{\rho}_m$ unless the motion is explicitly stated as an amplitude. The component of the mode's motion in the radial direction is then oscillating at the mode frequency ω_m with a phase $\phi_{i,m}$ that can be different for each ion i (see appendix A for details). The redundant use of $\sqrt{N}$, where N is the ion number, is to normalize the mode participations to order 1 such that they are crystal size independent. The total rms motion $\tilde{\rho}_m$ is then given by R_m the ratio of potential and kinetic energy for mode m, $\bar{n} \approx k_B T/\hbar\omega_m$ the average occupation of mode at a given temperature T where k_B is Boltzmann's constant,[1] and m the mass of $^9\text{Be}^+$. R_m is usually 1 for a harmonic oscillator but is order $1/500$ for cyclotron modes, 500 for magnetron modes in our current configuration, see figure 2.6. Finally, equation 7.9 describes an approximate form of the radial component of the mode participation of an ion i using the eigenvector for the mode m, $\vec{u}_{i,m}$, and the equilibrium radial position $\vec{\rho}_{0,i}$ to define the orientation of the radial gradient.

Equation 7.5 has an equilibrium ACSS term that ideally will be canceled, plus a motional term analogous to the axial ODF case with a few notable differences. First there are relative phase factors across the crystal, both radially and azimuthally from the $k_r r_i$ and $\phi_{i,m}$ phase factors respectively. Luckily, these can be ignored by averaging over the phase, which is already done for a thermal state, and is valid if sensing coherent states with a randomization of the phase of the DM or the coherent state's motional phase. Second, there are mode participation factors κ, which are uniformly equal to 1 for all ions for the axial COM mode. Sensing axial modes besides the COM will also have non-uniform mode participation factors but they are more simply given by the eigenvalues of the mode since all motion is in the z direction, the direction of the ACSS gradient, for axial motion. For the ions excluding the central ion this is approximated by equation 7.9, where $\vec{u}_m$ is the eigenvector for that mode, $\vec{u}_{i,m}$ are the eigenvector components for ion i, and $\vec{\rho}_{0,i}$ is the equilibrium position for ion i which gives the radial direction. For ions near the center this approximation gets worse, but is reasonable. If there is an ion on center, however, everything changes because the coordinate ρ is positive definite leading to radial time dependence at only even multiples of the mode frequency (see appendix A for details). For example, if perfectly on center and perfectly circular motion the radial

---

[1] Note for a thermal state of average mode occupation $\bar{n}$ the temperature is defined $\frac{1}{\bar{n}} = e^{\hbar\omega_m/k_B T} - 1$, which agrees with $\bar{n} = k_B T/\hbar\omega_m$ for large temperatures but disagrees when near or below the ground state $\bar{n} \lesssim 1$.

displacement is time independent. If perfectly on center and with an elliptical orbit the frequency of oscillation in ρ is dominantly $2\omega_m$ periodic for small ellipticity, with higher order even multiples of the mode frequency that are negligible until the motion is more elliptical. Therefore to mostly strongly induce dephasing on the central ion the beatnote should be at 2 times the mode frequency. For this reason the mode participation of the central ion from here out is modeled as 0 when <1 μm off center radially. This approximation will give at worst $\sim \frac{1}{N}$ error when sensing at even multiples of the motional frequency, but is largely suppressed much more than this due to most motion of the central ion having small ellipticity.

Usually the equilibrium term is fast oscillating when sensing axial motion with the ODF and can be ignored. Similarly, it can be ignored if sensing cyclotron motion. However, if sensing magnetron motion the mode frequencies are quite small, making the fast oscillating approximation $(U/\mu \ll 1)$ poor. To cancel this term, the arm time can be set $\mu\tau = 2\pi l$ for an integer l to oscillate the ACSS through a full 2π period and leave no residual ACSS. Alternatively, the correct phase advance in a spin echo can cancel the precession built up in the first; see appendix A for more details.

To calculate the spin-dephasing from each mode, either see appendix A where the Hamiltonian is directly integrated assuming classical dynamics, or follow the derivation of section 4.3.5 ignoring spin-spin dynamics which will generalize to:

$$\langle \hat{\sigma}_i^z \rangle_{\alpha_0} = e^{-|\alpha_{T,i}|^2} \cos(4\,\mathrm{Im}(\alpha_{T,i}\alpha_0^*)) \tag{7.10}$$

$$|\alpha_0| = \frac{\tilde{\rho}_m}{\sqrt{2}\tilde{\rho}_{0,m}} \tag{7.11}$$

$$\alpha_{T,i} = -i\frac{U k_r \tilde{\rho}_{0,m}}{2\delta\sqrt{N}} \kappa_{i,m} e^{i(kr_i - \phi_{i,m})}(1 - e^{i\theta_1})(1 - e^{i\theta_2}), \tag{7.12}$$

with $\theta_1 = \delta\tau, \theta_2 = \delta(\tau + t_\pi) + \phi_{adv}$ as described in section 4.3.5, and $\tilde{\rho}_{0,m}$ is the rms ground state wavefunction size for mode m (see equation 7.8). Equation 7.10 gives a negligible spin dephasing term $(e^{-|\alpha_{T,i}|^2})$[2] and an effective spin rotation for an initial coherent state α_0.

To maximize sensitivity we would like to make k_r as short wavelength as possible. For our

---

[2] Negligible until sensitive to motion the size of the ground state wavefunction.

current deformable mirror, the maximum displacement of a single actuator is $\sim 1.5\ \mu$m, with adjacent actuators 30 μm apart after the 10x magnification at the ions. This gives a minimum wavelength of $\lambda > 3\ \mu$m for $k_r = 2\pi/\lambda$. The ground state wavefunction size for the magnetron and cyclotron COM modes are equal and representative of the planar modes in general. For a crystal at 180 kHz and 100 ions, the per ion rms displacement is ~ 1.2 nm, compared to ~ 1.8 nm for the axial COM motion. Assuming maximum sensitivity of $\lambda = 3\ \mu$m, this gives approximately 7 times less effective α_T sensitivity compared to sensing axial COM motion with the same ACSS, accounting for κ of the in-plane COM modes. Experimentally it has only been possible to get a factor $\sim 3-6$ smaller k_r than this. In principle, since the ODF can measure the ground state wavefunction in a few hundred μs, applying the DM for a few ms could produce the same size dephasing when measuring displacements near the ground state. However, background spin dephasing from spontaneous emission will commensurately be larger by the same factor the time is increased if operated with the same ratio of ACSS to spontaneous emission. In general the background dephasing will be worse however if operated closer to resonance or without nulling the ACSS of each beam.

From equation 7.10, bright fractions can be calculated for sensing thermal and random phase coherent states. This requires averaging dephasing over each ion i like so:

$$\langle P_{\uparrow,i}\rangle_{coh} \approx \frac{1}{2}(1 - e^{-2\Gamma\tau}\sum_i \frac{1}{N} J_0(4|\alpha_{T,i}||\alpha_0|)) \tag{7.13}$$

$$\langle P_{\uparrow,i}\rangle_{th} \approx \frac{1}{2}(1 - e^{-2\Gamma\tau}\sum_i \frac{1}{N} e^{-4|\alpha_{T,i}|^2\bar{n}}). \tag{7.14}$$

Here $\bar{n} = |\alpha_0|^2$ is the total quanta of excitation, and dephasing from the zero point motion has been dropped. To make the form of the bright fraction clearer, ignoring the θ dependence of $\alpha_{T,i}$ by driving on resonance ($\delta = 0$) for a single arm τ gives:

$$J_0(4|\alpha_{T,i}||\alpha_0|) = J_0\left(\sqrt{2}\frac{U\tau k_r\tilde{\rho}_n}{\sqrt{N}}\kappa_{i,n}\right) \tag{7.15}$$

$$\approx 1 - \left(\frac{U\tau k_r\tilde{\rho}_n}{\sqrt{2N}}\kappa_{i,n}\right)^2 \tag{7.16}$$

$$e^{-4|\alpha_{T,i}|^2\bar{n}} = e^{-\left(\frac{U\tau k_r\tilde{\rho}_n}{\sqrt{2N}}\kappa_{i,n}\right)^2} \tag{7.17}$$

$$\approx 1 - \left(\frac{U\tau k_r\tilde{\rho}_n}{\sqrt{2N}}\kappa_{i,n}\right)^2. \tag{7.18}$$

Therefore, the spin dephasing for thermal and coherent states gives the same result to second order. To exactly carry out the averaging over i requires averaging over each ion's $\kappa_{i,n}$. To give a reasonable estimate, the distributions of $\kappa_{i,n}$ can be sampled over to reduce the number of averages needed, with simulations suggesting reasonable agreement using 3 averages until the dephasing is nearly saturated.

7.3 Linear gradient analytic expressions

An alternative experimental setup to a radial gradient is a linear gradient. At first this was the only scheme accessible experimentally, as it can be achieved simply by tilting the wavefronts of our ODF beams. However, this gradient pattern will not be static in both the rotating frame of the ion crystal and the lab frame. We can create static patterns in the rotating frame by setting the beatnote frequency difference of the ODF beams to multiples of the rotation frequency, but this does not guarantee undesired signals at multiples of the rotation frequency will be small. Defining our Hamiltonian in the lab frame now with a linear k vector $k_\perp$ and ion coordinates in the rotating frame $\rho_i(t), \phi_i$, and ignoring ϕ_i time dependence[3] for simplicity gives the result of equation 4.5 repeated

---

[3] By time dependence of ϕ_i this means the small motion in the $\hat{\phi}$ direction in the rotating frame from the in-plane modes, which could be ignored for a radial gradient as no ACSS gradient was present in the $\hat{\phi}$ direction. Ignoring this in the linear gradient case will be particularly poor for rocking mode motion that is almost entirely azimuthal, and for ion locations with strong gradients in the $\hat{\phi}$ direction.

here:

$$H_{ODF}/\hbar = \sum_i U\cos(k_\parallel z + \mu t + \Psi + k_\perp \rho_i \sin(\phi_i - \omega_r t - \phi_0))\hat{\sigma}_z^i \tag{7.19}$$

$$\approx \sum_\pm \sum_{i=1}^{N} \sum_{n=0}^{\infty} \frac{\tilde{U}}{2^{\delta_{0,n}}} J_n(k_\perp \rho_i)(\pm 1)^n \cos(\mu t + \Psi \pm n(\phi_i - \omega_r t - \phi_0))\hat{\sigma}_z^i, \tag{7.20}$$

where as in equation 4.5 $\tilde{U}$ includes a Debye-Waller factor. This already complicated expression will now get more complicated by expanding every $J_n(k_\perp \rho_i(t)) \approx J_n(k_\perp r_i) + \epsilon_i(t)\frac{\partial J_n}{\partial x}(k_\perp r_i)$, where $\epsilon_i(t) = k_\perp \tilde{\rho}_i(t)$, $\rho_i(t) = r_i + \tilde{\rho}_i(t)$ analogous to the definition in the radial gradient case, and $\frac{\partial J_n}{\partial x}(k_\perp r_i) = \left.\frac{\partial J_n(x)}{\partial x}\right|_{x=k_\perp r_i}$ for shorthand notation. $J_n(k_\perp r_i)$ terms are offset/equilibrium position terms that are not of interest and we would like to cancel, while $\frac{\partial J_n}{\partial x}(k_\perp r_i)$ terms are proportional to the signal of interest $\epsilon_i(t)$ and we would like to maximize.

Terms contributed by the equilibrium position ($J_n(k_\perp r_i)$ terms) that ideally we would like to cancel are given by equation 7.20 with $\rho_i = r_i$. Directly integrating all of these terms give precession angles $\theta_i(t)$:

$$\theta_i(\tau)_{eq} \approx \sum_\pm \sum_n \frac{2\tilde{U}}{2^{\delta_{n,0}}} J_n(k_\perp \rho_i)(\pm 1)^n \left[\frac{\sin((\mu \mp n\omega_r)t + \Psi \pm n(\phi_i - \phi_0))}{\mu \mp n\omega_r}\right]_{t=0}^{t=\tau}. \tag{7.21}$$

The factor of $2\tilde{U}$ is due to the definition of $\tilde{U}$ being half the differential ACSS. Note when $\mu = \pm n\omega_r$ the corresponding term is static in 7.20, so the term is simply multiplied by t. Canceling all of these terms (assuming $\mu \neq n\omega_r$) is analogous to the radial gradient case with the cancellation condition modified to $(\mu \pm n\omega_r)\tau = 2\pi l_{\pm n}$ for integers $l_{n\pm}$, since every sine term evaluated at $t = 0$ is equal to $t = \tau$. This is actually not difficult to achieve, as these conditions are satisfied if $\mu\tau = 2\pi l_\mu$, and $\omega_r \tau = 2\pi l_{\omega_r}$ since $(\mu \pm n\omega_r)\tau = 2\pi(l_\mu \pm n l_{\omega_r})$. Practically this just means τ must be a multiple of around 5.5 μs ($\tau\omega_r = 2\pi$) for our current rotation frequency, and the frequencies μ that can be used are multiples of $2\pi/\tau$. Looking now at our signal terms of interest ($\frac{\partial J_n}{\partial x}(k_\perp r_i)$ terms) from expanding equation 7.20 gives:

$$H_{ODF,sig}/\hbar \approx \sum_{\pm}\sum_{i=1}^{N}\sum_{n=0}^{\infty} \frac{\epsilon_i(t)\tilde{U}}{2^{\delta_{0,n}}}\frac{\partial J_n}{\partial x}(k_\perp \rho_i)(\pm 1)^n \cos(\mu t + \Psi \pm n(\phi_i - \omega_r t - \phi_0))\hat{\sigma}_z^i. \tag{7.22}$$

Putting in a single mode approximation of $\epsilon_i(t) \approx k_\perp(r_i + \tilde{\rho}_{i,m})$ oscillating at mode frequency ω_m allows direct integration assuming no spin motion entanglement:

$$\approx \sum_{\pm_1}\sum_{\pm_2}\sum_{i=1}^{N}\sum_{n=0}^{\infty} \frac{\tilde{\rho}_{i,m}\tilde{U}}{2^{1+\delta_{0,n}}}\frac{\partial J_n}{\partial x}(k_\perp \rho_i)(\pm_1 1)^n \cos((\mu \mp_1 n\omega_r \pm_2 \omega_m)t + \Psi \pm_1 n(\phi_i - \phi_0) \pm_2 \phi_{i,m})\hat{\sigma}_z^i. \tag{7.23}$$

While complicated looking, equation 7.23 can be analogous to the radial gradient case. If $\mu = \omega_m + \delta \pm l\omega_r$ where $\delta \ll \omega_r$ effectively the expansion over n gives many Bessel function sidebands that will be fast rotating for $n \neq l$ and can be ignored. Additionally, there will be co-rotating and counter-rotating terms relative to the motion $\pm_2\omega_m$ with the counter-rotating term ignored if $\delta \ll \omega_m$. However, the critical difference between the radial and linear gradient case is that the linear gradient sensitivity is reduced for large $k_\perp r_i$, with $J_n(x) \propto \frac{1}{\sqrt{x}}\cos(x)$ for large arguments. Additionally, when the phases are averaged over, there remains ions with no sensitivity at the nulls of $\frac{\partial J_n}{\partial x}(k_\perp r_i)$. This is only approximately true as motion about $\hat{\phi}$ from time dependence of ϕ_i has not been accounted for. Regardless, simulations of the full dynamics can give complete comparisons to experiment to gauge the temperature, while exact analytical forms can gauge the expected sensitivity.

In practical terms, the ideal setup should likely utilize $\mu = \omega_m$ or $\mu = \omega_m \pm \omega_r$, as higher order Bessel functions will have less sensitivity, and ions at $k_\perp r_i \ll 1$ have little sensitivity in the $J_0(k_\perp r_i)$ case. Likely the $\mu = \omega_m \pm \omega_r$ term (J_1 case) should perform best as it is most sensitive at small $k_\perp r_i$ until $k_\perp$ has wavelength λ some amount smaller than the crystal size, at which point the lower sensitivity at small $k_\perp r_i$ for the J_0 case will be compensated by the lower sensitivity at large radii in the J_1 case.

7.4 Simulation setups

With our framework set for how we would like to measure the in-plane modes we can now simulate signals we predict to measure for in-plane mode temperature ranges we expect, and identify what range $U, k_r, k_\perp, \tau$ we must obtain to measure reasonable signals.

The first set of code written was to update the mode analysis code to generate motion of the crystal over time for a given mode m and phase ϕ_m. This is done by first solving the equilibrium positions of an ion crystal as a 2N component x, y vector $\vec{\rho}_0$ for N ions, as described in section 2.3 and following references [24, 31]. Then planar eigenvectors from that equilibrium crystal are calculated in a 2N x 2N matrix with each column a 2N component normalized x, y vector $\vec{u}_m$ for mode m. The ion's positions at time t summing over all modes each with some rms motion $\tilde{\rho}_m$ is then $u(t) = \vec{\rho}_0 + \sum_m \sqrt{2}\,\mathrm{Re}[\tilde{\rho}_m \vec{u}_m e^{i(\omega_m t + \phi_{mot,m})}]$, taking the real part of the eigenvectors oscillating at the eigenmode frequencies and with each mode m having a motional phase $\phi_{mot,m}$. To approximate a thermal state the phases $\phi_{mot,m}$ then needs to be randomized and averaged over, while the amplitude $\tilde{\rho}_m$ is calculated from the temperature, frequency, and R_m of the mode (see equation 7.8, note $\tilde{\rho}_m$ is not averaged over a thermal distribution, equivalent to a coherent state average). Using this time dependent position for an approximate thermal state the equations for a radial and linear gradient were directly integrated over time, with a time step of 1-100 ns depending on the simulation.

Alternatively, a much faster analytical calculation can be done using equation 7.14. In principle, each ion i should calculate a dephasing $e^{-4|\alpha_{T,i}|^2\bar{n}}$ for each mode, with the total spin dephasing of that ion given by the product of the dephasing from each mode. As an approximation the total dephasing over all ions can be calculated for each mode using a sampling of $\kappa_{i,n}$ and the total dephasing taken as the product of the dephasing independently for each mode. This approximation breaks down if two modes near each other in frequency cause dephasing on the same subset of ions making the dephasing averaged over all ions not independent for each mode.

7.5 Experiment ODF

To calculate the in-plane temperature, the ACSS and $k_\perp$ must be determined. To do this, the ODF beams were tilted relative to each other in the horizontal direction using 2 pairs of motorized mirrors on the optics table. The horizontal direction is much more sensitive than the vertical direction due to the shallow ±10 degree angle vertically between them at the ions. Experimentally we were limited by the widths of the mirrors to order 30 μm wavelength $k_\perp$, or equivalently $\sim \pm 0.3$ degrees. As the ODF is tilted a rough $k_\perp$ wavelength measurement can be extracted by looking at the rotation sidebands of the crystal (see section 4.3.1). This gives a rough order of magnitude estimate, but the precise crystal details make the exact ratio of sidebands hard to model out at ~10 sidebands.

A much more reliable measurement is to imprint a pattern onto the crystal in the rotating frame that depends on $k_\perp$. The corresponding pattern can then be analyzed to fit the radial dependence of the pattern to estimate the tilt of the ODF. By setting the beatnote to the rotation frequency and applying the ODF for a time τ, the imparted rotation angle for each ion is

$$\theta_i \approx 2U\tau J_1(k\rho_i)\sin(\phi_i - \phi), \tag{7.24}$$

where ϕ is the relative phase between the ODF beatnote and the crystal rotation, which are ideally the same frequency. Applying a second pulse in a spin echo sequence with a phase advance of π adds the two arms coherently. As the wavefronts of the beams wander around from air currents or mirror motion the imparted pattern then rotates around.

The ODF beatnote frequency is generated by two RF tones from DDS's which have a minimum frequency resolution, referred to as one machine unit. Because the ODF beams pass through their acousto-optic modulators (AOMs) twice, the minimum frequency resolution of the beatnote is two machine units. Therefore the rotation frequency needs to be set to an even number of machine units, otherwise the beatnote would be a single machine unit in error corresponding to a frequency difference of ~ 0.5 Hz. If the relative phase is not stable the pattern rotates randomly from shot to shot and averages over ψ, producing the pattern

$$P_{\uparrow,i} \approx \frac{1 - J_0(4U\tau J_1(k\rho_i))}{2}, \tag{7.25}$$

where the pulse sequence is as given in figure 7.1. We can then straightforwardly plot the radial dependence of the bright fraction to estimate the ACSS and k vector wavelength using an estimated magnification of the camera imaging to get the wavelength at the ions. An example of this measurement scheme, with and without the phase stabilized is shown in fig 7.1. We consistently find that the wavelength of the J_0 oscillation seems to be shorter wavelength at larger radii, with an adjusted theory curve increasing the k vector 20% over the crystal in a gaussian way $k \approx (1 + .2(\rho/R_{max})^2 k_\perp)$. A possible physical explanation would be from wavefront distortions in the x direction due to the finite beam waist, but this has not been carefully analyzed.

With the ACSS and $k_\perp$ measured the dynamics can be simulated to compare measured spin dephasing as a function of ODF frequency. Experimentally we found two key issues with the measurement. The first is effects due to large Lamb-Dicke factors in the axial direction. For example, due to the small mode spacing in the axial direction we in principle should be able to measure second order terms in the Lamb-Dicke approximation that correspond to the difference frequency of the axial modes in the 1-100 kHz range. The evidence we have for these effects was demonstrated by ground state cooling the axial modes we substantially reduced these signals at low frequencies. However, it was still clear that working at the first rotation sideband rather than near DC would be preferable, and by EIT cooling we could mitigate much of the effect. The second issue we believe is due to phase jitter of the beatnote within shots of the experiment. We measured the beatnote on a photodiode and saw clear noise spurs at multiples of ~ 60 Hz as large as 12 dB below the main tone. To validate this noise source we attempted to imprint a the static pattern of figure 7.1 and then undo the rotation using a spin echo and measured the time dependence of error buildup. By actively stabilizing the phase of the beatnote we were able to drive for longer before building up the same errors suggesting the cancellation error was dominated by phase jitter. We believe this error gives a

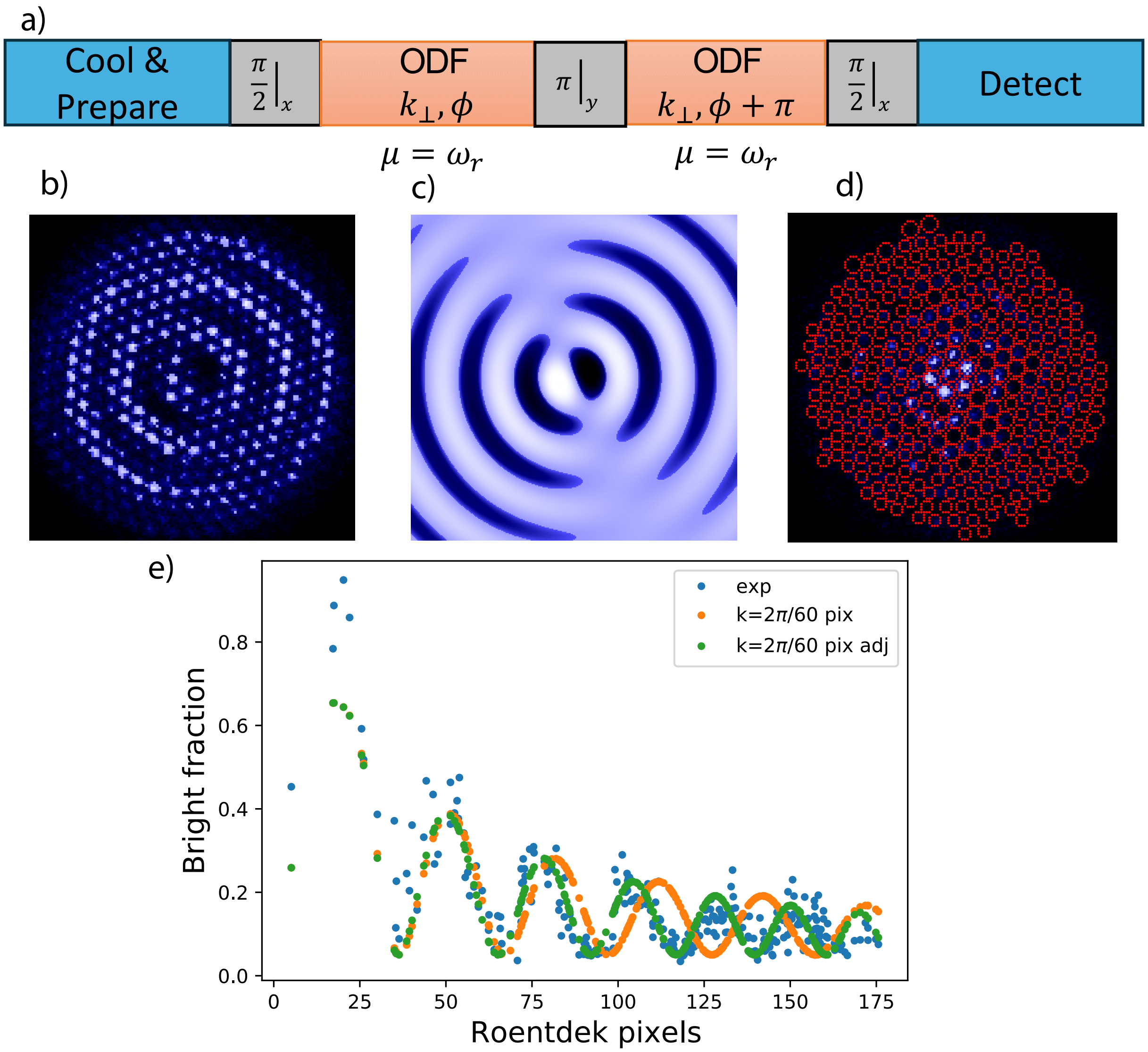

Figure 7.1: Imprinting the ODF in-plane k vector. a) Pulse sequence setting the ODF beatnote to the rotation frequency with some relative phase ϕ and with a tilted $k_\perp$ component. Applying the second arm in a spin echo with a phase advance of π adds coherently with the first arm. If ϕ is stable a final microwave phase advance to be about y discriminates between positive and negative rotations θ_i given by equation 7.24, resulting in deviations from 50% bright fraction. If ϕ is not stable a final microwave pulse about x converts spin dephasing into an increase in bright fraction given by equation 7.25. b) Imprinted k vector of wavelength ~ 50 μm onto a ~ 300 ion crystal with a phase stable ϕ and final microwave pulse about y. c) Compared theoretically predicted pattern. d) The same imprinted pattern on the same crystal but now with a randomized phase ϕ, and final microwave pulse about x. Red circles estimate ion locations using a reference Doppler cooled image taken ~ 2 seconds earlier giving relatively poor estimates at larger ion radii. At the time individual readout and reference images were not setup. Instead, images are built up over $\sim$1 second of averaging, equivalent to a few hundred experiments. e) Estimated bright fraction (blue) plotted versus ion radius in Roentdek pixels compared to a calculated bright fraction (orange) given by equation 7.25 with a $k_\perp$ of wavelength 60 Roentdek pixel and an adjusted model (green) given in the text.

signal that falls off as the beatnote frequency is detuned further from the rotation frequency, and leads to a background signal that is difficult to distinguish from the in-plane temperature.

As a heuristic of the background, assume the beatnote phase has a small phase modulation of amplitude α at a modulation frequency ω_{mod}. Looking only at the background signal at the first rotation sideband (see equation 7.20) with $\mu = \omega_r + \delta$ for some small detuning $\delta \ll \omega_r$ and dropping all phase factors for brevity:

$$
\begin{aligned}
H_{ODF}/\hbar &\approx -\sum_i \tilde{U} J_1(k_\perp \rho_i) \cos(\delta t + \alpha \sin(\omega_{mod} t)) \hat{\sigma}_z^i && (7.26)\\
&\approx -\sum_i \tilde{U} J_1(k_\perp \rho_i) \sum_\pm \sum_n \frac{J_n(\alpha)}{2^{\delta_{0,n}}} (\pm 1)^n \cos((\delta \pm n\omega_{mod})t) \hat{\sigma}_z^i && (7.27)\\
\theta_i &\approx \tilde{U} J_1(k_\perp \rho_i) \sum_\pm \sum_n \frac{J_n(\alpha)}{\delta 2^{\delta_{0,n}}} (\pm 1)^n \left[\sin((\delta \pm n\omega_{mod})t)\right]_{t=0}^{t=\tau} && (7.28)\\
&\approx \tilde{U} J_1(k_\perp \rho_i) \frac{J_1(\alpha)}{\delta} \left[\sin((\delta + n\omega_{mod})t) - \sin((\delta - n\omega_{mod})t)\right]_{t=0}^{t=\tau} && (7.29)\\
&\approx 2\tilde{U} J_1(k_\perp \rho_i) \frac{J_1(\alpha)}{\delta} \sin(\omega_{mod}\tau) && (7.30)\\
P_\uparrow &\approx \frac{1}{2}(1 - \exp\left(-(\langle \theta_i \rangle /2)^2\right) \langle \sigma_z^i \rangle). && (7.31)
\end{aligned}
$$

The result of a small phase jitter α to first order then is to cause a background dephasing term $\propto \exp(-(J_1(k_\perp \rho_i) \frac{J_1(\alpha)}{\delta})^2)$, which approaches unity (no dephasing) with a functional dependence $1/\delta^2$. Additionally, the pattern of the dephasing is at the maxima of $J_1(k_\perp \rho_i)$ in contrast to the motion dependent signals at the derivatives of J_1. Strictly speaking if the modulation is coherent (constant amplitude with random phase) the exponential form is instead a J_0 form. However, this gives rise to signals above 50% which are not seen experimentally, so the exp form is chosen instead.

Fig 7.2 shows two example scans of the in-plane temperature on a crystal of ~ 40 ions with an estimated 50 μm wavelength $k_\perp$ with a hot measured temperature using standard Doppler cooling and a colder temperature obtained using a new cooling technique, which will be described in the next section. Superposed is a simulation of benchmark temperatures of 1 and 10 mK, obtained with 25 phase averages over 5 ODF phases and 5 random motional phases for each mode. The 1 mK curve is shown with the model given in equation 7.31 using an estimated phase jitter of $\sim \pm 10$ degrees at ~240 Hz (dashed blue) and without the background phase jitter (blue stars). Overlaid at the top of the plot is the simulated in-plane mode frequencies mirrored about 180 kHz, representing where spin dephasing from motion should occur. A large uncertainty of precisely determining the temperature comes about from a combination of the above described issues. Often the higher frequency signal above the rotation frequency was larger than the lower frequency below rotation frequency, with no known explanation. Additionally, spikes at higher frequencies than the expected in-plane mode spectrum may have been due to higher order Lamb Dicke effects other than the in-plane temperature. In addition to those spikes at certain frequencies that were not always repeatable, the reliability of the EIT cooling heavily influenced how well a large background signal from higher order Lamb Dicke effects were canceled, possibly explaining some non-repeatability of certain spikes in signal. The sensitivity of this measurement hit a number of limits due to the k vector wavelength achievable and the background phase jitter that makes distinguishing in-plane temperatures difficult at low mode frequencies. Regardless, with this setup clean measurements of whether the temperature was very hot or reasonably cold were extremely useful and successful at initial diagnostics of the new coupling technique discussed in the next section.

7.6 Axialization

In most single ion Penning trap experiments the magnetron motion is cooled indirectly by coupling to either the axial or cyclotron motion [25, 73], often called axialization, sideband cooling (not to be confused with laser sideband cooling), radial centering, or mode coupling. By applying a beam splitter interaction $\hat{H} = \hbar g(\hat{a}\hat{b}^\dagger + \hat{b}\hat{a}^\dagger)$ between two harmonic oscillator modes $\hat{a}, \hat{b}$ the occupations (quanta) of the two modes swap sinusoidally at a rate $2g$. Cooling one of the two modes therefore can cool both modes as the occupation is swapped to the second mode. This technique has largely been described in a single ion picture in Penning traps, or equivalently with space charge playing a minimal role. One exception to this is laser cooling studies of small clouds that were carried out by Richard Thompson's group. They demonstrated the first axialization with laser cooling [74]

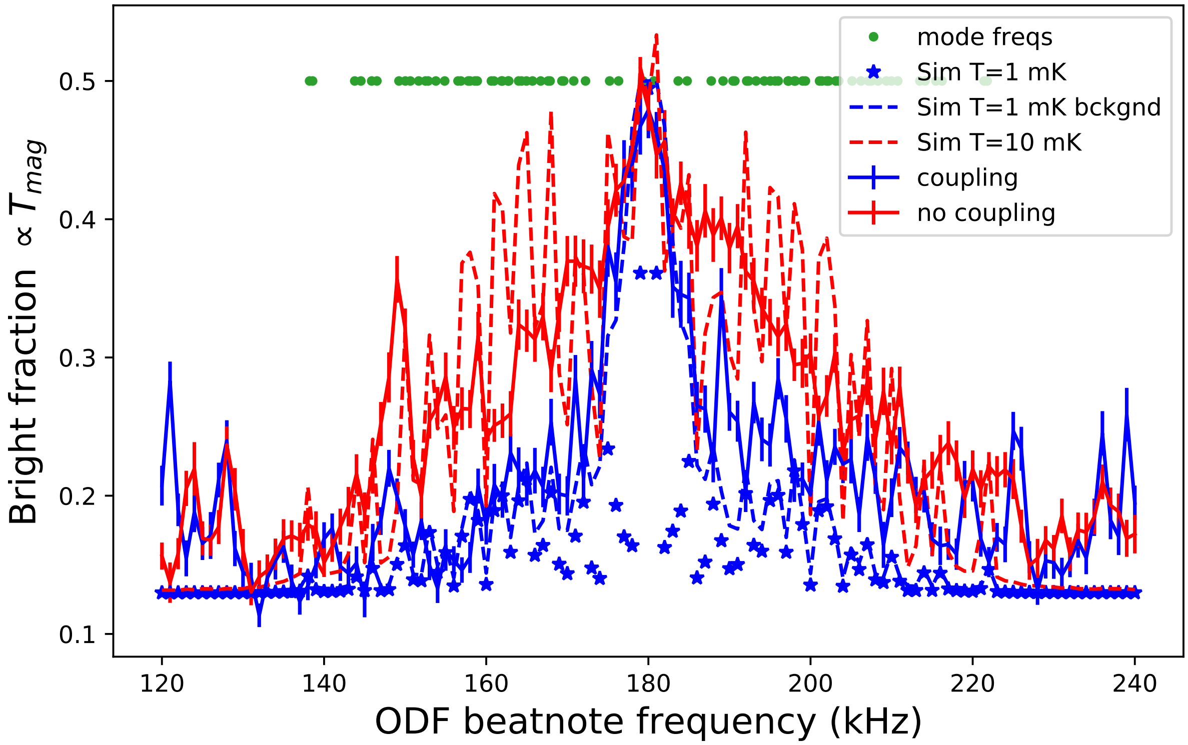

Figure 7.2: ODF magnetron temperature scans and simulations. In green are the simulated mode frequencies of a 40 ion crystal. Solid red and blue lines represent experimentally measured spin dephasing given by the bright fraction of a spin echo sequence with $k_\perp \approx \frac{2\pi}{50\mu\text{m}}$, $\tilde{U} \approx 35$ kHz, $\tau = 1$ ms, and beatnote frequencies at multiples of 1 kHz detuned from the rotation frequency of 180 kHz such that $\mu\tau$ is an integer multiple of 2π. The hotter solid red curve corresponds to measurements taken using standard Doppler laser cooling, and the solid blue using a new cooling technique involving coupling to the cyclotron modes described in the next section. A 10 mK temperature crystal is simulated in the red dashed lines, and a 1 mK simulation is given by the blue stars. Due to a background dephasing believed to be due to phase jitter the blue stars very poorly match onto the measured temperature at low frequencies. The dashed blue curve takes the simulated 1 mK temperature and applies an additional dephasing modeled by equation 7.31. Unknown asymmetry about 180 kHz leads to a hotter estimated temperature at positive detunings from 180 kHz, but regardless measurements generally fall between the 1 and 10 mK simulated bounds. Frequency spikes below 130 and above 220 kHz are not expected to be due to in-plane temperatures as the mode frequencies should be within this frequency range.

in a single ion, followed by a theory for laser cooling in the presence of coupling between the in plane COM modes [75] with experimental demonstrations of damping rates of the magnetron motion in small clouds [76]. Further experiments with up to 3 ions showed ground state cooling of the axial motion [77], followed by near ground state cooling the radial modes of a single ion [78]. In these studies no rotating wall was applied, and when working with multiple ions only damping rates of the magnetron and cyclotron center of mass motions were measured with no absolute temperature diagnostics of the radial motion. Unlike the dynamics of axialization as presented in the single ion case, instead it will be relevant to describe the dynamics of mode coupling in a way that generalizes to the multi-ion case [79, 80], which has been a ubiquitous technique of recent RF trap experiments in the ion storage group with two or three ions and two different species.

To understand axialization in 2D ion crystals, first we can calculate couplings between the cyclotron and magnetron mode for a single ion using the eigenvectors found in equation 2.11. For each eigenvector and eigenvalue pair we can associate a creation and annihilation operator like so:

$$\begin{pmatrix} x \\ y \\ \dot{x} \\ \dot{y} \end{pmatrix} = \frac{r_0}{\sqrt{2}} \left[\begin{pmatrix} 1 \\ -i \\ -i\lambda_+ \\ -\lambda_+ \end{pmatrix} a e^{-i\lambda_+ t} + \begin{pmatrix} 1 \\ i \\ -i\lambda_+ \\ \lambda_+ \end{pmatrix} a^\dagger e^{i\lambda_+ t} + \begin{pmatrix} 1 \\ i \\ -i\lambda_- \\ \lambda_- \end{pmatrix} b e^{-i\lambda_- t} + \begin{pmatrix} 1 \\ -i \\ -i\lambda_- \\ -\lambda_- \end{pmatrix} b^\dagger e^{i\lambda_- t} \right] \tag{7.32}$$

$$\lambda_\pm = \frac{\sqrt{\omega_c^2 - 2\omega_z^2} \pm \omega_c}{2} \mp \omega_r \tag{7.33}$$

$$r_0 = \sqrt{\frac{\hbar}{m(\lambda_+ + \lambda_-)}}. \tag{7.34}$$

Here a, b correspond to annihilation operators for the cyclotron and magnetron modes respectively. In the lab frame ($\omega_r = 0$), the eigenvalues for λ_- are negative, and hence are negative energy modes, with their rotation direction matching the cyclotron motion. In contrast, for rotation frequencies above the magnetron frequency and below the modified cyclotron frequency the magnetron motion is positive energy and has rotational motion in the opposite direction of the cyclotron motion. The normalization factor in front characterizes the size of the ground state wavefunction size and is equal for both cyclotron and magnetron motions.

We can now write two potentials that will produce couplings between the modes of the form

$x^2 \pm y^2$:

$$x^2 + y^2 = 2r_0^2(1 + a^\dagger a + b^\dagger b + ab e^{-i(\lambda_+ + \lambda_-)t} + a^\dagger b^\dagger e^{i(\lambda_+ + \lambda_-)t}) \tag{7.35}$$

$$x^2 - y^2 = r_0^2(aae^{-2i\lambda_+ t} + a^\dagger a^\dagger e^{2i\lambda_+ t} + bbe^{-2i\lambda_- t} + b^\dagger b^\dagger e^{2i\lambda_- t} + 2ab^\dagger e^{-i(\lambda_+ - \lambda_-)t} + 2a^\dagger b e^{i(\lambda_+ - \lambda_-)t}) \tag{7.36}$$

$$\lambda_+ + \lambda_- = \sqrt{\omega_c^2 - 2\omega_z^2} \tag{7.37}$$

$$\lambda_+ - \lambda_- = \omega_c + 2\omega_r. \tag{7.38}$$

If an $x^2 + y^2$ potential is applied, it is static in both the lab and rotating frames. Additionally, it can provide no net angular momentum change since it has no azimuthal dependence. A static potential will have static terms $a^\dagger a, b^\dagger b$, corresponding to shifting of the eigenvalues as the deconfining electric field strength changes. If the potential oscillates at the sum frequency of the rotating frame frequencies, which is the difference frequency in the lab frame because the magnetron motion is a negative energy in the lab frame, it will produce a resonant two-mode squeezing between the cyclotron and magnetron modes. This coupling creates or annihilates pairs of cyclotron and magnetron quanta so that no net angular momentum is created or destroyed. In contrast, the $x^2 - y^2$ potential can provide a change in angular momentum. It therefore can produce squeezing aa, bb terms by oscillating the potential at twice the eigenfrequencies in the rotating frame, and beam splitter terms $ab^\dagger$ by oscillating at the difference frequency of the cyclotron and magnetron rotating frame frequencies. These will be well-defined lab frequencies because the drive frequencies in the rotating frame have a frequency dependence of $2\omega_r$, which in the laboratory frame for a potential of $x^2 - y^2$ will remove the rotation frequency dependence.

To justify the angular momentum picture of the potentials it is useful to show that the angular momentum from a single quanta of cyclotron motion is equal and opposite the angular momentum of a single magnetron quanta. For a first intuitive picture, take the motions in a rotating frame at half the cyclotron frequency $\omega_r = \frac{qB}{2m}$. At this rotation frequency the cyclotron and magnetron mode frequencies are equal. From the derivation of the single ion eigenmodes, equation 2.9 shows that the off diagonal vector potential that splits the in-plane modes goes to 0, which is why the mode frequencies are equal at this rotation frequency since there is no effective vector potential to split the two degenerate modes given by a uniform planar confinement. With effectively no magnetic field, the angular momentum is simply $\vec{L} = m\vec{r} \times \vec{v} = m\vec{r} \times \vec{\omega}_{\pm} \times \vec{r}$ where $\vec{\omega}_{\pm}$ is the mode frequency of the magnetron (-) and cyclotron (+) motions pointing along a vector that the motions rotate about. Since at this rotation frequency $\omega_{+} = \omega_{-}$ and the eigenvectors for the positive energy values correspond to opposite helicity motion, along with the fact the ground state wavefunction sizes are the same the two modes have equal and opposite angular momentum. Specifically $\vec{L}_{\pm} = \mp m\omega_{\pm}\vec{r} \times \hat{z} \times \vec{r} = \mp m(\lambda_{+} + \lambda_{-})r^2\hat{z}$, which for a single quanta the orbit is $r = 2r_0$,[4] giving a single quanta of angular momentum is $L_{z,\pm} = \mp\hbar$.

In the lab frame the ground state wavefunctions are the same radius, but the motional frequencies are very different and even more confusingly they rotate in the same direction. The solution to this is the angular momentum is $\vec{L} = \vec{r} \times \vec{p}$, where $\vec{p}$ is the canonical angular momentum. $\vec{p}$ has a kinetic energy part as before, but in addition it contains a vector potential component which is opposite the rotation direction of the motion in the lab frame (along $+\hat{z}$), and proportional to the radius. Specifically, the canonical momentum is $\vec{p} = m\vec{v} + q\vec{A}$ where $\vec{A} = \frac{1}{2}\vec{B} \times \vec{r}$ is the vector potential from the magnetic field. Therefore in the lab frame the angular momentum of the two modes is $\vec{L}_{\pm} = \vec{r} \times (m\vec{\omega}_{\pm} + \frac{1}{2}q\vec{B}) \times \vec{r} = mr^2(-\omega_{\pm} + \frac{qB}{2m})\hat{z} = \mp mr^2(\omega_{+} - \omega_{-})\hat{z}$ the same result as before but now using the positive value lab frame eigenfrequencies $\omega_{\pm}$. In this case there is a fixed angular momentum from the vector potential pointing along $+\hat{z}$, with the two motions having a small (magnetron) and large (cyclotron) kinetic angular momentum pointing along $-\hat{z}$.

To calculate the coupling in the multi-ion case, we follow the same prescription as the single ion case, but now using the eigenvectors found in equation 2.24. To find the prefactor, we utilize the

---

[4] Note here r is an amplitude and r_0 is an rms size.

notation of [81]:

$$|\delta\hat{r}\rangle = \sum_n c_n(\hat{a}_n e^{-i\omega_n t}\,|u_n^r\rangle + \hat{a}_n^\dagger e^{i\omega_n t}\,|u_n^{r*}\rangle) \tag{7.39}$$

$$c_n = \sqrt{\frac{\hbar}{m\omega_n(1+R_n)\,\langle u_n^r|u_n^r\rangle}}, \tag{7.40}$$

Here R_n is the ratio of potential and kinetic energy for mode n, the "r" in $|u_n^r\rangle$ denotes the position components of the eigenvectors, and the eigenvectors are normalized by $\langle u_n^r|u_n^r\rangle$, which will be assumed to be 1 from now on. This equation reduces exactly to the position component of 7.32 for a single ion. For more than one ion, the eigenvectors $|u_n^r\rangle$ are $2N$ long, with the entries now consisting of displacements from the equilibrium position of each ion in the coordinates $\delta x_i^R, \delta y_i^R$ the displacements of each ion i in the rotating frame. Coupling drives now sum over all ions i to find the net coupling from each ion's individual coupling contribution. For example, to get the displacement operator for an ion i, we can write

$$\delta x_i^R = \sum_n c_n(\hat{a}_n e^{-i\omega_n t}\,\langle \delta x_i^R|u_n^r\rangle + \hat{a}_n^\dagger e^{i\omega_n t}\,\langle \delta x_i^R|u_n^{r*}\rangle) \tag{7.41}$$

$$\delta y_i^R = \sum_n c_n(\hat{a}_n e^{-i\omega_n t}\,\langle \delta y_i^R|u_n^r\rangle + \hat{a}_n^\dagger e^{i\omega_n t}\,\langle \delta y_i^R|u_n^{r*}\rangle). \tag{7.42}$$

We can then write the total strength of a coupling drive potential $U\cos(\omega t)$ as:

$$\sum_i U\cos(\omega t) = \frac{1}{2}\sum_i\sum_\alpha\sum_\beta \left.\frac{\partial U}{\partial\alpha\partial\beta}\right|_{r_i} \alpha_i\beta_i\cos(\omega t) \tag{7.43}$$

$$\sum_\alpha\sum_\beta\sum_i\sum_m\sum_n \frac{A_{\alpha,\beta,i}c_n c_m}{4}(\xi_{i,n}^{\alpha}\xi_{i,m}^{\beta}\hat{a}_n\hat{a}_m e^{-i(\omega_m+\omega_n)t} + \xi_{i,n}^{\alpha*}\xi_{i,m}^{\beta*}\hat{a}_n^\dagger\hat{a}_m^\dagger e^{i(\omega_m+\omega_n)t} \tag{7.44}$$

$$+ \xi_{i,n}^{\alpha*}\xi_{i,m}^{\beta}\hat{a}_n^\dagger\hat{a}_m e^{-i(\omega_m-\omega_n)t} + \xi_{i,n}^{\alpha}\xi_{i,m}^{\beta*}\hat{a}_n\hat{a}_m^\dagger e^{i(\omega_m-\omega_n)t})(e^{i\omega t}+e^{-i\omega t})$$

$$\xi_{i,n}^{\alpha} = \langle \alpha_i|u_n^r\rangle\,, \xi_{i,n}^{\alpha*} = \langle \alpha_i|u_n^{r*}\rangle \tag{7.45}$$

$$A_{\alpha,\beta,i} = \left.\frac{\partial U}{\partial\alpha\partial\beta}\right|_{r_i}. \tag{7.46}$$

Here $\xi^{\alpha}_{i,n}$ is the mode participation of ion i in mode n along axis $\alpha \in \delta x^R, \delta y^R$, and $A_{\alpha,\beta,i}$ is the curvature of the potential along axes α, β evaluated at the equilibrium position of ion i. The multi-ion case is identical[5] to the single ion case when coupling the two COM modes. When coupling the magnetron COM and cyclotron COM modes, the mode participations are equal for all ions, and $\xi^x_{i,cyc} = \xi^x_{i,mag} = i\xi^y_{i,cyc} = -i\xi^y_{i,mag}$. This leads to cancellation of the $\hat{a}^\dagger\hat{a}$ terms for the x^2+y^2 case and of the $\hat{a}\hat{a}$ terms for the x^2-y^2 case. Due to the magnetron modes having elliptical motion with some component $+1$ and -1 helicity, all magnetron modes excluding the magnetron center of mass mode can couple with some modes in the cyclotron branch to produce both the beam splitter and two mode squeezing terms for either drive potential $x^2 \pm y^2$. In general, the helicity of the magnetron modes is dominantly $+1$, meaning the relative coupling strengths agree with the single particle case.

As an example, assume a lab frame drive potential like so:

$$
\begin{aligned}
U &= qA(x^2-y^2)\cos(\omega t) && (7.47)\\
&= \frac{qA\rho^2}{2}(\cos(2\theta^R-(\omega+2\omega_r)t)+\cos(2\theta^R+(\omega-2\omega_r)t) && (7.48)\\
&= qA\frac{(x^{R^2}-y^{R^2})}{2}[\cos((\omega+2\omega_r)t)+\cos((\omega-2\omega_r)t)] && (7.49)\\
&+ qAx^Ry^R[\sin((\omega+2\omega_r)t)-\sin((\omega-2\omega_r)t)]\\
&= \frac{qA}{4}\left[e^{i(\omega+2\omega_r)t}(x^{R^2}-y^{R^2}-2ix^Ry^R)+e^{i(\omega-2\omega_r)t}(x^{R^2}-y^{R^2}+2ix^Ry^R)\right]+c.c. && (7.50)\\
&\to \frac{\hbar qA}{2}\sum_i\sum_{\pm_1}\sum_{\pm_2} c_{a,b}[(\xi^x_{i,a}\xi^x_{i,b}-\xi^y_{i,a}\xi^y_{i,b}\pm_1\mp_2 i(\xi^x_{i,a}\xi^y_{i,b}+\xi^y_{i,a}\xi^x_{i,b}))abe^{-i(\omega_a+\omega_b\mp_1(\omega\pm_2 2\omega_r)t}+c.c. && (7.51)\\
&+ (\xi^{x*}_{i,a}\xi^x_{i,b}-\xi^{y*}_{i,a}\xi^y_{i,b}\pm_1\mp_2 i(\xi^{x*}_{i,a}\xi^y_{i,b}+\xi^{y*}_{i,a}\xi^x_{i,b}))a^\dagger be^{i(\omega_a-\omega_b\pm_1(\omega\pm_2 2\omega_r))t}+c.c.]\\
c_{a,b} &= \frac{1}{m_i\sqrt{\omega_a\omega_b(1+R_a)(1+R_b)}}. && (7.52)
\end{aligned}
$$

Here ^{R} denotes rotating frame coordinates, q is the charge of the ion, A is the strength of the drive in V/cm^2, and equation 7.51 gives only the couplings between two specific modes a, b. Equation

---

[5] Note this may not be strictly true for impurity ions and due to the rotating wall causing some non-uniformity between ions and some ellipticity of the motion respectively.

7.50 shows the $x^2 - y^2$ oscillating lab frame potential becomes a co-rotating $(\omega + 2\omega_r)$ and counter-rotating $(\omega - 2\omega_r)$ potential in the rotating frame of the form $x^2 - y^2 \mp_2 2ixy$. In equation 7.51, $\pm_2$ corresponds to the co-rotating $(+_2)$ and the counter-rotating $(-_2)$ terms, while $\pm_1$ gives the positive and negative frequency components of the drive. The rotating frame form can be rewritten as $(x \pm_2 iy)^2 = (x \mp_2 iy)^*(x \pm_2 iy)$, which suggests a coupling that swaps opposite helicity motions. However, the co-rotating potential will not have any resonant coupling between the cyclotron and magnetron motion. Instead, for equation 7.51 taking the co-rotating term $+_2$, $\omega_a = \omega_m$ for a magnetron mode a, $\omega_b = \omega_c$ for a cyclotron mode b, the only non-zero coupling will correspond to the $-_1$ term which is fast rotating for $e^{i(\omega_m - \omega_c - (\omega + 2\omega_r))t}$. In this case $\omega_m < \omega_c$ making the drive frequency have the wrong sign.

By tuning the drive frequency in the rotating frame $\omega \pm 2\omega_r$ resonant with the sum or difference frequencies of the two modes, a resonant coupling strength can be calculated between modes a, b, while all other terms will oscillate with some detuning. From the form of 7.52, it becomes clear that the lowest frequency modes will have substantially enhanced coupling strengths. Plotted in figure 7.3 are the coupling strengths in Hz for pairs of cyclotron and low frequency magnetron modes when applying a 1 V amplitude drive on opposing rotating wall electrodes. A is 2520 $\mathrm{V/m}^2$ for this scheme as determined by table 3.2. A rotating wall strength of amplitude 6 V is assumed, which sets the rocking mode frequency at 1 kHz for the 100 ion crystal simulated.

In addition to beam splitter and two mode squeezing couplings, a third effect is dramatically important to the axialization dynamics. Mode-coupling occurs due to second order expansion of the coupling drive, but a larger effect comes from first-order expansion of the coupling drive that corresponds to linear driving of the modes. In RF trap experiments with multiple ions, the coupling potential is often carefully crafted to maximize the mode participations of the two modes being coupled, and the electric field is either carefully nulled at the ions or tuned such that the net force on the modes is zero. Additionally, the mode frequencies of the two modes are usually separated by $\sim$ MHz, such that the two-mode squeezing and linear drive terms are MHz off resonant. In contrast, as we have seen the largest coupling strength occurs between the rocking mode and two tilt modes.

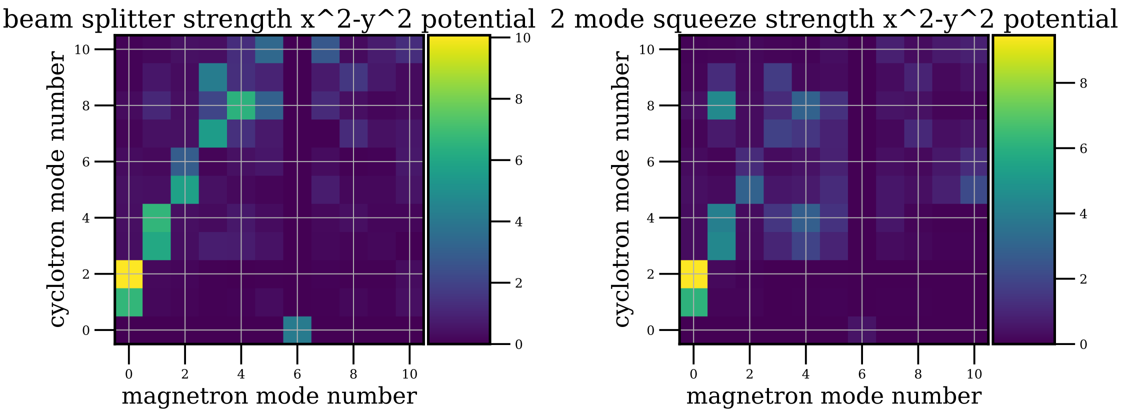

Figure 7.3: Mode coupling matrix with coupling strengths shown in Hz given by the color scale. The cyclotron COM (mode 0) can largely only couple to the magnetron COM mode, corresponding to magnetron mode number 6, in a beam splitter interaction using a counter-rotating $x^2 - y^2$ potential (left plot). This produces nearly no two mode squeezing between the two COM modes (right plot). In contrast the rocking mode (magnetron mode 0) couples most strongly to the two cyclotron tilt modes (cyclotron modes 1-2), with nearly equal beam splitter and two mode squeezing strength due to the helicity of the rocking mode being nearly equal clockwise (CW) and counter-clockwise (CCW) motion. Other magnetron modes couple less strongly due to poorer mode overlap and higher mode frequencies, and have generally stronger beam splitter than two mode squeezing interactions due to the more dominant CW helicity of the non-rocking magnetron modes.

In the rotating frame this corresponds to $\lesssim 1$ kHz for the rocking mode. As a result, when on resonance with the difference frequency of the modes to maximize the beam splitter contribution, a linear driving term is ~ 1 kHz off resonant from heating the cyclotron tilt mode(s), and ~ 2 kHz off resonant from driving the two-mode squeezing term. This contrasts with the single-ion axialization case, where the ion can be placed at the null of the axialization field to remove the first order contribution, and the two-mode squeezing term doesn't contribute due to the helicity mismatch of the modes being coupled compared to the potential applied.

To calculate the linear driving term, we follow the prescription above for the mode coupling calculation, this time only expanding to first order:

$$\sum_i U\cos(\omega t) = \sum_i \sum_\alpha \left.\frac{\partial U}{\partial \alpha}\right|_{r_i} \alpha_i \cos(\omega t) \tag{7.53}$$

$$\sum_\alpha \sum_i \sum_n \frac{A_{\alpha,i} c_n}{2} (\xi^{\alpha}_{i,n} \hat{a}_n e^{-i\omega_n t} + \xi^{\alpha *}_{i,n} \hat{a}^\dagger_n e^{i\omega_n t})(e^{i\omega t} + e^{-i\omega t}), \tag{7.54}$$

where analogously to the coupling formalism $A_{\alpha,i} = \frac{\partial U}{\partial \alpha}\big|_{r_i}$. As an example, assume a uniform electric field of strength A V/m in the x direction in the lab frame. This gives a drive strength of mode n of:

$$U_{lab} = qAx\cos(\omega t) \tag{7.55}$$

$$U^R = \frac{qA}{2}\left[x^R[\cos((\omega+\omega_r)t)+\cos((\omega-\omega_r)t)] + y^R[\sin((\omega+\omega_r)t)-\sin((\omega-\omega_r)t)]\right] \tag{7.56}$$

$$\rightarrow \sum_{\pm}\sum_{i}\frac{qAc_n}{4}(\xi^x_{i,n}\mp i\xi^y_{i,n})\hat{a}_n e^{i(\omega\pm\omega_r-\omega_n)t} + c.c. \tag{7.57}$$

This deceptively compact form shows that when a lab frame oscillating uniform electric field is applied, a co-rotating ($\omega+\omega_r$) and counter-rotating ($\omega-\omega_r$) drive are applied, which drive either counter-clockwise or clockwise motion respectively. For this reason, the cyclotron COM mode can only be driven with the counter-rotating drive, and the magnetron COM mode by the co-rotating drive. Therefore, to resonantly excite COM motion, the frequency must be set to $\omega_{cyc}+\omega_r$ for the cyclotron motion, and $\omega_{mag}-\omega_r$ for the magnetron motion where $\omega_{cyc/mag}$ are the mode frequencies in the rotating frame. Due to the mode structure, all other modes cannot be driven, with the drive suppressed by summing over the mode participations which cannot have a net COM displacement. We therefore can calculate the on-resonance drive strength as:

$$H \approx \hbar g(\hat{a}_n + \hat{a}_n^\dagger) \tag{7.58}$$

$$g \approx \frac{qA\sqrt{N}\rho_0}{2\sqrt{2}\hbar} \tag{7.59}$$

$$\approx qA\sqrt{\frac{N}{8m\hbar\omega_n(1+R_n)}} \tag{7.60}$$

$$\approx qA\sqrt{\frac{N}{8m\hbar\omega_{cyc}}}, \tag{7.61}$$

where ρ_0 is the ground state wavefunction size of the cyclotron or magnetron COM mode, which are the same size, and the simplification $\xi_x = 1/\sqrt{2N}, \xi_y = \pm i/\sqrt{2N}$ for the two COM mode participations was used. Compared to the form of driving the axial COM mode with a uniform axial electric field, the drive strength is $\sqrt{2}$ times larger due to the factor of $\sqrt{2}$ from $R_n \approx 0$ and smaller by $\sqrt{2}$ from the mode participations being $1/\sqrt{2N}$ instead of $1/\sqrt{N}$. Applying a resonant drive like this excites a coherent state $\alpha = gt$, which corresponds to a quanta of $\bar{n} = (gt)^2$.

For completeness, there are 5 possible radial drives of interest for this thesis. Two are uniform electric fields with co-rotating and counter-rotating drives as already completely described, as these cause no coupling between the modes. The next two drives are an $x^2 - y^2$ lab frame drive, which the coupling strength for the co-rotating and counter-rotating terms has been described above. Finally, there is an $x^2 + y^2$ potential which is static in both the lab and rotating frame. Below are the formulas for the coupling strength of the $x^2 + y^2$ drive, and the linear drive strengths for the $x^2 + y^2$, and co-rotating and counter-rotating $x^2 - y^2$ drives.

$$g_{x^2-y^2} = \frac{qA}{\hbar} \sum_i \sum_{\pm} c_n [(x_0 \mp i y_0) \xi^x_{i,n} + (-y_0 \mp i x_0) \xi^y_{i,n}] \tag{7.62}$$

$$g_{x^2+y^2} = \frac{qA}{\hbar} \sum_i c_n [x_0 \xi^x_{i,n} + y_0 \xi^y_{i,n}] \tag{7.63}$$

$$U_{x^2+y^2} = \hbar q A \sum_i c_{a,b} [(\xi^x_{i,a} \xi^x_{i,b} + \xi^y_{i,a} \xi^y_{i,b}) a b e^{i(\omega - (\omega_a + \omega_b))t} + (\xi^{x*}_{i,a} \xi^x_{i,b} + \xi^{y*}_{i,a} \xi^y_{i,b}) a^\dagger b e^{i(\omega - (\omega_b - \omega_a))t}] + c.c. \tag{7.64}$$

Here x_0, y_0 are the equilibrium positions of each ion (a sub index i is implied), and a factor of $\hbar$ is divided out such that the Hamiltonian is $\propto \hbar g$.

7.7 Experiment DM

7.7.1 DM temperature sensing setup

The setup for the deformable mirror (DM) to sense in-plane motion has largely been described in chapter 6, particularly the beam path setup, alignments and wavefront flattening procedure, and measured radial gradients. One crucial detail that was mentioned but not delved into was setting up ACSS nulling of both beams that form the interference independently. This is similar to the setup of the ODF, but in this case because the beams are brought along the magnetic field axis no $\hat{\pi}$ polarized light is possible. Therefore to null the differential ACSS for a single beam the ACSS from

$\hat{\sigma}_+$ polarization must have the opposite sign of $\hat{\sigma}_-$ corresponding to right and left hand circular polarizations. The ratio of the ACSS from $\hat{\sigma}_+$ to $\hat{\sigma}_-$ then sets the relative ellipticity of the polarization desired, which can be set by rotating the linear polarization going through a quarter waveplate to smoothly transition from pure $\hat{\sigma}_+$ to $\hat{\sigma}_-$ and all elliptical ratios in between. To choose whether the two beams' polarizations are aligned or cross polarized is then set by rotating the linear polarization $\pm\phi_0$ relative to linear polarization going through the quarter waveplate that produces $\hat{\sigma}_-$. To accomplish this, the laser detuning was set roughly 18 GHz detuned half way between two $\hat{\sigma}_-$ transitions $2s^2S_{1/2}(m_J = 1/2) \rightarrow 2p^2P_{3/2}(m_J = -1/2)$ and $2s^2S_{1/2}(m_J = -1/2) \rightarrow 2p^2P_{3/2}(m_J = -3/2)$. The next nearest transition is a $\hat{\sigma}_+$ transition $2s^2S_{1/2}(m_J = -1/2) \rightarrow 2p^2P_{1/2}(m_J = 1/2)$ approximately 20 GHz further detuned. This corresponds to a nulling angle of $\phi_0 \sim 61.4$ degrees when writing the polarization as $\vec{E} = E_0[\cos(\phi_0)\hat{\sigma}_- + \sin(\phi_0)\hat{\sigma}_+]$.

As mentioned previously, setting this polarization ended up being complicated by the fact that the parallel beam is combined with one of the DM beams using a polarizing beam splitter to have orthogonal linear polarization to the DM beams before the quarter waveplate. Therefore at this dominantly $\hat{\sigma}_+$ polarization the parallel cooling beam non-ideally was dominantly $\hat{\sigma}_-$, requiring more laser power to achieve the same scattering rate. This increased the background scattering rate on the bottom view images for the same fluorescence rate, roughly by a factor of 3-5x. Additionally, this means when adjusting the polarization individually of the combined DM1/parallel beam the fluorescence rate would also change within a scan, which is not too problematic for small angle searches near the null. Furthermore, it was found that putting a non-vertical polarization on the DM2 beam that bounces off the DM scrambled the polarization, requiring the polarization of all three beams to be rotated simultaneously after the DM2 beam was combined with the DM1 and parallel beam.

For all these reasons, initial tests with the DM temperature sensing were done instead at the previously described 3 GHz detuned frequency with much lower power necessary and much better imaging background. At this configuration the ratio of the effective ACSS to spontaneous emission rate was roughly order $\sim 50 - 100$, severely limiting the sensitivity of the measurement. By detuning the beams further we found that limit could only improve to $\sim 100-200$ due to intensity noise on the beams, which was not quickly remedied with active intensity stabilization. Going to this nulling configuration, improved ratios of ~ 1000 were achieved, substantially increasing the sensitivity. However, no imaging was done in this configuration with the substantially increased background scatter from the DM that would further degrade the Roentdek detection efficiency.

With the cross polarized configuration the effective maximum differential ACSS from the two beams is $4U\cos^2(61.4^\circ) \sim 0.92U$, where U is the single beam differential ACSS when $\hat{\sigma}_-$ polarized (maximum ACSS). The standard phase flopping scheme shown in figure 6.6 was found to substantially disagree with this prediction at large ACSS due to turn on effects giving shorter pulse lengths than the timing of the TTL pulse width. To solve this, a separate ACSS amplitude measurement was done by a standard Rabi scan of the microwave frequency to measure an ACSS while the DM phase is actively stabilized to $\pm\pi/2$ to give the maximum positive and negative ACSS. This agreed with the predicted $0.92U$ estimate, giving a much more accurate estimate of the average ACSS across the crystal with flat wavefronts at the maximum effective ACSS DM phase.

7.7.2 DM centering sensitivity

The deformable mirror temperature sensitivity in a radial gradient configuration can be extremely sensitive to the centering on the crystal. To see this, assume without loss of generality the DM is off center in the y direction by some distance y_{er} small compared to the crystal size. This modifies the Hamiltonian to

$$\hat{H}_{DM}/\hbar = \sum_i U\cos(k_r\sqrt{\rho_i(t)^2 - 2y_{er}y_i(t) + y_{er}^2} + \mu t)\hat{\sigma}_z^i \tag{7.65}$$

$$\approx \sum_i U\cos(k_r(\rho_i(t) - y_{er}\sin(\phi_i - \omega_r t)) + \mu t)\hat{\sigma}_z^i \tag{7.66}$$

$$= \sum_i\sum_n\sum_{\pm} \frac{U}{2^{\delta_{0,n}}} J_n(k_r y_{er})(\pm 1)^n \cos(k_r\rho_i(t) + \mu t \pm n(\phi_i - \omega_r t)))\hat{\sigma}_z^i \tag{7.67}$$

$$\approx \sum_i UJ_0(k_r y_{er})\cos(k_r\rho_i(t) + \mu t)\hat{\sigma}_z^i. \tag{7.68}$$

Here the square root is expanded to first order in y_{er} and the argument of the J_n Bessel functions is assumed small so that only the 0th order matters. For small y_{er} the effect to first order is to remove power at the carrier frequency μ at the expense of power added into sidebands at multiples of the rotation frequency, with the power in the sidebands determined by $J_n(k_r y_{er})$. This means the scale of the sensitivity to the DM centering is set by the error relative to the wavelength of the radial gradient. For example, at $k_r = \frac{2\pi}{20\mu\text{m}}$ a zero of the J_0 Bessel function occurs at $y_0 = 7.6$ μm, completely removing any temperature sensitivity unless measured at a rotation sideband. This sensitivity was not realized until after data was collected for this thesis. Analysis from the radial gradients in figure 6.11 suggest errors of order 7.5 μm were quite possible in the system using the standard centering procedure.

7.7.3 Experimental axialization dynamics

With the DM setup the first investigation was to improve the understanding of the axialization dynamics to validate the theory of section 7.6. Two reliable measurements emerged, the first a resonant coupling frequency measurement identified by measuring reduced magnetron temperature as the coupling drive frequency was scanned. The second measured the excited cyclotron modes that can easily be driven to very large amplitudes due to the linear driving terms described in section 7.6. Shown in figure 7.4 are examples of two such scans. In general, most scans set a radial gradient interference pattern made by displacing rings of actuators 230 nm per ring, corresponding to roughly $k_r \sim \frac{2\pi}{20\mu\text{m}}$. Due to surface displacement limits this was often limited to a radius of 4 DM pixels, with the pattern set to flat at larger radii.

The first scan set the DM beatnote to 15 kHz and measured spin dephasing of magnetron motion near that frequency using a spin echo with a phase advance in the second arm, with each arm time set to $\tau = 2$ ms. This frequency was chosen to be high enough to avoid low frequency background from potential phase jitter between the beams, while not too high to diminish sensitivity from smaller amplitude motion, and away from 9 kHz to avoid the magnetron COM mode that does not couple with the rest of the magnetron modes. Before each temperature measurement a

5-10 ms Doppler cooling pulse was applied with both parallel and perpendicular cooling beams applied simultaneously with a repump beam and an $x^2 \pm y^2$ drive to couple the magnetron and cyclotron motions together. Due to non-linearity in the magnetron modes all magnetron modes besides the COM mode couple together [82]. Therefore, cooling any magnetron mode by swapping its amplitude with a cyclotron mode and cooling that cyclotron mode can cool all magnetron motion excluding the magnetron COM mode. Scanning this coupling frequency with a weak coupling drive near the rotating frame cyclotron tilt mode frequencies (plus twice the rotation frequency for an $x^2 - y^2$ drive) produced cooling resonances of decreased magnetron temperature. Increasing the drive strength broadened the cooling resonances and could give a third resonance suspected to be a coupling between the rocking mode and the cyclotron $m = 3$ mode. Remarkably these drives were as small as $\sim$ 10 $\mathrm{mV_{pp}}$ on just two electrodes $\sim$ 1 cm away. These cooling resonance widths were very clearly not similar to the predicted coupling strengths, with this small of couplings expected to give resonances of at most $\sim$ 1 Hz, generally much less. Additionally, the expected coupling strengths clearly predict a strong coupling for the two cyclotron tilt modes, but many other resonances are predicted to be stronger than the $m = 3$ cyclotron to rocking mode coupling. However, the $m = 3$ to rocking mode coupling for many simulated crystals often was the next strongest rocking mode coupling besides the tilt modes, with its predicted relative strength to the tilt modes in reasonable agreement with the required increased drive strength. This suggested something unique about the rocking mode, potentially having large non-linearity to enhance its coupling rate over all other magnetron modes couplings.

To investigate this the cyclotron modes were interrogated to check where the cyclotron mode resonances were relative to the cooling resonances. To do this, after cooling a "tickle" was applied to excite a cyclotron mode using the linear drive terms described in section 7.6, after which the deformable mirror beatnote was set to that frequency to measure motion at that cyclotron frequency. Specifically, a tickle (and cooling) could be applied near the cyclotron mode frequencies in the rotating frame using an $x^2 + y^2$ potential which is at the same frequency in the lab and rotating frame. Alternatively the tickle could be applied at the mode frequency in the rotating frame plus twice the rotation frequency using an $x^2 - y^2$ potential. The result is shown in figure 7.4 with two different strength tickles each applied for 1 ms to narrow the heating resonance to split the nearly degenerate tilt mode frequencies, along with DM sensing arm times of 1 ms. For larger tickle strengths a third resonance more clearly appeared in agreement with the location of the cooling resonances. Very surprisingly, rather than the cooling resonances being detuned by the rocking mode frequency of $\sim$ 1-2 kHz for the strong rotating wall strength applied, the frequency discrepancies were often indistinguishable from 0. Effectively, cooling resonances appeared to be between the given cyclotron mode and a zero frequency rocking mode. This is still not understood, but the current theory speculates that non-linearity in the rocking mode may substantially increase the coupling rate and is strongest near zero frequency.

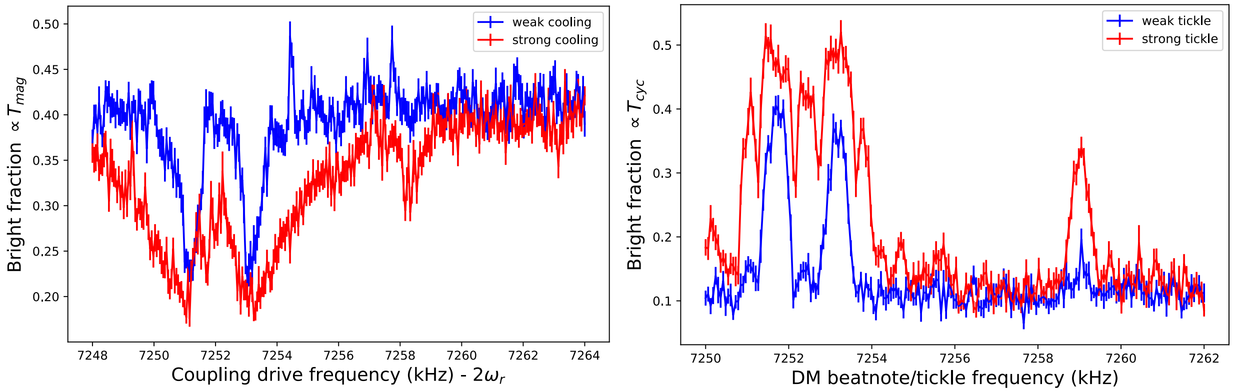

Figure 7.4: Axialization experimental measurements. The left plot shows cooling resonance frequencies of the axialization drive, as evidenced by dips in spin dephasing from magnetron motion at 15 kHz as the magnetron motion is cooled. For a stronger coupling drive the resonances broaden and a third resonance besides the two cyclotron tilt modes is found, suspected to correspond to coupling the rocking mode to a cyclotron m=3 mode. The right plot shows cyclotron mode excitations from a tickle as measured by spin dephasing from the cyclotron motion. The resonance locations match the cooling resonance locations, and similarly an m=3 cyclotron mode becomes more prominent at much larger tickle strengths.

Validating which modes corresponded to which resonances was confounded at first by impurity ions. As a first check to confirm the cyclotron tilt modes, the rotating wall strength was varied expecting to increase the tilt mode splitting as the crystal became more elliptical for larger wall strengths. In fact, at first the opposite effect was measured due to impurities. This is because the orientation of the cyclotron tilt modes is set by the aspect ratio of the Be$^+$ portion of the crystal, as the BeH$^+$ do not participate in the motion. When hydrides form they go to the furthest extended point of the crystal radially, corresponding to the major axis of the ellipse, causing the effective aspect ratio of the Be$^+$ portion of the crystal to reduce. Once enough hydrides form the aspect ratio of the Be$^+$ portion of the crystal can switch orientation relative to the overall crystal, at which point increasing the rotating wall strength actually decreases the aspect ratio of the Be$^+$ portion of the crystal, decreasing the tilt mode splittings. With a pure enough starting crystal the tilt modes do correctly increase their splitting for larger wall strength. To confirm exactly which resonances corresponded to which modes the spin dephasing from the tickle was imprinted onto the ions and imaged analogously to the axial drumhead modes shown in figure 6.1. Images of the three cyclotron mode resonances are shown in figure 7.5.

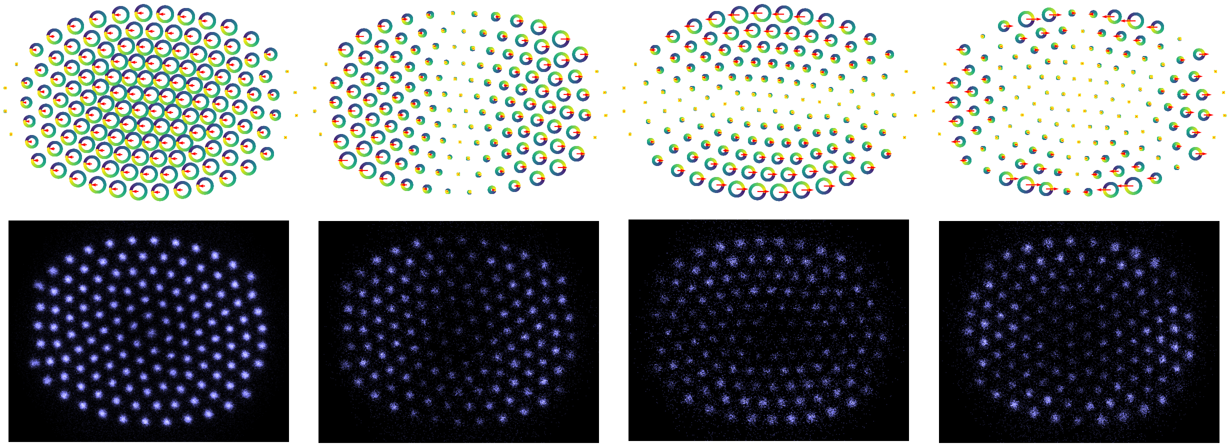

Figure 7.5: Cyclotron mode images obtained by imprinting spin dephasing on each ion's spin state proportional to the absolute participation in the mode. Dark ions therefore correspond to no spin dephasing, with some background from decoherence giving some background fluorescence rate from all ions. Simulated modes are given above each image to show the mode participation of each ion corresponds to larger clockwise rotational motion. The red arrows represent a single instant in time the displacement of all ions from the mode, with a full orbit represented by the colored traces with time increasing from purple to yellow colors identically to figure 2.5. From left to right the modes correspond to the cyclotron COM mode, the two cyclotron tilt modes, and finally a cyclotron m=3 mode. Note the cyclotron COM mode was not imprinted dephasing but is instead just a reference Doppler cooled image since all ions equally participate in the mode.

7.7.4 Two tone axialization studies

After validating a number of key predictions of the theory of section 7.6 (and failing to validate some others), a natural question was to see if a lower ultimate temperature could be achieved. A major problem with this scheme driving very near resonance to the cyclotron tilt modes is the linear drive term heating the mode that is swapping with the rocking mode to cool the magnetron motion. Without careful tuning of the drive frequencies, it is expected the linearly driven cyclotron mode would come to an equilibrium temperature set by the competition of the cyclotron cooling rate and the linear drive heating rate. This $\bar{n}$ would then set a limit for the lowest rocking mode $\bar{n}$ that could be swapped setting an ultimate temperature limit. Additional heating rates of the magnetron motion from the cooling beam scattering would also compete with the swap rate to set another temperature limit.

Experimentally it was found that setting the perpendicular cooling beam further off center improved the magnetron temperature, possibly due to the coupling rate being too small compared to the cyclotron cooling rate. Additionally it became clear that the excited cyclotron tilt mode limited how strongly the coupling could be turned up before problems occurred with the crystal. Figure 7.6 shows two obvious effects from the excited cyclotron tilt mode. The first is a change in the perpendicular beam fluorescence seen in the lab frame image. The diagonal line in the leftmost image shows a line of maximum fluorescence from the perpendicular beam under standard cooling conditions. Equivalently this corresponds to a line of constant Doppler shift from the rotational motion's component in the direction of the perpendicular beam. The perpendicular beam is detuned ~ 15 MHz from resonance, which is equal to the Doppler shift from ions ~ 4 μm on the blue side of the crystal orthogonal to the perpendicular beam. With the excited cyclotron tilt mode there is a large Doppler shift for further out ions that participate more in the cyclotron tilt mode, which changes the effective Doppler shift the perpendicular beam sees to increase with radius. Two new lines of maximum fluorescence emerge corresponding to where the red Doppler shift from the rotation and beam detuning equals the blue Doppler shift from the cyclotron tilt mode. Since the mode participation increases roughly linearly with radius while the red detuning from rotation increases with distance orthogonal to the perpendicular beam from the center of the crystal, this forms a "clock handle" pattern of mostly straight lines at a specific angle given by the rate of the Doppler shift increase as a function of radius. Turning up the strength of the linear drive heating the tilt mode commensurately brings the clock handles together corresponding to larger cyclotron tilt motion. This effect can be used to roughly tune up and identify the optimal coupling frequencies, and also if the drive strength is too large.

Once the drive strength gets very large the competing heating rate and cooling rates are no longer well balanced and an enormous increase in cyclotron tilt mode energy can occur. This is shown on the rightmost image of figure 7.6, which is a crystal image in the rotating frame showing a cold crystal excluding an extremely hot cyclotron tilt mode that is hot enough to see the orbits of the furthest out ions. Rough temperature estimates of the clock handle estimate suggest $\lesssim .5$ Kelvin, while the runaway heated condition of the right most image is astronomically higher at $\sim$ 1000 Kelvin order of magnitude.

One idea to improve the linear drive rate was to try and cancel the linear drive rate with a second drive tuned to the same drive strength g but out of phase. However, for the analyzed drive potentials listed in section 7.6 only the $x^2 + y^2$ and the counter rotating $x^2 - y^2$ potentials could substantially drive the cyclotron modes of interest. Therefore it was unclear if when an $x^2 + y^2$ drive and $x^2 - y^2$ drive were applied simultaneously to cancel their linear drive terms if that would also cancel the cooling from the second order coupling. Initial calculations suggested that the relative phase of the mode coupling to the linear drive should be opposite for the two drives, suggesting driving out of phase the linear terms would add the second order coupling in phase. Additionally, calculations suggested the relative phase of the two drives should be 0 for the lower frequency tilt and m=3 mode to cancel the linear term which would add the second order coupling in phase. In contrast the predicted relative phase of the two drives was π for the higher frequency tilt mode, but was still predicted to add the two second order couplings in phase. This suggested off resonant driving of the other cyclotron tilt mode would not be canceled using this technique.

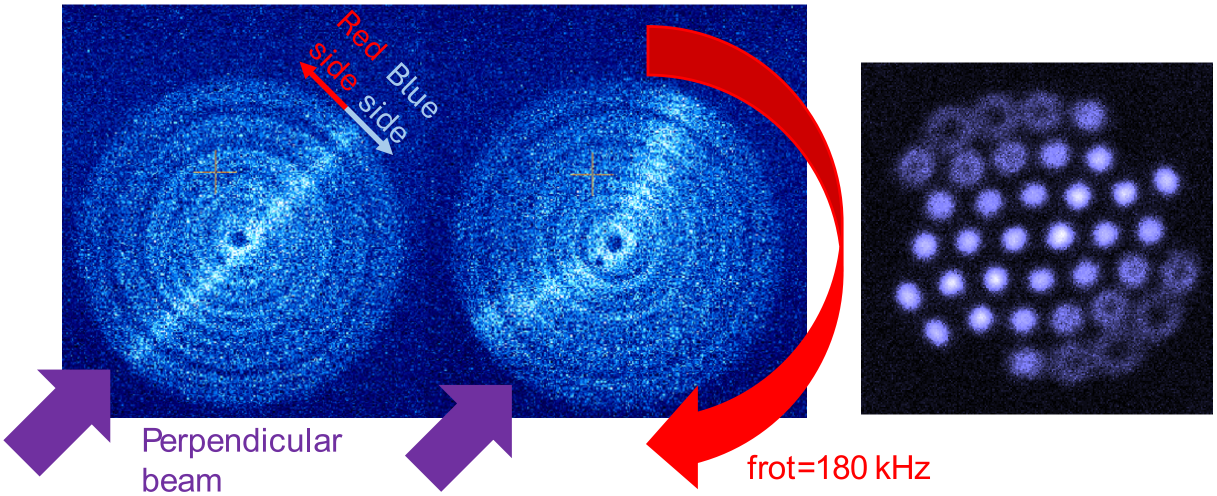

Figure 7.6: Driven cyclotron tilt mode effects in ion images. The left two images show lab frame bottom view images of crystals rotating clockwise with a perpendicular beam originating from the bottom left corner of the crystal at 45 degrees. A line of maximum fluorescence under standard cooling conditions is at a fixed distance a few microns on the blue side of the crystal. In contrast a clock handle fluorescence pattern emerges with axialization from the excited cyclotron tilt mode. When driven too hard a runaway heating effect can occur producing astronomically hotter cyclotron tilt modes as imaged in the rotating frame of the crystal in the rightmost image.

As a first diagnostic of the idea, a two tone tickle measurement was done analogously to the previous tickle measurements but now scanning the relative phase of the two drives. This requires setting the beatnote of the two drives to be exactly twice the rotation frequency such that the relative phase of the drives was a well defined constant, with the beatnote relative phase set to a time stamped reference of the rotating wall. Additionally, before scanning the relative phase of the two drives the amplitude of each drive was tuned to cause roughly the same spin dephasing at each mode that was driven. Figure 7.7(a) shows the cancellation of the two tones driving cyclotron motion for the three different modes. As the relative phase is scanned the spin dephasing varies proportional to the two tones adding constructively in phase or destructively out of phase. When driven in phase the excited motion causes a saturation of the dephasing giving a flat line near $40-50\%$ rather than at 50% because not all ions participate in the motion. As predicted the lower frequency tilt mode (blue) and m=3 cyclotron mode (green) have a relative phase near 0 when the two linear drive couplings are out of phase. In contrast the higher frequency tilt mode (red) has a cancellation at a relative phase of π.

With the relative phases found to cancel the linearly driven cyclotron motion next the cooling efficiency was investigated applying both tones. In this case both tones were applied during the 10 ms cooling pulse rather than from a tickle, and the magnetron temperature was measured. Figure 7.7(b) shows the resulting magnetron temperature proxy from spin dephasing caused by magnetron motion near 15 kHz as the relative phase of the two cooling tones was varied. Three different curves are shown corresponding to the two tones set near the lower frequency cyclotron tilt mode (blue), the higher frequency tilt mode (red), and the m=3 cyclotron mode (green). Compared to figure 7.7(a) it is clearly evident that the magnetron cooling was worst when the linear drive terms were canceled. The simplest interpretation is that when the linear drive terms are driven out of phase so are the second order coupling terms from the two drives. This is not in agreement with calculations but regardless some cooling should still occur as the coupling and linear drive ratios should not be exactly the same between the two tones. This was seen experimentally that the magnetron temperature did improve with the two tone coupling even at the weakest cooling phase compared to no axialization, but the added strength required to compensate would be mitigated by off-resonantly driving the other cyclotron tilt mode which is driven in phase. Future work on the possibility of two tone cooling would require more detailed theory modeling to explain the cooling worsening when canceling the linear drive term, or if other geometries or mode couplings could perform better.

7.7.5 DM temperature sensitivity calibration

To calibrate the sensitivity of the DM temperature measurement, a known coherent state was produced and then measured. To make the known coherent state, it is simplest to excite the cyclotron COM motion using a drive at the lab frame modified cyclotron frequency on a single rotating wall electrode. Advantages of the cyclotron COM are the uniform participation of all ions, the simple form of the calculated mode occupation for a linear drive, and the fast cooling of the mode allowing easy initialization on the next shot of the experiment. In contrast, the magnetron COM

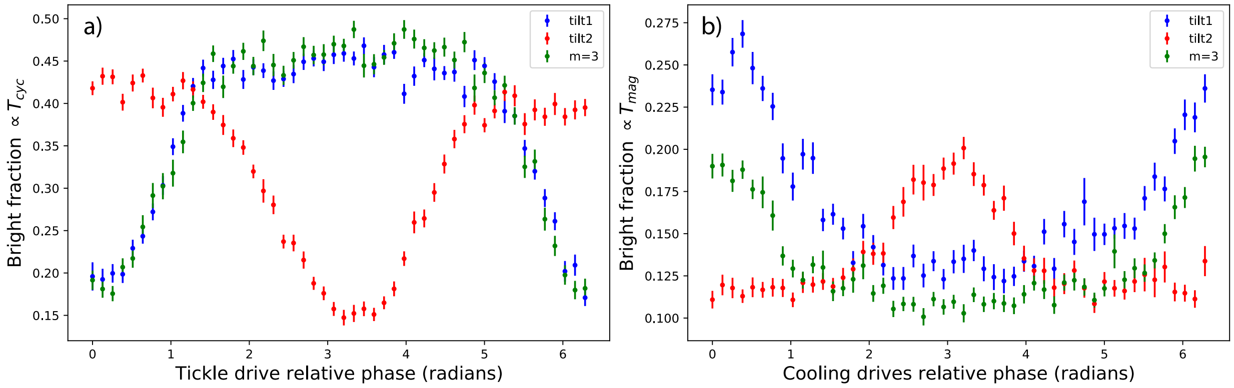

Figure 7.7: Two tone axialization dynamics. a) Constructively and destructively driven cyclotron motion from a tickle with two tones for the lower frequency cyclotron tilt mode (blue), higher frequency tilt mode (red), and m=3 mode (green). The x axis corresponds to the scanned relative phase of an $x^2 - y^2$ and $x^2 + y^2$ tickle driven on the corresponding mode. The y axis corresponds to a proxy of the cyclotron mode temperature from spin dephasing imparted by setting the DM beatnote to the cyclotron mode frequency. Tickle times and DM arm times of 1 ms were utilized. Dips at 0 for the lower frequency tilt mode and m=3 mode corresponded to the linear drive terms being driven out of phase, compared the dip at π for the higher frequency tilt mode. b) Magnetron temperature proxy as two coupling drives were applied during cooling with the relative phase of the drives scanned. The magnetron temperature was hottest in all three mode cases when the linear drive rate was canceled.

mode, which also has uniform participation and a simple calculated mode occupation, is difficult to cool, is difficult to distinguish from the dense forest of neighboring modes, and is difficult to scan the frequency of due to the background term from the low frequency DM beatnote. From equation 7.61, the created coherent state will have an $\bar{n}$ of

$$\sqrt{\bar{n}} \approx qAt\sqrt{\frac{N}{8m\hbar\omega_{cyc}}}. \tag{7.69}$$

Based on COMSOL simulations listed in table 3.2, the electric field strength A is $\approx$ (12.4 V_{tickle}) V/m, where V_{tickle} is the amplitude of the oscillating voltage of the tickle applied in volts.

With this created coherent state, equation 7.13 can be used to estimate the expected dephasing caused by a coherent state measured with the DM in a spin echo sequence assuming a randomized relative phase that is averaged over many shots. For the in-plane COM modes, $\kappa_i = 1\sqrt{2}$ uniformly for all ions, simplifying the expression to

$$\langle P_{\uparrow} \rangle \approx \frac{1}{2}\left(1 - e^{-2\Gamma\tau} J_0\left(4|\alpha_T|\sqrt{\bar{n}}\right)\right) \tag{7.70}$$

$$|\alpha_T| \approx \frac{Uk}{2\delta}\sqrt{\frac{\hbar}{2Nm\omega_{cyc}}}\left|\left(1 - e^{i\theta_1}\right)\left(1 - e^{i\theta_2}\right)\right|, \tag{7.71}$$

where ω_{cyc} is the rotating frame cyclotron COM frequency, $\theta_1 = \delta\tau$, $\theta_2 = \delta\tau + t_\pi + \phi_{adv}$, and U is half the maximum differential ACSS from the DM in units of radians/second. The expected signal is identical to the ODF axial COM measurement but now ignoring spin-spin interactions and zero-point fluctuations due to the much weaker spin dependent force from the long wavelength k_r. Depending on the phase advance ϕ_{adv}, spin dephasing will canceled ($\phi_{adv} = 0$) or add in phase ($\phi_{adv} = \pi$) between the two arms on resonance, see figure 4.9 for more details. Figure 7.8 shows two such example measurements plotted with corresponding fits to equation 7.70. For these measurements a tickle of 10 μs was applied with an amplitude of 5 mV, and the ion number was estimated to be 150. The expected $\bar{n}$ from this drive is 2550 quanta, with a measured $\bar{n} = 1920$ with $\tau = 1$ ms, $k_r = \frac{2\pi}{20\mu\text{m}}, U/(2\pi) = 9$ kHz. This disagreement suggests a reasonable estimate of the ion number, k_r, and azimuthal trap coefficient, all of which were not precisely measured, along with potential amplitude non-uniformity of the DM beams across the crystal, centering errors, and potential finite size effects if the crystal was larger than the set pattern.

While this agreement suggests the model well captures the dynamics of the measurement and drives, some concerning behavior was also measured when varying k_r. When lowering the amplitude displacement of the radial gradient pattern by factors of 2 to increase the wavelength of the gradient the expected sensitivity should decrease by a factor of 2, or equivalently a factor of 4 in $\bar{n}$. This was not consistently measured, giving larger $\bar{n}$ estimates equivalent to having a larger sensitivity than predicted at longer wavelength k_r. In particular, going from a 40 μm wavelength to 80 μm wavelength k_r actually gave the same spin dephasing signal strength, suggesting somehow the sensitivity was 4 times stronger than expected at the 80 μm case. In contrast measurements of $\bar{n}$ were self consistent when varying the tickle time and drive amplitude corresponding to varying the set coherent state size. A number of details may explain the non-ideal k_r estimate at shorter wavelength, particularly FLIR camera images suggested short wavelength phase patterns were present radially that were fractionally larger compared to the desired radial gradient for small k_r. Analysis of the radial gradients in figure 6.11 suggest centering errors could also contribute substantially, but would not be expected to reduce sensitivity so substantially at $\sim 40\ \mu$m wavelength k_r.

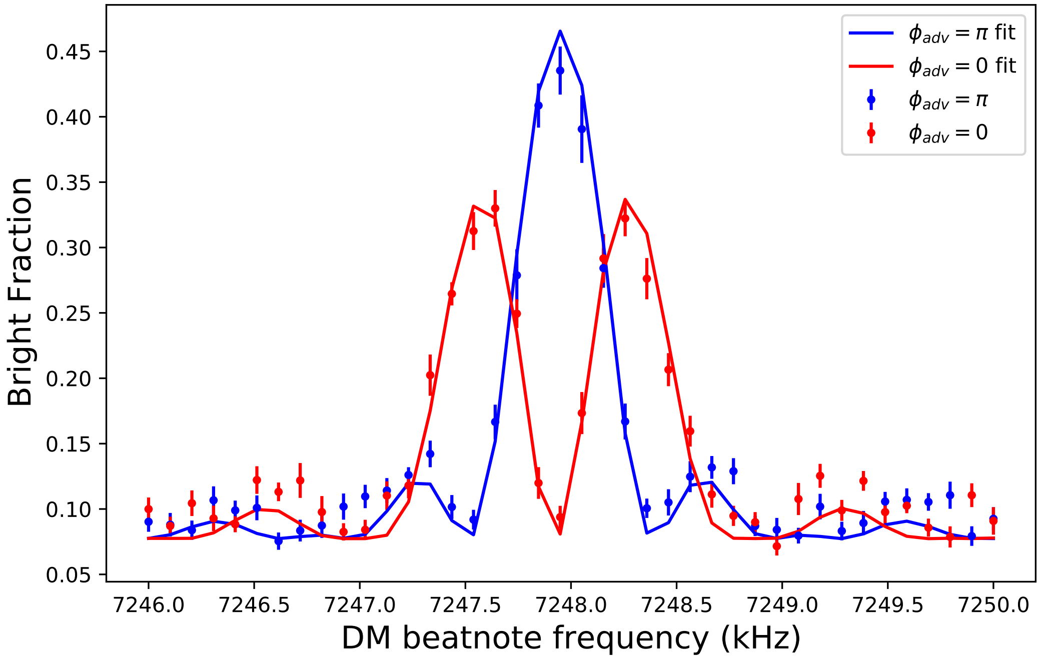

Figure 7.8: Cyclotron COM calibration. Two scans corresponding to with (blue) and without (red) a phase advance in the second DM arm. In both scans a 10 μs pulse of amplitude 5 mV was applied, with estimated DM settings of $\tau = 1$ ms, $k_r = \frac{2\pi}{20\mu\text{m}}, U/(2\pi) = 9$ kHz, and an estimated ion number of 150. Note the ion number was not precisely calibrated in this scan. The fit extracted an estimated $\bar{n}$ of 1920 ± 35 quanta. Using equation 7.69 predicts an $\bar{n}$ of 2550, which is likely within the error of k_r, N, and azimuthal trap coefficient estimates. Due to the quadratic nature of the fitted $\bar{n}$ compared to the k_r value, this would require only a 15% error in the wavelength or trap coefficient, or a 30% error in ion number.

7.7.6 Magnetron temperature scans

Ultimately the most desirable measurement is an estimate of the magnetron mode temperatures to see how well the cooling works. For unknown reasons the estimated magnetron temperature from simulations compared to experimental measurements seem inconsistent with baseline temperature estimates. Figure 7.9 shows two example scans set near the largest sensitivity achievable, with $U = 24$ kHz, $\tau = 1$ ms, $k_r \sim \frac{2\pi}{20\mu\mathrm{m}}$. In the two scans either the axialization coupling was turned off (red dots) or pulsed (blue dots) during Doppler cooling. Simulations shown in solid lines used an estimate of 125 Be$^+$ and 15 BeH$^+$ ions and temperatures of 40 and 400 μK, in reasonable agreement with the measured curves with and without the coupling respectively.

Looking at a number of other measurements taken around this time period, experiments without axialization consistently underestimate the expected temperature, as the coldest temperature expected without the coupling is $\sim$ 10 mK, whereas the hottest reference curve around that time was at most a few mK. One hope for the discrepancy is that no data has been taken cross referenced with the cyclotron COM temperature calibration, with a slim possibility of reference temperatures having a poor sensitivity estimate from possible centering errors. Future measurements plan to additionally compare temperature estimates from images of the crystal which can give reasonable bounds of the rocking mode in the few mK regime. These image temperature estimates will rely on the assumption the rocking mode temperature is in equilibrium with all other magnetron modes excluding the COM mode.

7.8 Conclusion and future outlook

In conclusion we have experimentally demonstrated a new in-plane temperature diagnostic technique able to sense experimentally achievable magnetron temperatures and excited cyclotron temperatures. This technique was first demonstrated using an ACSS gradient in the plane of the ions from tilting the ODF beams, and subsequently using a radial gradient generated from interference of two laser beams using a deformable mirror. The sensitivity of the ODF is believed to be limited to $\sim$ 1 mK by phase jitter between the beams and the easily achievable tilt. Additionally, the sensitivity from a tilt in the lab frame is limited to some degree due to the strength of the J_1 Bessel function reducing for large arguments. In contrast the deformable mirror in principle can sense magnetron motion much colder than mK temperatures. Initial temperature sensitivities calibrated with a tickle of the cyclotron COM mode suggest the theoretical model can capture the dynamics of the system,

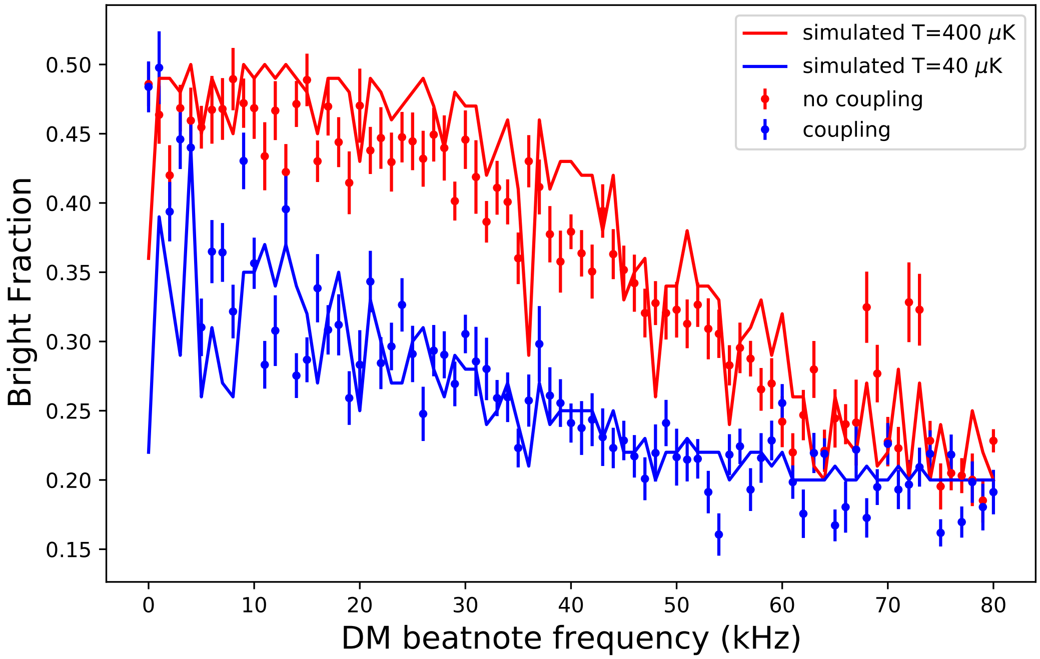

Figure 7.9: Magnetron temperature measurements compared with simulation. The DM beatnote is scanned from 0 to 80 kHz in 1 kHz time steps with DM arm times of 1 ms such that $\mu\tau = 2\pi l$. The experimental measurement with coupling (blue dots) are clearly substantially colder than without coupling (red dots). Simulation curves at 400 μK (red solid) and 40 μK (blue solid) are in reasonable agreement with the measured curves suggesting a temperature reduction of $\sim$ 10x. However the absolute temperature estimates seem to substantially underestimate the expected temperature of $\sim$ 10 mK without the coupling.

however magnetron temperature measurements seem to anomalously underestimate the temperature currently.

Additionally, a novel cooling technique that couples the magnetron rocking mode to a number of long wavelength cyclotron modes has been experimentally demonstrated and characterized. Theoretical predictions from a model of the coupling largely agree with experiment. However, the coupling strength seems anomalously large and the effective rocking mode frequency extracted from the coupling much smaller than the expected rocking mode frequency, consistent with 0 frequency in many cases.

Using these techniques a number of cyclotron modes were also imaged for the first time using imprinted spin dephasing from the deformable mirror. These cyclotron modes get excited by the coupling drive and seem to limit the achievable drive strengths as identified by a number of new phenomenon present with excited cyclotron tilt mode occupations. An attempt to cancel this linear drive using two phase coherent coupling drives confirmed a number of theoretical predictions of the relative drive phases, however did not successfully improve the cooling in disagreement with theoretical calculations.

A vast array of future work is possible with these new techniques. Finer scans of the magnetron mode frequency could be carried out using a phase advance cancellation technique of the background rather than the $\mu\tau = 2\pi l$ cancellation technique. In particular the magnetron COM mode could be calibrated analogously to the cyclotron COM. Future work comparing the temperature measurements with images of the crystal can hope to resolve the discrepancy between estimated and expected magnetron temperatures. Multiple echo pulses could be used to reduce the effect of background signal from phase jitter of the beams, or even better active stabilization of the beatnote could reduce this effect almost entirely. Additionally, coupling rates could in principle be measured by looking at the time scale of the cooling. If the rocking mode could be experimentally measured, swaps between the rocking mode and various cyclotron modes could also be investigated more directly.

More theoretical modeling would help tremendously in trying to identify the discrepancies in the effective rocking mode frequency, coupling strength, and cancellation of cooling with two tone axialization. Particularly any estimate of the effect of non-linearity of the rocking mode would help validate the idea the coupling is enhanced from it. With a more accurate model dramatic improvement in the achievable temperature could be possible allowing much larger coupling rates and lower heating rates of the cyclotron modes. In principle if cyclotron modes of anywhere near the Doppler cooling limit of $\bar{n} \sim 1$ could be achieved and swapped to the rocking mode, temperatures in the 100 nK range or even colder could be achieved corresponding to a rocking mode temperature of a single quanta.

In a less likely future direction, the deformable mirror could in principle be used to implement quantum operations on the in-plane modes, possibly including cooling. For the current setup a minimum wavelength of 3 μm could potentially be achieved which would set a very small effective

Lamb-Dicke parameter of any coupling and would make any spin-motion entanglement difficult. However, if a DM with more actuators or larger displacements was available tunable wavelength gradients at each ring of ions are possible and could be competitive with the ODF in coupling strength. However, the phase variation across the crystal would restrict to couplings that may not have as obvious utility as the ODF axial COM motion.

Chapter 8

Future Experiments

This chapter will discuss some future directions the experiment might take, heavily motivated by a series of theory papers from our collaborators.

8.1 Direct extensions of this thesis

Listed at the end of each experiment result of this thesis is an array of direct extensions to each result. Here I give a quick recount of some of the most near term demonstrations.

For the Dicke model, more direct quantum measurements of the generated two mode squeezed entangled states can be carried out using a beam splitter operation and time reversal [59]. Additionally, active phase stabilization of the ODF may offer interesting direct measurements of the coherent state of the boson after a repump of the spin states which will perturb the motion at the ~ 1 quanta level. Farther in the future, clearer measurements of the chaotic regime of the Dicke model can also be carried out using information scrambling in the chaotic regime which is recovered using time reversal [67]. Additionally, improvements in the decoherence of the system from further detuning the ODF off resonance or parametric amplification (see section 8.2) may allow higher fidelity entangled states to be produced.

Using the deformable mirror can most straightforwardly initialize spin states corresponding to linear gradients or radial domain walls or annuluses. Future work on more complex patterns would likely need a DM with more actuators to reach single ion addressing. One immediate application of a non-trivial spin state, and even possibly dynamics from the DM, is a quantum simulation of $p + ip$

superconductivity listed below in section 8.3

The in-plane temperature measurements have a number of disagreements with theory that would require further theory insights to make the most progress. Specifically, modeling of the non-linearity of the rocking mode and two tone axialization could try and resolve the coupling strength and effective zero frequency rocking mode disagreements with theory and the failure to improve the cooling with two tones. Larger radial gradients could allow ground state temperature measurements of the cyclotron modes and possibly even quantum operations or cooling. Substantially improved magnetron temperatures may also be possible if disagreements with theory can be accounted for to improve the cooling scheme.

8.2 Parametric amplification

Before the magnet broke in 2021, the primary experimental focus was on motional squeezing of the axial COM motion using parametric amplification. Parametric amplification involves a modulation of the harmonic potential at twice the motional frequency. In our system this corresponds to modulating the trap frequency of the axial COM motion at twice the axial COM frequency. This can be applied by driving on the neighboring T2/T3 electrodes with an oscillating voltage at ~ 3.2 MHz. The resulting operation is a resonant motional squeezing operator. Motional squeezing can be used to amplify small displacements using a squeeze, displace, unsqueeze operation. Additionally, applying the motional squeezing simultaneously with a displacement can amplify that displacement. This allows the ODF spin-dependent force to be amplified by simultaneous motional squeezing, which can in-principle increase the ratio of the interaction strength to spontaneous emission [5, 50, 83, 84].

Parametric amplification is an extremely low hanging fruit for the experiment. All pieces of sensing weak electric fields and displacements with enhancement from parametric amplification have been demonstrated. In particular, a near ground state cooled squeezed state was characterized with 5.4 dB of squeezing below the standard quantum limit (SQL), and squeezing rates up to 15 kHz were demonstrated [50]. Predictions of 10 dB of enhancement in sensing small displacements are estimated from the achieved squeezing applied directly to the previous motional sensing results [6, 50]. Holding up the implementation of these pieces together was phase instability of the ODF and the magnet breaking. Now with improved boxing of the beam paths and the addition of tracking to the experiment the phase stability issues should be substantially mitigated. Additionally, COM frequency fluctuations limited previous results and are likely limited by in-plane temperatures which we can now substantially improve. With more reliable EIT cooling larger crystals could be also be used which were previously inaccessible due to the Lamb-Dicke parameter getting too large as the bandwidth of the axial modes got larger. Depending on the reduction in COM fluctuations possible with improved in-plane cooling, parametric amplification could potentially improve the ratio of the ODF spin-dependent force strength to spontaneous emission. These results could also be potentially enhanced using spin-squeezing.

8.3 Simulating p+ip superconductivity

One near-term experiment of interest is a quantum simulation of $p + ip$ superconductivity [85]. The simulation works on the principle of the Anderson pseudo-spin mapping, where the presence or absence of a cooper pair is mapped into spin up or down of each ion. In $p+ip$ superconductivity, there is a chiral nature to the pair creation process that is modeled in the Penning trap experiment using the rotation of the crystal to generate radially and azimuthally dependent potentials. In the original proposal [85], the ingredients necessary for the simulation were chiral spin state preparation, Raman beams with tunable radial dependence from the waist of the beams, and tilted ODF wavefronts to couple to the radial degree of freedom. This would require substantial overhead added to the experiment in terms of tunable waist Raman beams, and it is known that poorly aligned ODF beams generally increase decoherence. Additionally, the implementation relies on a number of rotating wave approximations that suggests going to higher rotation frequency to better tune out the counter rotating terms.

A natural question is whether the schemes of the DM can be used to circumvent these downsides. This may be possible using Bessel function modulation analogously to chapter 6. To demonstrate this, the spin state initialization can be achieved by driving the microwaves on a rotation sideband, the strength and radial dependence of which can be tuned by a linear gradient static in the lab frame. Before formally showing this, it is useful to write this in terms of phase modulation of the transverse $\vec{B}$ field from the microwave drive. The instantaneous frequency of the oscillating $\vec{B}$ field experienced by the ions can be written:

$$\omega_B(t) = \omega_0 + \omega_r + Uk\rho\cos(\phi - \omega_r t) \tag{8.1}$$

$$\vec{B}(t) = B_0\hat{x}e^{i((\omega_0+\omega_r)t - \frac{Uk\rho}{\omega_r}\sin(\phi-\omega_r t))} + c.c. \tag{8.2}$$

$$\vec{B}(t) = B_0\hat{x}e^{i\omega_0 t}\sum_{n=-\infty}^{\infty} J_n\left(-\frac{Uk\rho}{\omega_r}\right)e^{i((\omega_r - n\omega_r)t + n\phi)} + c.c. \tag{8.3}$$

$$\vec{B}(t) \approx -B_0\hat{x}e^{i\omega_0 t}J_1\left(\frac{Uk\rho}{\omega_r}\right)e^{i\phi} + c.c. \tag{8.4}$$

In equation 8.1, ω_0 is the qubit frequency of $\sim$ 124 GHz, ω_r is the rotation frequency of $\sim$ 180 kHz, U is the DM ACSS amplitude, and k is the k vector of the linear gradient applied by the DM statically in the lab frame. The final result of this Bessel function expansion is infinitely many fast rotating terms at multiples of the rotation frequency, along with a effective transverse $\vec{B}$ field that rotates with azimuthal coordinate ϕ and increases radially with $J_1(\frac{Uk\rho}{\omega_r})$ dependence. It is straightforward from this derivation to see that higher order m azimuthal patterns, and varying radial dependencies can be generated by varying the pattern set on the DM and choosing higher order rotation sidebands.

For a more formal derivation we can write the Hamiltonian of the simultaneous resonant microwave drive and static linear gradient from the DM.

$$H/\hbar = \sum_i B_0\cos(\omega_{mw}t)\hat{\sigma}_x^i/2 + (\omega_0 + Uk\rho_i\cos(\phi_i - \omega_r t))\hat{\sigma}_z^i/2. \tag{8.5}$$

Here the Rabi rate of the transverse field is given by B_0, with the microwave drive frequency ω_{mw}. The DM is set to give a linear gradient with wavelength k and ACSS amplitude U which is static in the lab frame. Using a unitary transformation $\hat{U}_1 = e^{i\omega_0\sigma_z^i/2}$ to go into the rotating frame of the qubit modifies the dynamics $\hat{H} \to \hat{U}\hat{H}\hat{U}^\dagger + i\hbar\dot{\hat{U}}\hat{U}^\dagger$. Using $\hat{\sigma}_x^i = \hat{\sigma}_+^i + \hat{\sigma}_-^i$ and taking a rotating wave approximation ignoring fast rotating ω_0 terms gives:

$$\hat{H}/\hbar \approx \sum_i \frac{B_0}{4}\left(\hat{\sigma}_+^i e^{i(\omega_0-\omega_{mw})t} + \hat{\sigma}_-^i e^{-i(\omega_0-\omega_{mw})t}\right) + Uk\rho_i\cos(\phi_i - \omega_r t)\hat{\sigma}_z^i/2 \tag{8.6}$$

A further rotating frame transformation can be made to remove the DM $\hat{\sigma}_z^i$ term. The corresponding unitary is given by $\hat{U}_2 = e^{-i\frac{Uk\rho_i}{\omega_r}\sin(\phi_i-\omega_r t)\sigma_z^i/2}$. The resulting Hamiltonian is given by:

$$\hat{H}/\hbar \approx \sum_i \frac{B_0}{4}\left(\hat{\sigma}_+^i e^{i(\omega_0-\omega_{mw})t} e^{-i\frac{Uk\rho_i}{\omega_r}\sin(\phi_i-\omega_r t)} + \hat{\sigma}_-^i e^{-i(\omega_0-\omega_{mw})t} e^{i\frac{Uk\rho_i}{\omega_r}\sin(\phi_i-\omega_r t)}\right) \tag{8.7}$$

$$= \sum_i \sum_{n=-\infty}^{\infty} \frac{B_0 J_n\left(\frac{Uk\rho_i}{\omega_r}\right)}{4}\left((-1)^n\hat{\sigma}_+^i e^{i(\omega_0-\omega_{mw}-n\omega_r)t+in\phi_i} + \hat{\sigma}_-^i e^{-i(\omega_0-\omega_{mw}+n\omega_r)t+in\phi_i}\right) \tag{8.8}$$

$$\approx \sum_i \frac{-B_0 J_1\left(\frac{Uk\rho_i}{\omega_r}\right)}{4}\left(\hat{\sigma}_+^i e^{i\phi_i} + \hat{\sigma}_-^i e^{-i\phi_i}\right). \tag{8.9}$$

To go from equation 8.7 to 8.8 the Jacobi-Anger identity $e^{iz\sin(\omega t)} = \sum_{-\infty}^{\infty} J_n(z)e^{in\omega t}$ was used. This gives an infinite series of transverse fields oscillating at multiples of the rotation frequency ω_r. By setting $\omega_{mw} = \omega_0 + \omega_r$, the first rotating sideband, only one J_1 term is resonant for each $\hat{\sigma}_\pm^i$ operator. All other terms are fast rotating at multiples of ω_r giving equation 8.9. The resulting Hamiltonian is a rotation of each ion i about a vector on the equator of the Bloch sphere with the orientation set by ϕ_i. The corresponding transverse field strength is reduced from B_0 by $J_1\left(\frac{Uk\rho_i}{\omega_r}\right)$, which is zero on center and could in principle be tuned to approach $J_1(0.586\pi) \sim 0.58$, the maximum of the J_1 Bessel function at the edge of the crystal (see section 6.5.4 for details). The fast rotating terms will be small assuming $B_0/\omega_r \ll 1$, and will all oscillate through a full 2π period when the Hamiltonian is applied for an arm time $\tau\omega_r = 2\pi l$ for an integer l.

Additionally, there are static gradients of the magnetic field in the plane, and Doppler shifts of the microwaves due to an in-plane component of the microwave k vector that could supply the static gradient term in the lab frame to generate the initial spin texture effectively without any source of decoherence or phase instability. The tradeoff will be that these are generally small and so will suffer from microwave decoherence for long application times. It remains unclear if this approach can be extended to incorporate the ODF spin-dependent force in the axial direction to couple the motion to the chiral spin interactions. If possible, this would remove a substantial amount of overhead to implement a simulation of $p + ip$ superconductivity.

8.4 Mølmer-Sørensen gate and 3D crystals

With increasing competition of 2D RF trap experiments which have now been demonstrated with up to 512 ions [22], a clear motivation is to move beyond 2D crystals. Quantum operations with the ODF are no longer straightforward when all ions are no longer in a single plane. Now each plane in the z direction will have a different phase of the ODF which can only coarsely be tuned by the angle of the ODF beams. As an alternative a different spin-motion entanglement can be engineered called a Mølmer-Sørensen (MS) gate. This spin-motion entanglement is driven using blue sideband (BSB) and red sideband (RSB) Raman transitions, driving gates about x or y instead of the $\hat{\sigma}_z$ gate of the ODF. The MS gate can be driven in two schemes depending on the frequency of the RSB and BSB beams relative to a carrier beam [86]. A "phase-sensitive" scheme occurs if the frequencies of the RSB and BSB can be described by $\omega = \omega_0 + \omega_{sf} \pm \omega_{mot}$ where ω_0 is the carrier beam frequency, ω_{sf} is the spin flip frequency to span the qubit, and ω_{mot} is the frequency of the motional mode. In contrast, if the beams' frequencies can be written $\omega = \omega_0 \pm \omega_{sf} \pm \omega_{mot}$ the scheme is called phase insensitive. The naming scheme refers to the phase of the corresponding spin rotation being sensitive to the ion's phase in the traveling wave of the beams. When in the phase insensitive scheme the two traveling waves of the BSB and RSB are in opposite directions causing the phase of the spin rotation to be determined by the relative phase of the BSB and RSB. In contrast the phase sensitive scheme will cause the phase of the spin rotation to vary at each plane of the crystal, which depends on the relative phase of the ion's positions in the co-propagating traveling waves [87].

In our system it is generally hard to span the qubit frequency of 124 GHz phase coherently between two lasers, and so a phase sensitive scheme is simpler only requiring 2 lasers. In the phase sensitive scheme the spin-dependent displacement's phase is phase insensitive to the ions position in the traveling waves. In turn the phase insensitive scheme is actually phase sensitive to the motional displacement. Using the phase sensitive scheme allows a spin-dependent displacement that is the same for all ions even at different planes in the z-axis, removing the difficulty of the ODF phase varying across the crystal. Additionally, the phase of the displacement is set by the beatnote of the BSB and RSB tones separated by only twice the motional frequency and with the beams co-propagating allowing potentially very high phase stability. The downside to this scheme is that each plane of the crystal will be rotated about a different spin axis, making global rotations from the microwaves incompatible with these pulses. Instead, global spin flips can be engineered using the same MS beams using one of the BSB/RSB beams no longer detuned by a motional sideband. The local rotation axis of all spins can then be set relative to the rotation axis of the MS interactions.

The beam setup for the MS is then exactly the same as the EIT cooling beams but now with two tones in one of the beams to set the BSB/RSB tones and the overall laser detuning must be much larger to do coherent operations. A key question to investigate the feasibility of using the MS gate for sensing and simulation applications in 3D crystals is how well near ground state cooling of the axial modes can work with 3D crystals. Additionally, the magnetron modes can acquire an axial component that may substantially increase the Lamb-Dicke parameter of the system without substantial cooling of the magnetron modes.

8.5 Bilayer crystals

In addition to larger system sizes possible with 3D crystals, interesting physics occurs with a bilayer crystal investigated in [81]. With the addition of an anharmonic C_4 quartic potential two "clean" planes of ions can approximately be produced with each plane having a small spread in the axial direction, with a scaffolding of ions on the outermost edge in between the planes. With this geometry the axial drumhead modes acquire a chiral nature to their motions, making it possible to investigate chiral spin-exchange models. Additionally, by having clean bi-layers the ODF rather than the MS gate was studied varying the angle of the ODF beams to vary the interactions between the bi-layers. Besides the difficulties associated with 3D crystals already mentioned, it is difficult to engineer a large C_4 value of the right sign while maintaining high axial trap frequencies in our current trap.

References

[1] C. M. Löschnauer, J. M. Toba, A. C. Hughes, S. A. King, M. A. Weber, R. Srinivas, R. Matt, R. Nourshargh, D. T. C. Allcock, C. J. Ballance, C. Matthiesen, M. Malinowski, and T. P. Harty, *Scalable, high-fidelity all-electronic control of trapped-ion qubits*, `https://arxiv.org/abs/2407.07694`, 2024 (Cited on p. 1).

[2] J. P. Gaebler, T. R. Tan, Y. Lin, Y. Wan, R. Bowler, A. C. Keith, S. Glancy, K. Coakley, E. Knill, D. Leibfried, and D. J. Wineland, "High-fidelity universal gate set for $^9\mathrm{Be}^+$ ion qubits", Phys. Rev. Lett. **117**, 060505 (2016) (Cited on p. 1).

[3] M. C. Marshall, D. A. R. Castillo, W. J. Arthur-Dworschack, A. Aeppli, K. Kim, D. Lee, W. Warfield, J. Hinrichs, N. V. Nardelli, T. M. Fortier, J. Ye, D. R. Leibrandt, and D. B. Hume, "High-stability single-ion clock with 5.5×10^{-19} systematic uncertainty", Phys. Rev. Lett. **135**, 033201 (2025) (Cited on p. 1).

[4] H. N. Hausser, J. Keller, T. Nordmann, N. M. Bhatt, J. Kiethe, H. Liu, I. M. Richter, M. von Boehn, J. Rahm, S. Weyers, E. Benkler, B. Lipphardt, S. Dörscher, K. Stahl, J. Klose, C. Lisdat, M. Filzinger, N. Huntemann, E. Peik, and T. E. Mehlstäubler, "$^{115}\mathrm{In}^+ - ^{172}\mathrm{Yb}^+$ coulomb crystal clock with 2.5×10^{-18} systematic uncertainty", Phys. Rev. Lett. **134**, 023201 (2025) (Cited on p. 1).

[5] S. C. Burd, R. Srinivas, J. J. Bollinger, A. C. Wilson, D. J. Wineland, D. Leibfried, D. H. Slichter, and D. T. C. Allcock, "Quantum amplification of mechanical oscillator motion", Science **364**, 1163 (2019) (Cited on pp. 1, 180).

[6] K. A. Gilmore, M. Affolter, R. J. Lewis-Swan, D. Barberena, E. Jordan, A. M. Rey, and J. J. Bollinger, "Quantum-enhanced sensing of displacements and electric fields with two-dimensional trapped-ion crystals", Science **373**, 673 (2021) (Cited on pp. 1, 2, 101, 181).

[7] T. Sägesser, S. Jain, P. Hrmo, A. Ferk, M. Simoni, Y. Cui, C. Mordini, D. Kienzler, and J. Home, *A 3-dimensional scanning trapped-ion probe*, 2024 (Cited on p. 1).

[8] G. Schneider, A. Mooser, M. Bohman, N. Schön, J. Harrington, T. Higuchi, H. Nagahama, S. Sellner, C. Smorra, K. Blaum, Y. Matsuda, W. Quint, J. Walz, and S. Ulmer, "Double-trap measurement of the proton magnetic moment at 0.3 parts per billion precision", Science **358**, 1081 (2017) (Cited on pp. 1, 10).

[9] X. Fan, T. G. Myers, B. A. D. Sukra, and G. Gabrielse, "Measurement of the electron magnetic moment", Phys. Rev. Lett. **130**, 071801 (2023) (Cited on pp. 1, 10).

[10] C. Smorra, S. Sellner, and M. B. et al., "A parts-per-billion measurement of the antiproton magnetic moment.", Nature **550**, 371 (2017) (Cited on pp. 1, 10).

[11] F. Heiße, F. Köhler-Langes, S. Rau, J. Hou, S. Junck, A. Kracke, A. Mooser, W. Quint, S. Ulmer, G. Werth, K. Blaum, and S. Sturm, "High-precision measurement of the proton's atomic mass", Phys. Rev. Lett. **119**, 033001 (2017) (Cited on pp. 1, 10).

[12] S. Sturm, F. Köhler, J. Zatorski, A. Wagner, Z. Harman, G. Werth, W. Quint, C. H. Keitel, and K. Blaum, "High-precision measurement of the atomic mass of the electron", en, Nature **506**, 467 (2014) (Cited on pp. 1, 10).

[13] J. W. Britton, B. C. Sawyer, A. C. Keith, C.-C. J. Wang, J. K. Freericks, H. Uys, M. J. Biercuk, and J. J. Bollinger, "Engineered two-dimensional Ising interactions in a trapped-ion quantum simulator with hundreds of spins", en, Nature **484**, 489 (2012) (Cited on p. 1).

[14] J. G. Bohnet, B. C. Sawyer, J. W. Britton, M. L. Wall, A. M. Rey, M. Foss-Feig, and J. J. Bollinger, "Quantum spin dynamics and entanglement generation with hundreds of trapped ions", Science **352**, 1297 (2016) (Cited on pp. 2, 62).

[15] M. Gärttner, J. G. Bohnet, A. Safavi-Naini, M. L. Wall, J. J. Bollinger, and A. M. Rey, "Measuring out-of-time-order correlations and multiple quantum spectra in a trapped-ion quantum magnet", en, Nature Physics **13**, 781 (2017) (Cited on p. 2).

[16] A. Safavi-Naini, R. J. Lewis-Swan, J. G. Bohnet, M. Gärttner, K. A. Gilmore, J. E. Jordan, J. Cohn, J. K. Freericks, A. M. Rey, and J. J. Bollinger, "Verification of a many-ion simulator of the dicke model through slow quenches across a phase transition", Phys. Rev. Lett. **121**, 040503 (2018) (Cited on p. 2).

[17] J. Cohn, A. Safavi-Naini, R. J. Lewis-Swan, J. G. Bohnet, M. Gärttner, K. A. Gilmore, J. E. Jordan, A. M. Rey, J. J. Bollinger, and J. K. Freericks, "Bang-bang shortcut to adiabaticity in the dicke model as realized in a penning trap experiment", New Journal of Physics **20**, 055013 (2018) (Cited on p. 2).

[18] E. Jordan, K. A. Gilmore, A. Shankar, A. Safavi-Naini, J. G. Bohnet, M. J. Holland, and J. J. Bollinger, "Near ground-state cooling of two-dimensional trapped-ion crystals with more than 100 ions", Phys. Rev. Lett. **122**, 053603 (2019) (Cited on pp. 2, 74).

[19] A. Shankar, E. Jordan, K. A. Gilmore, A. Safavi-Naini, J. J. Bollinger, and M. J. Holland, "Modeling near ground-state cooling of two-dimensional ion crystals in a penning trap using electromagnetically induced transparency", Phys. Rev. A **99**, 023409 (2019) (Cited on p. 2).

[20] D. J. Wineland, C. Monroe, W. M. Itano, D. Leibfried, B. E. King, and D. M. Meekhof, "Experimental issues in coherent quantum-state manipulation of trapped atomic ions", Journal of Research of the National Institute of Standards and Technology **103**, 259 (1998) (Cited on p. 6).

[21] D. Kiesenhofer, H. Hainzer, A. Zhdanov, P. C. Holz, M. Bock, T. Ollikainen, and C. F. Roos, "Controlling two-dimensional coulomb crystals of more than 100 ions in a monolithic radio-frequency trap", PRX Quantum **4**, 020317 (2023) (Cited on p. 6).

[22] S.-A. Guo, Y.-K. Wu, J. Ye, L. Zhang, W.-Q. Lian, R. Yao, Y. Wang, R.-Y. Yan, Y.-J. Yi, Y.-L. Xu, B.-W. Li, Y.-H. Hou, Y.-Z. Xu, W.-X. Guo, C. Zhang, B.-X. Qi, Z.-C. Zhou, L. He, and L.-M. Duan, "A site-resolved two-dimensional quantum simulator with hundreds of trapped ions", en, Nature **630**, 613 (2024) (Cited on pp. 6, 184).

[23] M. D'Onofrio, Y. Xie, A. J. Rasmusson, E. Wolanski, J. Cui, and P. Richerme, "Radial two-dimensional ion crystals in a linear paul trap", Phys. Rev. Lett. **127**, 020503 (2021) (Cited on p. 6).

[24] C.-C. J. Wang, A. C. Keith, and J. K. Freericks, "Phonon-mediated quantum spin simulator employing a planar ionic crystal in a penning trap", Phys. Rev. A **87**, 013422 (2013) (Cited on pp. 8, 15–17, 146).

[25] L. S. Brown and G. Gabrielse, “Geonium theory: physics of a single electron or ion in a penning trap”, Rev. Mod. Phys. **58**, 233 (1986) (Cited on pp. 10, 151).

[26] R. C. Davidson, *Physics of nonneutral plasmas* (Addison-Wesley Company, 1990) (Cited on p. 10).

[27] X.-P. Huang, F. Anderegg, E. M. Hollmann, C. F. Driscoll, and T. M. O’Neil, “Steady-state confinement of non-neutral plasmas by rotating electric fields”, Phys. Rev. Lett. **78**, 875 (1997) (Cited on pp. 13, 59).

[28] X.-P. Huang, J. J. Bollinger, T. B. Mitchell, W. M. Itano, and D. H. E. Dubin, “Precise control of the global rotation of strongly coupled ion plasmas in a penning trap”, Physics of Plasmas **5**, 1656 (1998) (Cited on p. 13).

[29] B. C. Sawyer, J. G. Bohnet, J. W. Britton, and J. J. Bollinger, “Reversing hydride-ion formation in quantum-information experiments with Be^+”, Phys. Rev. A **91**, 011401 (2015) (Cited on p. 13).

[30] D. H. E. Dubin, “Normal modes, rotational inertia, and thermal fluctuations of trapped ion crystals”, Physics of Plasmas **27**, 102107 (2020) (Cited on p. 15).

[31] A. Shankar, C. Tang, M. Affolter, K. Gilmore, D. H. E. Dubin, S. Parker, M. J. Holland, and J. J. Bollinger, “Broadening of the drumhead-mode spectrum due to in-plane thermal fluctuations of two-dimensional trapped ion crystals in a penning trap”, Phys. Rev. A **102**, 053106 (2020) (Cited on pp. 15, 18, 19, 137, 146).

[32] D. J. Wineland, R. E. Drullinger, and F. L. Walls, “Radiation-pressure cooling of bound resonant absorbers”, Phys. Rev. Lett. **40**, 1639 (1978) (Cited on pp. 19, 38).

[33] N. Shiga, W. M. Itano, and J. J. Bollinger, “Diamagnetic correction to the $^9\mathrm{be}^+$ ground-state hyperfine constant”, Phys. Rev. A **84**, 012510 (2011) (Cited on p. 20).

[34] D. M. Fairbank, A. L. Banducci, R. W. Gunkelman, J. B. VanArsdale, and S. M. Brewer, “Measurement of the unresolved $^9\mathrm{Be}^+$ $^2P_{3/2}$ hyperfine splittings using quantum-interference-enhanced state-selective repump spectroscopy”, Phys. Rev. A **109**, 012809 (2024) (Cited on p. 22).

[35] W. M. Itano and D. J. Wineland, “Precision measurement of the ground-state hyperfine constant of $^{25}\mathrm{Mg}^+$”, Phys. Rev. A **24**, 1364 (1981) (Cited on p. 22).

[36] S. B. Torrisi, J. W. Britton, J. G. Bohnet, and J. J. Bollinger, “Perpendicular laser cooling with a rotating-wall potential in a penning trap”, Phys. Rev. A **93**, 043421 (2016) (Cited on p. 39).

[37] W. Johnson, A. Shankar, J. Zaris, J. J. Bollinger, and S. E. Parker, “Rapid cooling of the in-plane motion of two-dimensional ion crystals in a penning trap to millikelvin temperatures”, Phys. Rev. A **109**, L021102 (2024) (Cited on pp. 40, 137).

[38] W. Johnson, B. Bullock, A. Shankar, J. Zaris, J. J. Bollinger, and S. E. Parker, *Adiabatic cooling of planar motion in a penning trap ion crystal to sub-millikelvin temperatures*, `https://arxiv.org/abs/2507.12429`, 2025 (Cited on p. 40).

[39] K. Gilmore, “Quantum sensing with large two-dimensional crystals of ions in a penning trap”, `https://scholar.colorado.edu/concern/graduate_thesis_or_dissertations/8910jv68k`, PhD thesis (University of Colorado Boulder, 2021) (Cited on p. 41).

[40] A. L. Carter, S. R. Muleady, A. Shankar, J. F. Lilieholm, B. B. Bullock, M. Affolter, A. M. Rey, and J. J. Bollinger, “Comparison of spontaneous emission in trapped-ion multiqubit gates at high magnetic fields”, Phys. Rev. A **107**, 042618 (2023) (Cited on p. 44).

[41] F. Diedrich, J. C. Bergquist, W. M. Itano, and D. J. Wineland, “Laser cooling to the zero-point energy of motion”, Phys. Rev. Lett. **62**, 403 (1989) (Cited on p. 50).

[42] G. Morigi, J. Eschner, and C. H. Keitel, “Ground state laser cooling using electromagnetically induced transparency”, Phys. Rev. Lett. **85**, 4458 (2000) (Cited on p. 50).

[43] I. I. Rabi, “Space quantization in a gyrating magnetic field”, Phys. Rev. **51**, 652 (1937) (Cited on p. 52).

[44] N. F. Ramsey, “A molecular beam resonance method with separated oscillating fields”, Phys. Rev. **78**, 695 (1950) (Cited on p. 54).

[45] J. W. Britton, J. G. Bohnet, B. C. Sawyer, H. Uys, M. J. Biercuk, and J. J. Bollinger, “Vibration-induced field fluctuations in a superconducting magnet”, Phys. Rev. A **93**, 062511 (2016) (Cited on p. 59).

[46] A. W. Trivelpiece and R. W. Gould, “Space charge waves in cylindrical plasma columns”, Journal of Applied Physics **30**, 1784 (1959) (Cited on p. 59).

[47] D. J. Heinzen, J. J. Bollinger, F. L. Moore, W. M. Itano, and D. J. Wineland, “Rotational equilibria and low-order modes of a non-neutral ion plasma”, Phys. Rev. Lett. **66**, 2080 (1991) (Cited on p. 59).

[48] J. J. Bollinger, J. W. Britton, and B. C. Sawyer, *Simulating quantum magnetism with correlated non-neutral ion plasmas*, tech. rep. 2658, `https://tf.nist.gov/general/pdf/2658.pdf` (National Institute of Standards and Technology (NIST), 2013) (Cited on p. 70).

[49] B. C. Sawyer, J. W. Britton, and J. J. Bollinger, “Spin dephasing as a probe of mode temperature, motional state distributions, and heating rates in a two-dimensional ion crystal”, Phys. Rev. A **89**, 033408 (2014) (Cited on p. 73).

[50] M. Affolter, W. Ge, B. Bullock, S. C. Burd, K. A. Gilmore, J. F. Lilieholm, A. L. Carter, and J. J. Bollinger, “Toward improved quantum simulations and sensing with trapped two-dimensional ion crystals via parametric amplification”, Phys. Rev. A **107**, 032425 (2023) (Cited on pp. 74, 180, 181).

[51] R. H. Dicke, “Coherence in spontaneous radiation processes”, Phys. Rev. **93**, 99 (1954) (Cited on pp. 83, 86).

[52] R. J. Lewis-Swan, S. R. Muleady, D. Barberena, J. J. Bollinger, and A. M. Rey, “Characterizing the dynamical phase diagram of the dicke model via classical and quantum probes”, Phys. Rev. Res. **3**, L022020 (2021) (Cited on pp. 84–86).

[53] J. A. Muniz, D. Barberena, R. J. Lewis-Swan, D. J. Young, J. R. K. Cline, A. M. Rey, and J. K. Thompson, “Exploring dynamical phase transitions with cold atoms in an optical cavity”, Nature **580**, 602 (2020) (Cited on pp. 84, 86).

[54] J. Zhang, G. Pagano, P. W. Hess, A. Kyprianidis, P. Becker, H. Kaplan, A. V. Gorshkov, Z.-X. Gong, and C. Monroe, “Observation of a many-body dynamical phase transition with a 53-qubit quantum simulator”, en, Nature **551**, 601 (2017) (Cited on p. 84).

[55] H. Lipkin, N. Meshkov, and A. Glick, “Validity of many-body approximation methods for a solvable model: (i). exact solutions and perturbation theory”, Nuclear Physics **62**, 188 (1965) (Cited on p. 85).

[56] M. A. Norcia, M. N. Winchester, J. R. K. Cline, and J. K. Thompson, “Superradiance on the millihertz linewidth strontium clock transition”, Science Advances **2**, e1601231 (2016) (Cited on p. 86).

[57] R. J. Lewis-Swan, A. Safavi-Naini, J. J. Bollinger, and A. M. Rey, “Unifying scrambling, thermalization and entanglement through measurement of fidelity out-of-time-order correlators in the Dicke model”, en, Nature Communications **10**, 1581 (2019) (Cited on p. 86).

[58] J. Schachenmayer, A. Pikovski, and A. M. Rey, “Many-body quantum spin dynamics with monte carlo trajectories on a discrete phase space”, Phys. Rev. X **5**, 011022 (2015) (Cited on p. 93).

[59] D. Barberena, S. R. Muleady, J. J. Bollinger, R. J. Lewis-Swan, and A. M. Rey, “Fast generation of spin squeezing via resonant spin-boson coupling”, Quantum Science and Technology **9**, 025013 (2024) (Cited on pp. 97, 101, 179).

[60] Y. Zhang, J. C. Zuñiga Castro, and R. J. Lewis-Swan, “Harnessing quantum chaos in spin-boson models for all-purpose quantum-enhanced sensing”, Phys. Rev. Res. **7**, 013227 (2025) (Cited on pp. 97, 101).

[61] A. Qu, B. Evrard, J. Dalibard, and F. Gerbier, “Probing spin correlations in a bose-einstein condensate near the single-atom level”, Phys. Rev. Lett. **125**, 033401 (2020) (Cited on p. 97).

[62] B. Lücke, M. Scherer, J. Kruse, L. Pezzé, F. Deuretzbacher, P. Hyllus, O. Topic, J. Peise, W. Ertmer, J. Arlt, L. Santos, A. Smerzi, and C. Klempt, “Twin matter waves for interferometry beyond the classical limit”, Science **334**, 773 (2011) (Cited on p. 97).

[63] E. M. Bookjans, C. D. Hamley, and M. S. Chapman, “Strong quantum spin correlations observed in atomic spin mixing”, Phys. Rev. Lett. **107**, 210406 (2011) (Cited on p. 97).

[64] A. T. Black, E. Gomez, L. D. Turner, S. Jung, and P. D. Lett, “Spinor dynamics in an antiferromagnetic spin-1 condensate”, Phys. Rev. Lett. **99**, 070403 (2007) (Cited on p. 97).

[65] L. Zhao, J. Jiang, T. Tang, M. Webb, and Y. Liu, “Dynamics in spinor condensates tuned by a microwave dressing field”, Phys. Rev. A **89**, 023608 (2014) (Cited on p. 97).

[66] K. Kim, J. Hur, S. Huh, S. Choi, and J.-y. Choi, “Emission of spin-correlated matter-wave jets from spinor bose-einstein condensates”, Phys. Rev. Lett. **127**, 043401 (2021) (Cited on p. 97).

[67] P. Hayden and J. Preskill, “Black holes as mirrors: quantum information in random subsystems”, Journal of High Energy Physics **2007**, 120 (2007) (Cited on pp. 101, 179).

[68] A. M. Polloreno, A. M. Rey, and J. J. Bollinger, “Individual qubit addressing of rotating ion crystals in a penning trap”, Phys. Rev. Res. **4**, 033076 (2022) (Cited on pp. 104, 105, 107).

[69] B. Hemmerling, F. Gebert, Y. Wan, and P. O. Schmidt, “A novel, robust quantum detection scheme”, New Journal of Physics **14**, 023043 (2012) (Cited on p. 120).

[70] R. N. Wolf, J. H. Pham, J. Y. Z. Jee, A. Rischka, and M. J. Biercuk, “Efficient site-resolved imaging and spin-state detection in dynamic two-dimensional ion crystals”, Phys. Rev. Appl. **21**, 054067 (2024) (Cited on p. 135).

[71] B. J. McMahon, K. R. Brown, C. D. Herold, and B. C. Sawyer, “Individual-ion addressing and readout in a penning trap”, Phys. Rev. Lett. **133**, 173201 (2024) (Cited on p. 135).

[72] M. Ammenwerth, H. Timme, V. Giardini, R. Tao, F. Gyger, O. Lib, D. Berndt, D. Kourkoulos, T. Rom, I. Bloch, and J. Zeiher, “Dynamical spatial light modulation in the ultraviolet spectral range”, Phys. Rev. Appl. **24**, 034031 (2025) (Cited on p. 136).

[73] E. A. Cornell, R. M. Weisskoff, K. R. Boyce, and D. E. Pritchard, "Mode coupling in a penning trap: π pulses and a classical avoided crossing", Phys. Rev. A **41**, 312 (1990) (Cited on p. 151).

[74] H. F. Powell, D. M. Segal, and R. C. Thompson, "Axialization of laser cooled magnesium ions in a penning trap", Phys. Rev. Lett. **89**, 093003 (2002) (Cited on p. 151).

[75] R. J. Hendricks, E. S. Phillips, D. M. Segal, and R. C. Thompson, "Laser cooling in the penning trap: an analytical model for cooling rates in the presence of an axializing field", Journal of Physics B: Atomic, Molecular and Optical Physics **41**, 035301 (2008) (Cited on p. 152).

[76] E. S. Phillips, R. J. Hendricks, A. M. Abdulla, H. Ohadi, D. R. Crick, K. Koo, D. M. Segal, and R. C. Thompson, "Dynamics of axialized laser-cooled ions in a penning trap", Phys. Rev. A **78**, 032307 (2008) (Cited on p. 152).

[77] G. Stutter, P. Hrmo, V. Jarlaud, M. K. Joshi, J. F. Goodwin, and R. C. Thompson, "Sideband cooling of small ion coulomb crystals in a penning trap", Journal of Modern Optics **65**, 549 (2018) (Cited on p. 152).

[78] P. Hrmo, M. K. Joshi, V. Jarlaud, O. Corfield, and R. C. Thompson, "Sideband cooling of the radial modes of motion of a single ion in a penning trap", Phys. Rev. A **100**, 043414 (2019) (Cited on p. 152).

[79] P.-Y. Hou, J. J. Wu, S. D. Erickson, G. Zarantonello, A. D. Brandt, D. C. Cole, A. C. Wilson, D. H. Slichter, and D. Leibfried, "Indirect cooling of weakly coupled trapped-ion mechanical oscillators", Phys. Rev. X **14**, 021003 (2024) (Cited on p. 153).

[80] P. Hou, J. Wu, and S. E. et al., "Coherent coupling and non-destructive measurement of trapped-ion mechanical oscillators.", Nat. Phys. **20**, 1636 (2024) (Cited on p. 153).

[81] S. Hawaldar, P. Shahi, A. L. Carter, A. M. Rey, J. J. Bollinger, and A. Shankar, "Bilayer crystals of trapped ions for quantum information processing", Phys. Rev. X **14**, 031030 (2024) (Cited on pp. 156, 185).

[82] C. Tang, A. Shankar, D. Meiser, D. H. E. Dubin, J. J. Bollinger, and S. E. Parker, "Equilibration of the planar modes of ultracold two-dimensional ion crystals in a penning trap", Phys. Rev. A **104**, 023325 (2021) (Cited on p. 165).

[83] W. Ge, B. C. Sawyer, J. W. Britton, K. Jacobs, M. Foss-Feig, and J. J. Bollinger, "Stroboscopic approach to trapped-ion quantum information processing with squeezed phonons", Phys. Rev. A **100**, 043417 (2019) (Cited on p. 180).

[84] W. Ge, B. C. Sawyer, J. W. Britton, K. Jacobs, J. J. Bollinger, and M. Foss-Feig, "Trapped ion quantum information processing with squeezed phonons", Phys. Rev. Lett. **122**, 030501 (2019) (Cited on p. 180).

[85] A. Shankar, E. A. Yuzbashyan, V. Gurarie, P. Zoller, J. J. Bollinger, and A. M. Rey, "Simulating dynamical phases of chiral $p + ip$ superconductors with a trapped ion magnet", PRX Quantum **3**, 040324 (2022) (Cited on p. 181).

[86] P. C. Haljan, K.-A. Brickman, L. Deslauriers, P. J. Lee, and C. Monroe, "Spin-dependent forces on trapped ions for phase-stable quantum gates and entangled states of spin and motion", Phys. Rev. Lett. **94**, 153602 (2005) (Cited on p. 184).

[87] C. Monroe, *Primer on gates in trapped ions*, Lecture notes, Boulder School, Available at boulderschool.yale.edu, 2020 (Cited on p. 184).

Appendix A

Classical derivation of spin dephasing for a radial gradient

This appendix gives an alternative classical derivation of spin dephasing compared to the quantum calculation given in 4.3.5. Specifically, the calculation is done for coherent and thermal states using a radial gradient for comparison with the result in chapter 7.

A.1 Radial time dependence of in-plane motion

As a more careful derivation of equation 7.7, assume an ion crystal with only a single in-plane mode m initialized with an energy $\bar{n}\hbar\omega_m \approx k_B T$[1] with all other modes at zero temperature. The single mode will oscillate at ω_m with a phase ϕ_{mot} that is randomized over for a thermal state. For brevity let $\theta = \omega_m t + \phi_{mot}$. The mode amplitude is given by $\tilde{\rho}_m = \tilde{\rho}_{0,m}\sqrt{2\bar{n}+1} = \sqrt{\frac{\hbar(2\bar{n}+1)}{(1+R_m)m\omega_m}}$ (equation 7.8), where $\tilde{\rho}_{0,m}$ is the rms ground state wavefunction size for mode m, which corresponds to the total rms motion of all ions. Specifically, let the eigenvector of all ion's (x, y) participations in the mode be given by $\vec{u}$ normalized such that $|\vec{u}| = 1$. The x, y, coordinate of a given ion i's displacement is $\delta\rho_i = \sqrt{2}\tilde{\rho}_m \operatorname{Re}\left[\begin{pmatrix} u_{x,i} \\ u_{y,i} \end{pmatrix} e^{i\theta}\right]$, where $\operatorname{Re}(\alpha) = \frac{1}{2}(\alpha+\alpha^*)$ is the real part of the complex argument. As an example, for the center of mass cyclotron mode $\vec{u}_i = \begin{pmatrix} u_{x,i} \\ u_{y,i} \end{pmatrix} = \frac{1}{\sqrt{2N}}\begin{pmatrix} 1 \\ -i \end{pmatrix}$ for all ions i, giving $\delta\rho_{tot}^2 = \sum_i \delta\rho_i^2 = \sum_i \tilde{\rho}_m^2(\cos(\theta)^2 + \sin(\theta)^2)/N = \tilde{\rho}_m^2$ confirming the definition of the total rms motion of the mode. The radial position as a function of time for of an ion i with

---

[1] Note for a thermal state of average mode occupation $\bar{n}$ the temperature is defined $\frac{1}{\bar{n}} = e^{\hbar\omega_m/k_B T} - 1$, which agrees with $\bar{n} = k_B T/\hbar\omega_m$ for large temperatures but disagrees when near or below the ground state $\bar{n} \lesssim 1$.

equilibrium position $\vec{\rho}_0 = \begin{pmatrix} x_0 \\ y_0 \end{pmatrix}$ ($\rho_0 = |\vec{\rho}_0|$) is then given by

$$\vec{\rho}_i(t) = \vec{\rho}_0 + \sqrt{2}\tilde{\rho}_m \operatorname{Re}[\vec{u}_i e^{i\theta}] \tag{A.1}$$

$$\rho_i^2(t) = (x_0 + \sqrt{2}\tilde{\rho}_m \operatorname{Re}[u_{x,i}e^{i\theta}])^2 + (y_0 + \sqrt{2}\tilde{\rho}_m \operatorname{Re}[u_{y,i}e^{i\theta}])^2 \tag{A.2}$$

$$= \rho_0^2 + 2\tilde{\rho}_m^2(\operatorname{Re}[u_{x,i}e^{i\theta}]^2 + \operatorname{Re}[u_{y,i}e^{i\theta}]^2) + 2\sqrt{2}\tilde{\rho}_m \operatorname{Re}[x_0 u_{x,i}e^{i\theta} + y_0 u_{y,i}e^{i\theta}] \tag{A.3}$$

$$= \rho_0^2 + \tilde{\rho}_m^2((\vec{u}_i \cdot \vec{u}_i)e^{2i\theta} + c.c. + 2|\vec{u}_i|^2)/2 + \sqrt{2}\tilde{\rho}_m(\vec{\rho}_0 \cdot \vec{u}_i e^{i\theta} + c.c), \tag{A.4}$$

where *c.c* stands for complex conjugate of the preceding term. From here it is worth pointing out a few limits of this equation. The most useful case is when an ion is located off center, with a small enough energy to approximate $\tilde{\rho}_m \ll \rho_0$. In this limit $\rho_i(t) = \sqrt{\rho_i^2(t)}$ is given by Taylor expanding the square root to first order in $\tilde{\rho}_m$

$$\rho_i(t) \approx \rho_0 + \tilde{\rho}_m \frac{\vec{\rho}_0 \cdot \vec{u}_i}{\sqrt{2}\rho_0} e^{i\theta} + c.c \tag{A.5}$$

$$= \rho_0 + \tilde{\rho}_m \frac{\sqrt{2}|\vec{\rho}_0 \cdot \vec{u}_i|}{\rho_0} \cos(\omega_m t + \phi_{mot} + \arg(\vec{\rho}_0 \cdot \vec{u}_i)), \tag{A.6}$$

where $\arg(\alpha)$ is the phase ϕ_{arg} of a complex argument $\alpha = Ae^{i\phi_{arg}}$ for real positive A. For example, $\vec{u}_i = \frac{1}{\sqrt{2N}}\begin{pmatrix} 1 \\ -i \end{pmatrix}$ for the cyclotron COM mode for an ion i, whereas $\vec{\rho}_0$ will be a vector pointing along the equilibrium position for an ion at $\vec{\rho}_0 = \begin{pmatrix} x_0 \\ y_0 \end{pmatrix}$. Therefore the phase of each ion's radial time dependence is $\phi_{mot} + \arg(x_0 - iy_0) = \phi_{mot} - \phi_0$ where ϕ_0 is the equilibrium position of the ion in polar r, ϕ coordinates. If a coherent COM motional state was prepared and the motion was sensed phase coherently, the resulting spin precession then will have a linear gradient across it due to the ϕ_0 azimuthal dependence of the relative phase to the deformable mirror (DM) beams phase, in addition to radial dependence from the kr_i factors (see equation 7.5). Since these phase factors will be averaged over in all calculations the azimuthal phase factors $\phi_{mot} + \arg(\vec{\rho}_0 \cdot \vec{u}_i)$ have been replaced with a catch all factor $\phi_{i,m}$ to emphasize each ion i in mode m may have a different phase factor of it's motion in the radial direction.

If the ions are not off center this limiting form is not correct. For an ion exactly on center ($\rho_0 = 0$) the radial time dependence is

$$\rho_i(t) = \tilde{\rho}_m \sqrt{|\vec{u}_i \cdot \vec{u}_i| \cos(2\omega_m t + 2\phi_{mot} + \arg(\vec{u}_i \cdot \vec{u}_i)) + |\vec{u}_i|^2}. \tag{A.7}$$

The factor $|\vec{u}_i \cdot \vec{u}_i|$ corresponds to a measure of the ellipticity of the motion, with uniform circular motion like the COM mode having 0 ellipticity ($\vec{u} \cdot \vec{u} = 0$), making $\rho(t) = \tilde{\rho}_m \frac{1}{\sqrt{N}}$ a constant. For non-zero ellipticity expanding the square root gives oscillating motion at multiples of $2\omega_m$, with higher order multiples negligible until the ellipticity is no longer small $|\vec{u}_i \cdot \vec{u}_i| \sim |\vec{u}_i|^2$. For the highest ellipticity motion corresponding to real eigenvectors $|\vec{u}_i \cdot \vec{u}_i| = |\vec{u}_i|^2$ (oscillatory instead of rotational motion), this motion is $\rho_i(t) = \sqrt{2}\tilde{\rho}_m |\cos(\omega_m t + \phi_{mot})|$, with the absolute value stemming from the fact the ρ coordinate is positive definite and gives many harmonics at even multiples of the mode frequency.

A.2 Spin dephasing from coherent and thermal states

Applying a single mode approximation of $\epsilon_i = k_r \tilde{\rho}_{i,m}(t)$ (equation 7.6) using the formalism of the preceding appendix section gives our starting Hamiltonian equation 7.5 reproduced below and expanded for a single mode:

$$H/\hbar \approx \sum_i U \hat{\sigma}_z^i [\sin(k_r r_i + \mu t) + \epsilon_i(t) \cos(k_r r_i + \mu t)] \tag{A.8}$$

$$\approx \sum_i U \hat{\sigma}_z^i [\sin(k_r r_i + \mu t) + k_r \kappa_{i,m} \frac{\sqrt{2}\tilde{\rho}_m}{\sqrt{N}} \cos(\omega_m t + \phi_{i,m}) \cos(k_r r_i + \mu t)]. \tag{A.9}$$

Assuming no spin motion entanglement the Hamiltonian can be directly integrated for some application time τ to give differential spin precession angles between $|\uparrow\rangle$ and $|\downarrow\rangle$:

$$\theta_i = \int_0^\tau 2U \left[\sin(k_r r_i + \mu t) + k_r \kappa_{i,m} \frac{\sqrt{2}\tilde{\rho}_m}{\sqrt{N}} \cos(\omega_m t + \phi_{i,m}) \cos(k_r r_i + \mu t)\right] \tag{A.10}$$

$$= 2U \left[-\frac{1}{\mu} \cos(k_r r_i + \mu t) + \sum_{\pm} \frac{k_r \kappa_{i,m} \tilde{\rho}_m}{\sqrt{2N}(\mu \pm \omega_m)} \sin((\mu \pm \omega_m)t + k_r r_i \pm \phi_{i,m})\right]_{t=0}^{t=\tau}. \tag{A.11}$$

Note as described in chapter 7, the factor of $2U$ is due to the definition of U and the Pauli operator $\hat{\sigma}_z^i$ such that U is half the differential ACSS in units of radians/second. Ideally to sense motion the first term, from here on called the equilibrium term arising from the applied ACSS at the equilibrium position, should be canceled while driving up the term proportional to $\tilde{\rho}$ over time. The second term for the $-$ sign case in the sum over $\pm$ can be driven up over time by setting $\mu = \omega_m + \delta$ where δ is some detuning from the mode ideally small compared to $2\pi/\tau$. The equilibrium term can be ignored if $\mu \gg U$, but this is not valid for the low frequency magnetron modes. One scheme to cancel the equilibrium term is to set $\mu\tau = 2\pi l$ where l is some integer, which causes $\cos(k_r r_i + \mu\tau) = \cos(k_r r_i)$ and is therefore canceled in a single application time τ. Alternatively, if two arms of the DM are applied in a spin echo sequence with a phase advance $\phi_{adv} = -\mu(\tau + t_\pi)$ where t_π is the pi time of the echo pulse between DM applications the equilibrium term is canceled. Using the identity $\cos(a) - \cos(b) = -2\sin(\frac{a+b}{2})\sin(\frac{a-b}{2})$ gives precession angles from the equilibrium term

$$\theta_{i,eq} = \frac{4U}{\mu}[\sin(k_r r_i + \mu\tau/2)\sin(\mu\tau/2)] - \frac{4U}{\mu}[\sin(k_r r_i + \mu\tau/2 + \mu(\tau + t_\pi) + \phi_{adv})\sin(\mu\tau/2)] \tag{A.12}$$

$$= \frac{4U}{\mu}\sin(\mu\tau/2)[\sin(k_r r_i + \mu\tau/2) - \sin(k_r r_i + \mu\tau/2 + \mu(\tau + t_\pi) - \mu(\tau + t_\pi))] = 0. \tag{A.13}$$

Effectively the second arm accumulates the same phase as the first by phase lagging to the same starting phase as the first arm, canceling the two arms due to the spin echo. Additionally, it is also clear from this form how setting $\mu\tau = 2\pi l$ satisfies canceling the equilibrium term for the two arms, not necessitating a varying phase advance which depends on the beatnote frequency μ.

Focusing now on the term of interest proportional to $\tilde{\rho}_m$, letting $\Phi = k_r r_i - \phi_{i,m}$ for brevity, and ignoring the fast oscillating term at $\omega_m + \mu$, a spin echo sequence with a phase advance ϕ_{adv} in the second arm gives precession angles

$$\begin{aligned}\theta_{i,sig} = {} & \frac{\sqrt{2}U k_r \kappa_{i,m} \tilde{\rho}_m}{\delta\sqrt{N}}[\sin(\Phi + \delta\tau) - \sin(\Phi) \qquad \text{(A.14)}\\ & - \sin(\Phi + \delta(2\tau + t_\pi) + \phi_{adv}) + \sin(\Phi + \delta(\tau + t_\pi) + \phi_{adv})]\\ = {} & -\frac{\sqrt{2}U k_r \kappa_{i,m} \tilde{\rho}_m}{\delta\sqrt{N}}\mathrm{Im}[e^{i(k_r r_i - \phi_{i,m})}(1 - e^{i\theta_1})(1 - e^{i\theta_2})], \qquad \text{(A.15)}\end{aligned}$$

where $\theta_1 = \delta\tau, \theta_2 = \delta(\tau + t_\pi) + \phi_{adv}$. From here a bright fraction can be calculated assuming a coherent state, as derived so far, but now randomizing the phase of the motion $\phi_{i,m}$, equivalent to randomizing the relative phase of the DM beatnote.

$$\langle P_\uparrow \rangle_{coh} \approx \frac{1}{2}\left[1 - e^{-2\Gamma\tau}\sum_i \frac{1}{N}\left\langle \cos(\theta_{i,sig})\right\rangle_{\phi_{i,m}}\right], \qquad \text{(A.16)}$$

where $\langle P_\uparrow \rangle_{coh}$ represents the average population averaged over all ions and for a randomized coherent state motional phase, and $\langle \cos(\theta_{i,sig})\rangle_{\phi_{i,m}}$ represents an average over the coherent state motional phase. Evaluating the average of the cosine term over the motional phase gives

$$\begin{aligned}\langle \cos(\theta_{i,sig})\rangle_{\phi_{i,m}} &= \frac{1}{2\pi}\int_0^{2\pi} \cos(\theta_{i,sig})d\phi_{i,m} \qquad \text{(A.17)}\\ &= \frac{1}{2\pi}\int_0^{2\pi} \cos(|\theta_{i,sig}|\sin(k_r r_i - \phi_{i,m} + \arg[(1 - e^{i\theta_1})(1 - e^{i\theta_2})])d\phi_{i,m} \qquad \text{(A.18)}\\ &= J_0(|\theta_{i,sig}|), \qquad \text{(A.19)}\end{aligned}$$

where arg is defined as above to be the phase of a complex argument, and the identity $J_0(x) = \frac{1}{2\pi}\int_0^{2\pi}\cos(x\cos(\theta))d\theta$ was used to identify the Bessel function form. The result of equation A.16 with the functional form of equation A.19 is in agreement with the results of equations 7.13,7.15 in chapter 7.

To calculate the result for the thermal state, the cosine averaging now needs to be done over a thermal state distribution of $\tilde{\rho}$ rather than a fixed amplitude coherent state. A thermal distribution at average mode occupation $\bar{n}$ in terms of coherent states can be written as

$$\hat{\rho}_{den} = \frac{1}{\bar{n}\pi} \int e^{-|\beta|^2/\bar{n}} \left|\beta\right\rangle \left\langle\beta\right| d^2\beta, \tag{A.20}$$

where $\hat{\rho}_{den}$ is a density matrix over coherent states $|\beta\rangle$. Associating $\tilde{\rho}_m = \sqrt{2\bar{n}+1}\tilde{\rho}_{0,m}$, where $\tilde{\rho}_{0,m}$ is the rms ground state wavefunction size over all ions in mode m, with the phase factor identified in equation A.18 gives a coherent state representation to average over in the thermal distribution $\beta = \sqrt{\bar{n}}e^{i\phi}$ where ϕ is the phase factor averaged over in equation A.18. Let $\alpha_{T,i} = \frac{Uk_r\kappa_{i,m}\tilde{\rho}_{0,m}}{2\delta\sqrt{N}}|(1-e^{i\theta_1})(1-e^{i\theta_2})|e^{i\phi}$.

$$\langle\hat{\sigma}_z^i\rangle_{th} = \frac{1}{\bar{n}\pi} \int e^{-|\beta|^2/\bar{n}} \cos(Im[4\alpha_T\beta]) d^2\beta. \tag{A.21}$$

Converting the integral from complex values β to $\beta = re^{i\theta}$ and integrating over r, θ gives

$$\langle\hat{\sigma}_z^i\rangle_{th} = \frac{1}{\bar{n}\pi} \int\int re^{-r^2/\bar{n}} \cos(4|\alpha_T| r\cos(\theta)) dr d\theta. \tag{A.22}$$

Integrating first over θ using the previously utilized Bessel function identity gives

$$\langle\hat{\sigma}_z^i\rangle_{th} = \frac{2}{\bar{n}} \int re^{-r^2/\bar{n}} J_0(4|\alpha_T| r) dr. \tag{A.23}$$

Finally using the integral solution $\int_0^\infty re^{-ar^2}J_0(br)dr = \frac{1}{2a}e^{-b^2/4a}$ with $a = \frac{1}{\bar{n}}$ and $b = 4|\alpha_T|$ gives

$$\langle\hat{\sigma}_z^i\rangle_{th} = e^{-4|\alpha_T|^2\bar{n}}. \tag{A.24}$$